MECHANICAL MODELING OF BRAIN AND BREAST TISSUE

A Dissertation
Presented to
The Academic Faculty

by

Cem Ozan

In Partial Fulfillment
of the Requirements for the Degree
Doctor of Philosophy in the
School of Civil and Environmental Engineering

Georgia Institute of Technology
April 2008

MECHANICAL MODELING OF BRAIN AND BREAST TISSUE

Approved by:

Dr. Leonid N. Germanovich, Advisor
School of Civil and Environmental Engineering
Georgia Institute of Technology

Dr. Srinivasan Mukundan
Department of Radiology –Neuroradiology
Duke University

Dr. Oskar Skrinjar
School of Biomedical Engineering
Georgia Institute of Technology

Dr. Alexander M. Puzrin
Institute of Geotechnical Engineering
Swiss Federal Institute of Technology

Dr. Paul W. Mayne
School of Civil and Environmental Engineering
Georgia Institute of Technology

Dr. Glenn J. Rix
School of Civil and Environmental Engineering
Georgia Institute of Technology

Date Approved: January 31, 2007

ACKNOWLEDGEMENTS

I am immensely grateful to Dr. Leonid Germanovich for his generous guidance and mentoring during my work on this thesis. Working with Dr. Puzrin on the constitutive modeling of engineering materials has been an invaluable experience. Likewise, working with Dr. Skrinjar greatly enhanced my understanding of state-of-the-art medical image analysis.

I am also indebted to the members of the Rock and Fracture Mechanics Laboratory at Georgia Tech for their technical and personal support throughout this work. In particular, I thank Gence Genc, Jongwon Choi, Devon Gwaba, Sihyun Kim, Pierre Ramondenc, Chanin Ruangthaveekoon, Robert Hurt, and Ruiting Wu for many days and nights spent during the several years of my graduate studies. I would like to extend my thanks to my friend, Fikret Atalay, for his support and Ms. Anne Balter for proofreading this dissertation. I am especially grateful to Robert Hurt who kindly edited the manuscript of this thesis.

I would like to thank my Ph.D. dissertation committee members, Drs. L.N. Germanovich, O. Skrinjar, P.W. Mayne, S. Mukundan, A.M. Puzrin, and G.J. Rix, for taking their valuable time and reading this thesis.

Last but not least, none of this would have been possible without the love, the patience and immeasurable understanding of my family. I thank my mother and father who provided me the freedom to pursue my goals. I am particularly grateful to my brother, Ercument Ozan, for his support and care over the last four years.

The work on this dissertation has been supported by the National Institutes of Health (Grant numbers EB02957 and LM08128) and Schlumberger Foundation.

TABLE OF CONTENTS

LIST OF TABLES

Page

LIST OF FIGURES

Page

SUMMARY

Soft tissue is a material that supports, surrounds, or connects organs or structures of the human body. Frequently, injuries and diseases (such as tumors) that develop in soft tissue are most problematic to treat because it is difficult to diagnose changes in a highly deformable material under the skin. This dissertation focuses on three inter-related topics: (1) characterization of mechanical properties of human brain tissue *in-vivo* for applications in therapy and neurosurgery; (2) effect of mechanical properties of breast tissue on female breast deformation; and (3) mechanics of subdural hematoma caused by neurosurgical procedures.

Currently, image guided neurosurgery is based on pre-operative (non-deformed) brain images, even though the brain undergoes considerable deformations when the skull is opened. This effect is called "brain shift," and such deformations strongly affect many high-risk neurosurgical operations. Here, we propose a new approach for defining mechanical properties of the brain tissue *in-vivo* by taking MRI or CT images of a brain response to ventriculostomy operations, i.e., the relief of the elevated intracranial pressure in the ventricular cavities. Then, based on 3-D image analysis, the displacement fields are recovered from these images. Constitutive parameters of the brain tissue are determined using inverse analysis and a numerical method allowing for computations of large-strain deformations. We tested this approach in controlled laboratory experiments with silicone brain models mimicking brain geometry, mechanical properties, and boundary conditions. The ventriculostomy was simulated by inflating and deflating internal cavities that model cerebral ventricles. Subsequently, the silicone brain model

was described by a hyperelastic (neo-Hookean) material. The obtained mechanical properties have been verified with direct laboratory tests. Properties of real brain tissue are more complicated, but the proposed approach requires only conventional medical images collected before and after ventriculostomy.

Breast cancer is the second most prevalent cancer in women, and an operative mastectomy, in which breast tissue is removed, is frequently a part of the treatment. Women often choose to follow a mastectomy with a reconstruction surgery using a breast implant. Furthermore, there is a growing demand for breast augmentation for the sake of aesthetic improvement. In this dissertation, we also developed a quantitative large-strain 3-D mechanical model of female breast deformation. The results show that the stiffness of skin and the constitutive parameters of the breast tissue are important factors affecting breast shape. Our results also suggest that the published Mooney-Rivlin parameters of breast tissue are underestimated by at least one or two orders of magnitude. Scale analysis, representing female breast as a cantilever beam, confirms these conclusions.

Subdural hematoma (tearing and bleeding between scull and brain) is one of the major complications of the ventriculostomy operations. Understanding the mechanism of subdural hematoma is critically important for development of more effective medical treatments. In this work, we developed a simple, spherically-symmetrical poroelastic model of the ventriculostomy operation and studied brain response to the pressure change in the ventricles. The observed effect of the material properties on the occurrence of subdural hematoma may be useful for making clinical decisions.

CHAPTER I

INTRODUCTION

1.1 Ventriculostomy as a Technique to Characterize Brain Properties

The main obstacle in the development of reliable constitutive models of the brain tissue is that standard element tests (i.e., uniaxial compression/extension and pure shear) are not feasible *in-vivo*, while the *ex-vivo* mechanical properties of the tissue may be quite different. The only way of acquiring mechanical properties of tissues *in-vivo* is to take global images (MRI, CT, ultrasound, etc.) of the brain response to a surgery and performing an inverse analysis. One possible way of acquiring the mechanical properties of tissues *in-vivo* is to take the global images of the brain response to indentation of its surface during a surgery, which may be difficult to obtain due to both technical and ethical reasons. Also, in indentation boundary-value problems, the resulting images of displacement fields are reliable only in the vicinity of the indentation and the inverse analysis of these problems is rather difficult.

The ideal clinical procedure for this purpose is the ventriculostomy – the relief of the elevated intracranial pressure (ICP). This procedure is very common, i.e., a large hospital (e.g., Duke, Emory) performs several hundred ventriculostomies per year [*Mukundan*, personal communication, 2003]. The ICP can easily be monitored during the procedure. CT scans are regularly taken before and after the procedure, providing the brain configuration at the two known levels of ICP. The change in the boundary conditions involves the entire brain, and the boundary conditions are not very complex.

We propose to derive the mechanical properties of brain tissue *in-vivo* by taking global CT or MRI images of the brain response to ventriculostomy. Using 3-D image analysis, these images can be translated into displacement fields. Using inverse analysis of the brain response, the constitutive models of brain tissue can be developed.

1.2 Anatomy of the Human Head

The human head consists of solid (scalp, meninges, brain, blood vessels) and liquid (blood, cerebrospinal fluid) components. Figure 1.1 shows the major components of the human head in the sagittal cross section [after *Purves et al.*, 1997]. The outer surface of the head is known as the *scalp*, a soft tissue layer covering the skull with a thickness ranging from 3 to 6 mm. Underneath, the *skull* with a thickness of 9.5 to 12.7 mm is present. The skull is a rigid structure and encloses the brain with the exception of the region where the brain and the spinal cord are connected. The next inwards structure is the *meninges* which lay between and connect the brain and skull. The brain is located just below the meninges. The *cerebrospinal fluid* (*CSF*) fills the *ventricular cavities* within the brain and *the subarachnoid space* in the meninges. The scalp and the skull are not considered to influence the mechanical response of the brain to the quasi-static loading conditions and will be ignored thereafter. The structure of the brain, the meninges, and the ventricular system are further discussed in the following sections.

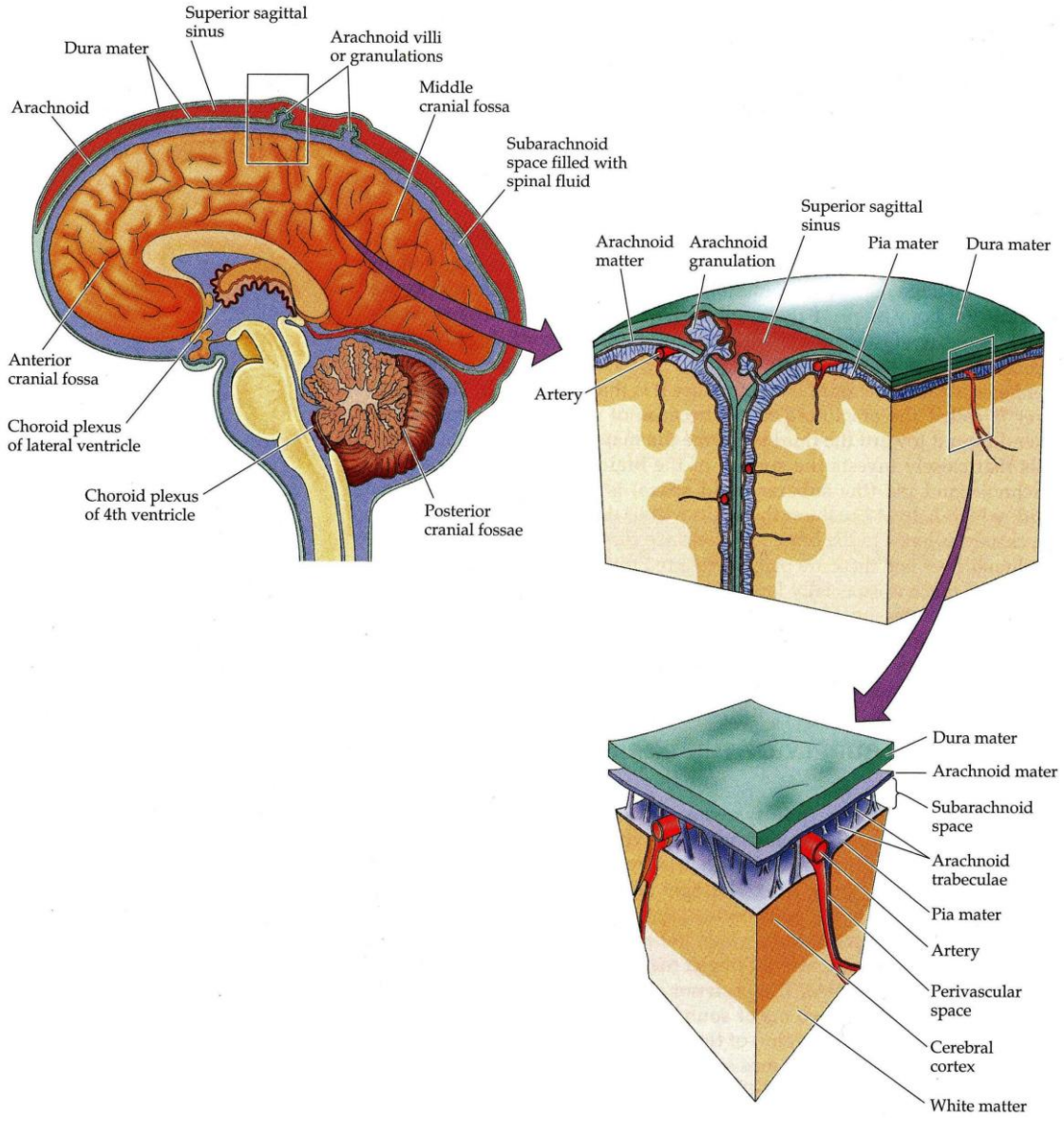

Figure 1.1. Principle parts of human head [*Purves et al.*, 1997].

Brain

The nervous tissue, like all other organs, is made up of cells. The brain contains two principle types of cells: nerve cells (neurons), which are responsible for signaling and information processing and a variety of supporting cells (glial cells), which have various supporting roles [*Nolte*, 2002]. A typical neuron cell is composed of 3 parts: dendrites, the cell body, and axons. Dendrites arise from the cell body and receive information from other cells. The cell body supports the metabolic needs of the rest of the neuron. Axons conduct information in the form of electrical signals away from the cell body. On the other hand, glial cells are quite different from neurons. They are generally smaller than nerve cells, and may not possess dendrites and/or axons. Figure 1.2 illustrates the components of a typical neuron cell [*Nolte*, 2002].

Due to the special arrangement of neurons and glial cells, the brain can be visually categorized into gray matter and white matter. Gray matter has a pinkish-gray color due to the predominance of dendrites, cell bodies and glial cells. The area where the gray matter is distributed over the surface of the brain is known as the cortex. Many axons are covered with myelin sheath, which has a whitish color. In area where neural axons dominate is called white matter. A bundle of nerve fibers (axons) following a path through the white matter of the brain is referred to as a fasciculus or a tract. In Figure 1.3, a coronal section of the brain is illustrated [after *Purves et al.*, 1997].

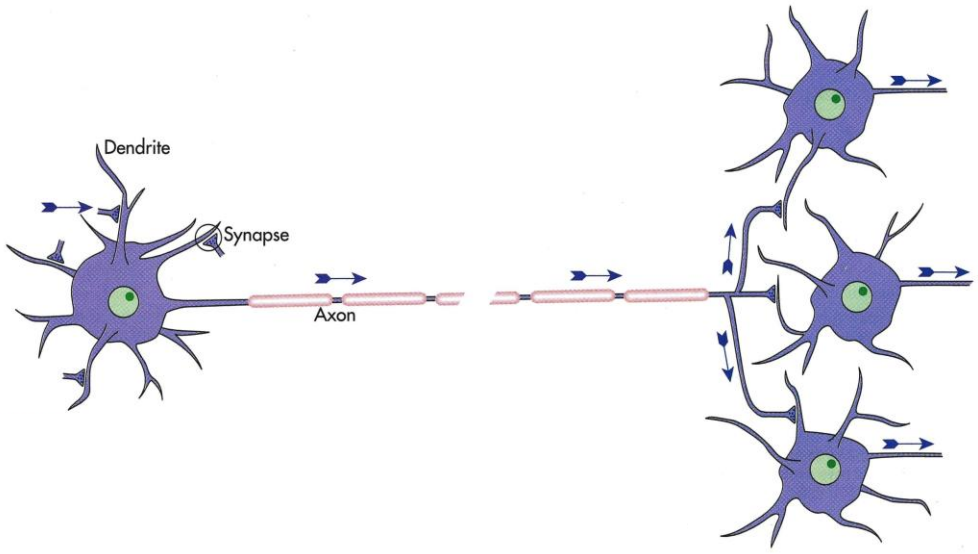

Figure 1.2. Schematic of a typical neuron cell [*Nolte*, 2002].

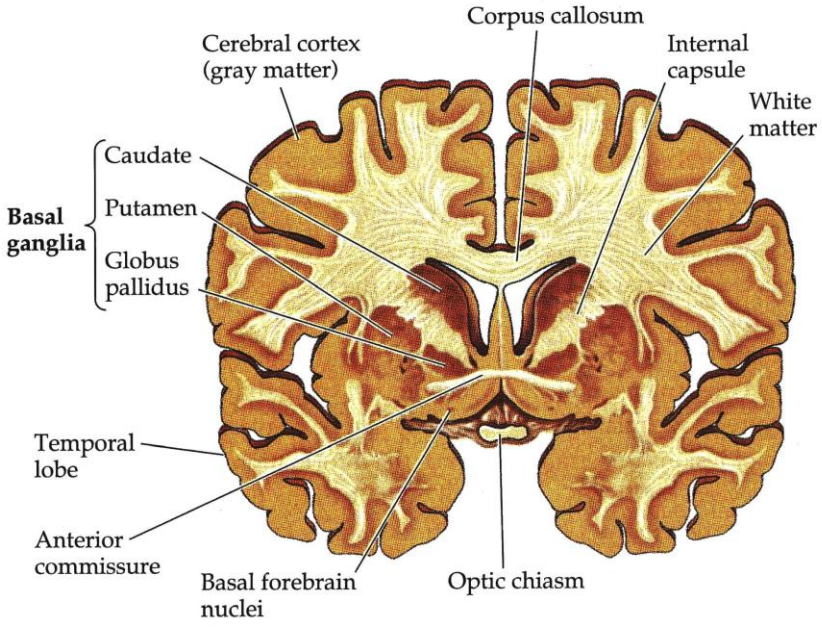

Figure 1.3. Internal structures of the brain as seen in coronal section [after *Purves et al.*, 1997].

The human brain has three major structures: the cerebrum, the cerebellum, and the brain stream. The cerebrum is composed of two cerebral hemispheres and the diencephalons. The two cerebral hemispheres are joined by a huge tract, known as corpus callosum (Figure 1.3). They have highly convoluted surfaces. Each ridge is called a gyrus and similarly, each valley between two ridges is called a sulcus, particularly deep sulci are called fissures. The surface of the cerebral hemispheres is covered with 2 to 4 of a mm thick layer of cerebral cortex (gray matter). The major divisions of the central nervous system (the brain and the spinal cord) are shown in Figure 1.4 [after *Purves et al.*, 1997].

Meninges

The meninges (Figure 1.1) are comprised of the dura mater (pachymeninges) and the leptomeninges (the arachnoid mater and the pia mater) [*Purves et al.*, 1997]. The meninges stabilize the shape and the position of the brain and protect it from external mechanical effects. The brain is anchored to the skull via the layers of meninges which constraints the movement of the brain. Moreover, the space between arachnoid and pia is filled with cerebrospinal fluid in which the brain suspends [*Nolte*, 2002; *Weller*, 2005].

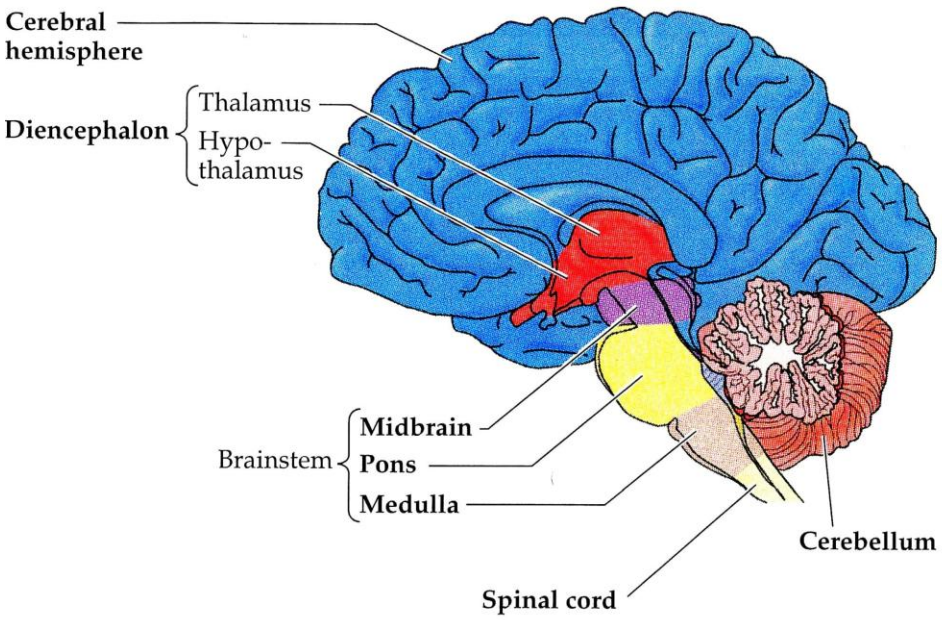

Figure 1.4. Major structures of the central nervous system (CNS) as seen in a mid-sagittal plane [after *Purves et al.*, 1997].

In the skull, the cranial dura mater forms a tough, collagenous membrane with a thickness of about 0.3 to 1 mm [*Blinkov,* 1968], anchored to the inner surface of the skull. In several regions, the dura mater folds on itself into cranial cavity and forms sheetlike structures which are called dural reflections. The principal dural reflections are the falx cerebri, which separates the two cerebral hemispheres and the tentorium cerebelli, which intervenes between the cerebral hemispheres and the cerebellum. At some edges of the dural reflections, folding layers of the dura form channels, known as dural venous sinuses, as shown in Figure 1.1. Cerebral veins drain into these channels. Moreover, cerebrospinal fluid in the subarachnoid space is reabsorbed into the venous system through these channels. Figure 1.5 shows the locations of dural reflections in the cranial cavity [*Nolte,* 2002].

The arachnoid mater is a semitransparent layer composed of a few layers of cells interspersed with bundles of collagen. The outer surface of the arachnoid mater anchors to the inner layer of the dura mater. The transition layer between dura and arachnoid is not clear. This interface layer is about 100 μm thick and contains no collagen. Furthermore, cells in the upper arachnoid layer are connected to each other by tight junctions, which are impermeable to cerebrospinal fluid. Arachnoid trabeculae, small strands of collagenous tissue, leave this interface layer and connect to pia mater. Arachnoid layer follows the general shape of the brain but does not dip into sulci.

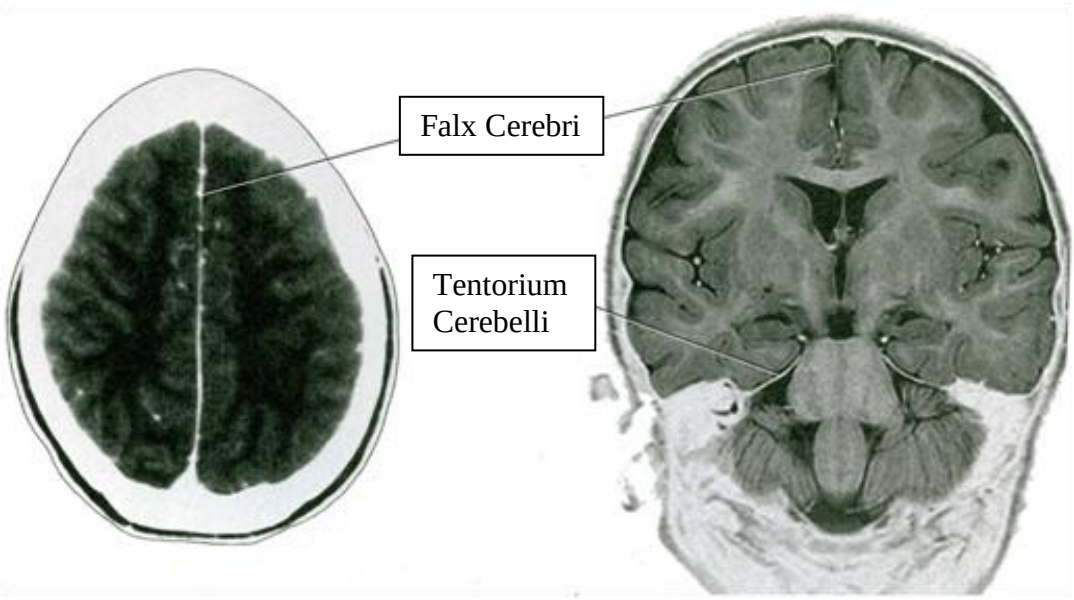

(a) (b)

Figure 1.5. (a) CT image showing the falx cerebri in a horizontal section and (b) MRI image showing the falx cerebri and the tentorium cerebelli in a coronal section [after *Nolte*, 2002].

The pia mater is a thin layer that, unlike the arachnoid, forms a continuous layer over the surface of the brain. Pia is mostly one cell thick. The space between pia and arachnoid is filled with cerebrospinal fluid. This space is narrow over gyri and large in some regions, known as subarachnoid cisterns. The interface between the pia mater and the brain contains collagen fibers that are connected to arachnoid trabeculae, crossing the subarachnoid space. Figure 1.1 illustrates the structure of the leptomeninges [after *Purves et al.*, 1997].

Ventricular System

The ventricular system is a series of connected cerebrospinal fluid filled cavities within the brain and brainstem. Ventricles are lined with closely packed ependymal cells. In each cerebral hemisphere, there is a lateral ventricle. These lateral ventricles are connected with the third ventricle, located between the left and right diencephalons, through the interventricular foramina (formina of Monro). The third ventricle communicates with the fourth ventricle through the narrow cerebral aqueduct (aqueduct of Sylvius). The fourth ventricle narrows to form the central canal of the spinal cord. In the fourth ventricle, there are three apertures: a median aperture and two lateral apertures. Through these structures, ventricles can communicate with the subarachnoid space around the brain and spinal cord. At any instant, the average total volume of CSF within and around the brain and subarachnoid space is approximately 150 ml. The ventricles contain about 25 ml of this total fluid volume and the subarachnoid space is occupied by the rest. The total volume of the third and fourth ventricles is about 2 ml. The volume of

the aqueduct and central canal are negligible. The ventricular system is illustrated in Figure 1.6 [*Nolte,* 2002].

CSF is a clear and colorless fluid. Most of the CSF is secreted by a specialized tissue, the choroids plexus, in the lateral, third, and fourth ventricles. CSF produced in the lateral ventricles flows through the interventricular foramina into the third ventricle. Then, through the cerebral aqueduct, it drains into the fourth ventricle, and then through apertures into the cistern magna and pontine cistern. From the cisterns, the fluid moves up over the cerebral hemispheres and, through specialized structures called arachnoid villi (large arachnoid villi called arachnoid granulations), drains into the superior sagittal sinus. The arachnoid villi behaves like a one-way valve, i.e., the CSF flow is allowed only in one direction, from the subarachnoid space to the superior sagittal sinus. Moreover, some of the CSF in the cisterns moves to the lumbar subarachnoid space. Most of this is absorbed in dural sleeves of the spinal nerves, although a small amount returns to the brain. Additionally, the CSF is in free communication with the extracellular space of the brain. The rate of formation of the CSF is about 0.35 cm^3/min, and it is completely circulated about three times per day. The CSF moves in the pulsatile manner within the ventricles and within the subarachnoid space toward the arachnoid villi since the pressure in the cranial cavity changes with each heartbeat. Circulation of CSF in the ventricular system is illustrated in Figure 1.7 [*Nolte*, 2002].

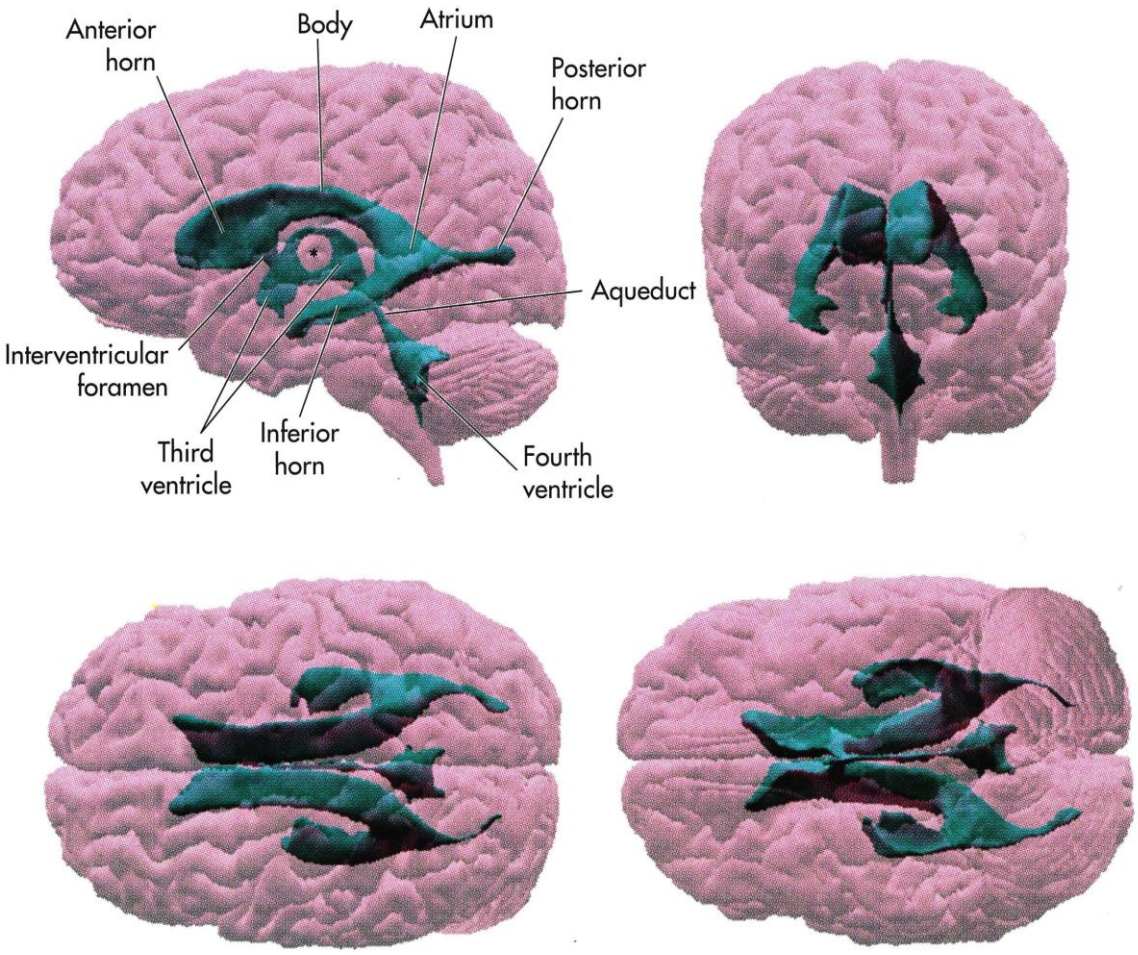

Figure 1.6. Ventricular system [*Nolte*, 2002].

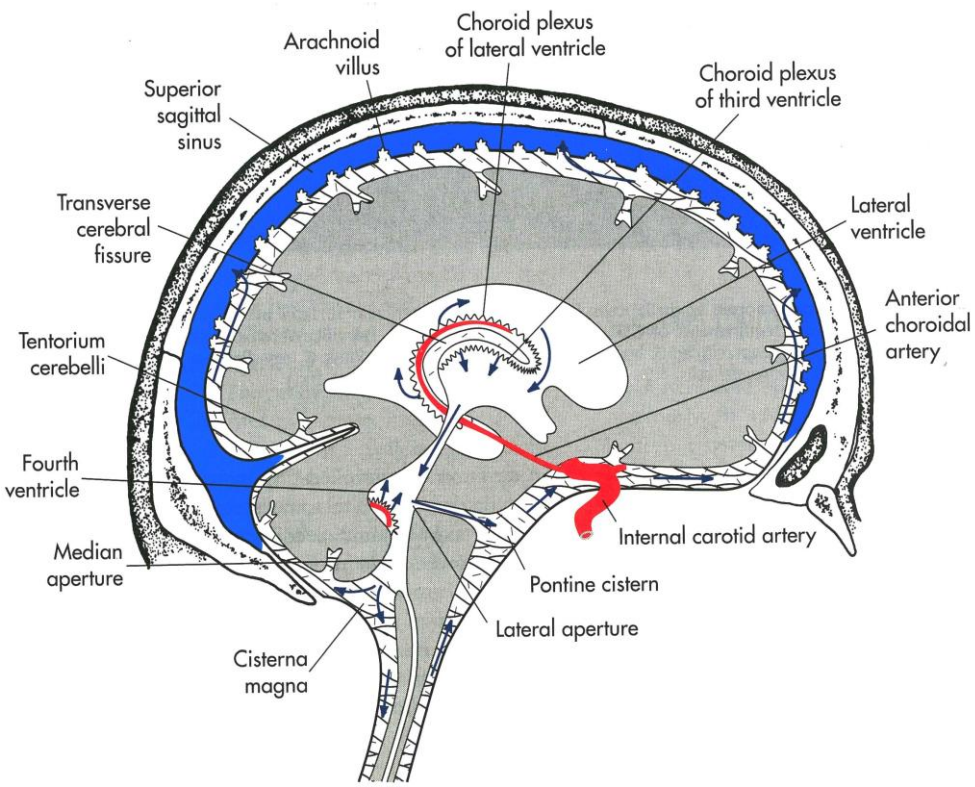

Figure 1.7. Circulation of CSF in the ventricular system [*Nolte*, 2002].

1.3 Hydrocephalus and Its Treatments

The term hydrocephalus is originated from the Greek words "hydro" meaning water and "cephalus" meaning head. It is a neurological condition in which there is an excessive accumulation of CSF in the ventricles and/or subarachnoid space of the brain. As a result of this abnormally large amount of fluid in the ventricular system, ventricles dilate.

Hydrocephalus could result from an excess production of CSF, from the obstruction of CSF circulation, or from deficiency in CSF absorption. It can be classified according to the time of development. Congenital hydrocephalus is already developed at birth. Acquired hydrocephalus develops later in life. Furthermore, hydrocephalus can be categorized depending on whether both lateral ventricles are in communication with the subarachnoid space. If the flow of CSF is blocked before it exits the ventricles, it is called non-communicating hydrocephalus, which is caused by occlusion of one or more of the pathways connecting the ventricles. Communicating hydrocephalus occurs when the flow of CSF is obstructed after draining out of the ventricles. Finally, in normal pressure hydrocephalus, the ventricles are enlarged, while the pressure of the CSF remains within normal range. Hydrocephalus may result from genetic inheritance, developmental disorders, intraventricular hemorrhage, subarachnoid hemorrhage, tumors, or traumatic head injury [*Toporek and Robinson*, 1999].

The aim of any treatment for hydrocephalus is to release the pressure on the brain caused by excess cerebrospinal fluid in the cranial cavity. For this purpose, currently used procedures focus on reducing the CSF production, reopening obstructed flow pathways (i.e., direct removal of the causative lesion) or increasing absorption of CSF.

Treatments for hydrocephalus can be classified as non-surgical and surgical procedures. Non-surgical procedures include pharmacological products used to reduce the CSF production and lumbar punctures to drain the excess CSF. These procedures are not considered as long term treatments and generally precede surgical procedures. Surgical interventions include external ventricular drain (EVD), third ventriculostomy, and shunting [*Grant and McLone*, 1997; *Aschoff et al.*, 1999; *Hellwig et al.*, 2005].

External ventricular drains (EVD), also known as external ventriculostomy, are generally temporary systems used for the treatment of hydrocephalus caused by hemorrhage, acute infection or neoplasm that requires immediate drainage of CSF. In EVD, the CSF is evacuated into an external container via inserting a probe into the ventricle [*Arriada and Sotelo*, 2002]. On the other hand, third ventriculostomy is performed by making a hole in the floor of third ventricle to establish communication between the ventricular system and the subarachnoid space. This procedure is more appropriate for treating non-communicating hydrocephalus. Note that, any procedure performed by creating an opening in a cerebral ventricle is generally called ventriculostomy. Finally, the placement of a shunt is a common treatment of hydrocephalus. In shunting, a silicone catheter is placed within the locus of increased pressure. This catheter is connected to a one-way valve, which regulates CSF flow. The shunt valve is connected to a distal catheter that is placed in another part of the body, commonly peritoneal cavity of the abdomen. The shunt system diverts the excess fluid to the area where distal catheter is placed [*Arriada and Sotelo*, 2002]. Figure 1.8 shows example pre-operative and post-operative images of the brain, acquired before and after ventriculostomy operation [*Mukundan*, 2003].

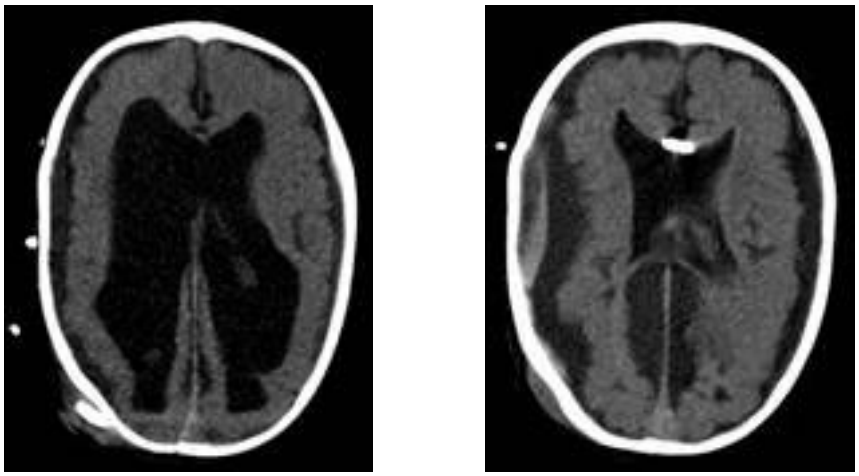

(a) (b)

Figure 1.8. (a) Pre-operative and (b) post-operative axial CT slices of ventriculostomy operation [*Mukundan*, 2003].

1.4 Constitutive Models of Brain Tissue

In order to quantify the behavior of the brain under different loading conditions, a wide range of models have been proposed in the last 40 years. These models have been mainly chosen based on observed responses to different loading conditions as well as structural and histological characteristics of the tissue. Quasi-static processes, such as neurosurgical retraction, brain shift, hydrocephalus, and cerebral edema, have been studied using poroelastic [e.g., *Subramaniam et al.*, 1995; *Kaczmarek et al.*, 1997; *Pena et al.*, 1999; *Miga et al.*, 2000; *Miga et al.*, 2001; *Taylor and Miller*, 2004], linear elastic [e.g., *Ferrant et al.*, 2000; *Skrinjar et al.*, 2001], viscoelastic [e.g., *Sivaloganathan et al.*, 2005a, 2005b], and hyperelastic models [*Sahay et al.*, 1992].

Miller [1998] pointed out that poroelastic models are not able to describe the strain-rate dependent behavior of the brain tissue, and should be used with caution. *Cheng and Bilston* [2006] measured stress relaxation response of white mater samples collected from calves performed under unconfined compression (5% strain). Their results demonstrated that poroelastic model can only account for the long-term response of the tissue and cannot describe the viscoelastic nature of the white mater. Additionally, they showed that purely viscoelastic model underestimates the instantaneous response of the tissue in stress relaxation experiment while this issue is less significant at low-strain rate conditions. Poroviscoelastic model was found to be able to account for both instantaneous and long term response of white mater within the strain levels used in their experiments.

Pamidi and Advani [1978] were among the first to employ a constitutive model based on the concept of strain energy. They chose the strain energy function proposed by

Mooney [1940] leading to the non-linear viscoelastic model. Model parameters were calculated by fitting the model to the unconfined compression data reported by *Estes and McElhaney* [1970]. *Mendis et al.* [1995] used the same data and strain energy function while they defined parameters of the energy function in the form of exponential series in order to account for the time-dependent behavior. *Sahay et al.* [1992] inflated lateral ventricle of dog models by injecting a special solution, and simultaneously measured the pressure inside and outside the brain tissue. They used the strain energy function proposed by *Hart-Smith* [1966] and evaluated model parameters by fitting model predictions to experimental data.

To model the constitutive behavior of the brain tissue, recent works [*Miller and Chinzei*, 1997; *Miller*, 1999; *Miller et al.*, 2000; *Brands et al.*, 2004] used a Mooney-Rivlin type strain energy function, originally developed for incompressible rubbers [*Rivlin*, 1984]. It appeared, however, that this function cannot account for a different behavior in extension than that of in compression, exhibited by brain tissue. Instead, it was suggested to use the *Ogden* [1972] strain energy function, which accounts well for the complex mechanical behavior of brain tissue [*Miller and Chinzei*, 2002]. Similarly, *Prange and Margulies* [2002] used the Ogden strain energy function to evaluate their experimental results (simple shear and unconfined compression), and reported that it is an effective model to describe brain tissue in both shear and compression. *Velardi et al.* [2006] utilized a transversely isotropic Ogden model proposed by *Merodio and Ogden* [2003] and evaluated model parameters based on uniaxial tension tests performed on porcine brain tissue specimens.

1.5 Goal and Objectives

The long term goal of this work is the development of reliable constitutive models of *in-vivo* mechanical behavior of soft tissues.

Motivated by this goal, the development of the image guided mechanical computational approach for applications in therapy and neurosurgery is the initial focus. We call this approach Image Guided Constitutive Modeling (IGCM). Its importance arises from the fact that image guided neurosurgery is mainly based on pre-operative (non-deformed) images of brain, in spite of the fact that the brain undergoes considerable deformations when the skull is opened. Such deformations strongly affect many high-risk neurosurgical operations and in some cases lead to fatal results. Applications of IGCM include:

- Subdural electrode placement in epilepsy surgery
- Brain shift compensation during craniotomy
- Needle guidance during brain biopsy
- Simulating specific complicated neurosurgical procedures before performing them on real patients or for the purpose of training surgeons.

One important application of IGCM lays in treatment of tumors that obstruct the circulation of cerebrospinal fluid and cause non-communicating hydrocephalus. Hydrocephalus typically requires ventriculostomy, which can be used for obtaining the constitutive parameters of the brain tissue for each patient undergoing this procedure. When such a tumor needs to be removed, these parameters could be used for planning

and guidance of the tumor resection operation on the same patient for whom they had been previously determined using the ventriculostomy and IGCM.

The objective of this work is to develop and test the concepts of the image guided constitutive modeling in the controlled laboratory environment, that is, using physical brain models with the best possible simulation of the *in-vivo* brain geometry, mechanical properties, and boundary conditions.

Similar to brain tissue, there are other parts of the human body (such as liver, kidney, or breast) that can also be characterized by IGCM principles. Our second objective is to develop a quantitative large-strain 3-D mechanical model of female breast deformation. Breast cancer is the second most prevalent cancer in women, and an operative mastectomy, in which breast tissue is removed, is frequently a part of the treatment. Women often choose to follow a mastectomy with a reconstruction surgery using a breast implant. Furthermore, there is a growing demand for breast augmentation for the sake of aesthetic improvement. Yet, millions of women requested revisional operations because the resulted breast forms differed from their expectations. This is why accurate pre-operative simulation of these augmenting and reconstructive procedures is important. Additionally, a mechanical understanding of factors affecting breast deformation and shape, such as properties of skin and breast tissue, may affect the therapeutic procedures and non-operative augmentation techniques (e.g., choosing proper breast skin care).

Subdural hematoma (tearing and bleeding between scull and brain) is one of the major complications of the ventriculostomy operations. It is important to understand the

mechanism of subdural hematoma in order to develop more effective medical treatments. The last objective of this work is to simulate the behavior of brain during shunt emplacement using a poroelastic model and to study the factors affecting the appearance of subdural hematoma due to ventriculostomy procedures.

CHAPTER II

ELEMENTS OF SOFT TISSUE BIOMECHANICS

2.1 Strain and Stress Measures in Soft Tissue Biomechanics

The purpose of this section is to introduce the framework for the subsequent mechanical analysis of soft tissues in a human body. The description below is based mainly on the books by *Malvern* [1969], *Atkin and Fox* [1980], *Ogden* [1997], and *Holzapfel* [2000].

Consider the deformation of a continuum body from an initial (undeformed) configuration Ω_0 to a current (deformed) configuration Ω_t (Figure 2.1). Initially, the location of each particle of the body is uniquely determined by its position vector $\mathbf{X} = (X_1, X_2, X_3)$ and, therefore, the coordinates (X_1, X_2, X_3) uniquely "label" the particle. They are known as material or Lagrangian coordinates. As a result of the deformation, particle $\mathbf{X}$ moves to a new position $\mathbf{x} = \boldsymbol{\chi}(\mathbf{X}, t)$. Accordingly, the body deformation can be viewed as a mapping from the initial to current configuration by the vector function $\mathbf{x} = \boldsymbol{\chi}(\mathbf{X}, t)$, which we write in equivalent form of $x_a = \chi_a(X_A, t)$ corresponding to three scalar functions $x_1 = \chi_1(X_1, X_2, X_3)$, $x_2 = \chi_2(X_1, X_2, X_3)$, $x_3 = \chi_3(X_1, X_2, X_3)$. Coordinates (x_1, x_2, x_3) are known as spatial or Eulerian coordinates. In this work we only use Cartesian coordinate sets.

Sometimes we are interested in introducing another configuration Ω such that the body did not necessarily occupy this configuration during its actual motion between the initial and current configurations. This can be done, for example, if the labeling particles

is more convenient in Ω rather than in Ω_0 or, which is characteristic for biomechanics, when the initial configuration is not necessarily stress-free and one may want to chose the stress-free configuration as a reference (if it exists). We call Ω the reference configuration and it may or may not coincide with Ω_0. At this point, we do not have to distinguish between the initial and reference configurations. More discussion on this matter will be given in Chapter 3.

Suppose now that two particles of the body are located at points **X** and **X** + **dX** in the undeformed configuration at time $t = 0$ (Figure 2.1), so that after the deformation at time t, they are positioned at $\mathbf{x} = \boldsymbol{\chi}(\mathbf{X}, t)$ and $\mathbf{x} = \boldsymbol{\chi}(\mathbf{X} + \mathbf{dX}, t)$, respectively. Here, the total differential **dx** is given by

$$\mathbf{dx} = \mathbf{F}\mathbf{dX}, \qquad \mathbf{F} = \frac{\partial \mathbf{x}}{\partial \mathbf{X}} \tag{2.1.1a}$$

or, in index notation,

$$dx_a = F_{aA} dX_A , \qquad F_{aA} = \frac{\partial x_a}{\partial X_A} \tag{2.1.1b}$$

where **F** is the deformation-gradient tensor, F_{aA}, dx_a, and dX_A are the components of tensors **F**, **dx**, and **dX**, respectively, in the Cartesian coordinates with basis vectors, e_a (a =1, 2, 3) (Figure 2.1), and we adopted the summation convention introduced by *Einstein* [1916] (i.e., the summation over repeated tensorial indices from 1 to 3 is assumed). In this work, we use lower-case, bold-face Latin letters to denote vectors in the undeformed configuration (e.g., **dx**) and upper-case, bold-face Latin letters for tensors (e.g., **F**) and vectors in the deformed configuration (e.g., **dX**). When we employ index

notations, we use upper-case letter indices for undeformed configuration (as in dX_A) and lower-case letter indices for deformed configuration (as in dx_a). Most of the expressions, we write both in tensor (vector) and index forms.

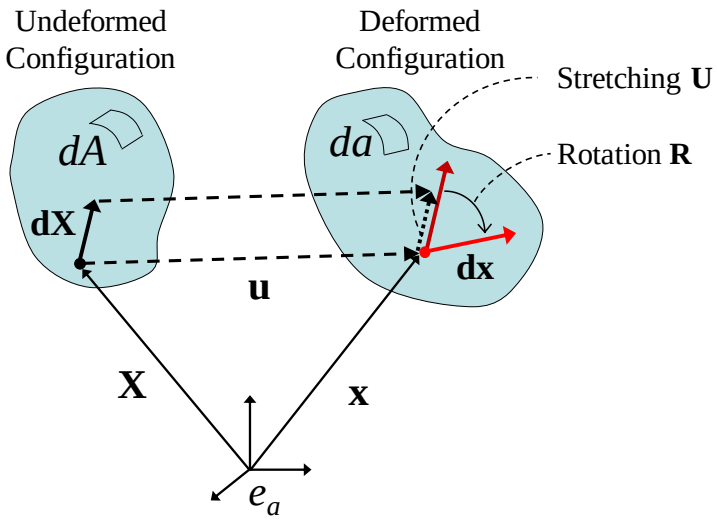

Figure 2.1. Deformed and undeformed configurations of a continuum body.

The determinant of the deformation-gradient tensor, $J = \det \mathbf{F} = \det(\partial \chi_a / \partial X_A)$ is the Jacobian of the transformation $\mathbf{x} = \boldsymbol{\chi}(\mathbf{X}, t)$. In general, J is a function of $\mathbf{X}$ and we consider only such motions $\boldsymbol{\chi}$ for which J exists at every point and for which $J > 0$. This condition guaranties [e.g., *Atkin and Fox*, 1980] that the motion $\mathbf{x} = \boldsymbol{\chi}(\mathbf{X}, t)$ has the unique inverse $\mathbf{X} = \boldsymbol{\chi}^{-1}(\mathbf{x}, t)$ and that material cannot be deform from a finite volume to zero-volume point and cannot interpenetrate itself (e.g., multi-connected domains cannot be created simply by deformation). In addition, J is equal to the ratio of the infinitesimal volume elements, dv and dV, in the deformed and undeformed configurations, i.e., $J = dv / dV$. Therefore, J is a convenient measure of volume change due to the deformation. For a volume preserving motion or for incompressible materials, $J = 1$.

The deformation-gradient tensor $\mathbf{F}$ permits unique decompositions [*Atkin and Fox*, 1980]

$$\mathbf{F} = \mathbf{RU}, \qquad \mathbf{F} = \mathbf{VR} \tag{2.1.2a}$$

which, in index notation, are equivalent to

$$F_{aA} = R_{aB} U_{BA}, \qquad F_{aA} = V_{ab} R_{bA} \tag{2.1.2b}$$

Here, $\mathbf{R}$ is the rotation tensor, i.e., the proper orthogonal tensor such that $\mathbf{R}^{\mathbf{T}}\mathbf{R} = \mathbf{R}\mathbf{R}^{\mathbf{T}} = \mathbf{I}$ and $\det\mathbf{R} = 1$ (or, in other words, $R_{aA}R_{aB} = R_{Aa}R_{Ba} = \delta_{AB}$ and $\det R_{aA} = 1$), $\mathbf{U}$ is the right stretch tensor, and $\mathbf{V}$ is the left stretch tensor, $\mathbf{I}$ is the unit tensor, and δ_{AB} is the Kronecker delta (i.e., $\delta_{AB} = 1$ if $A = B$ and $\delta_{AB} = 0$ if $A \neq B$). Both $\mathbf{U}$ and $\mathbf{V}$ are positive-definite, symmetric tensors.

The physical significance of decomposition (2.1.2) can be seen from representing (2.1.1) as

$$\mathbf{dx} = \mathbf{R}\mathbf{dy}, \quad \mathbf{dy} = \mathbf{U}\mathbf{dX} \tag{2.1.3a}$$

or, in index notation, as

$$dx_a = R_{aA}dy_A, \quad dy_B = U_{BA}dX_A \tag{2.1.3b}$$

which means that the deformation of the line element **dX** into **dx** can be done in two steps: (1) from **dX** to **dy** and then (2) from **dy** to **dx**. Because **U** is a positive-definite, symmetric tensor, there exists a set of coordinate axes in which **U** is diagonal [*Atkin and Fox*, 1980]. These are principal axes (directions) of **U** and by definition, the positive diagonal components, U_1, U_2, and U_3, of **U** in the principal axes are called the principal values of **U** (also known as eigenvalues of **U**). In these axes, the second expression in (2.1.3) becomes

$$dy_1 = U_1 dX_1, \quad dy_2 = U_2 dX_2, \quad dy_3 = U_3 dX_3 \tag{2.1.4}$$

where quantities U_1, U_2, and U_3 are also known as the principal stretches (i.e., stretch ratios in the principal directions) and frequently denoted as λ_1, λ_2, and λ_3, respectively (or, $U_i = \lambda_i$). Because the first expression in (2.1.3) describes a rigid-body rotation of the line element from **dy** to **dx**, the entire deformation may be visualized as the line element **dX** first translated from **X** to **x**, then stretched as prescribed by tensor **U**, and finally, rotated as a rigid body as determined by tensor **R** (Figure 2.1). The decomposition of **V** can be interpreted in a similar way except, in this case, the rotation occurs before the stretching

[*Atkin and Fox*, 1980]. It turns out that the principal stretches of **U** and **V** are the same (i.e., $U_i = V_i = \lambda_i$) and $J = \det \mathbf{F} = \lambda_1\lambda_2\lambda_3$.

Stretch ratio is a simple and useful measure of deformation [*Malvern*, 1969] and defined as the ratio $\lambda = |\mathbf{dx}| / |\mathbf{dX}|$ (Figure 2.1) of deformed to undeformed lengths of the line elements that are not necessarily oriented in the directions of principal axes. Indeed, when the deformation-gradient tensor is known, the stretch ratio can be found in any arbitrary direction. For example, if **Y** is a unit vector in the direction of **dX** (in the undeformed state), then the stretch ratio and the deformation-gradient tensor are related by

$$\lambda^2 = \mathbf{Y}\mathbf{F}^{\mathrm{T}}\mathbf{F}\mathbf{Y} = \mathbf{Y}\mathbf{U}^{\mathrm{T}}\mathbf{U}\mathbf{Y} \tag{2.1.5a}$$

or, in index notation, by

$$\lambda^2 = Y_A F_{aA} F_{aB} Y_B = Y_A U_{DA} U_{DB} Y_B \tag{2.1.5b}$$

As an example, consider *homogeneous* deformation defined by

$$\mathbf{x} = \mathbf{Q}\mathbf{X} + \mathbf{c} \tag{2.1.6a}$$

or, equivalently,

$$x_a = Q_{aA} X_A + c_a \tag{2.1.6b}$$

where Q_{aA} and c_a are arbitrary constants (independent of coordinates) and x_a and X_A ($a, A = 1, 2, 3$) are the position vector components in deformed and undeformed configuration, respectively (Figure 2.1). Using the second equation in (2.1.1), the

deformation-gradient tensor can be written as $\mathbf{F} = \mathbf{Q}$ or $F_{aA} = Q_{aA}$, and the volume ratio defined by $J = \det\mathbf{F}$ becomes $J = \det\mathbf{Q}$. Tensor $\mathbf{F}$ does not depend upon coordinates, hence, the name "homogeneous deformation."

In the special case, consider the motion

$$x_1 = \alpha X_1, \quad x_2 = \beta X_2, \quad x_3 = \gamma X_3 \tag{2.1.7}$$

where α, β, and γ are arbitrary constants. Then, the deformation-gradient tensor and the volume ratio can be written as

$$\mathbf{F} = \begin{bmatrix} \alpha & 0 & 0 \\ 0 & \beta & 0 \\ 0 & 0 & \gamma \end{bmatrix}, \quad J = \alpha\beta\gamma \tag{2.1.8}$$

and condition $J > 0$ requires that the constants α, β, and γ were constrained by $\alpha\beta\gamma > 0$.

For $\alpha > 0$ and $\beta = \gamma < 0$, the deformation-gradient tensor can be decomposed into

$$\mathbf{U} = \begin{bmatrix} \alpha & 0 & 0 \\ 0 & -\beta & 0 \\ 0 & 0 & -\beta \end{bmatrix}, \quad \mathbf{R} = \begin{bmatrix} 1 & 0 & 0 \\ 0 & -1 & 0 \\ 0 & 0 & -1 \end{bmatrix} \tag{2.1.9}$$

which can be checked directly by utilizing (2.1.2).

Because the off-diagonal components of $\mathbf{U}$ are zero, the diagonal components of $\mathbf{U}$ are the principal stretches, i.e., $\lambda_1 = \alpha$, $\lambda_2 = \lambda_3 = -\beta$. Furthermore, since the rotation tensor, $\mathbf{R}$, is different from the identity tensor, $\mathbf{I}$, the motion (2.1.7) includes the components of the solid-body rotation. In this case, the body rotation occurs through an

angle π about axis e_1 (Figure 2.1) or, which is the same about axis X_1 in the undeformed configuration.

If $\beta \neq \gamma$, but all α, β, and γ are positive constants, then

$$\mathbf{U} = \begin{bmatrix} \alpha & 0 & 0 \\ 0 & \beta & 0 \\ 0 & 0 & \gamma \end{bmatrix}, \quad \mathbf{R} = \mathbf{I} = \begin{bmatrix} 1 & 0 & 0 \\ 0 & 1 & 0 \\ 0 & 0 & 1 \end{bmatrix} \tag{2.1.10}$$

and this motion corresponds to the homogeneous deformation (extension or contraction) in three perpendicular directions along axes X_1, X_2, and X_3 in the undeformed body. Denoting $\alpha = \lambda_1$, $\beta = \lambda_2$, and $\gamma = \lambda_3$, we can rewrite (2.1.7) in a more conventional form of

$$x_1 = \lambda_1 X_1, \quad x_2 = \lambda_2 X_2, \quad x_3 = \lambda_3 X_3 \tag{2.1.11}$$

which represents contraction along axis i if $0 < \lambda_i < 1$ and extension if $\lambda_i > 1$ (i = 1, 2, 3).

In a particular case of the uniaxial compression of a rectangular prism (Figure 2.2), the stretch ratios are equal to

$$\lambda_1 = \frac{l_1}{l_1^0}, \quad \lambda_2 = \frac{l_2}{l_2^0}, \quad \lambda_3 = \frac{l_3}{l_3^0} \tag{2.1.12}$$

where l_1^0, l_2^0, l_3^0 and l_1, l_2, l_3 are the dimensions of the prism before and after the deformation, respectively (Figure 2.2). The motion (deformation) is described by (2.1.11) and (2.1.10), if the direction of axis X_1 coincides with the direction of compression (as shown in Figure 2.2).

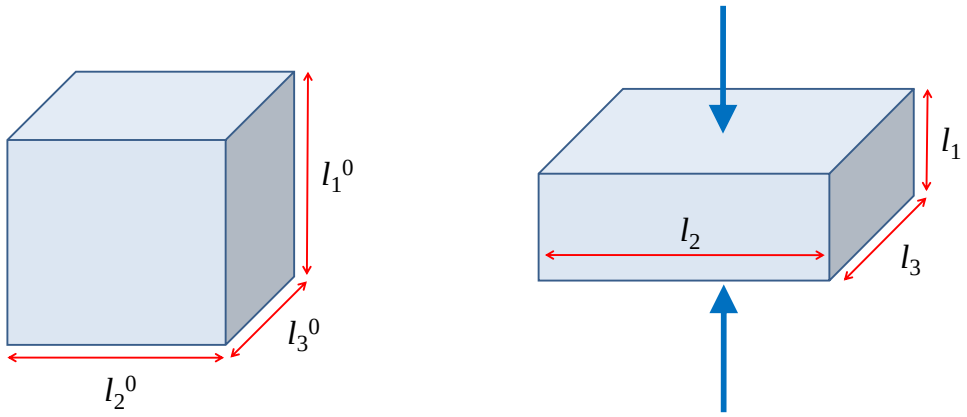

(a) (b)

Figure 2.2. Uniaxial compression of a rectangular prism (a) before and (b) after the deformation.

Example (2.1.9) shows that the deformation-gradient tensor, **F**, may contain not only deformation (i.e., stretching defined by **U**), but also a rigid-body motion contribution specified by **R.** While such contribution is expected because of decomposition (2.1.2), it suggests that the deformation-gradient tensor may not be the best measure of body deformation. Furthermore, consider a proper orthogonal tensor **Q** in (2.1.6) (i.e., $\mathbf{Q}^{\mathbf{T}}\mathbf{Q} = \mathbf{Q}\mathbf{Q}^{\mathbf{T}} = \mathbf{I}$ and $\det\mathbf{Q} = 1$). Then, **Q** defines a rigid-body rotation while (2.1.1) results in $\mathbf{F} = \mathbf{Q}$, so that the deformation-gradient tensor may have no deformational component at all.

In addition, computation of tensors **U** and **V** directly from **F** is often quite cumbersome because **R** and **U** (or **V**) are coupled in $\mathbf{F} = \mathbf{RU}$ (or in $\mathbf{F} = \mathbf{VR}$) and are both

unknown. Hence, in order to find **U**, one typically considers transposed equation $\mathbf{F^T = U^T R^T}$ and then factors it with the original equation $\mathbf{F = RU}$ obtaining $\mathbf{F^T F = U^T R^T RU}$ where $\mathbf{R^T R = I}$, $\mathbf{U^T = U}$ (because **U** is symmetric), and **U** can be found solving equation $\mathbf{U}^2 = \mathbf{F^T F}$ for **U**. Similarly, **V** can be obtained solving equation $\mathbf{V}^2 = \mathbf{F F^T}$ for **V**.

Instead, quantity $\mathbf{F^T F}$ or $\mathbf{F F^T}$ can be used directly to characterize the deformation of the body. Given this, two other measures of deformation are defined by tensors

$$\mathbf{C} = \mathbf{F}^{\mathrm{T}}\mathbf{F}, \quad \mathbf{B} = \mathbf{F}\mathbf{F}^{\mathrm{T}} \tag{2.1.13a}$$

with components

$$C_{AB} = F_{aA}F_{aB}, \quad B_{ab} = F_{aA}F_{bA} \tag{2.1.13b}$$

where **C** and **B** are called right and left Cauchy-Green tensors, respectively. Tensors **C** and **B** allow one to calculate the difference between the squared lengths of the line elements in undeformed and deformed configurations, but in different coordinate sets [*Atkin and Fox*, 1980]:

$$|\mathbf{dx}|^2 - |\mathbf{dX}|^2 = \mathbf{dX(C - I)dX}, \quad |\mathbf{dx}|^2 - |\mathbf{dX}|^2 = \mathbf{dx(I - B^{-1})dx} \tag{2.1.14a}$$

or, in index notation,

$$|\mathbf{dx}|^2 - |\mathbf{dX}|^2 = (C_{AB} - \delta_{AB})dX_A\, dX_B, \quad |\mathbf{dx}|^2 - |\mathbf{dX}|^2 = (\delta_{ab} - B_{ab}{}^{-1})dx_a dx_b \tag{2.1.14b}$$

where tensor $\mathbf{B}^{-1}$ is the inverse of tensor **B** and $B_{ab}{}^{-1}$ are the Cartesian components of tensor $\mathbf{B}^{-1}$.

Both **C** and **B** are symmetric, second-order tensors related to tensors **U** and **V** by

$$\mathbf{C} = \mathbf{U}^{\mathrm{T}}\mathbf{R}^{\mathrm{T}}\mathbf{R}\mathbf{U} = \mathbf{U}^{\mathrm{T}}\mathbf{U}, \quad \mathbf{B} = \mathbf{V}^{\mathrm{T}}\mathbf{R}^{\mathrm{T}}\mathbf{R}\mathbf{V} = \mathbf{V}^{\mathrm{T}}\mathbf{V} \tag{2.1.15a}$$

or, in index notation,

$$C_{AB} = R_{aC}U_{CA}R_{aD}U_{DB} = U_{DA}U_{DB}, \quad B_{ab} = V_{ac}R_{cA}V_{bd}R_{dA} = V_{ac}V_{bc} \tag{2.1.15b}$$

The principal values, λ_0, for **C** can be found from the characteristic equation

$$\det\left[C_{AB} - \lambda_0\delta_{AB}\right] = 0 \tag{2.1.16a}$$

which is equivalent to the cubic equation

$$\lambda_0^3 - I_1\lambda_0^2 + I_2\lambda_0 - I_3 = 0 \tag{2.1.16b}$$

where [*Atkin and Fox,* 1980]

$$I_1 = C_{AA}, \quad I_2 = \tfrac{1}{2}(C_{AA}C_{BB} - C_{AB}C_{AB}), \quad I_3 = \varepsilon_{ABL}C_{1A}C_{2B}C_{3L} = \det\mathbf{C} \tag{2.1.17}$$

are called the principal scalar invariants of **C**. Values of these scalars do not depend on the coordinate system and, therefore, are invariant with respect to rotations of the coordinate axes. It turns out that the principal values, λ_0, are equal to the squares of the principal stretches, λ_i (i = 1, 2, 3), and, therefore, denoted as ${\lambda_1}^2$, ${\lambda_2}^2$, and ${\lambda_3}^2$. In (2.1.17), ε_{ABL} is the permutation symbol (i.e., $\varepsilon_{123} = \varepsilon_{231} = \varepsilon_{312} = 1$, $\varepsilon_{321} = \varepsilon_{213} = \varepsilon_{132} = -1$, $\varepsilon_{ABL} = 0$ if there is a repeated index). In the principal axes, expression (2.1.17) can be written as

$$I_1 = \lambda_1^2 + \lambda_2^2 + \lambda_3^2, \quad I_2 = \lambda_1^2\lambda_2^2 + \lambda_2^2\lambda_3^2 + \lambda_1^2\lambda_3^2, \quad I_3 = \lambda_1^2\lambda_2^2\lambda_3^2 \tag{2.1.18}$$

and tensors **C** and **B** have the same scalar invariants and principal values (although different principal directions). As discussed in Section 2.2, invariants, I_1, I_2, and I_3 have an important role in the constitutive equations of isotropic materials [e.g., *Malvern*, 1969].

A useful physical interpretation of I_3 is given by its relation with $J = \det\mathbf{F}$ [*Atkin and Fox*, 1980]:

$$I_3 = \det\mathbf{C} = \det\mathbf{B} = J^2 = (\det\mathbf{F})^2 \tag{2.1.19}$$

Here, for an incompressible (volume preserving) material, $J = 1$ or, equivalently, $I_3 = 1$.

As seen from (2.1.14), tensor **C** is a conventional measure of the stretching part of the deformation. If $\mathbf{C} = \mathbf{I}$, the body does not deform and moves as a rigid body. Therefore, $\mathbf{C} - \mathbf{I}$ may be viewed as a characteristic of the change of the body shape and a similar consideration suggests that tensor $\mathbf{I} - \mathbf{B}^{-1}$ may be thought of as a measure of a change in shape, as well. Accordingly, tensors

$$\mathbf{E} = \tfrac{1}{2}(\mathbf{C} - \mathbf{I}), \qquad \mathbf{e} = \tfrac{1}{2}(\mathbf{I} - \mathbf{B}^{-1}) \tag{2.1.20a}$$

with components

$$E_{AB} = \tfrac{1}{2}(C_{AB} - \delta_{AB}), \qquad e_{ab} = \tfrac{1}{2}(\delta_{ab} - B_{ab}^{-1}) \tag{2.1.20b}$$

are often introduced in continuum mechanics and yield zero tensors when there is no deformation [*Holzapfel*, 2000]. Tensors **E** and **e** are known as Green-Lagrange and Euler-Almansi strain tensors and can be expressed in terms of vector

$$\mathbf{u} = \mathbf{x} - \mathbf{X} \tag{2.1.21}$$

of displacement of particle **X** (Figure 2.2), which may be more convenient than using its current position **x**. Because **x** = **u** + **X**, according to (2.1.1)

$$\mathbf{F} = \mathbf{I} + \mathbf{H} \tag{2.1.22}$$

or, in index notation,

$$F_{aA} = \delta_{aA} + H_{aA} \tag{2.1.23}$$

where **H** denotes the displacement-gradient tensor with the components $H_{aA} = \partial u_a / \partial X_A$. Then, **E** can be expressed in the form

$$\mathbf{E} = \tfrac{1}{2} [\mathbf{F}^{\mathbf{T}}\mathbf{F} - \mathbf{I}] = \tfrac{1}{2} [\mathbf{H} + \mathbf{H}^{\mathbf{T}} + \mathbf{H}^{\mathbf{T}}\mathbf{H}] \tag{2.1.24}$$

and a similar expression can be written for tensor **e** using another displacement-gradient tensor **h** with components $h_{ab} = \partial u_a / \partial x_b$:

$$\mathbf{e} = \tfrac{1}{2} [\mathbf{I} - (\mathbf{F}^{-1})^{\mathbf{T}}\mathbf{F}^{-1}] = \tfrac{1}{2} [\mathbf{h} + \mathbf{h}^{\mathbf{T}} - \mathbf{h}^{\mathbf{T}}\mathbf{h}] \tag{2.1.25}$$

In index notation, expressions (2.1.24) and (2.1.25) become [*Holzapfel*, 2000]

$$E_{AB} = \frac{1}{2}\left[\frac{\partial u_B}{\partial X_A} + \frac{\partial u_A}{\partial X_B} + \frac{\partial u_C}{\partial X_A}\frac{\partial u_C}{\partial X_B}\right] \tag{2.1.26}$$

and

$$e_{ab} = \frac{1}{2}\left[\frac{\partial u_b}{\partial x_a} + \frac{\partial u_a}{\partial x_b} - \frac{\partial u_c}{\partial x_a}\frac{\partial u_c}{\partial x_b}\right] \tag{2.1.27}$$

respectively.

Using tensors **E** and **e**, the change in the squared lengths of the line elements in undeformed and deformed configurations given in (2.1.14) can be written as

$$|\mathbf{dx}|^2 - |\mathbf{dX}|^2 = 2\mathbf{dX\ E\ dX} = 2\mathbf{dx\ e\ dx} \tag{2.1.28a}$$

or

$$|\mathbf{dx}|^2 - |\mathbf{dX}|^2 = 2E_{AB}dX_A dX_B = 2e_{ab}dx_a dx_b \tag{2.1.28b}$$

When displacement gradients are small compared to unity, the product terms in (2.1.24), (2.1.25), (2.1.26), and (2.1.27) become of a higher order and can be neglected relative to the linear terms. In this case, the difference between **E** and **e** can be ignored [*Malvern*, 1969] which correspond to the small-strain theory of elasticity. Tensor

$$\boldsymbol{\varepsilon} = \tfrac{1}{2}\,[\mathbf{H} + \mathbf{H}^{\mathbf{T}}] \tag{2.1.29a}$$

with components

$$\varepsilon_{ab} = \tfrac{1}{2}\,(\partial u_b / \partial x_a + \partial u_a / \partial x_b) \tag{2.1.29b}$$

is called the infinitesimal strain tensor [*Atkin and Fox*, 1980]. Note that in the infinitesimal theory of elasticity, displacements are not necessarily small and only strains (or components of displacement-gradient tensor) are required to be small. For instance, in the theory of plate bending, strains can be rather small even in the case of considerable displacements.

As an example, consider homogeneous deformation

$$x_1 = X_1 + c\,X_2\,, \quad x_2 = X_2, \quad x_3 = X_3 \tag{2.1.30}$$

where c is a constant. This deformation is called *simple shear* [*Atkin and Fox*, 1980] and is also a special case of (2.1.6). As seen from Figure 2.3, particles move only in the direction of X_1−axis and their displacements are proportional to their X_2 coordinates. In Figure 2.3, X_3−axis is perpendicular to the plane of drawing, and planes parallel to X_1−axis rotate about X_3 clockwise through an angle $\theta = \arctan(c)$. This angle is called angle of shear. Planes $X_3 = \text{const}$ (parallel to the plane of drawing in Figure 2.3) are known as planes of shear, while planes $X_2 = \text{constant}$ are called shearing planes.

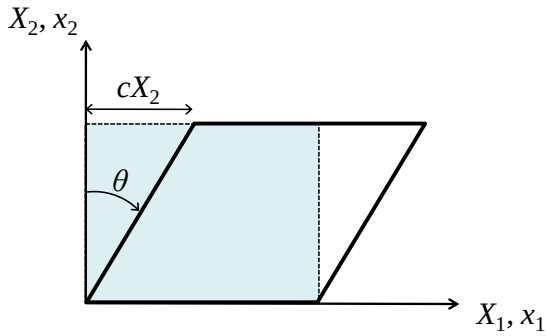

Figure 2.3. Simple shear deformation of a rectangular block.

Using (2.1.30) together with (2.1.1), the deformation-gradient tensor for the motion (2.1.30) can be written as

$$\mathbf{F} = \begin{bmatrix} 1 & c & 0 \\ 0 & 1 & 0 \\ 0 & 0 & 1 \end{bmatrix} \tag{2.1.31}$$

and the Cauchy-Green tensors become

$$\mathbf{C} = \mathbf{F}^{\mathbf{T}}\mathbf{F} = \begin{bmatrix} 1 & c & 0 \\ c & 1+c^2 & 0 \\ 0 & 0 & 1 \end{bmatrix}, \quad \mathbf{B} = \mathbf{F}\mathbf{F}^{\mathbf{T}} = \begin{bmatrix} 1+c^2 & c & 0 \\ c & 1 & 0 \\ 0 & 0 & 1 \end{bmatrix} \tag{2.1.32}$$

The strain invariants of **C** and **B** can be computed based on (2.1.17):

$$I_1 = I_2 = 3+c^2, \quad I_3 = 1 \tag{2.1.33}$$

Therefore, one can see that simple shear does not cause a volume change of the deforming body ($J = 1$ per (2.1.19)).

Because the inverse of tensor **B** in (2.1.32) is

$$\mathbf{B}^{-1} = \begin{bmatrix} 1 & -c & 0 \\ -c & 1+c^2 & 0 \\ 0 & 0 & 1 \end{bmatrix} \tag{2.1.34}$$

the Green-Lagrange and Euler-Almansi strain tensors become

$$E = e = \frac{1}{2}\begin{bmatrix} 0 & c & 0 \\ c & c^2 & 0 \\ 0 & 0 & 0 \end{bmatrix} \tag{2.1.35}$$

Let us now consider description of stresses in non-linear theory of elasticity. In this work, we used two different stress measures. Due to the deformation, the area element, *dA*, in undeformed configuration transforms into the area element, *da*, in the deformed configuration (Figure 2.1). The nominal (the first Piola-Kirchhoff) stress, *P*, is defined by the force divided by the area, *dA*, in the original (undeformed) body. The true (Cauchy) stress, σ, is defined by the force divided by the area in the deformed body, *da*. For example, for the uniaxial compression of the rectangular prism under the force *F* (Figure 2.2), the true stress is defined as

$$\sigma_1 = \frac{F}{l_2 l_3} \tag{2.1.36}$$

while the nominal stress is

$$P_1 = \frac{F}{l_2^0 l_3^0} \tag{2.1.37}$$

Each stress definition has its advantages and disadvantages and not all of their components have a clear physical meaning [*Holzapfel*, 2000]. For example, in general, the deformed configuration of the body often is not known *a priori*. Accordingly, the first Piola-Kirchhoff stress is frequently used for the interpretation of experimental data. Yet, it is not always convenient for the formulation of boundary-value problems since it is, in general, not symmetric. On the other hand, because Cauchy stress is defined in deformed configuration, it can be difficult to define or measure. However, it is more advantageous to use Cauchy stress, a symmetric tensor, while formulating and solving boundary-value problems. Moreover, due to the symmetry of Cauchy stress tensor, it is

more commonly used while presenting numerical results. Although these two stress measures have different properties, they are interrelated as [*Holzapfel*, 2000]

$$\boldsymbol{\sigma} = \frac{1}{J}\mathbf{P}\mathbf{F}^{\mathbf{T}} \tag{2.1.38a}$$

or, in index notation,

$$\sigma_{ab} = \frac{1}{J}P_{aA}F_{bA} \tag{2.1.38b}$$

2.2 Constitutive Equations

A constitutive equation characterizes the response of a material to applied loads and generally determines the stress state at any point resulting from intrinsic physical properties of the material. These equations are formulated to approximate the physical observations of the behavior of a real material. They are used together with the equations of mass conservation and motion to formulate and solve boundary-value problems [*Malvern*, 1969; *Ogden*, 1997; *Holzapfel*, 2000].

A material is called Cauchy-elastic (or elastic) if the state of stress in deformed configuration is determined only by the state of deformation of this configuration relative to the undeformed configuration. In other words, the Cauchy stress $\boldsymbol{\sigma}$ does not depend on the deformation history. In this work, only isothermal processes are considered, so the effect of temperature will not be discussed. The constitutive equation of an isotropic, isothermal, and homogeneous elastic body can be expressed in the most general form as $\boldsymbol{\sigma} = f(\mathbf{F})$. If this function is independent of the rigid-body rotations, it can be regarded as

a function of any other strain measure introduced above: **U**, **V**, **C**, **B**, **E**, or **e** (the argument showing that this is indeed the case is exactly the same as for the strain energy function $W(\mathbf{F})$ below). Then, the constitutive equation can be written as

$$\boldsymbol{\sigma} = f(\mathbf{B}) \tag{2.2.1}$$

where $f(\mathbf{B})$ is an isotropic tensor function (that is, $f(\mathbf{B})$ satisfies the identity $\mathbf{Q}f(\mathbf{B})\mathbf{Q}^{\mathbf{T}} = f(\mathbf{QBQ}^{\mathbf{T}})$ for an arbitrary proper orthogonal tensor **Q**) and **B** is a left Cauchy-Green strain tensor defined by the second expression in (2.1.13). Indeed, a rigid-body rotation **Q** corresponds to the replacement of tensor **F** with tensor **QF**, so that $\mathbf{B} = \mathbf{FF}^{\mathbf{T}}$ is replaced by $(\mathbf{QF})(\mathbf{QF})^{\mathbf{T}} = \mathbf{QFF}^{\mathbf{T}}\mathbf{Q}^{\mathbf{T}} = \mathbf{QBQ}^{\mathbf{T}}$, which should not change the value of the function $f(\mathbf{B})$. On the other hand, $\boldsymbol{\sigma}$ is a tensor, and the rigid-body rotation **Q** simply corresponds to the rotation of the coordinate set, so that the new value of $\boldsymbol{\sigma}$ becomes $\mathbf{Q}\boldsymbol{\sigma}\mathbf{Q}^{\mathbf{T}}$.

It turns out that such a function may be represented in the form

$$\boldsymbol{\sigma} = f(\mathbf{B}) = \alpha_0\mathbf{I} + \alpha_1\mathbf{B} + \alpha_2\mathbf{B}^2 \tag{2.2.2}$$

or, in alternative form

$$\boldsymbol{\sigma} = f(\mathbf{B}) = \beta_0\mathbf{I} + \beta_1\mathbf{B} + \beta_2\mathbf{B}^{-1} \tag{2.2.3}$$

where α_0, α_1, α_2 and β_1, β_2, β_3 are called the response coefficients. The response coefficients are the scalar functions of the invariants I_1, I_2, I_3 of **B**. Hence, the stress state of an isotropic material can be described by only three parameters. Equations (2.2.2) and (2.2.3) are known as first and second representation theorems for isotropic tensor

functions, respectively. From these equations, it can be deduced that the Cauchy stress $\boldsymbol{\sigma}$ and the left Cauchy-Green Tensor $\mathbf{B}$ are coaxial, that is, principal directions of $\boldsymbol{\sigma}$ and $\mathbf{B}$ coincide.

An elastic material for which a strain energy function $W(\mathbf{F})$ exists and is independent of rigid-body motions is known as hyperelastic (or Green-elastic) material. The strain energy function $W(\mathbf{F})$ is a measure of the energy accumulated in the body as a result of deformation, and is usually defined per unit of the undeformed volume. A hyperelastic material is a special case of Cauchy elasticity. Let $\mathbf{Q}$ be an arbitrary proper orthogonal tensor, which, therefore, represents a rigid-body rotation. Since the strain energy function is unaffected by rigid-body motions, $W(\mathbf{F}) = W(\mathbf{QF}) = W(\mathbf{QRU})$, so that choosing $\mathbf{Q} = \mathbf{R}^{\mathbf{T}}$ and recalling that $\mathbf{R}^{\mathbf{T}}\mathbf{R} = \mathbf{I}$ suggests that $W(\mathbf{F}) = W(\mathbf{U})$. Similarly, $W(\mathbf{F}) = W(\mathbf{V})$ and because $\mathbf{U}$ is a positive-definite, symmetric tensor, it is uniquely determined by $\mathbf{U}^2 = \mathbf{C}$. Hence, $W(\mathbf{U})$ can be regarded as a function of $\mathbf{C}$. This is why different representations of the strain energy W as a function of different deformation measures are used for hyperelastic materials:

$$W = W(\mathbf{F}) = W(\mathbf{U}) = W(\mathbf{V}) = W(\mathbf{C}) = W(\mathbf{B}) \tag{2.2.4}$$

where for the notational simplicity, the same letter W is used for functions $W(\mathbf{C})$ and $W(\mathbf{B})$ as for other functions in (2.2.4).

The stress-deformation relations can be represented in the general form [*Holzapfel*, 2000]

$$\mathbf{P} = \frac{\partial W}{\partial \mathbf{F}}, \qquad \boldsymbol{\sigma} = \frac{1}{J}\frac{\partial W}{\partial \mathbf{F}}\mathbf{F}^{\mathbf{T}} \tag{2.2.5a}$$

or, in components as

$$P_{aA} = \frac{\partial W}{\partial F_{aA}}, \qquad \sigma_{ab} = \frac{1}{J} F_{Aa} \frac{\partial W}{\partial F_{Ab}} \tag{2.2.5b}$$

and in alternative form

$$\mathbf{P} = 2\mathbf{F} \frac{\partial W}{\partial \mathbf{C}}, \qquad \boldsymbol{\sigma} = \frac{2}{J} \mathbf{F} \frac{\partial W}{\partial \mathbf{C}} \mathbf{F}^{\mathbf{T}} \tag{2.2.6a}$$

or

$$P_{aA} = 2F_{aB} \frac{\partial W}{\partial C_{AB}}, \qquad \sigma_{ab} = \frac{2}{J} F_{aA} F_{bB} \frac{\partial W}{\partial C_{AB}} \tag{2.2.6b}$$

If a material behaves isotropically with respect to the undeformed configuration, then the strain energy function W may be expressed in terms of the principal invariants of its arguments. Given that the principal invariants are, in turn, functions of principal stretch ratios (expressions (2.1.18)), the strain energy function for isotropic materials may be represented as

$$W = W(I_1\, I_2, I_3) = W(\lambda_1, \lambda_2, \lambda_3) \tag{2.2.7}$$

and, accordingly, the constitutive relations for isotropic hyperelastic materials in terms of the principal invariants can be expressed as [*Holzapfel*, 2000]

$$\boldsymbol{\sigma} = \frac{2}{J} \left[\left(I_2 \frac{\partial W}{\partial I_2} + I_3 \frac{\partial W}{\partial I_3} \right) \mathbf{I} + \frac{\partial W}{\partial I_1} \mathbf{B} - I_3 \frac{\partial W}{\partial I_2} \mathbf{B}^{-1} \right] \tag{2.2.8a}$$

or, in index notation, as

$$\sigma_{ab} = \frac{2}{J}\left[\left(I_2 \frac{\partial W}{\partial I_2} + I_3 \frac{\partial W}{\partial I_3}\right)\delta_{ab} + \frac{\partial W}{\partial I_1} B_{ab} - I_3 \frac{\partial W}{\partial I_2} B_{ab}^{-1}\right] \tag{2.2.8b}$$

In addition, the stress-deformation relations for isotropic hyperelastic materials can be written as [*Holzapfel*, 2000]

$$\boldsymbol{\sigma} = \frac{2}{J}\mathbf{B}\frac{\partial W}{\partial \mathbf{B}} = \frac{1}{J}\mathbf{V}\frac{\partial W}{\partial \mathbf{V}} \tag{2.2.9a}$$

or, in index notation, as

$$\sigma_{ab} = \frac{2}{J} B_{ac} \frac{\partial W}{\partial B_{cb}} = \frac{1}{J} V_{ac} \frac{\partial W}{\partial V_{cb}} \tag{2.2.9b}$$

Since the Cauchy stress, **σ**, the left Cauchy-Green strain tensor, **B**, and the left stretch tensor, **V**, are coaxial (i.e., their principal directions coincide), using (2.2.9), the principal Cauchy stresses σ_i for the isotropic hyperelastic materials can be written as [*Holzapfel*, 2000]

$$\sigma_i = \frac{\lambda_i}{J}\frac{\partial W}{\partial \lambda_i} \tag{2.2.10}$$

where λ_i are the principal stretches, i = 1, 2, 3, and the summation is not implied over the index i. In addition, if **R** = **I** or $R_{aA} = \delta_{aA}$, the principal components of the first Piola-Kirchhoff stress tensor can be expressed as [*Holzapfel*, 2000]

$$P_i = \frac{\partial W}{\partial \lambda_i} \tag{2.2.11}$$

For some materials, a convenient form for the constitutive equations is that in which certain geometrical restrictions are explicitly introduced to describe the motion of which the material is capable. Such restrictions are called constraints and the most common constraint is that of incompressibility. Some materials do not significantly change their volume even after sustaining rather large deformations. This property is idealized as incompressibility and the corresponding class of motions is called isochoric deformations. Incompressibility is the only constraint, due to the material properties, which we consider in this work. The corresponding mathematical expression of this constrain is given by

$$J = 1 \tag{2.2.12}$$

or other equivalent expressions that follow from (2.1.19).

Boundary conditions present different type of constraints that are required to formulate boundary-value problems.

Equations presented above are only valid for unconstrained hyperelastic behavior. For a material with internal constraints (i.e., incompressibility), the components of strain measures are not arbitrary (independent), and the constitutive equations presented above for unconstrained hyperelastic materials must be modified. Stress-deformation relations for incompressible hyperelastic material can be represented in terms of the principal invariants as [*Holzapfel*, 2000]

$$\boldsymbol{\sigma} = -p\mathbf{I} + 2\frac{\partial W}{\partial I_1}\mathbf{B} - 2\frac{\partial W}{\partial I_2}\mathbf{B}^{-1} \tag{2.2.13a}$$

or, in index notation,

$$\sigma_{ab} = -p\delta_{ab} + 2\frac{\partial W}{\partial I_1}B_{ab} - 2\frac{\partial W}{\partial I_2}B_{ab}^{-1} \tag{2.2.13b}$$

In terms of principal stretches, this expression reads

$$\sigma_i = -p + \lambda_i \frac{\partial W}{\partial \lambda_i} \tag{2.2.14}$$

and using (2.2.14) together with (2.2.10) and (2.2.11), the principal components of the first Piola-Kirchhoff stress tensor can be expressed as

$$P_i = -\frac{1}{\lambda_i}p + \frac{\partial W}{\partial \lambda_i} \tag{2.2.15}$$

The arbitrary term $-p$ is known as the reaction stress, and is the workless reaction to the motion (i.e., the reaction without displacements). It enforces incompressibility and may only be determined using equilibrium and boundary conditions.

2.3 Strain Energy Functions in Soft Tissue Biomechanics

The majority of strain energy functions used in the literature to model soft tissue behavior (brain or breast) was originally developed for the characterization of rubber-like materials (e.g., rubber or elastomer). The aim of this section is to present some forms of strain energy functions which are employed in this dissertation.

Polynomial strain energy function was proposed by *Rivlin* [1948] for isotropic materials and has the form of

$$W = \sum_{i+j+k=1}^{N} C_{ij} (I_1 - 3)^i (I_2 - 3)^j (I_3 - 3)^k \tag{2.3.1}$$

For incompressible materials ($I_3 = 1$), the equation (2.3.1) reduces to

$$W = \sum_{i+j=1}^{N} C_{ij} (I_1 - 3)^i (I_2 - 3)^j \tag{2.3.2}$$

where C_{ij} are the model parameters and have the units of stress (e.g., Pa). When only the first term is retained in (2.3.1), it reduces to the neo-Hookean strain energy function

$$W = C_{10}(I_1 - 3) \tag{2.3.3}$$

If we keep the first two terms in (2.3.2), it becomes

$$W = C_{10}(I_1 - 3) + C_{01}(I_2 - 3) \tag{2.3.4}$$

which is proposed by *Mooney* [1940] and also known as Mooney or Mooney-Rivlin strain energy function.

Consider simple tension/compression of an incompressible hyperelastic material. This deformation is characterized by the homogeneous deformation (2.1.11) for $\lambda_2 = \lambda_3$. Because the material is incompressible, using the condition $J = \lambda_1\lambda_2\lambda_3 = 1$, we can write $\lambda_1 = \lambda$ and $\lambda_2 = \lambda_3 = 1/\sqrt{\lambda}$. Since we consider uniaxial deformation, the stress state in the

body can be assumed to be $\sigma = \sigma_1$, $\sigma_2 = \sigma_3 = 0$. Given this and using (2.2.13), the stress-stretch relation can be written as [*Holzapfel*, 2000]

$$\sigma = 2\left(\lambda^2 - \frac{1}{\lambda}\right)\left(\frac{\partial W}{\partial I_1} + \frac{1}{\lambda}\frac{\partial W}{\partial I_2}\right) \tag{2.3.5}$$

or, using (2.2.14) and (2.2.15) together with (2.3.5), as [*Holzapfel*, 2000]

$$P = 2\left(\lambda - \frac{1}{\lambda^2}\right)\left(\frac{\partial W}{\partial I_1} + \frac{1}{\lambda}\frac{\partial W}{\partial I_2}\right) \tag{2.3.6}$$

Utilizing (2.3.3) and (2.3.6), the stress-stretch relation for the neo-Hookean material becomes [*Holzapfel*, 2000]

$$P = 2\left(\lambda - \frac{1}{\lambda^2}\right)C_{10} \tag{2.3.7}$$

Similarly, combining (2.3.4) and (2.3.6) gives the response of the Mooney-Rivlin material [*Holzapfel*, 2000]

$$P = 2\left(\lambda - \frac{1}{\lambda^2}\right)\left(C_{10} + \frac{1}{\lambda}C_{01}\right) \tag{2.3.8}$$

Now, consider the simple shear deformation which is characterized by the expression (2.1.30). Substituting the second expression in (2.1.32) into (2.2.13), the stress-deformation relation can be written as [*Holzapfel*, 2000]

$$\sigma_{12} = 2c\left(\frac{\partial W}{\partial I_1} + \frac{\partial W}{\partial I_2}\right) \tag{2.3.9}$$

where σ_{12} is the shear stress. Using (2.3.9) and (2.3.3), the response of the neo-Hookean material can be found as [e.g., *Atkin and Fox*, 1980]

$$\sigma_{12} = 2cC_{10} \tag{2.3.10}$$

Similarly, the stress-deformation relation for the Mooney-Rivlin material can be obtained substituting (2.3.4) into (2.3.9) as

$$\sigma_{12} = 2c(C_{10} + C_{01}) \tag{2.3.11}$$

For small-strains, the shear modulus G has the values of $2C_{10}$ and $2(C_{10} + C_{01})$ for the neo-Hookean and Mooney-Rivlin materials, respectively [*Holzapfel*, 2000].

The neo-Hookean model has been frequently used to model the behavior of the silicone gel material (see Chapter 5). In biomechanics, the polynomial form of strain energy function has been used to characterize brain response. *Pamidi and Advani* [1978] were among the first to employ a constitutive model based on the concept of strain energy. They modified the strain energy function given in (2.3.4) leading to the non-linear viscoelastic model. Model parameters were calculated by fitting the model to the unconfined compression data reported by *Estes and McElhaney* [1970]. *Mendis et al.* [1995] used the same data and strain energy function while they defined parameters of the energy function in the form of exponential series in order to account for the time-dependent behavior. *Miller* [1999] used a viscoelastic extension of (2.3.2) to describe their experimental data in which they performed constant strain-rate unconstrained compression tests on cylindrical samples excised from porcine brain tissue. The coefficients of the polynomial strain energy function that they obtained under high strain-

rate (instantaneous) and low strain-rate (relaxed) loading conditions are given in Table 2.1.

Table 2.1. Parameters of the polynomial strain energy function reported in *Miller* [1999].

	Instantaneous Coefficients C_{ij}^{0}	Relaxed Coefficients C_{ij}^{∞}
C_{10}	263 Pa	48.7 Pa
C_{01}	263 Pa	48.7 Pa
C_{11}	0 Pa	0 Pa
C_{20}	491 Pa	90.8 Pa
C_{02}	491 Pa	90.8 Pa

2.4 Computational Implementation of Forward and Inverse Analyses

The purpose of inverse analysis is to characterize a physical system, for instance to evaluate parameters of a model which is assumed to describe fundamental physics of the system, using collected observations, i.e., experimental data [*Tarantola*, 1987]. This work deals with the inverse problem and, in particular, focuses on finding the model parameters of chosen constitutive models from the experimental measurements. The inverse problem is solved by trial and error, such as successively performing forward simulations for different parameter sets until achieving a reasonable agreement between simulations and experimental data. The parameter set which provides the best model-simulation agreement is accepted as the solution of the inverse problem. However, the search for the solution in this method is not a random process. There are different search procedures suggested to update model parameters at the end of each successive forward simulation. One alternative is to use optimization algorithms (e.g., Newton's method, Monte Carlo method) to minimize the error between observations and forward simulations. This has been used effectively in the biomechanics community [i.e., *Moulton et al.*, 1995; *Kyriacaou et al.*, 1996; *Kauer et al.*, 2001]. Most of the existing algorithms are based on the approach proposed by *Levenberg* [1944] and *Marquardt* [1963], whose application to soft tissue is very promising. Accordingly, in this work, the Levenberg-Marquardt method is chosen as a search algorithm.

Let y_i^m and y_i^s be some measured and simulated quantities, respectively, for i = 1,…, M, and x_n be the solution space for n = 1,…, N. It is necessary to minimize the objective function f, sum of the squares of the residual between y_i^m and y_i^s which is also known as square of L_2-norm , such that

$$f = \sum_{i=1}^{M} (y_i^m - y_i^s)^2 \tag{2.4.1}$$

$$L_2 = \sqrt{\sum_{i=1}^{M} (y_i^m - y_i^s)^2} \tag{2.4.2}$$

Let,

$$s_i = y_i^m - y_i^s \tag{2.4.3}$$

The Jacobian of s_i can be defined as

$$J_{ij} = \frac{\partial s_i}{\partial x_j} \tag{2.4.4}$$

In the Levenberg-Marquardt method, the equations for successive iterations are given as [*Aster et al.*, 2005]

$$\Delta x_n (\lambda \delta_{mn} + \sum_k J_{km} J_{kn}) = -\sum_k J_{km} s_k \tag{2.4.5}$$

where λ is the positive Marquardt parameter, Δx_n is the iteration step for $n = 1,\ldots, N$. A basic Levenberg-Marquardt algorithm is therefore,

- Choose an initial set of parameters, x_n^0, $n = 1,\ldots, N$
- Compute J_{ij} and s_i, $i = 1,\ldots, M$, $j = 1,\ldots, N$
- Solve (2.4.5) for Δx_n, $n = 1,\ldots, N$

- Calculate $x_n^{k+1} = \Delta x_n^k + x_n^k$ until reaching a stopping criteria

The Marquardt parameter is adjusted during iterations to ensure convergence. For very small values of λ, (2.4.5) reduces to the Gauss-Newton Method,

$$\Delta x_n \sum_k J_{km} J_{kn} = -\sum_k J_{km} s_k \tag{2.4.6}$$

and for very large values of λ

$$\lambda \delta_{mn} + \sum_k J_{km} J_{kn} \approx \lambda \delta_{mn} \tag{2.4.7}$$

Hence, (2.4.5) reduces to the steepest-descent method,

$$\Delta x_n = -\frac{1}{\lambda} J_{kn} s_k \tag{2.4.8}$$

Although, the steepest-descent method provides a relatively slow convergence, the convergence is quite reliable. Conversely, Gauss-Newton Method is potentially fast but in this method convergence is not guaranteed. The strategy of the Levenberg-Marquardt algorithm is to keep small values of λ as long as the Gauss-Newton Method works, and to use larger values of λ when the Gauss-Newton Method cannot make any progress [*Aster et al.*, 2005].

In this study, forward simulations are performed using the finite element method. In order to carry out finite element simulations, *ABAQUS* [2004], commercially available finite element analysis software, is chosen due to its ability to handle both geometrical

and material non-linearities, and its wide hyper-elastic model library, which includes the ones used in this work.

2.5 Conclusions

In this chapter, we introduced the framework for the subsequent mechanical analysis of soft tissue (brain and breast) in a human body and for the inverse analysis which is used for parameter estimation in the following chapters. In the first part of this chapter, we presented the basics of non-linear continuum mechanics as applied to soft tissue biomechanics. For this purpose, first, we discussed strain and stress measures (with related examples), which are commonly employed in the literature. Then, we introduced constitutive models that are used in this work and in the brain and breast biomechanics community. In the second part, we presented the details of forward and inverse analysis.

CHAPTER III

MATHEMATICAL MODELING OF THE PROPOSED EXPERIMENT

3.1 Mechanics of Brain Tissue

Living brain is a soft and mushy structure that is submerged in CSF within cranial cavity [*Nolte*, 2002]. It is seriously deformed and may even tear under the effect of gravity without the structural support of the meninges and the buoyant effect of CSF [*Kyriacou et al.*, 2002]. Cellular elements and blood vessels comprise about 80% of the total volume of the brain and the rest is extracellular space filled with extracellular fluid [*Sykova et al.*, 2000].

Mechanical properties of the brain tissue have been measured in different modes, such as tension, compression, simple/tortional shear, and indentation. *Miller and Chinzei* [1997; 2002] performed constant strain-rate unconstrained tension/compression tests on cylindrical samples excised from porcine brain tissue. Their results indicate that the stress-strain relationship of the brain is non-linear and strain-rate dependent. Moreover, they found that the stiffness of the brain in compression is higher than in extension. *Franceschini* [2006] verified these results by measuring the stress-strain response of human brain tissue samples collected during an autopsy in unconfined tension /compression (constant strain rate). In order to characterize the behavior of the brain tissue in shear, *Bilston et al.* [2001] collected samples from bovine models and performed shear relaxation, oscillatory, and constant strain-rate testing using parallel plate torsional

rheometry. They demonstrated that the brain tissue has a non-linear strain softening behavior in shear. Similar behavior was observed by *Prange and Margulies* [2002] and *Coats and Margulies* [2006] in parallel plate simple shear relaxation testing of porcine brain tissue samples and by *Brands et al.* [2000] in torsional shear relaxation experiments on porcine brain tissue. On the other hand, *Donnelly and Medige* [1997] observed shear hardening behavior in their simple shear experiments performed on the specimens obtained from human cadavers.

In-vivo versus In-vitro Properties

Most of the available mechanical data for the brain tissue has been derived from *in-vitro* experiments. However, *in-vivo* brain is composed of a network of neural components and vascular structures which are pressurized by blood flow. It has been hypothesized that pressurized vasculature stiffens the brain tissue, and 2-D finite element simulations showed that the perfusion might increase the tissue stiffness [*Bilston*, 2002]. Additionally, the walls of the cerebral bloods vessel, which have an elastic modulus on the order of 10 MPa [*Monson et al.*, 2000], are stiffer than the brain tissue by approximately 4 orders of magnitudes [*Gefen and Margulies*, 2004]. Accordingly, the vascular tree may increase the apparent stiffness of the brain tissue [*Zhang et al.*, 2002]. There are other factors which may be responsible for different mechanical behavior of the *in-vivo* and *in-vitro* brain tissue, such as tissue degradation, sample dehydration, and difficulty in forming appropriate specimens [*Bilston*, 2002].

Metz et al. [1970] defined a "pumping modulus," a measure of tissue's resistance to expansion of a balloon catheter. They inflated the catheter in a rhesus monkey's brain at 5, 20, and 45 minutes after death and demonstrated a decrease in this modulus. On the other hand, *Gefen and Margulies* [2004] performed indentation tests on *in-vivo*, *in-vitro*, and *in-situ* porcine brain tissue and concluded that although there is a difference in mechanical response of *in-vivo* and *in-vitro* brain, the perfusion does not contribute significantly to the mechanical behavior of the brain tissue.

Volumetric Response

Brain parenchyma is a fluid-saturated porous material. Accordingly, the tissue is expected to be incompressible during impact situations while its response to quasi-static loading may be significantly compressible. Nevertheless, there is a lack of experimental work for the characterization of brain tissue compressibility [*Kyriacou et al.*, 2002]. *Miller and Chinzei* [1997] measured the radial displacement of tissue samples by a laser distance meter during uniaxial compression test in order to determine the level of tissue incompressibility. Although they could not obtain repeatable results due to technical reasons, *Kyriacou et al.* [2002] pointed out that no volume change was observed in their experiments. Similarly, *Franceschini* [2006] performed unconfined compression tests on specimens excised from autopsy and found that initial undrained and drained Poisson's ratios, υ, equal to 0.5 and 0.496, respectively.

Isotropy and Homogeneity

White mater is mainly composed of axonal fibers (tracts) which are highly oriented, while gray mater consists of cell bodies and supporting network of cells and vasculature. In order to explore the effect of structural characteristics of the brain on its mechanical behavior, *Prange and Margulies* [2002] performed simple shear and unconfined compression stress relaxation tests on samples collected from bovine gray and white maters. Their test results demonstrated that gray mater is isotropic while there is a directional dependence of stiffness in white mater, up to 90% stiffer in a preferred direction depending on the neuroarchitecture. Moreover, they reported that inhomogeneity exists between gray mater and white mater, and between different regions of white mater.

However, since *Prange and Margulies* [2002] performed experiments on the samples that were 1 mm wide, *Miller et al.* [2005] concluded that the fibrous nature of the tissue would lead to detectable directional dependence of the stiffness and at large length scales, most soft tissues can be assumed to be isotropic.

3.2 Silicone Gel as a Material Simulating Brain Tissue

Physical models have been frequently used to investigate the mechanical response of soft tissue. In these studies, different brain substitute materials have been used. For example, *Audette et al.* [1999] used a brain phantom made of Polyvinyl Alcohol Cryogel to simulate the brain shift problem. *Bradshaw et al.* [2001] and *Ivarsson et al.* [2000] used a silicone gel brain model to analyze the effect of a head impact on brain injury.

Brands et al. [2000] performed oscillatory and stress relaxation experiments on silicone gel using rotational rheometer. They reported that Dow Corning® Sylgard 527 Dielectric Silicone Gel [*Dow Corning*, 2005] mimics closely the viscoelastic brain tissue properties at low frequency quasi-static loads (Figure 3.1). Another important similarity of brain and silicone gel is their specific gravities. The specific gravity (G) of silicone gel is 0.97 [*Dow Corning*, 2005]. The density of brain tissue is reported to be 1.039 g/cm^3 in white mater and 1.036 g/cm^3 in gray mater [*Velardi et al.*, 2006], which corresponds to a specific gravity of ~1.04. Beyond the quantitative similarity, the specific gravities (G) of both materials are close to unity, so that both practically suspend in water. This is particularly important in forward simulation of the experiments.

Dokos et al. [2000] developed a new simple shear test device, capable of applying forces in different directions, simultaneously, and performed experiments on silicone gel samples. Moreover, in order to validate their results, they measured the stress deformation response of the silicone gel in simple tension and rotational shear modes. They reported that in simple shear, the shear stress-shear strain behavior is linear. Additionally, in uniaxial tension, the relationship between the first Piola-Kirchhoff stress and the stretch ratio was found to be linear, featuring a slight softening with deformation. They concluded that the neo-Hookean model provides reasonable fit to the data and can be used to model silicone gel material. Similarly, *Rajagopal et al.* [2004] performed uniaxial tension test on silicone gel and showed that silicone gel can be modeled by the neo-Hookean material law. *Azar et al.* [2000] showed that its mechanical behavior can also be described by the Mooney-Rivlin model.

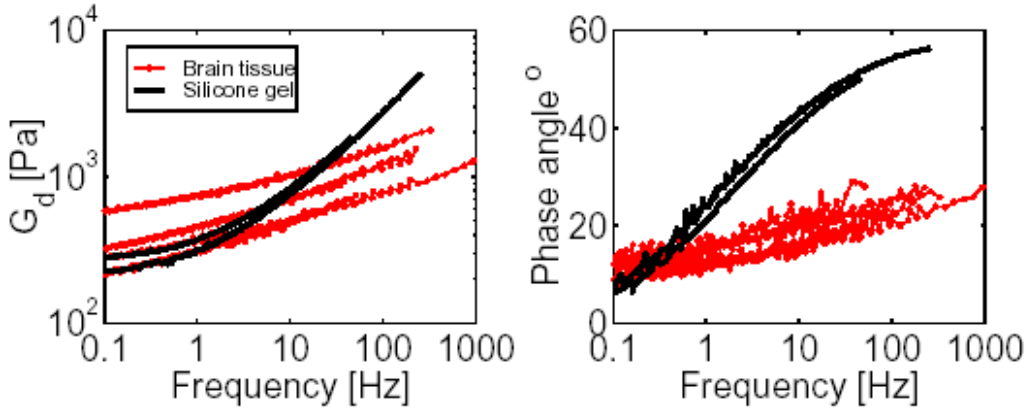

Figure 3.1. Response of silicone gel and porcine brain tissue to oscillatory loading [after *Brands*, 2002].

3.3 Boundary Conditions

Skull

The skull is composed of inner and outer layers of bone sandwiching a vesicular layer, which has a honeycomb-like structure. Bone is composed of collagen fibers and calcium salts. The skull is transversely isotropic material which has mean tangential and radial compression modules of 5.51 GPa and 2.41 GPa, respectively [*Goldsmith*, 2001].

Meninges

The dura mater is highly anisotropic. It is attached to the inner surface of the skull. The modulus of elasticity of the dura mater is reported to be in the order of 40 MPa [*Goldsmith*, 2001].

There are no direct measurements done in the literature to characterize the mechanical behavior of the leptomeninges. Both arachnoid and pia are comprised of collagen fiber bundles, which extend through the arachnoid trabeculae. The elastic modulus of collagen is approximately 1000 MPa [*Fung,* 1993]. Accordingly, the elastic modulus of arachnoid and pia are assumed to be in the same order of magnitude as dura mater [*Wittek et al.*, 2005; *Zoghi-Moghadam et al.*, 2003; *Zhang et al.*, 2002]. The subarachnoid space (SAS) is occupied by the cerebrospinal fluid and sheet-like arachnoid trabeculae extend from the arachnoid mater and blend into the pia mater. *Wittek et al.* [2006] reported rigid body movements of the brain within cranial cavity, which means that the arachnoid trabeculae do not completely restrict movement of the brain relative to the skull. Due to the complex fluid-structure interaction within SAS, which is not well understood, simplified boundary conditions have been used to represent SAS, such as:

fixing the outer surface of the brain to the skull [*Kaczmarek et al.*, 1997; *Taylor and Miller*, 2004], considering SAS as linear elastic solid [*Miller et al.*, 1999; *Brands et al.*, 2002], modeling the behavior of SAS by frictional interface [*Miller et al.*, 1999; *Miller et al.*, 2005], and applying uniform pressure over the surface of the brain [*Sahay et al.*, 1992].

Ventricles and Cerebrospinal Fluid

The cerebrospinal fluid (CSF) is derived from blood plasma and composed of 99% water. It has a specific gravity of 1.004-1.007 and contains a small amount of protein, blood cells (in pathological conditions), glucose, and ionic constituents [*Fishman*, 1992; *Bloomfield et al.*, 1998; *Goldsmith*, 2001]. In some pathological conditions, its composition may change. It can be classified as a newtonian fluid and its viscosity at body temperature is 1.02-1.027 MPa·s [*Goldsmith*, 2001]. Based on experiments performed on CSF samples mostly from patients with hydrocephalus, *Bloomfield et al.* [1998] reported that the viscosity of CSF at body temperature is similar to distilled water and does not significantly change with protein, blood cell, or glucose content.

To summarize, the boundary conditions at brain-skull interface are not well understood [*Wittek et al.*, 2006]. In the literature, simplified boundary conditions have been employed to model the brain-meninges interaction.

Since the brain is submerged in the CSF, the boundary condition at the outer surface of the brain can be modeled as pressure for low-strain rate loading conditions,

such as deformations due to development of hydrocephalus or application of ventriculostomy. Similarly, since ventricles are filled with CSF and there is no other structural support of the ventricular surfaces, pressure boundary condition can also be employed for ventricles.

The falx cerebri, one of the principal dural reflections, separates two cerebral hemispheres. The elasticity modulus of the dura mater was reported to be in the order of 40 MPa [*Goldsmith*, 2001], which is approximately 4 order of magnitudes stiffer than that of brain tissue. Moreover, due to the symmetry of the cerebral hemispheres with respect to the falx cerebri, the resultant force applied on the falx cerebri during the development of hydrocephalus and during the ventriculostomy procedure is zero. Accordingly, the falx cerebri is assumed to be rigid and attached to the cerebral hemispheres.

Under normal physiological conditions, the pressure of CSF (intracranial pressure) is normally in the range of 600-1500 Pa [*Goldsmith*, 2001]. As discussed in Chapter 1, most of the CSF is produced in ventricles and absorbed almost entirely in the subarachnoid space (SAS). According to *Penn et al.* [2005], a pressure gradient between ventricles and SAS (transmantle pressure gradient) in the range of 5-10 Pa is needed to drive CSF. In a hydrocephalic brain, the circulation of CSF is obstructed, leading to an increase in the ventricular pressure. *Mindermann* [1999] reported that transmantle pressure gradients of up to 4000 Pa may be observed in a hydrocephalic brain. *Kaczmarek et al.* [1997] found transmantle pressure gradient of 2746 Pa in their analytical calculations and reported that this falls in the range of observations in human hydrocephalus. *Conner et al.* [1984] performed experiments on cat models and found

that pressure gradients exist between ventricles and SAS in acute hydrocephalus. They also showed that although transmantle pressure gradient exists in rapidly progressing hydrocephalus, the pressure difference subsequently vanishes. *Stephensen et al.* [2002] performed experiments on human volunteers with communicating and non-communicating hydrocephalus. They measured the intracranial pressure in the ventricles and SAS. They reported that the pressure difference between ventricular and subarachnoid sensors is within the limits of hydrostatic pressure difference and there is no transmantle pressure gradients existing in both cases of hydrocephalus. A number of authors [see the comments to *Stephensen et al.*, 2002] suggested that a transmantle pressure gradient develops in acute hydrocephalus, and then gradually dissipates as the mechanical properties of the brain change. *Penn et al.* [2005] measured the pressure in the ventricles, in the brain parenchyma and in the subarachnoid space of dog models. They found no transmantle pressure gradients before and during the development of hydrocephalus. However, they hypothesized that in acute non-communicating hydrocephalus, large transmantle pressure difference might occur.

3.4 Effect of Gravity

Due to the low stiffness of the silicone gel and the large volume of silicone samples used in this work, the weight of the material may be an important factor in the forward simulations. In this section, the effect of gravity on the response of silicone phantom is investigated.

For this purpose, a simplified model of a brain phantom, the geometry of which is half-ellipsoid with dimensions 186 × 148 × 74 mm, was developed in *ABAQUS* [2004]. A similar geometry was used in the experimental program of this work (see Chapter 4). The incompressible neo-Hookean material was used for these simulations. The model parameter was chosen as C_{10} = 250 Pa. The specific gravity (G) was chosen as 0.97. Due to the incompressibility constraint and large element distortions, the model was meshed using modified second order tetrahedron hybrid elements (C3D10MH). Total of 13199 nodes and 8799 elements were generated (Figure 3.2). Three types of loading conditions were simulated. The boundary conditions for all models are illustrated in Figure 3.3. For the first case (Figure 3.3a), hydrostatic pressure was applied at both inner and outer surface of the phantom. The values of the hydrostatic pressures at the bottom of the phantom were 1274 Pa and 945.7 Pa for inner and outer surfaces, respectively. The body forces due to gravity were also considered. The bottom of the model was fixed to simulate falx cerebri. For the other two cases, the same model was used. However, Case 2, gravity was removed from the model, and for Case 3, a zero pressure boundary condition was applied to the outer surface.

The variations of the total displacements in the three cases along the lines A and B are shown in Figure 3.4. The maximum total displacement along line A in Case 1 is observed at 5 cm above the bottom of the phantom and is about 2 mm. The corresponding maximum displacement in Case 2 and Case 3 are approximately 6 and 11 mm, respectively. Similarly, along line B, the maximum total displacement is about 1 mm at 5 cm above the bottom of the phantom in Case 1. At the same position, displacements in Case 2 and Case 3 are approximately 5 and 10 mm, respectively. The

variations of maximum principal stresses in each model are also given in Figure 3.4. Along line A, all cases are in compression up to 3 cm above the bottom. The stress state in Case 3 changes at this point and becomes tension while others are still in compression. Along line B, all cases are in compression while the stress state in Case 3 changes at about 4 cm above the bottom and becomes tensile.

As seen in Figure 3.4, the difference of the total displacements between the three cases is 10 mm. Since the objective function in inverse analysis is formulated based on displacements, ignoring gravity and hydrostatic pressure on the outer surface would lead to unrealistic converged model parameters. Moreover, the difference in the maximum principal stresses is up to 800 Pa, which is close to the magnitude of the applied hydrostatic pressure. These results show that it is important to take the weight into account in our forward simulations.

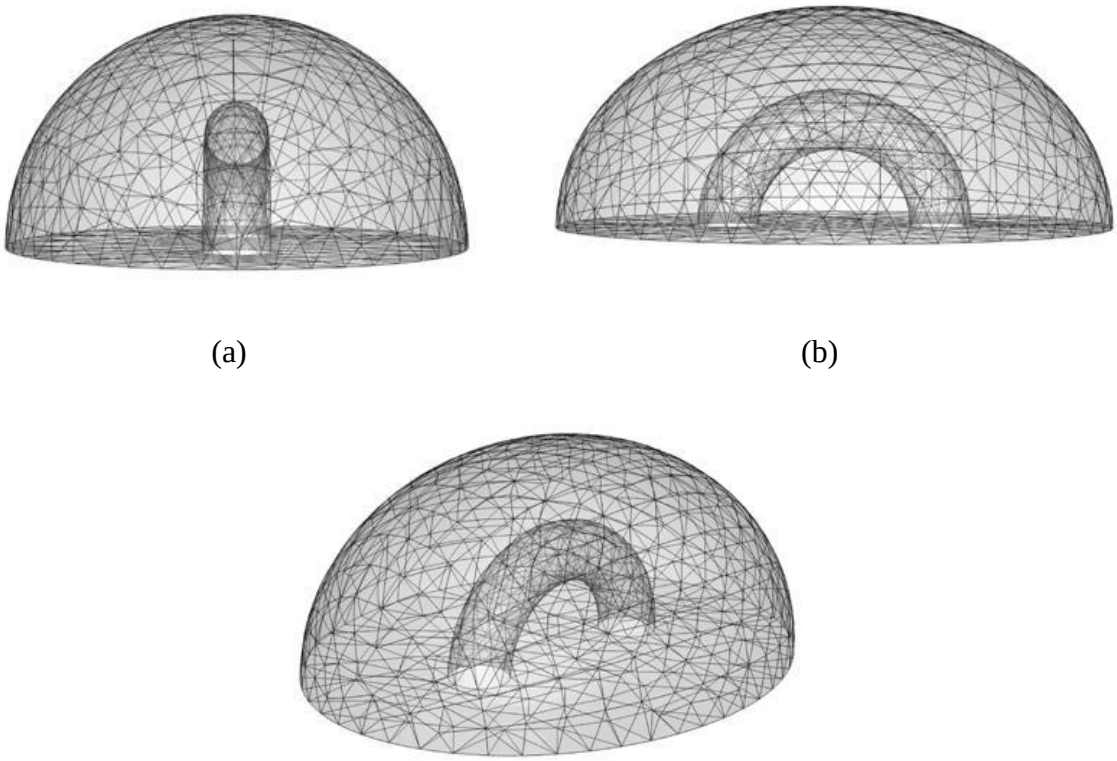

(a) (b)

(c)

Figure 3.2. Meshed geometry of the simplified brain model: (a) front view, (b) side view, and (c) perspective view.

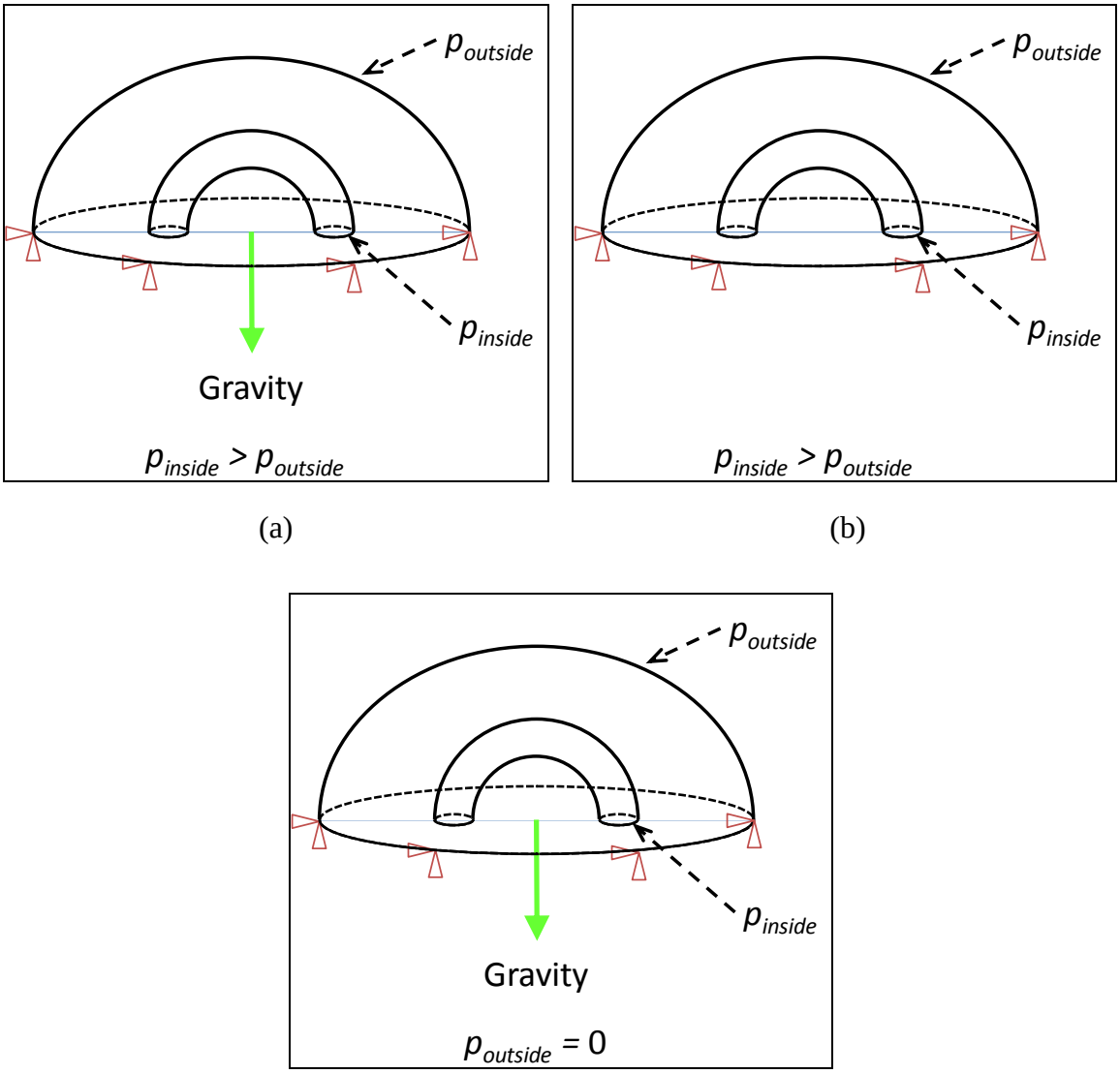

Figure 3.3. Boundary and loading conditions for (a) case 1, (b) case 2, and (c) case 3.

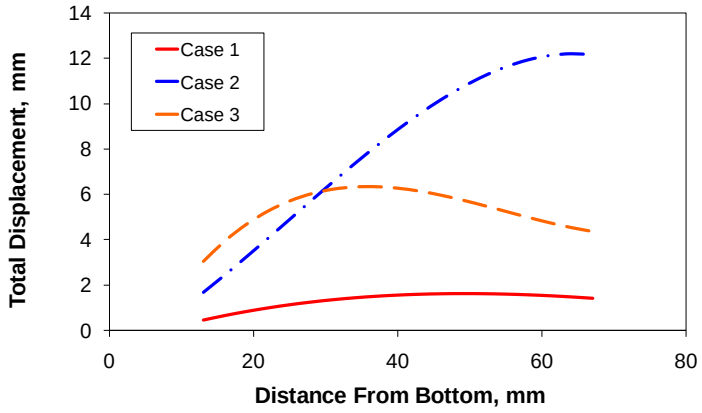

(a)

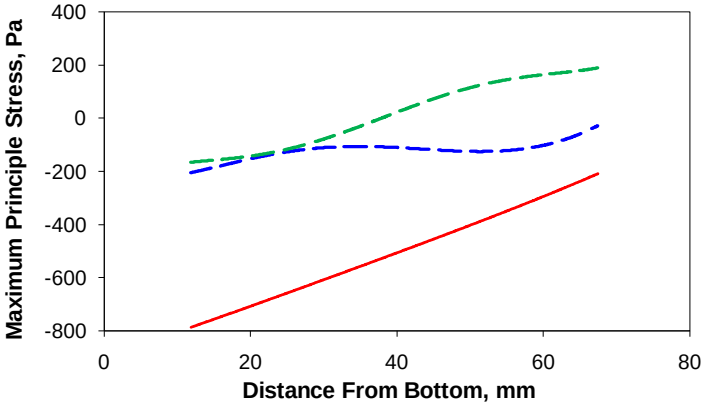

(b)

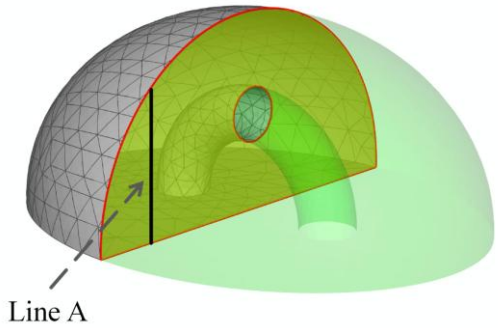

(c)

Figure 3.4. Variation of (a) total displacement and (b) maximum principal stress along line A. (c) Position of line A. Variation of (d) total displacement and (e) maximum principal stress along line B. (f) Position of line B.

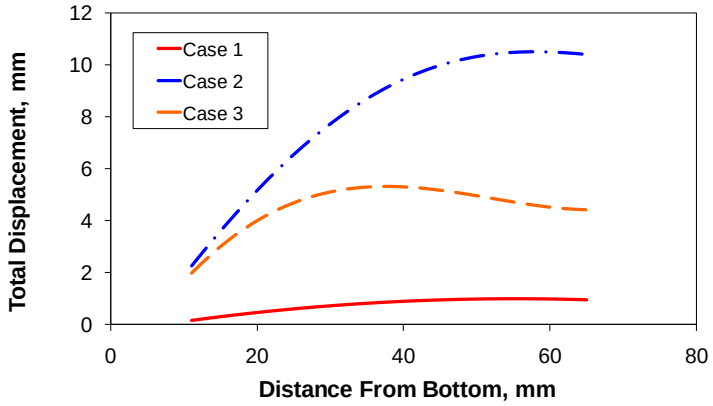

(d)

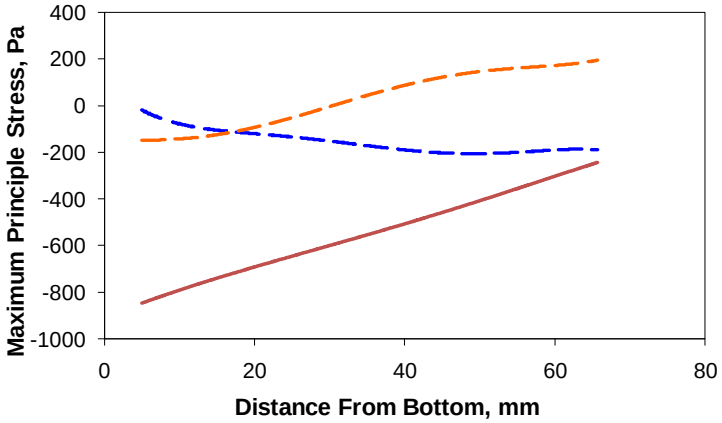

(e)

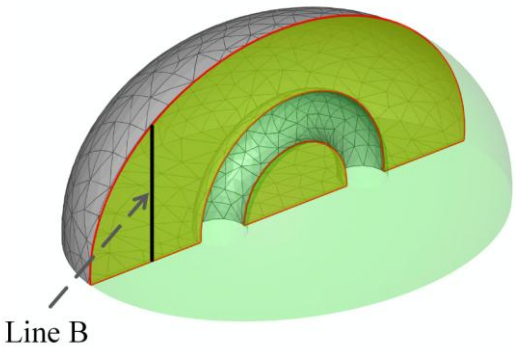

(f)

Figure 3.4. continued.

3.5 Mathematical Simulation of a Theoretical Ventriculostomy Operation

The kinematics of the operation is illustrated in Figure 3.5. We assume that a stress-freee reference configuration exists. The development of non-communicating hydrocephalus was simulated. First, the same magnitude of hydrostatic pressure was applied on both inner and outer surfaces of the phantom (initial configuration), which corresponds to the healthy brain. The value of the pressure at the bottom of the phantom in this pre-disease stage was 945.7 Pa. Next, the pressure in the cavity was increased to deform the phantom (current configuration), corresponding to the hydrocephalus stage. In this stage, the pressure at the bottom of the cavity was 2102.1 Pa. Note that we model the disease (hydrocephalus) rather than the operation (ventriculostomy). However, this does not affect the general aspect of the proposed procedure, due to the reversibility of the disease-operation process in our experiments, i.e., due to the stress relaxation in the brain during hydrocephalus, transmantle pressure gradients dissipate, and internal and external pressures equalize (see Section 3.2).

In reality, the initial configuration corresponds to the pre-operative stage and the current configuration corresponds to the post operative stage. The 3-D CT (or MRI) images are taken both at the initial and the current configurations, and the intracranial pressure is monitored during the operation. If the stress state in the initial configuration is known, stresses and displacements in the current configuration may be calculated. However, since the stress state and geometry of the body in the reference configuration is not known, it is not possible to determine the stress state in initial configuration. We assume that the reference configuration is stress-free. Although, this assumption

simplifies the problem, the only way to determine the geometry of the body in reference configuration is to start the operation under zero gravity conditions.

The brain is submerged in CSF, which has similar properties with distilled water, and the specific gravity of the brain tissue is close to unity. As a result, the brain suspends in the CSF (see Section 3.1). This fact may help us to establish the relationship between the reference and initial configurations. In order to establish this relationship, the simplified brain model developed in Section 3.4 was used. The boundary conditions of the initial configuration were applied as shown in Figure 3.5. The incompressible neo-Hookean material model was used for the simulations. Six simulations were performed for different model parameters. The model parameters were chosen as C_{10} = 250, 500, 750, 1500, 2500, and 5000 Pa for all models. These model parameters correspond to small-strain shear modulus of 500, 1000, 1500, 3000, 5000, and 10000 Pa, respectively.

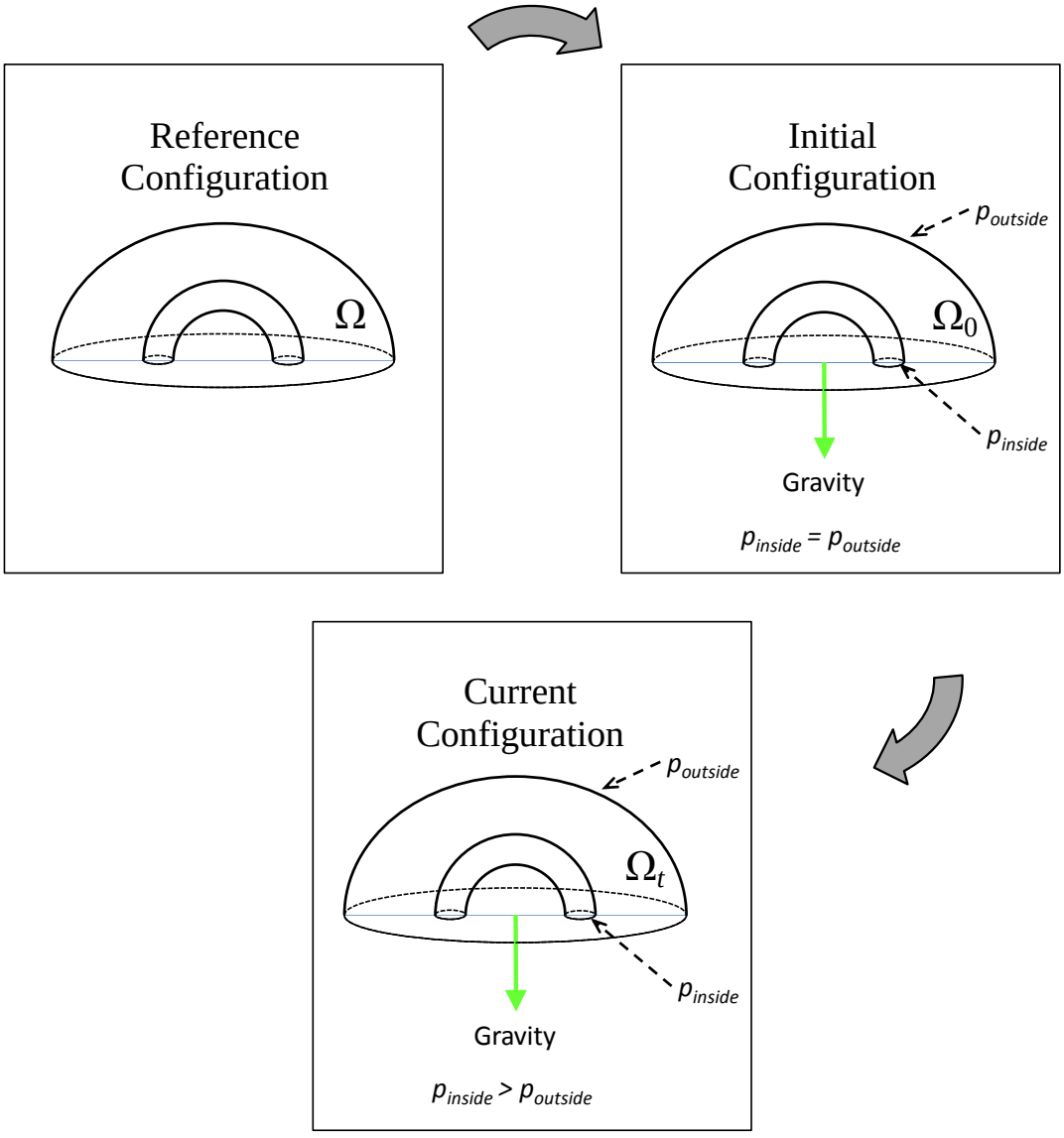

Figure 3.5. Kinematics of the theoretical operation.

Figure 3.6 shows the maximum principal stresses developed in the body for different model parameter. Due to the incompressibility of the silicone gel, the volume of the phantom does not change. Furthermore, the corresponding hydrostatic stress state develops inside the material as if it was a liquid of the same specific density. In other words, for all practical purposes, the stress response in the body in the initial configuration is independent of material parameters.

The variation of the maximum and average displacements in the model with a change in shear modulus is shown in Figure 3.7. It is seen that displacements increase as the shear modulus decrease. For the range of parameters used in these simulations, the maximum deformation is observed in the simulation with the shear modulus of 500 Pa. The maximum displacement in this model is 0.35 mm and the average displacement is 0.16 mm. The voxel size of the CT images used in this study is 0.68 mm, so the maximum displacement is about one half of the voxel size and the average displacement is about one third of the voxel size. Since the simplified brain model is about twice the size of human brain, it may be expected that displacements would be even smaller for the real brain geometry. From Figure 3.7, it can be concluded that all the deformations in the brain are negligible under the hydrostatic boundary loading conditions in the initial configuration.

Since the relationship between the configurations was established, in order to illustrate the effectiveness of the inverse analysis for the loading and boundary conditions shown in Figure 3.5 and described above, a theoretical operation was simulated and the model parameter was derived using inverse analysis. The simplified brain geometry developed in Section 3.4 was used. The incompressible neo-Hookean material model

was used for the simulations. The model parameter was chosen as C_{10} = 500 Pa, which corresponds to the model parameter determined from the inverse analysis. The data (displacement values of randomly chosen 60 points in the model) was generated using correct model parameter. Figure 3.8 shows the undeformed and deformed meshes of the phantom. In Figure 3.9 and Figure 3.10, the maximum principal stresses and the maximum principal logarithmic strains in 3 different cross-sections are shown, respectively. It is seen that due to the pressure increase in the cavity simulating ventricles, both compressive and tensile stresses and strains develop in the body. This is important while modeling the deformation of a real brain as the stiffness of the brain in compression is higher than in extension [*Miller and Chinzei*, 1997, 2002; *Franceschini*, 2006]

We define the objective function, described in (2.4.1), as the least square difference between model-predicted and measured (generated) displacements

$$f = \sum_{i=1}^{M} (u_{1_i}^{m} - u_{1_i}^{s})^2 + (u_{2_i}^{m} - u_{2_i}^{s})^2 + (u_{3_i}^{m} - u_{3_i}^{s})^2 \tag{3.5.1}$$

where $u_{1_i}^{m}$, $u_{2_i}^{m}$, $u_{3_i}^{m}$ are measured displacements, $u_{1_i}^{s}$, $u_{2_i}^{s}$, $u_{3_i}^{s}$ are simulated displacements, and M is the number of measurements, in this case M = 60. The inverse analysis algorithm converges to the solution in 10 iterations.

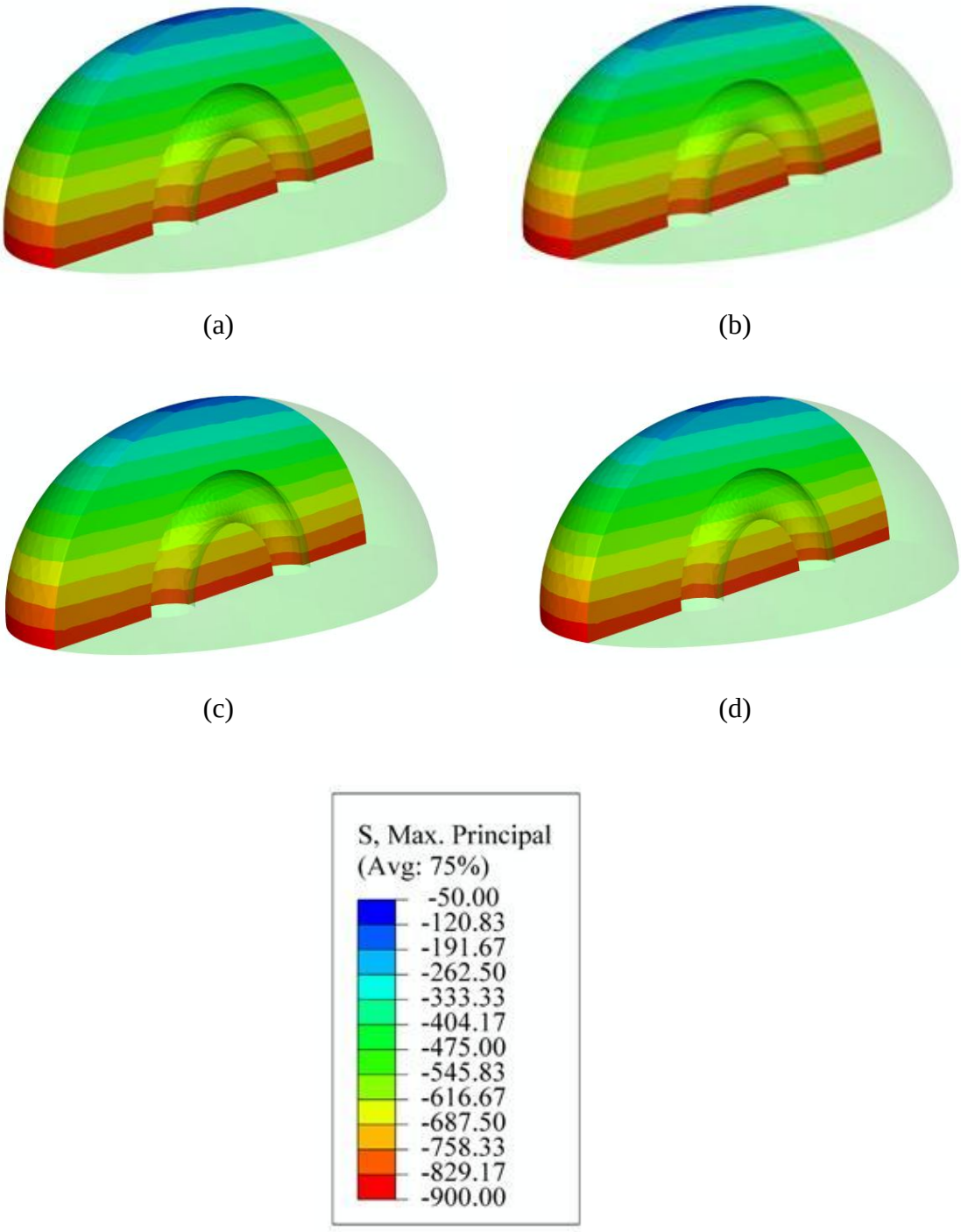

Figure 3.6. Maximum principal stress distribution in the phantom for different shear module: (a) 500, (b) 1500, (c) 3000, and (d) 10000 Pa, respectively. (e) Legend (contour map for stress magnitude in Pa).

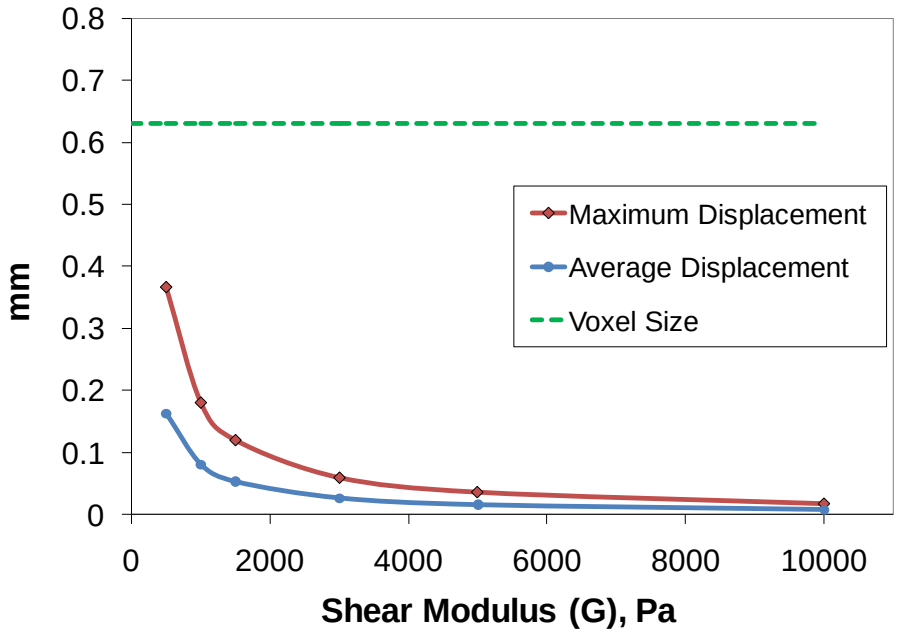

Figure 3.7. Variation of the maximum and average displacements with shear modulus.

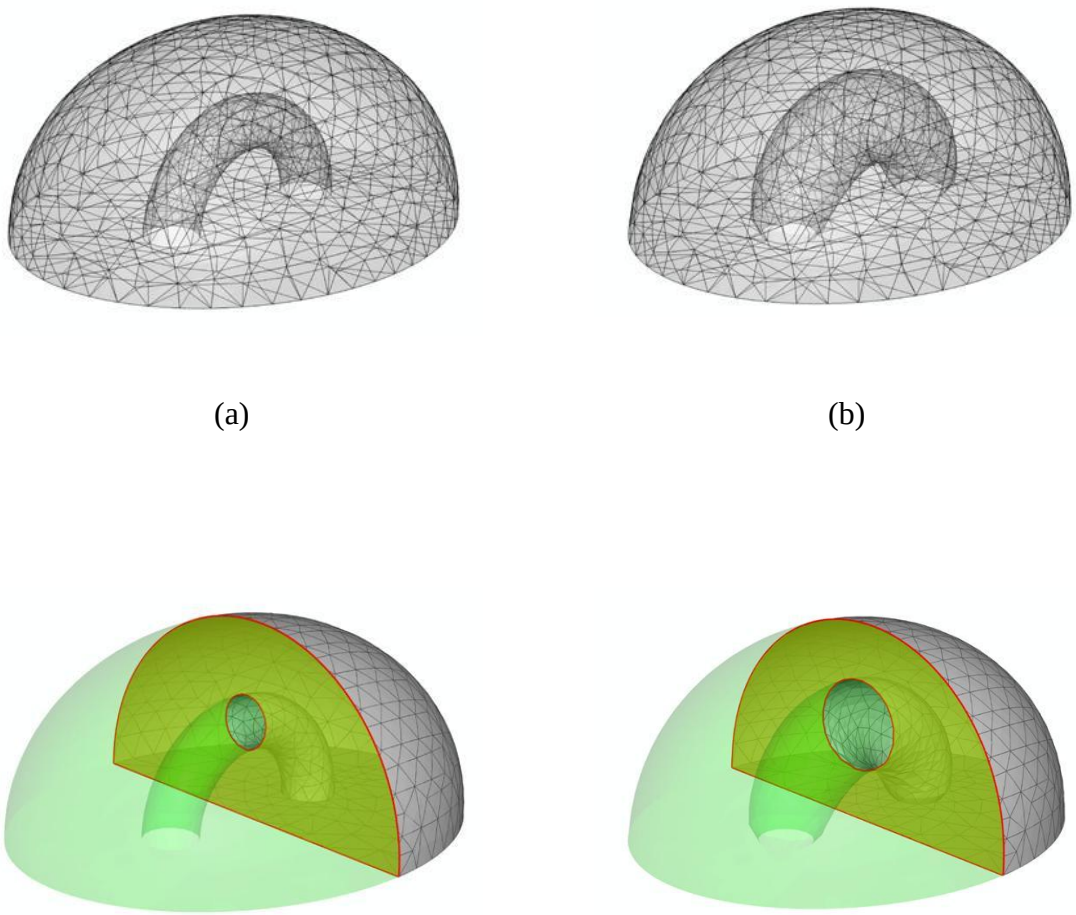

(a) (b)

(c) (d)

Figure 3.8. (a) Undeformed and (b) deformed meshes. (c) Undeformed and (d) deformed cross-sections of the phantom.

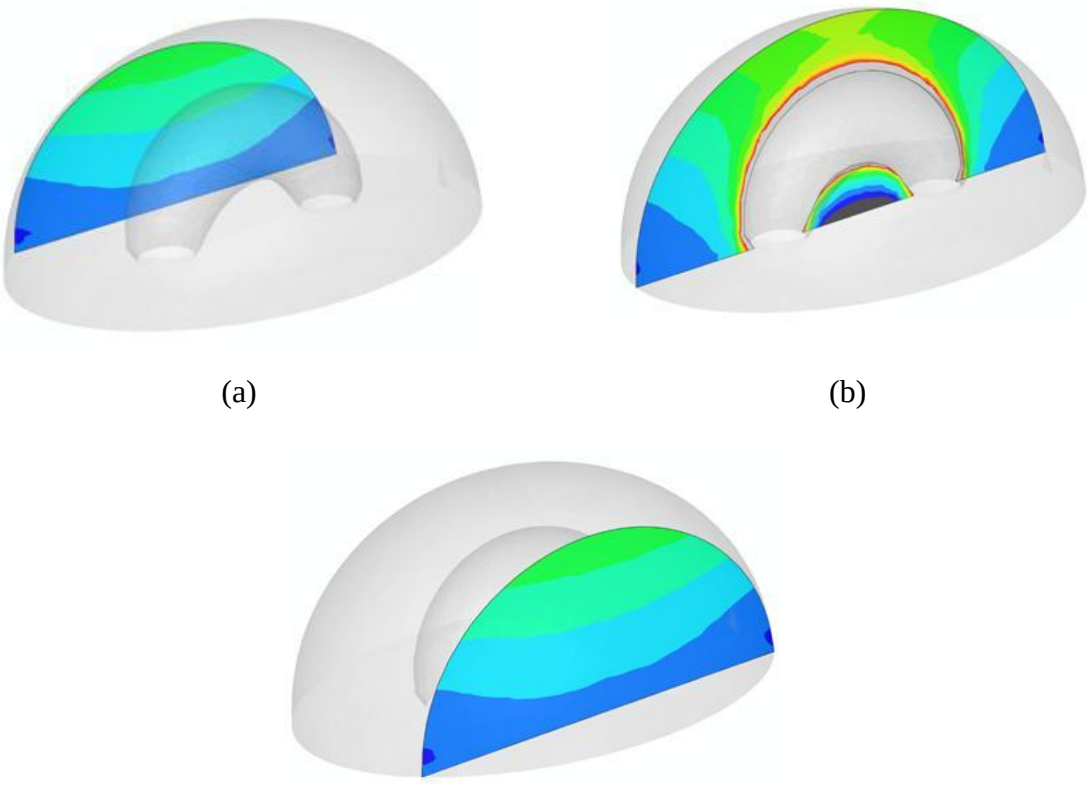

Figure 3.9. (a, b, c) Maximum principal stresses in the phantom in three cross-sections. (d) Legend (contour map for stress magnitude in Pa).

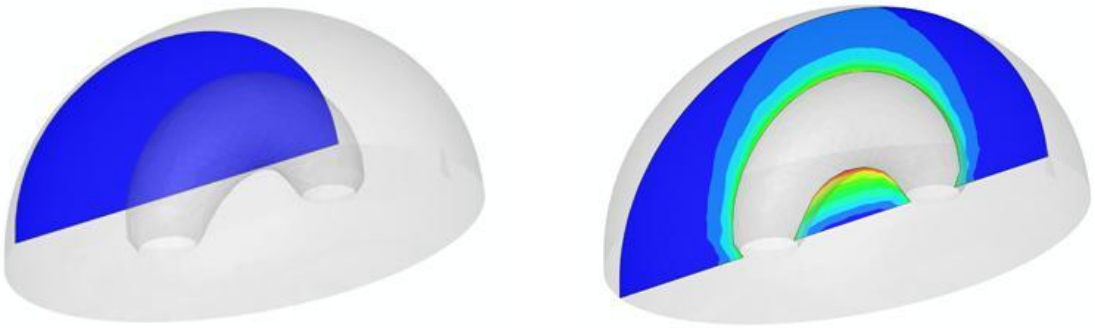

(a) (b)

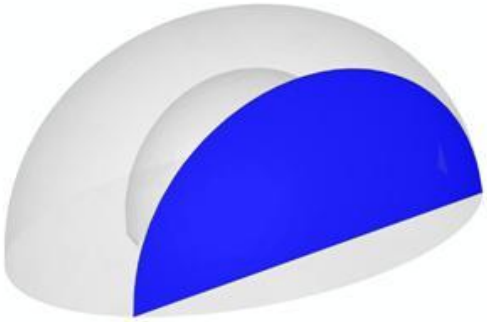

(c)

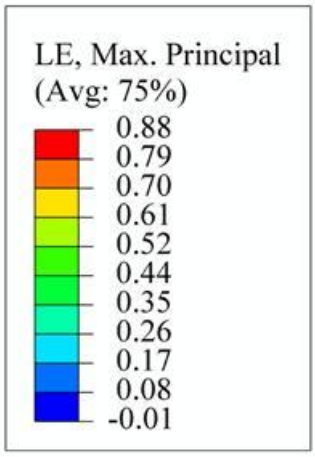

(d)

Figure 3.10. (a, b, c) Maximum principal logarithmic strains in three cross-sections. (d) Legend (contour map for strain magnitude).

3.6 Conclusions

In this chapter, we developed the tools which are used for the forward and inverse problems in Chapter 4 and 5. First, we presented the related literature used to choose proper material model and boundary conditions that are utilized in the experimental program and forward FE simulations. Then, we investigated the effect of gravity on the response of silicone phantom. To accomplish this, we performed simulations using three different loading conditions and concluded that it is important to take the weight into account in our finite element calculations. Moreover, we showed that since the specific gravity of the brain and the silicone gel is close to unity, for all practical purposes, all deformations in the silicone phantom are negligible under the hydrostatic boundary loading conditions in the initial configuration and the corresponding hydrostatic stress state develops inside the material which is independent of the material parameter. Finally, we carried out a simulation of a theoretical ventriculostomy operation with subsequent inverse analysis and determined the model parameters to show the effectiveness of the proposed method.

CHAPTER IV

EXPERIMENTAL PROGRAM

4.1 Sample Preparation

A plastic mold (Figure 4.1a) - about 23 x 18 x 11 mm - of the left hemisphere of a human brain was used to cast the brain phantom (Figure 4.1b) using Dow Corning® Sylgard 527 Dielectric Silicone Gel. This silicone gel system is composed of 2 parts, catalyst and resin, that are mixed to prepare the gel. In our experiments, catalyst and resin were mixed with a volume ratio of 1:1 and were stirred for 15 minutes. The mixture is then poured into the plastic mold. In addition, some of the mixture is poured into 2 cylindrical molds with a diameter and height of 82 mm for independent uniaxial compression testing. The samples were cured at 55^{o} C for 16 hours. While curing the silicone gel in the plastic mold, a plastic pipe of 2 cm diameter circular cross section was placed at the center of the mold (Figure 4.1c). After the curing, the pipe was removed and a rubber membrane was placed inside the hole to model the lateral ventricle. One millimeter diameter inclusions ("bubbles"), made by mixing white lithium grease with graphite powder with a weight ratio of 1:1, were injected into the phantom in a regular 3-D grid of about $1.5 \times 1.5 \times 1.5$ cm^3 in order to enable the detection of the displacement field in the CT images (Figure 4.1b).

During the experiment, two CT images are acquired: one at the pre-operative and one at the post-operative stage. To facilitate the registration of these two images, control bubbles are injected into silicone adhesive which is attached to the pedestal.

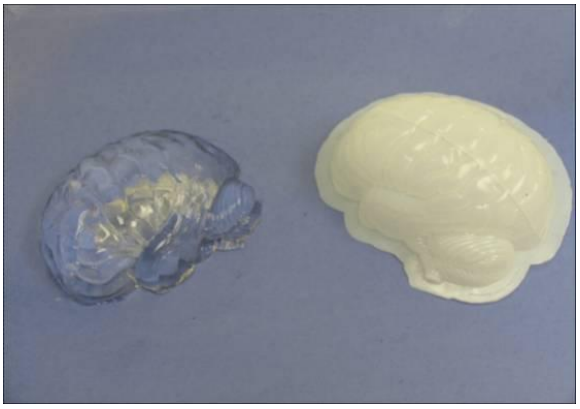

(a)

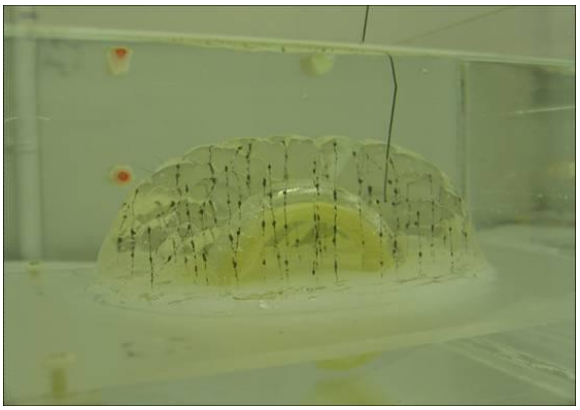

(b)

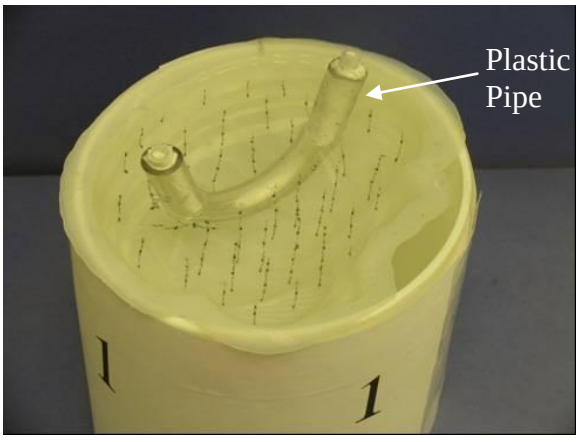

(c)

Figure 4.1. (a) Plastic mold, (b) “bubbles” in brain phantom, and (c) plastic pipe.

4.2 Preliminary Tests

The CT images acquired during the experiments are first used to construct the surface mesh of the phantom from the segmented slices and, second, to derive the displacement field by matching control points implanted in the phantom (see Chapter 5). To detect the control points within the phantom and the boundaries of silicone sample in acquired images, there must be a certain level of image contrast at the silicone-water and silicone-control point interface. If the necessary contrast at the interfaces could not be achieved, it would not be possible to distinguish silicone from water or from control points.

In order to find the best possible control point material that would give the best image contrast without impairing the images and to test the experimental setup in the imaging room, we carried our two sets of experiments. For the first set, we used a cylindrical silicone sample with diameter of 82 mm and height of 38 mm which was prepared as described in the previous section. Stainless steel beads of 1 mm diameter were randomly implanted into the silicone sample. The silicone batch was then placed into a plastic container to ease handling and transportation.

The experiment was carried out at Emory University Hospital in the General Electric LightSpeed 16 Computed Tomography Scanner (Figure 4.2) that has submillimeter resolution. Acquired CT images of the samples were composed of 279 slices. Images are composed of isotropic voxels with a resolution of 0.68 mm. The same scanner has been used for all experiments. The results of the experiment are shown in Figure 4.3. The silicone gel generates an almost constant gray level and the background is dark colored in the images. Steel beads appear as whitish in color. It is observed that

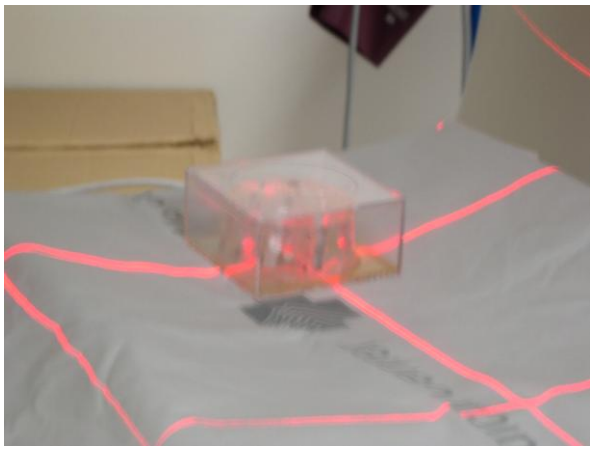

(a)

(b)

Figure 4.2. (a) First and (b) second set of experiments in the CT scanner.

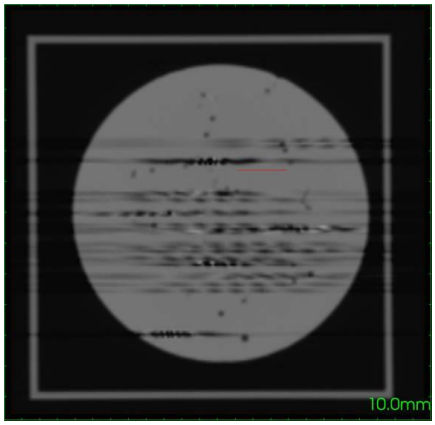

(a)

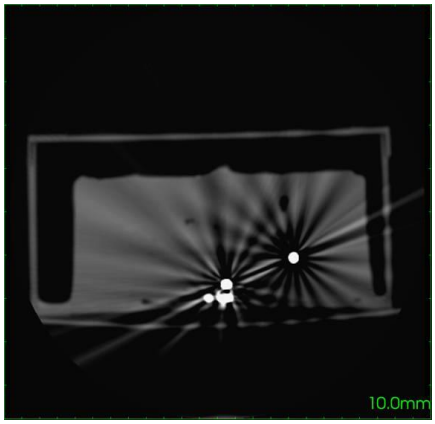

(b)

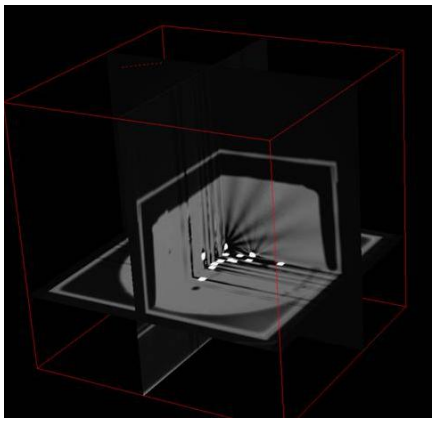

(c)

Figure 4.3. (a) Top and (b) side view of the cylindrical sample and (c) orthogonal slices from CT images of the first set of experiments.

although steel beads generate a good image contrast, it impairs the images. It was concluded that it cannot be used as control point material.

The second set of experiment was performed after manufacturing the experimental setup (see Section 4.3). A silicone gel brain phantom was prepared as discussed in the previous section. In this case, grease-graphite mixture control points were injected into the phantom. The first image was acquired in the undeformed state. Then, the cavity was inflated by applying hydrostatic pressure into the cavity. The second image was acquired at this state (Figure 4.2b). Resulting images are shown in Figure 4.4. As a result of this set of experiment, it was concluded that (i) the setup discussed in Section 4.3 was appropriate for the experimental program, (ii) grease-silicone mixture appears whitish in the images and does not impair the quality of the images, and (iii) the boundaries of the silicone phantom can be detected visually at the silicone-water interface.

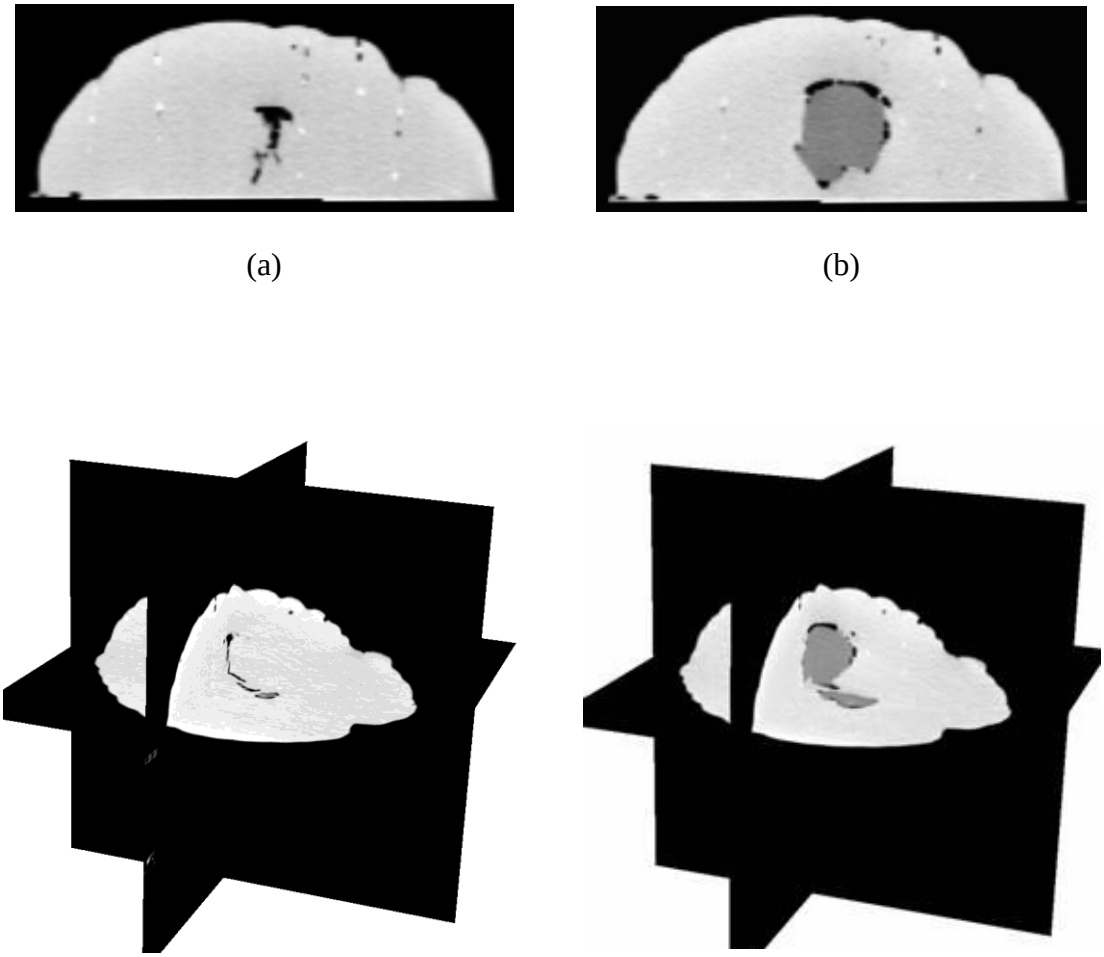

Figure 4.4. (a) Undeformed and (b) deformed CT slices. (c) Undeformed and (d) deformed orthogonal slices from the CT images of the second set of experiments.

4.3 Experimental Setup and Procedure

The experimental setup was designed to model both communicating and non-communicating "hydrocephalus" with subsequent "ventriculostomies" by independently controlling the outer and inner pressures in the phantom. The schematic of the experimental setup is given in Figure 4.5. No metal parts were used in the setup construction allowing for the experiments to be conducted in both CT and MRI environments. The setup consists of a transparent Plexiglas cell and a lid. A gasket of cured silicone sealant was used between cell and lid to create a hermetic system. During the experiments, the brain phantom which is fixed to a pedestal using silicone sealant to simulate falx cerebri, was placed into the cell. Two standpipes were connected to the hermetic cell. These standpipes allow for independent pressure/volume control both in the cell and in the cavity, simulating the pressures in the subarachnoid space and ventricles, respectively. The available pressure range is $0 - 5$ kPa with a resolution of 0.01 kPa, which is consistent with the range of both normal and abnormal CSF pressures. Figure 4.6 illustrates the experimental set up.

The kinematics of the experimental procedure were discussed in Chapter 3 (Figure 3.5). First, the same magnitude of hydrostatic pressure was applied on both the inner and outer surfaces of the phantom (initial configuration), which corresponds to the healthy brain (before the disease). The value of the pressure at the bottom of the phantom (both outside and inside) in this pre-disease stage was 945.7 Pa. Next, the pressure in the cavity was increased to deform the phantom (current configuration), corresponding to the hydrocephalus stage. In this current configuration, which is the pre-operative stage in the experiment, the pressure distribution on the outer surface was kept at the same level as

before (945.7 Pa at the bottom of the phantom), while hydrostatic pressure in the rubber membrane was increased, so that the pressure at the bottom of the cavity was 2102.1 Pa. The 3-D CT images were taken both at the initial and the current configurations.

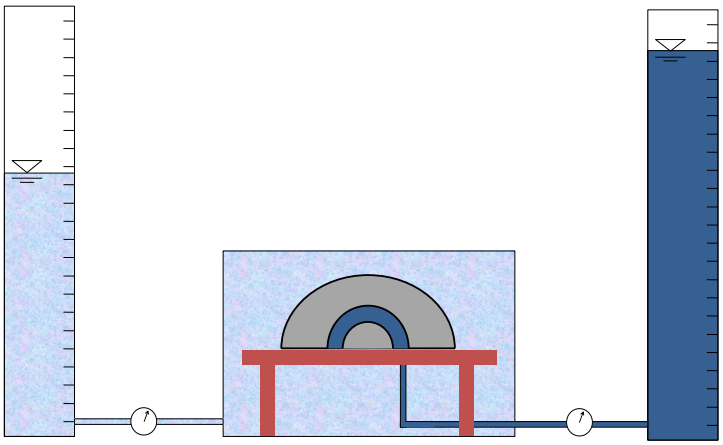

Figure 4.5. Schematic of the experimental setup.

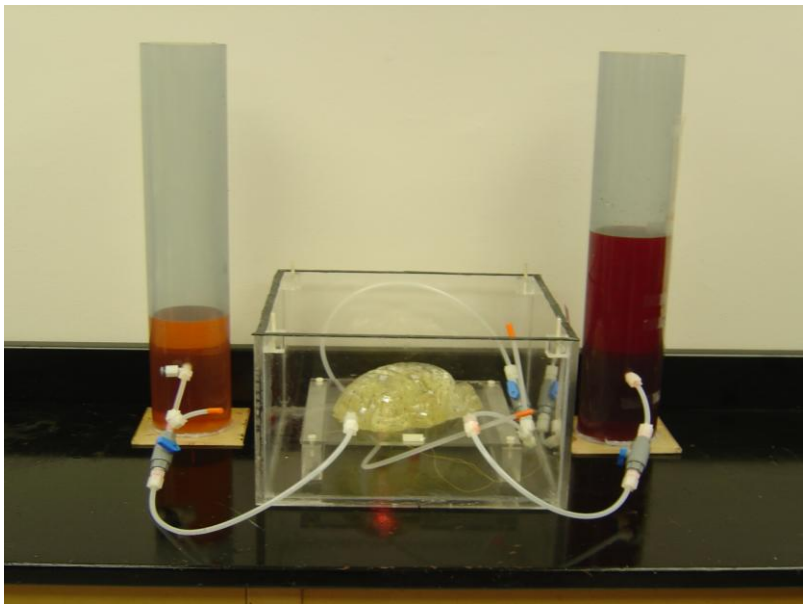

Figure 4.6. Experimental setup.

4.4 Direct Measurement of the Silicone Gel Properties

In order to demonstrate the reliability of IGCM, we also derived the material properties of the silicone gel via independent tests without using any image guidance. For this purpose, two cylindrical specimens with diameter and height of 82 mm were prepared as described in Section 4.1.

The specimens are tested in uniaxial compression with no-slip boundary conditions. Note that the *slip boundary condition* using lubricated sample ends would be much easier to interpret the test results since this case is truly one dimensional and does not require any numerical simulation. However, even a small uncertainty in shear tractions at the sample ends may considerably affect the test results [*Wu et al.*, 2004; *Miller et al.*, 2005]. Therefore, we decided to use the no slip boundary condition which makes the test interpretation more complex but facilitates much less uncertainity. The experiment was performed with the specimens immersed in water to minimize the effect of gravity.

In order to perform the uniaxial compression test, INSTRON 3288 U.T.M. was used. Due to technical problems, force measurements could not be done using built-in force transducer of the INSTRON loading frame. Instead, the loading frame was modified as shown in Figure 4.7. In order to measure the applied force during the experiment, a scale was placed next to the built-in force transducer of the frame. A cylindrical transparent cell was manufactured in order to perform the experiment in water. A loading plate was attached to the bottom of the transparent cell. A steel rod was attached to the mobile part of the frame, so that the loading plate on the cell aligns with the loading plate attached to this metal rod. The no-slip boundary conditions were

created by attaching coarse sandpaper to the faces of loading plates. The displacement of the sample boundaries versus the applied axial load were recorded manually during the experiment. The first data point was recorded when the distance between the loading plates was equal to the height of a sample, measured when the sample was in the cylindrical mold. Figure 4.8 shows undeformed and deformed shape of the sample 1.

Although, the analytical solution to this problem is available, it still requires the numerical solution of a system of transcendental algebraic equations [*Klingbeil and Shield*, 1966]. This is why, to determine the material parameter, the inverse analysis approach was employed using the neo-Hookean model. Forward simulations were modeled in ABAQUS. The 8-node biquadratic hybrid reduced integration (CAX8RH) elements were used in the simulations. This type of element works well for axisymmetric finite element modeling of large deformations of incompressible materials [*Kyriacou et al.*, 2002; *ABAQUS*, 2004]. We defined the objective function, described in (2.4.1), as

$$f = \sum_{i=1}^{M} (P_i^m - P_i^s)^2 \tag{4.4.1}$$

where P_i^m is the measured first Piola-Kirchhoff stress, P_i^s is the simulated first Piola-Kirchhoff stress, and M is the number of measurements. Finally, we calculated the parameter of the neo-Hookean model (Table 4.1) by minimizing (4.4.1).

In Figure 4.9, the undeformed and deformed geometries of the simulation are shown. Stress-stretch (in this case, stretch is defined as the ratio of final to initial length of the sample) plots of the uniaxial compression experiments, and neo-Hookean model predictions for both samples are given in Figure 4.10.

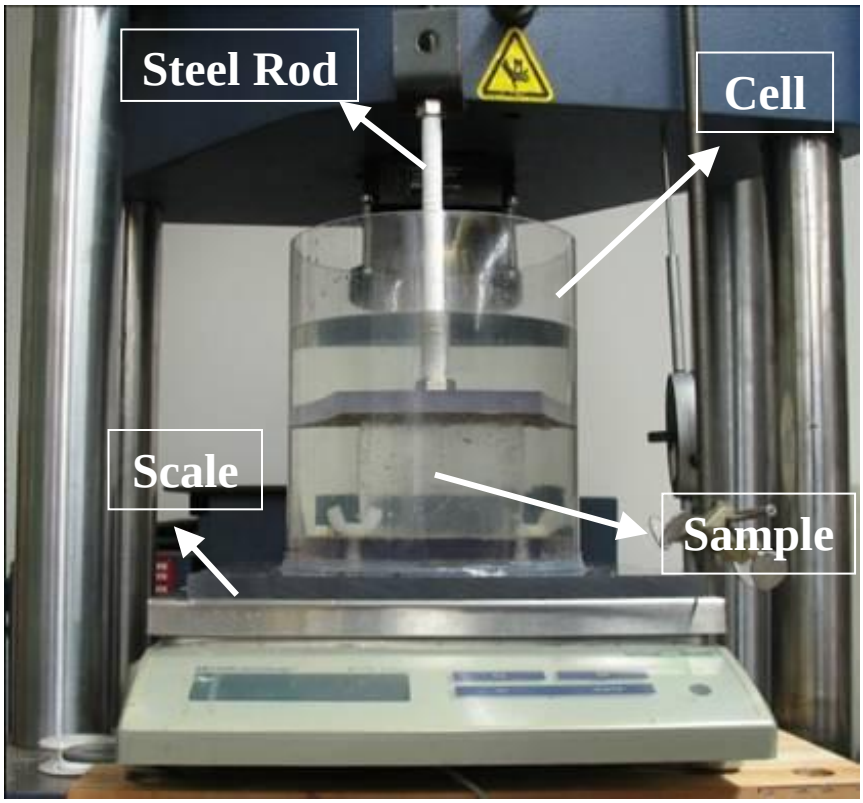

Figure 4.7. Experimental setup in the INSTRON 3288 U.T.M. loading frame.

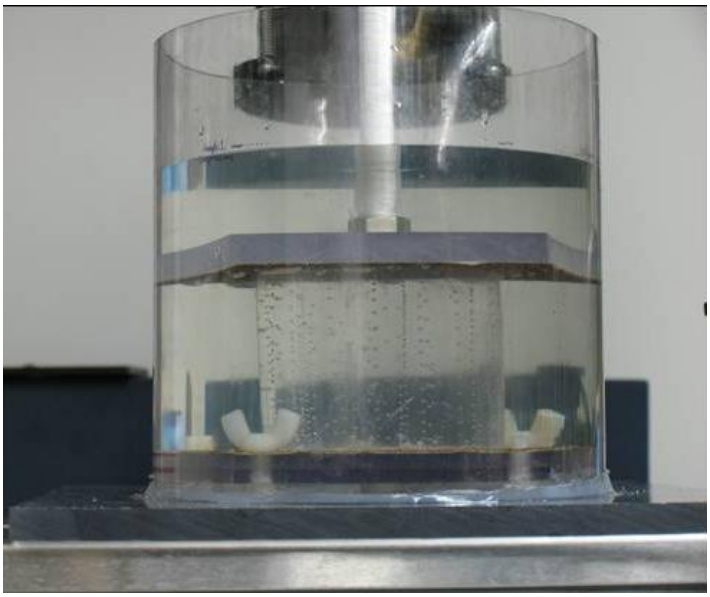

(a)

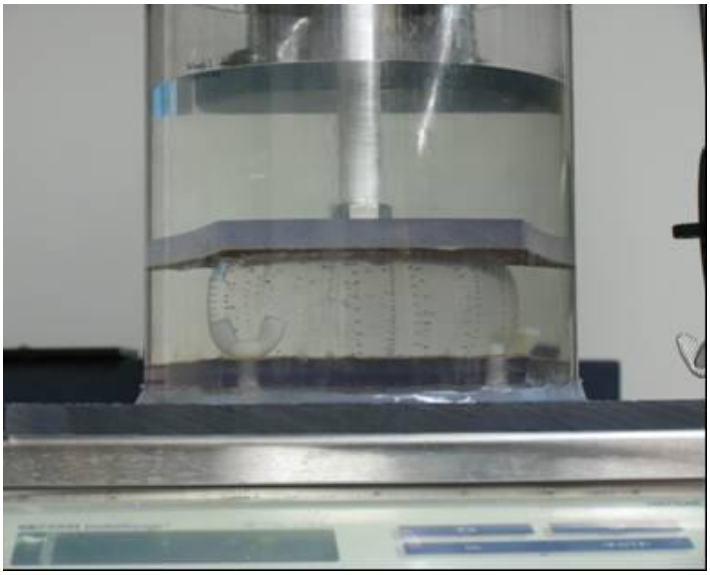

(b)

Figure 4.8. (a) Undeformed and (b) deformed shapes of sample 1.

Table 4.1. Neo-Hookean constitutive parameters determined from uniaxial compression experiment.

Model Parameter	Neo-Hookean Model Parameters C_{10}
Sample 1	846.6 Pa
Sample 2	798.8 Pa

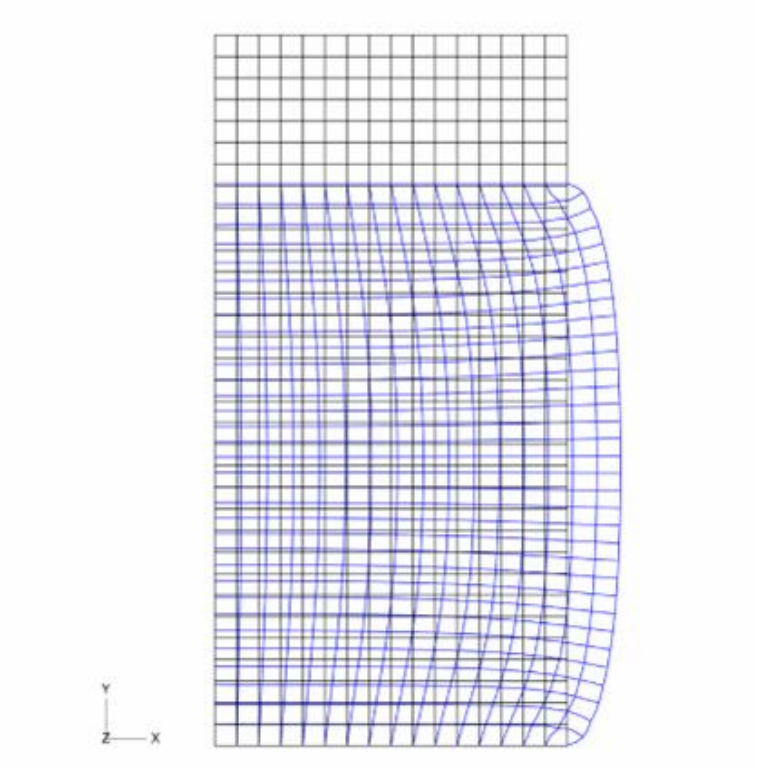

Figure 4.9. Undeformed (black mesh) and deformed (blue mesh) geometries of the finite element simulation used for sample 1.

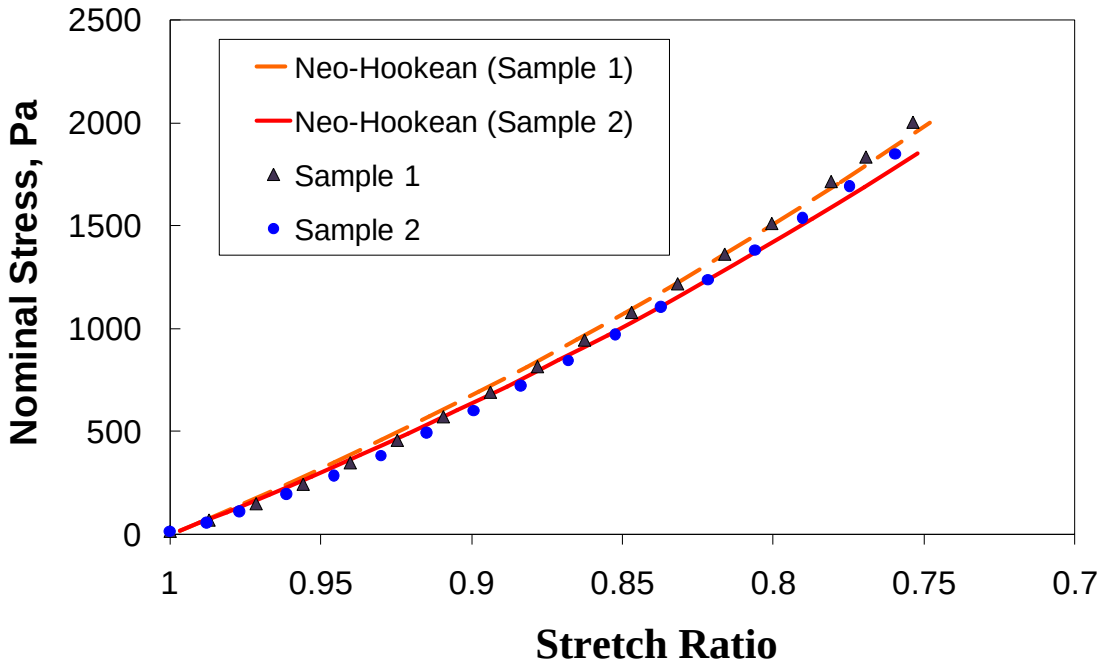

Figure 4.10. Experimental data and neo-Hookean model predictions.

4.5 Conclusions

In this chapter, we presented the experimental program of this dissertation. First, we discussed the experimental setup and procedure. Subsequently, we derived the material properties of the silicone gel via independent physical tests without using any image guidance. For this purpose, we performed uniaxial compression tests on cylindrical silicone samples. The subsequent forward and inverse analysis allowed for determination of the hyper-elastic (neo-Hookean) constitutive parameter of the silicone gel material which is used to verify the results obtained in Chapter 5.

CHAPTER V

INVERSE MODELING OF BRAIN PHANTOM

5.1 Analysis and Processing of Acquired Images

Acquired CT images for undeformed and deformed phantom are composed of 368 and 342 slices, respectively. Images are composed of isotropic voxels with a resolution of 0.68 mm. Since the silicone gel is homogeneous, it generates an almost constant gray level in the images. Silicone-graphite bubbles appear whitish in color and the background is dark colored throughout each slice. Figure 5.1 shows some sample slices captured from the undeformed and deformed phantom images.

In order to distinguish between the background and the silicone gel and to provide underlying geometry for the mesh generation, the images were segmented using ANALYZE [*ANALYZE*, 2002], a commercial medical image software (Figure 5.2). To ensure that we get an accurate estimate of the displacement field in the presence of a relatively small number of image features, we have manually determined the locations of the corresponding bubbles. Due to the noise in the images, only 56 bubbles could be identified (Figure 5.3). Using the same procedure, four control bubbles, injected into the silicone adhesive on the pedestal for rigid registration purposes, were identified (see Section 4.1).

Both the phantom and the cavity surfaces that were extracted from the acquired CT images were meshed using an in-house meshing algorithm. The current version of this meshing algorithm generates surface mesh with triangular elements. The resulting

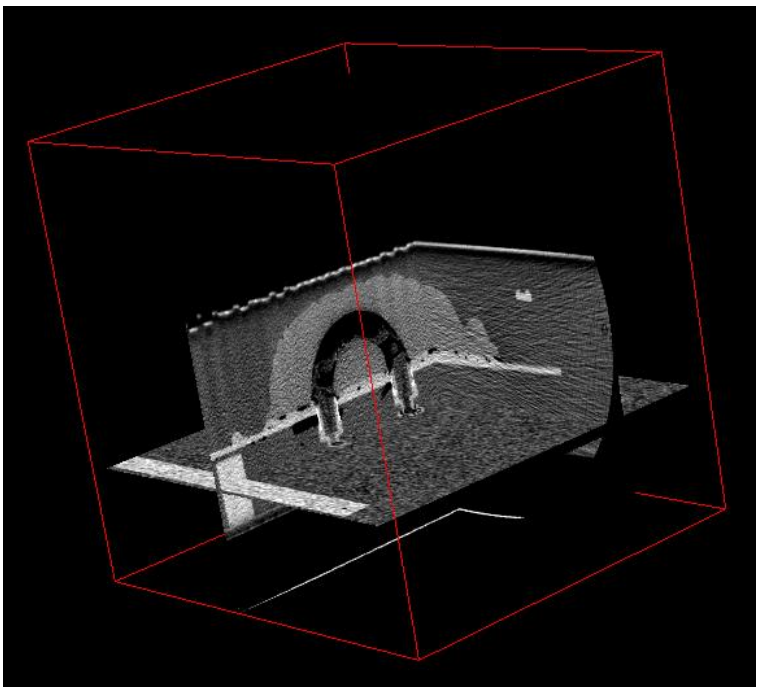

(a)

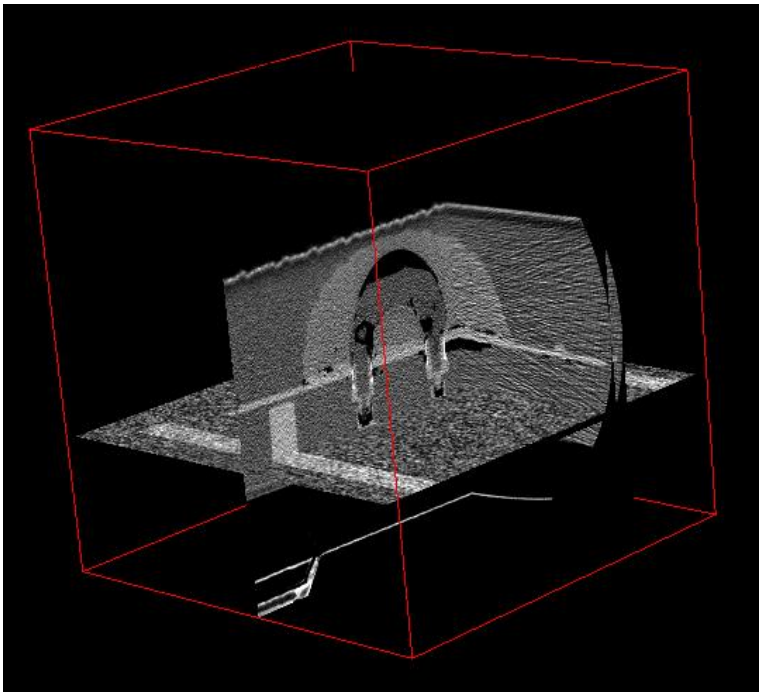

(b)

Figure 5.1. Examples of CT images in (a, c, d, e) undeformed and (b, f, g, h) deformed states.

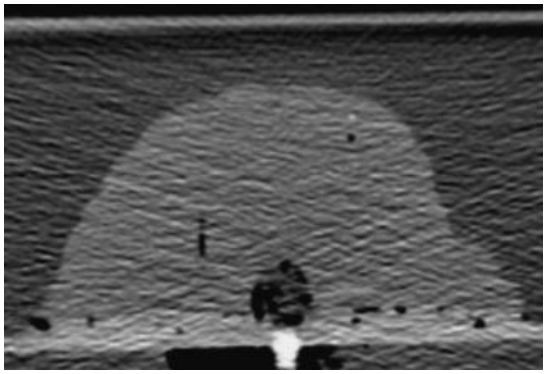

(c)

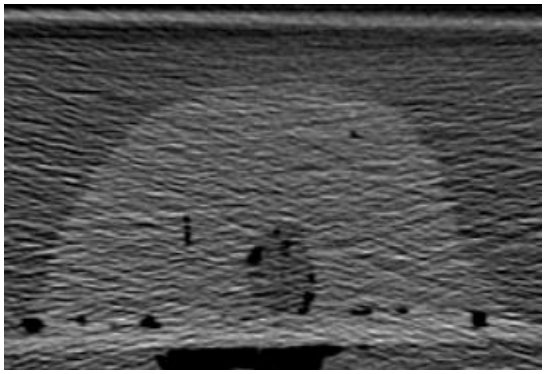

(f)

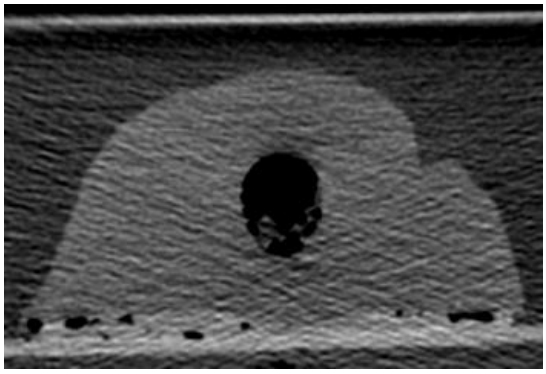

(d)

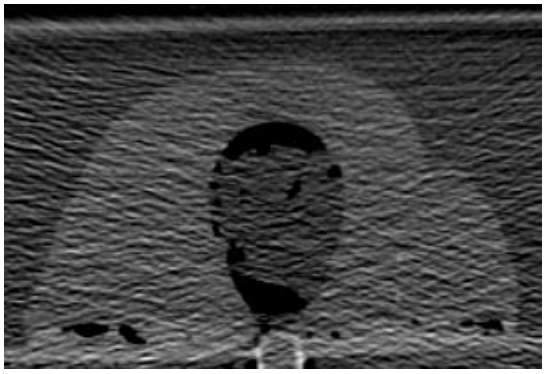

(g)

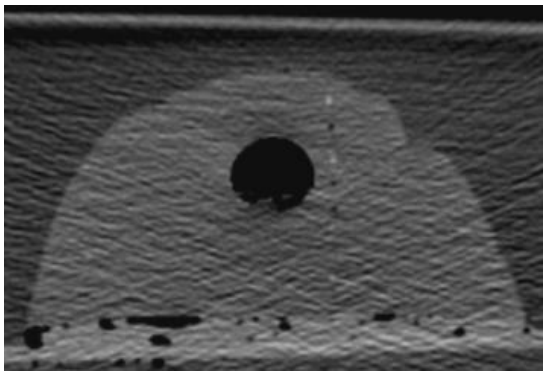

(e)

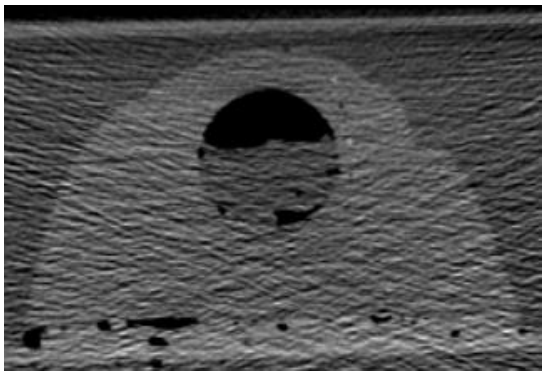

(h)

Figure 5.1. continued.

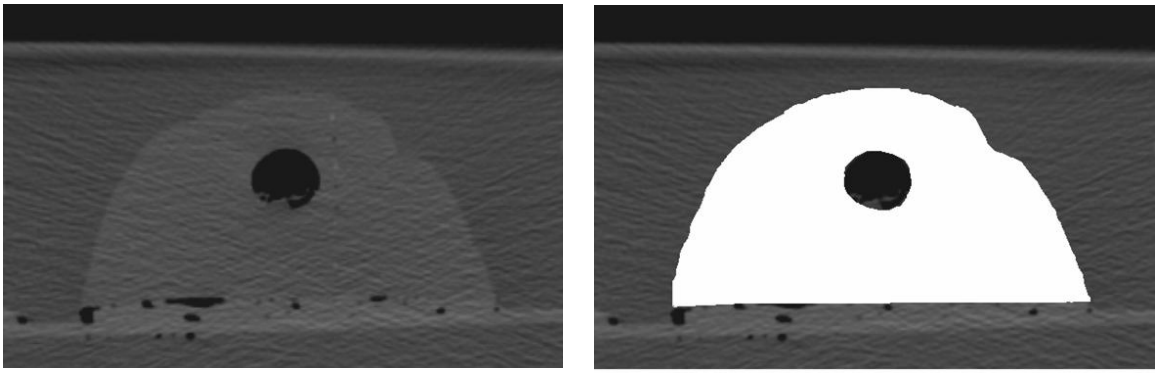

(a) (b)

Figure 5.2. (a) Raw and (b) segmented CT images of the phantom.

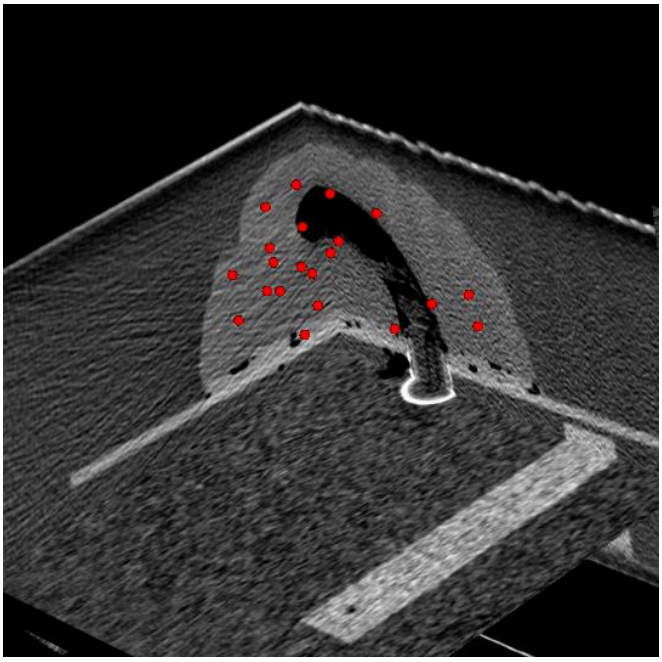

(a)

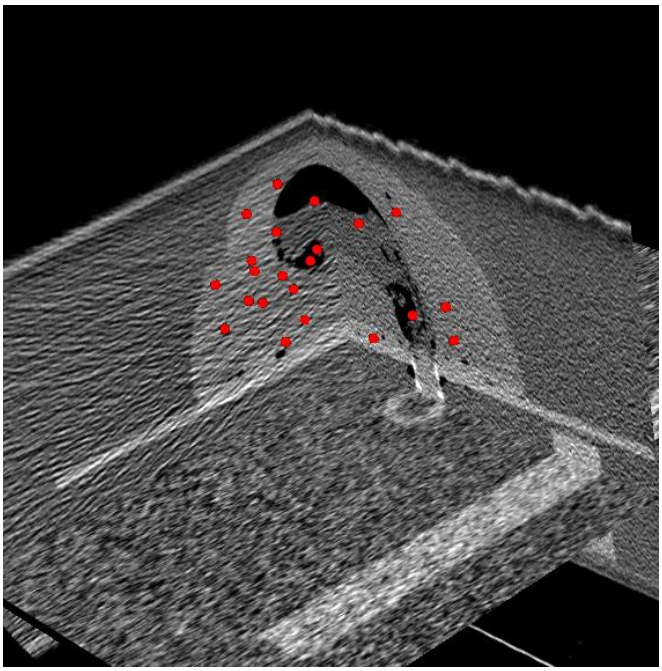

(b)

Figure 5.3. Location of the bubbles in (a) undeformed and (b) deformed images.

mesh is composed of 5000 triangular elements (Figure 5.4a). For illustration purposes, the deformed phantom images were also segmented and the surface meshes of the segmented image were generated (Figure 5.4a).

5.2 Boundary Value Problem for Forward Numerical Simulation

The meshed surfaces for the non-deformed phantom (Figure 5.4a) were imported into ABAQUS for the Finite Element Analysis. Surface mesh transfers were performed using IGES (Initial Graphics Exchange Standard) [*Smith et al.*, 1988]. The transferred triangular surface mesh was converted to tetrahedral elements using ABAQUS built-in meshing functions [*ABAQUS*, 2004]. In Figure 5.5, the meshed geometry of the brain phantom is shown. Since the material is assumed to be incompressible and large element distortions near the inner surface were expected, modified second order tetrahedron hybrid elements (C3D10MH) were used. Based on the transferred surface mesh, a FEM mesh with 14752 nodes and 9538 elements was generated. However, it is not possible to define the coordinates of a specific node when using ABAQUS built-in meshing functions. For this reason, the nodes that are closest to each bubble were determined. Then, the coordinates of these nodes were redefined as the coordinates of the closest bubbles. These modified nodes are used in the inverse analysis. Meshing the model, boundary conditions are defined as described in Section 3.2 in order to be able to model the experimental procedure. The neo-Hookean strain energy function was utilized for the forward simulations. Successive forward simulations were performed for different neo-Hookean model parameters until a reasonable match between simulations and experiment

was achieved, and the model parameter, C_{10} = 650 Pa, which provides a satisfactory match, was used as the initial guess in the inverse analysis.

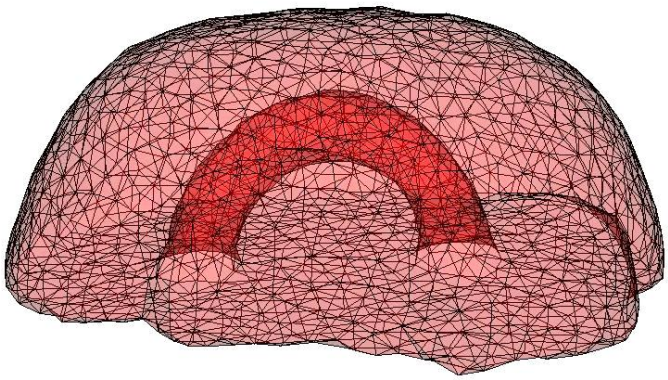

(a)

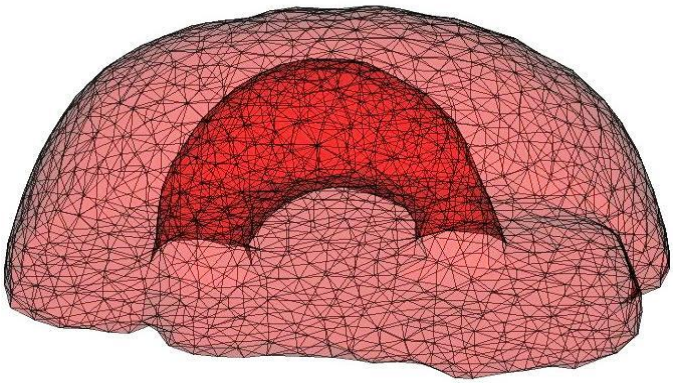

(b)

Figure 5.4. Surface meshes of the brain phantom in (a) undeformed and (b) deformed configurations.

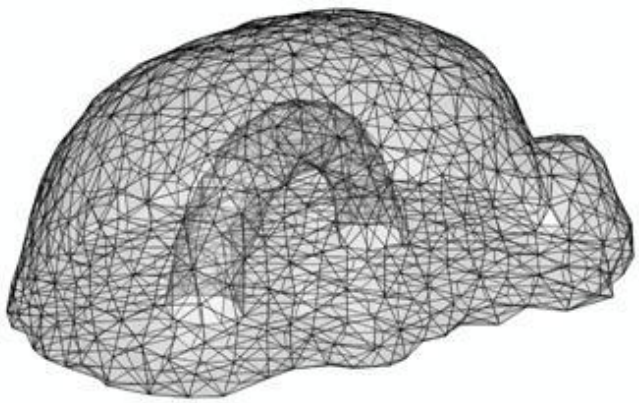

Figure 5.5. Meshed geometry of the brain phantom as seen in perspective view.

5.3 Brain Phantom Properties Based on Inverse Analysis

The inverse analysis was performed as described in Chapter 2. The objective function defined in (3.5.1) was used but in this case, the number of measurements, *M*, is 56.

Table 5.1 summarizes the initial and calculated neo-Hookean model parameters. In order to demonstrate the performance of the inverse analysis, the L_2-norm (expression (2.4.2)), error in maximum total displacements, and average error in total displacements are also tabulated. In addition, in order to estimate the sensitivity of the estimated parameter to the noise in the input data (i.e., 3-D displacement field), 95% confidence interval for the estimated parameter was calculated and is given in Table 5.1. For this purpose, the finite element model, developed in Section 5.2, was used. The incompressible neo-Hookean material model was utilized for the simulation. The model parameter was chosen as C_{10} = 663.7 Pa, which corresponds to the estimated model parameter from the inverse analysis. Then, normally distributed zero mean noise with standard deviation of 0.7 mm, approximately equal to the image voxel size, was added to the 3-D control point displacements. Finally, 95% confidence interval for the estimated parameter was calculated (Table 5.1) using statistics toolbox of *MATLAB* [2007] (i.e., *nlparci* built-in function).

Figure 5.6 shows the undeformed and deformed meshes and geometries of the finite element simulations. In Figure 5.7 and Figure 5.8, the maximum principal stress and maximum principal logarithmic strain predictions of the neo-Hookean model in 3 cross-sections are shown, respectively. From Figure 5.7 and Figure 5.8, it is seen that

both compressive and tensile stresses develop in the silicone phantom. Figure 5.9 presents the slices of finite element meshes and corresponding image slices.

Table 5.1. Model parameter, L_2-norm, maximum and average errors in total displacements, and confidence interval of the inverse analysis.

Initial Model Parameter C_{10}	Converged Model Parameter C_{10}	L_2-norm ($\times 10^{-3}$)
650 Pa	663.7 Pa	7.81
Maximum Error in Total Displacements	**Average Error in Total Displacement**	**Confidence Interval C_{10}**
1.48 mm	0.57 mm	511.1 - 816.4 Pa

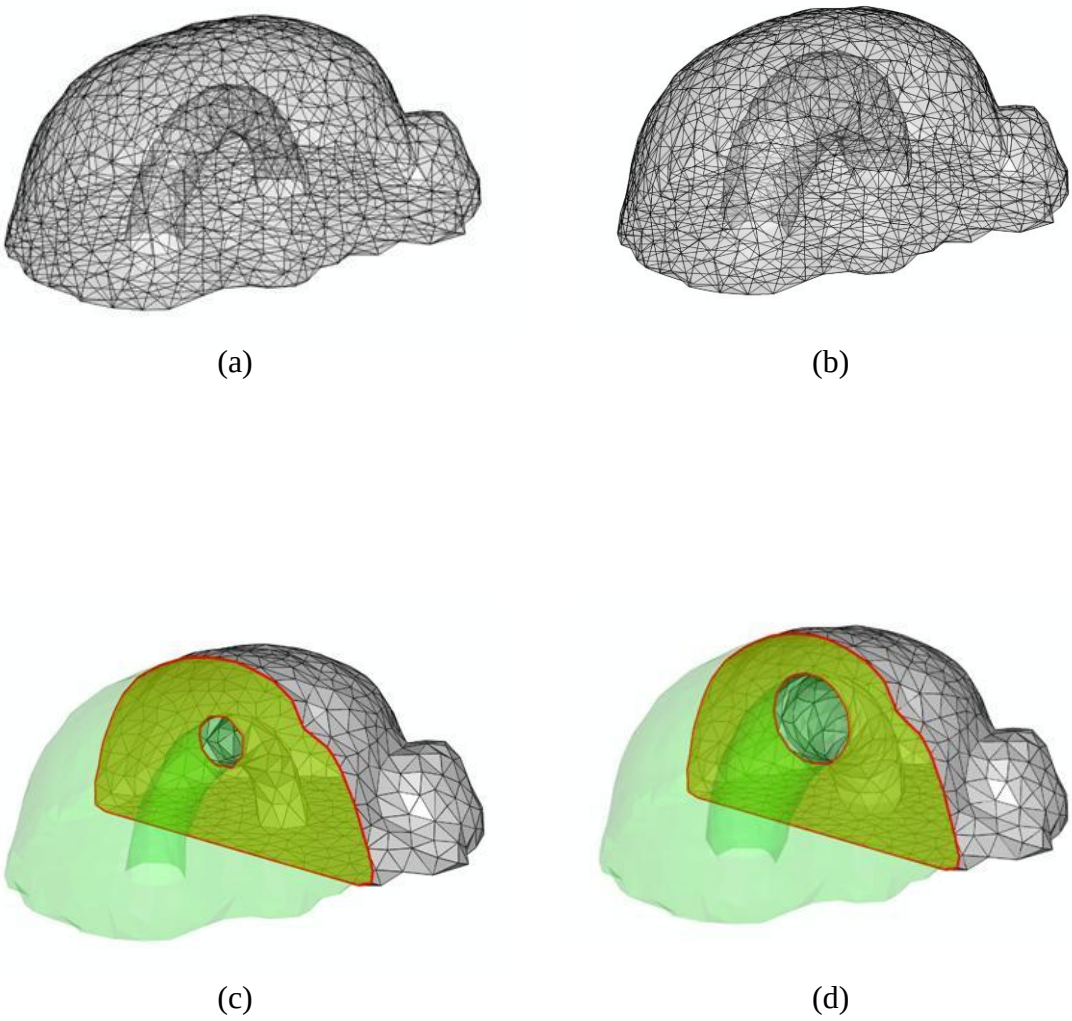

Figure 5.6. (a) Undeformed and (b) deformed finite element meshes of the forward simulations. (c) Undeformed and (d) deformed cross-sections of the forward simulations.

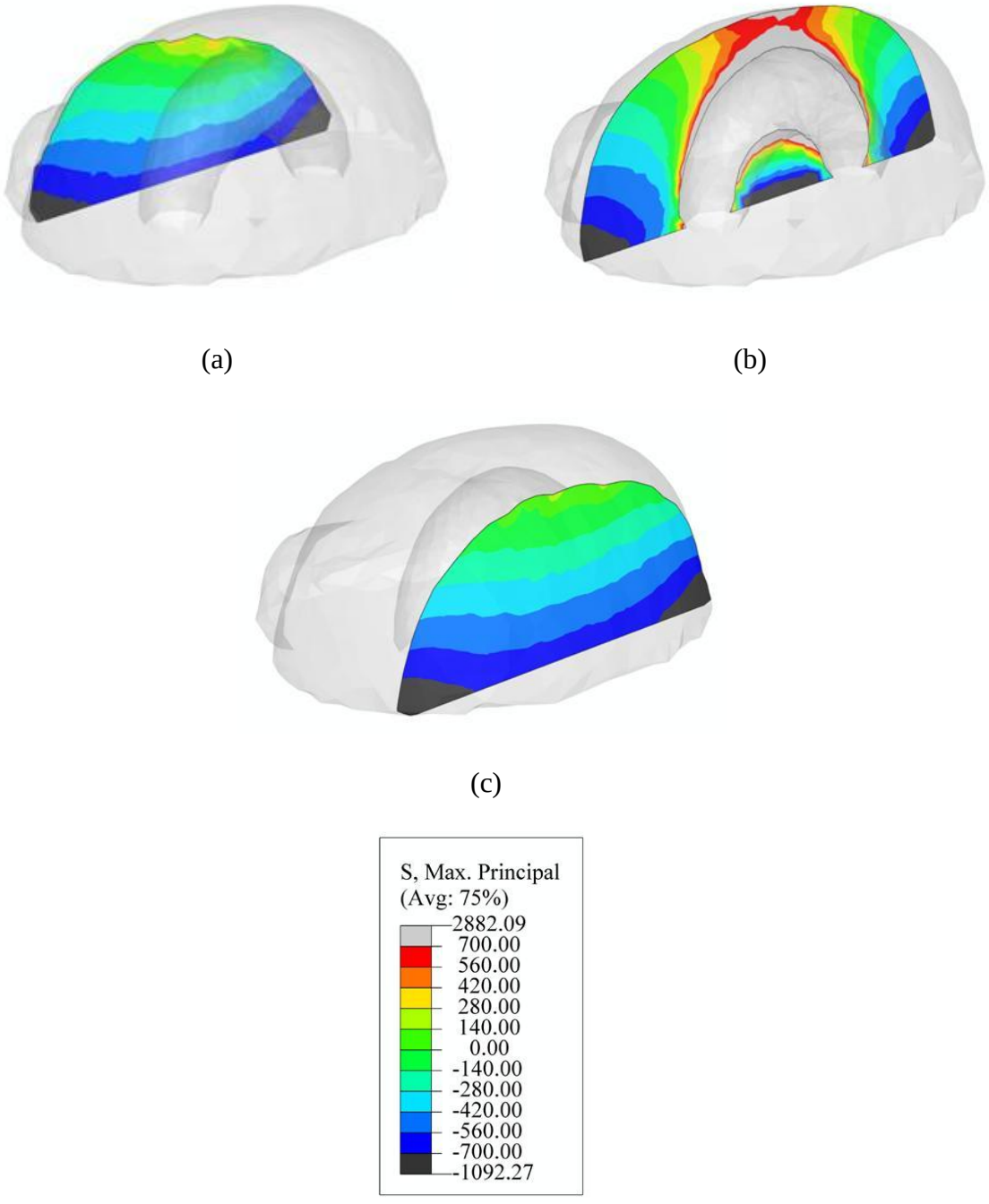

Figure 5.7. (a, b, c) Maximum principal stresses calculated using the neo-Hookean model in three cross-sections. (d) Legend (contour map for stress magnitude in Pa).

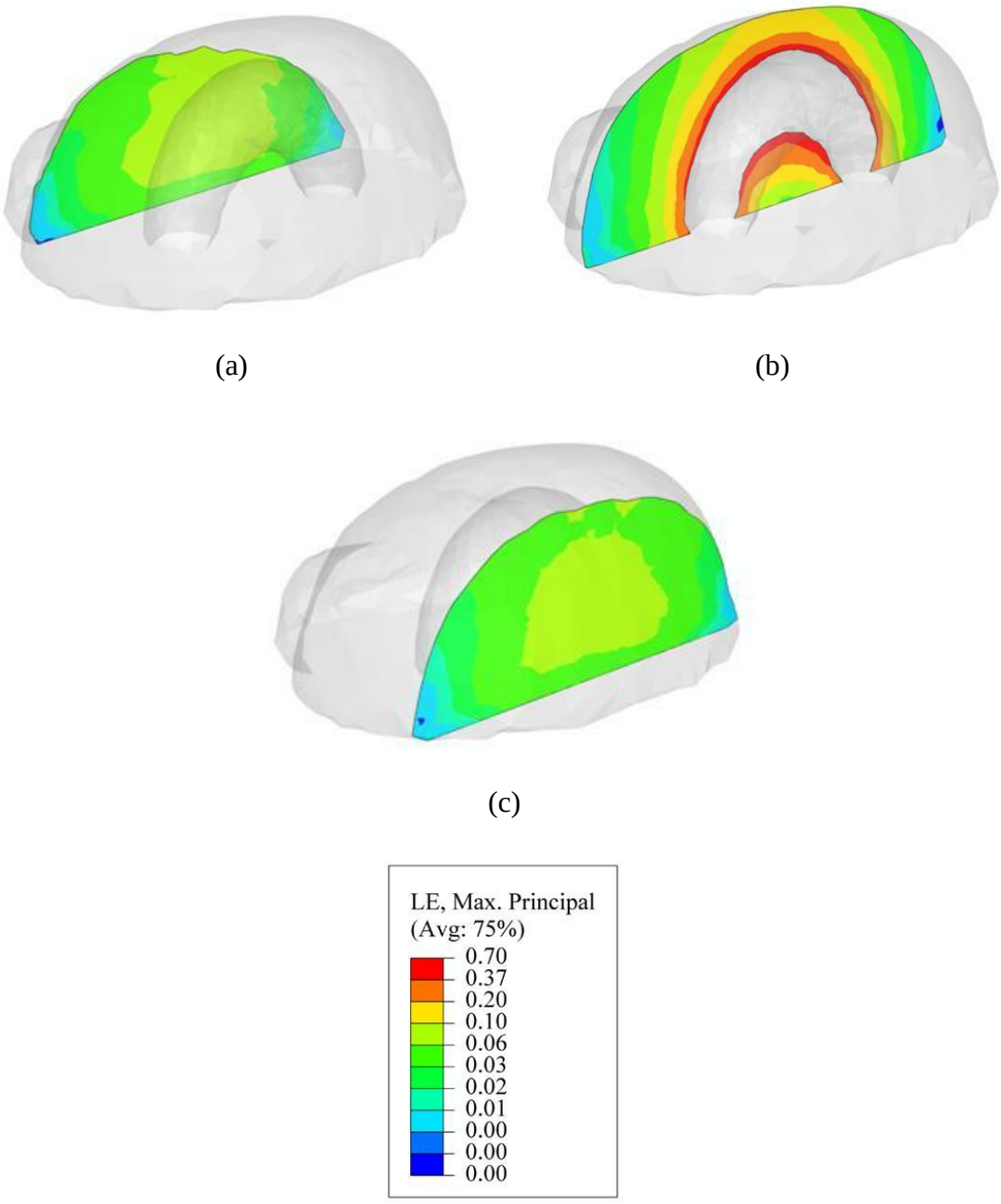

Figure 5.8. (a, b, c) Maximum principal logarithmic strains calculated using the neo-Hookean model in three cross-sections. (d) Legend (contour map for strain magnitude).

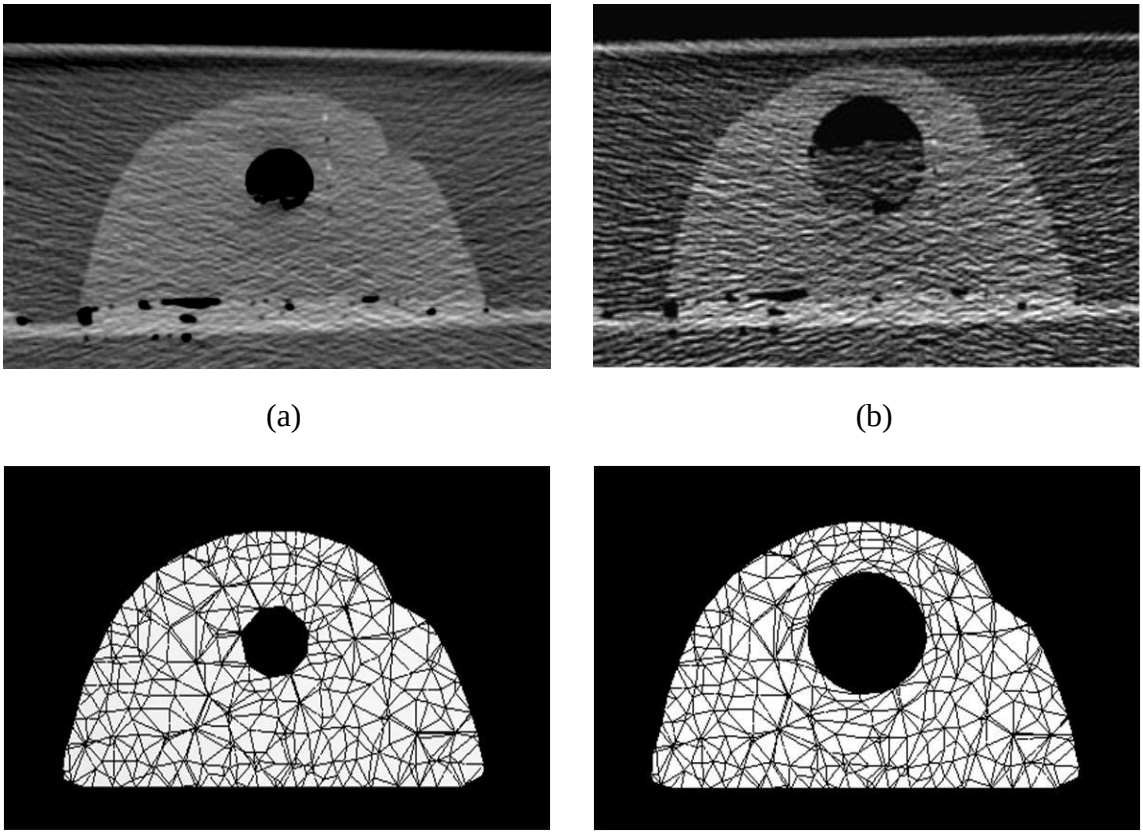

(a) (b)

(c) (d)

Figure 5.9. A scanned image slice (a) before and (b) after the deformation. The corresponding slices of the finite element meshes are shown in (c) and (d), respectively.

5.4 Discussion of Results

As seen in Table 5.1, the maximum error between measurements and neo-Hookean model predictions is 1.48 mm, which is about twice the voxel size, and the average error in total displacements is 0.57 mm, which is less than the resolution of the images.

The calculated parameter values for the neo-Hookean model falls well within the range of the corresponding parameter values given in the literature (Table 5.2). The stiffness of silicone gel can be controlled by the catalyst-resin ratio of the mixture, i.e., increasing the proportion of resin increases gel stiffness [*Azar et al.*, 2004]. This explains the large difference of the calculated parameter C_{10} between this study and *Dokos et al.* [2000] as well as *Augenstein et al.* [2005] and *Azar et al.* [2004], since in their study the catalyst to resin ratio is twice greater than ours (Table 5.2). In *Rajagopal et al.* [2004] and *Chung et al.* [2005], there is no information about curing conditions of the gels tested. In our laboratory, we observed that time and temperature of curing may have strong effect on the stiffness of the silicone gel. In addition to different catalyst-resin ratio, one possible explanation for the difference in our C_{10} and that obtained by *Rajagopal et al.* [2004] and *Chung et al.* [2005] may be the curing conditions.

The material parameter of the silicone gel, derived using the proposed approach and independent uniaxial compression test, differ by 20% from each other. A similar magnitude of deviation is observed by *Dokos et al.* [2000]. They performed 3 different tests (tensile, rotational shear and simple shear tests) on silicone gel and their tensile and simple shear test results also showed approximately 20% difference. Such magnitude of deviation is also typical for experiments with rubber compounds [*Raos*, 1993; *Dokos et*

al., 2000]. As a result, we conclude that material parameter calculated by the proposed approach and uniaxial compression test agree reasonably well.

Table 5.2. Neo-Hookean model parameter reported in the literature for the silicone gel.

C_{10} (kPa)	Reference	Catalyst to Resin Ratio
8.99-13.31	*Dokos et al.* [2000]	1:2
8.72-8.91	*Augenstein et al.* [2005]	1:2
0.426	*Chung et al.* [2005]	N/A
6.35	*Azar et al.* [2004]*	1:1.7
29.8	*Azar et al.* [2004]*	1:5.7
3.11	*Rajagopal et al.* [2004]	N/A
0.6637	Proposed approach	1:1
0.8466	Uniaxial test, Sample 1	1:1
0.7988	Uniaxial test, Sample 2	1:1

* Obtained by fitting (2.3.7) to the experimental data presented in *Azar et al.* [2004]

5.5 Conclusions

In this chapter, we tested the proposed approach in a controlled laboratory experiment with a silicone brain model mimicking the *in-vivo* brain geometry, mechanical properties, and boundary conditions. We processed the experimental data and developed the finite element model. Then, using the inverse analysis approach presented in Chapter 2 and 3, we determined the hyper-elastic (neo-Hookean) constitutive parameter of the silicone gel material. The calculated parameter was consistent with those found in the literature and those obtained from the independent uniaxial compression tests (Chapter 4), providing justification for the future application of the proposed approach to *in-vivo* brain tissue.

CHAPTER VI

MODELING FEMALE BREAST DEFORMATION

Similar to brain tissue, there are other parts of the human body (such as liver, kidney, or breast) that can also be characterized by IGCM principles. Breast cancer is the second most prevalent cancer type in women, and an operative mastectomy, in which breast tissue is removed, is frequently part of the treatment. Women often undergo mastectomy followed by a reconstruction surgery using a breast implant. There is also a growing demand for breast augmentation for the sake of aesthetic improvement. Yet, millions of women requested revisional operations because the implants resulted in a breast form that differs from their expectations. This is why accurate pre-operative simulation of these augmenting and reconstructive procedures is important. Additionally, a mechanical understanding of factors affecting breast deformation and shape, such as the properties of skin and breast tissue, may affect the therapeutic procedures and non-operative augmentation techniques (e.g., choosing the proper breast skin care).

In this chapter, we describe a quantitative large-strain 3-D mechanical model of female breast deformation developed by *Germanovich et al.* [2008]. Breast deformation is simulated using finite element modeling.

6.1 Introduction

The *breasts* or *mammae* are accessory glands of the generative system [*Gray*, 1995]. More specifically, the mammary glands in breasts are accessory to reproduction in women, but are rudimentary and functionless in men [*Moore and Dalley*, 2006]. Functionally, female breasts are related to the reproductive system in females because they produce milk for the nourishment of offsprings [*Scanlon and Sanders*, 2007]. The size, shape, and weight of the breast vary at different periods of life and per individual. In females, breasts are two quasi-hemispherical humps positioned between the second or third and the sixth or seventh ribs [*Gray*, 1995; *Netter*, 2006]. They are small in size before puberty, but enlarge as the generative organs develop [*Gray*, 1995]. Changes such as the branching of the lactiferous ducts occur in the breast tissue during menstrual periods and pregnancy [*Fergusson et al.*, 1992; *Moore and Dalley*, 2006]. Breasts further enlarge during pregnancy and especially after delivery [*Gray*, 1995], and they usually become smaller in elderly women [*Moore and Dalley*, 2006].

The left breast is generally a little larger than the right one. Their bases are nearly circular, flattened or slightly concave [*Gray*, 1995]. The outer breast surface is convex [*Gray*, 1995; *Moore and Dalley*, 2006]. The most prominent feature of the breast is the *nipple* or *mammilla* [*Gray*, 1995; *Moore and Dalley*, 2006; *Netter*, 2006], which is surrounded by a circular pigmented area of skin, the *areola*. Anatomically, female breast forms can be categorized into three general types [*Schider*, 1954] that affect breast deformation and breast tissue-skin interaction in the gravity field (Figure 6.1).

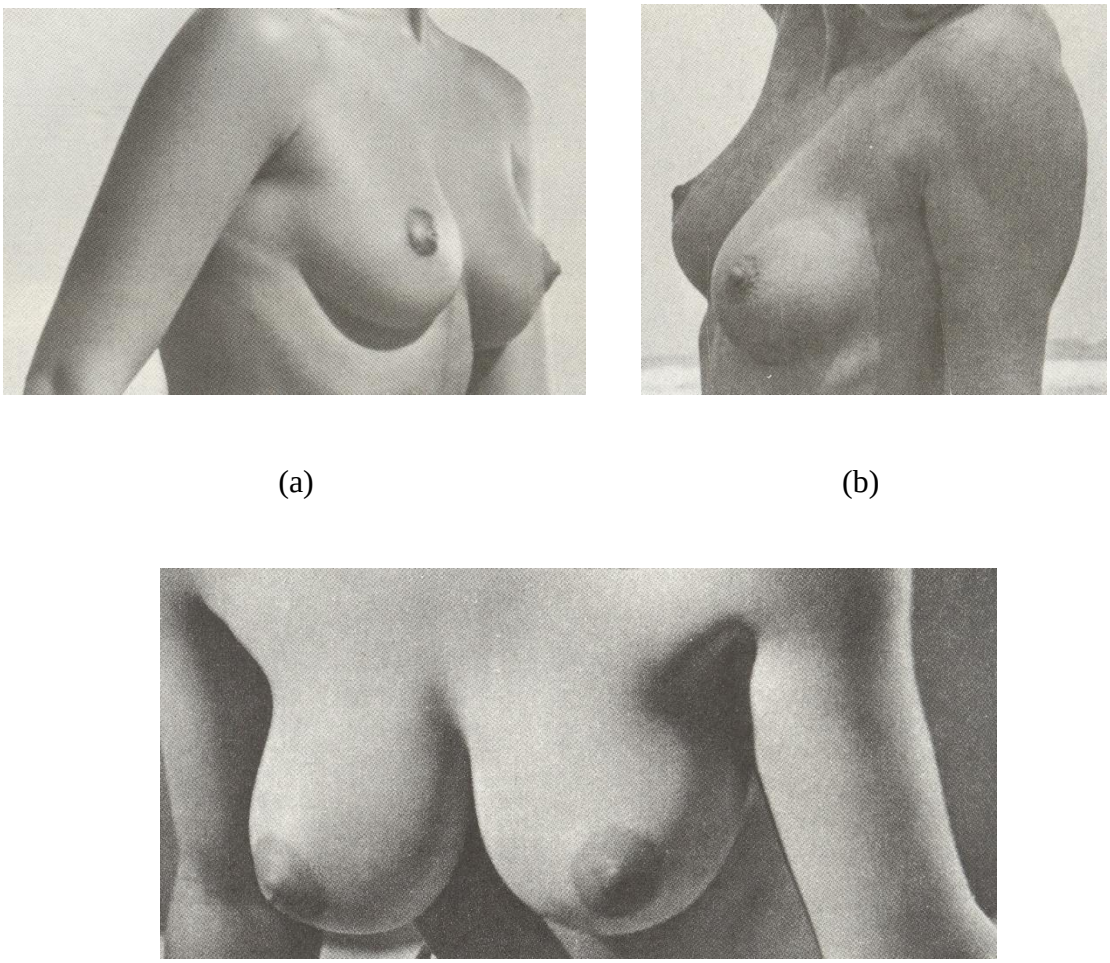

(a) (b)

(c)

Figure 6.1. Types (a) I, (b) II, and (c) III of female breast form [*Schider*, 1954].

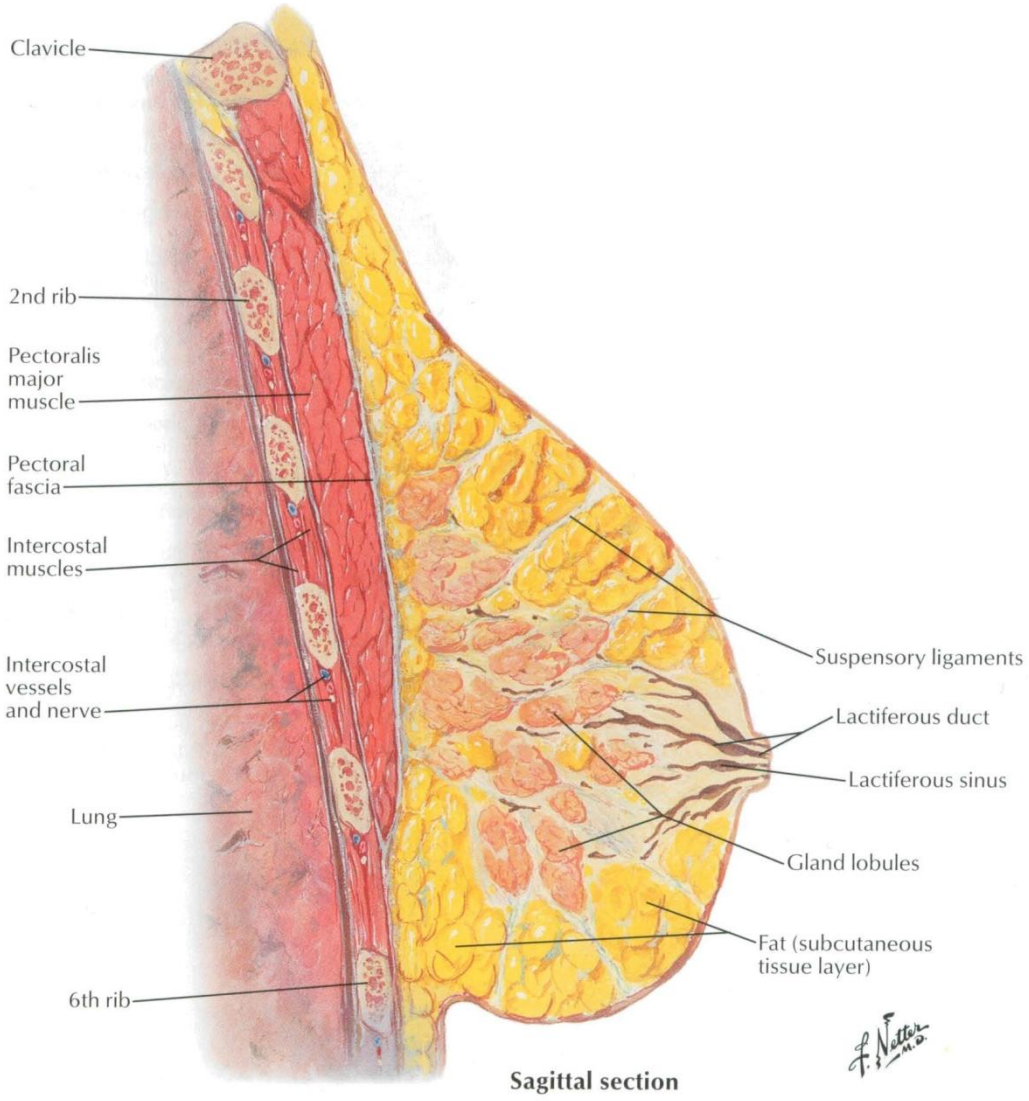

Figure 6.2. Typical structure of a female breast [*Netter*, 2006, Plate 182].

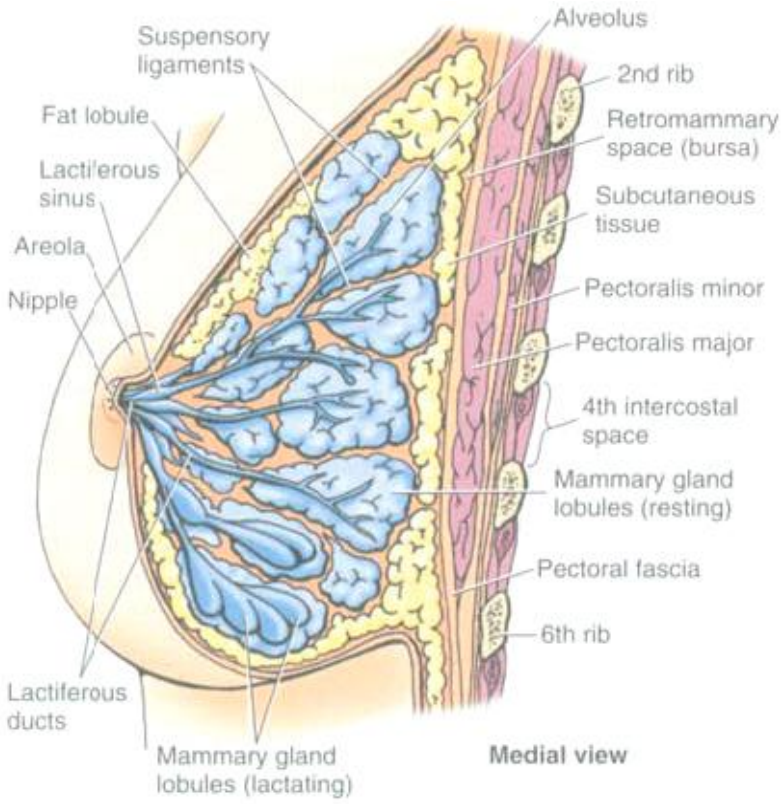

Figure 6.3. Typical structure of a female breast [*Moore and Dalley*, 2006, Figure 1.20]. The breast consists of glandular tissue and fibrous and adipose tissue between the lobes and lobules of glandular tissue, together with blood vessels, lymphatic vessels, and nerves. The superior two thirds of the figure demonstrates the suspensory ligaments and alveoli of the breast with resting mammary gland lobules; the interior part shows lactating mammary lobules [*Moore and Dalley*, 2006, Figure 1.20].

Structurally, breasts are connected to the skin; enclosed within the breasts, the *mammary glands* are anterior to the *pectoralis muscles* (Figures 6.2, 6.3) [*Scanlon and Sanders*, 2007]. The breast is composed of three predominant types of tissue: skin, fat, and glandular tissue (or mammary gland). The glandular tissue supports lactation, and the amount of fat around the glandular tissue determines the size and form of the breast [*Gray*, 1995; *Moore and Dalley*, 2006]. The fatty layer of the superficial fascia surrounding the mammary gland is thicker here than in most parts of the body [*Joseph*, 2006]. An example of ultrasound image of the normal breast tissue is shown in Figure 6.4. Mammograms of the breast tissue containing tumors are shown in Figure 6.5.

The mammary gland consists of gland *lobes* connected by *fibrous* tissue; the lobes are composed of *lobules* (Figures 6.2, 6.3) connected together by areolar tissue, blood vessels, and ducts [*Gray*, 1995]. The fibrous tissue invests the entire breast surface and penetrates between the lobes, connecting them together [*Gray*, 1995]. In the adult breast, there are typically 15 to 20 lobules of glandular tissue [*Moore and Dalley*, 2006]. Each lobule is drained by a lactiferous duct, which usually opens independently on the nipple [*Moore and Dalley*, 2006; *Netter*, 2006], which is a conical or cylindrical eminence [*Gray*, 1995]. Nipples have no fat or glands, their tips are fissured with *lactiferous ducts* (Figures 6.2, 6.3) opening into them, and they are composed mostly of circularly arranged smooth muscle fibers that erect the nipples in response to stimulation [*Moore and Dalley*, 2006]. The fat tissue surrounds the surface of the mammory gland and occupies the space between its lobes [*Gray*, 1995].

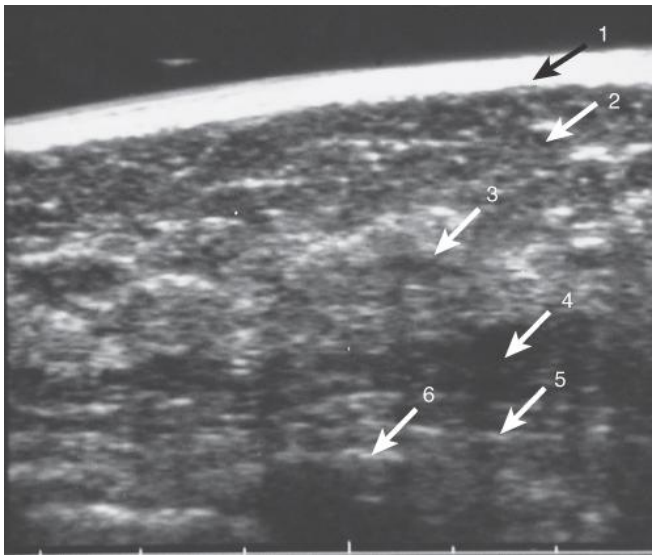

Figure 6.4. Ultrasound image of breast tissue [*Sutton et al.*, 1999, p. 1432, Fig. 53.7]. Legend: 1 - skin; 2 - subcutaneous fat; 3 - glandular tissue; 4 - retromammary fat; 5 - pectoralis muscle; and 6 – rib.

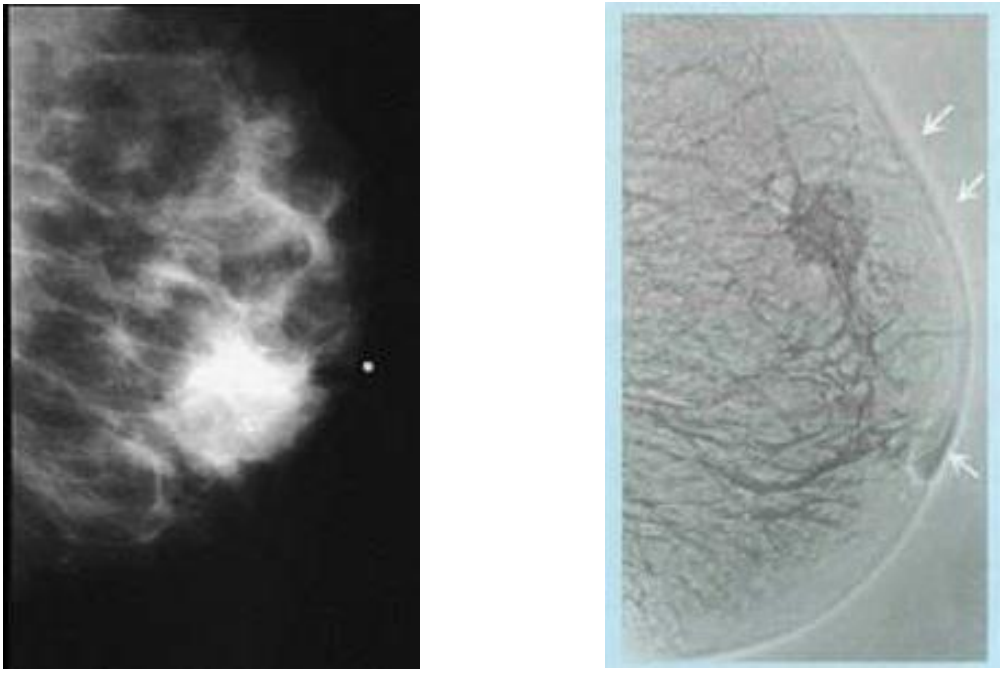

(a) (b)

Figure 6.5. Breast Mammograms showing (a) large irregular radio-dense tumor (white region) [*Robbins and Cotran*, 2005, CD companion] and (b) a carcinoma tumor that appears as a large, jagged density indicated by two upper arrows (the lower arrow points to the depressed nipple) [*Moore and Dalley*, 2006].

The mammary gland is *firmly* attached to the overlying skin by the *suspensory ligaments* (Figures 6.2, 6.3), also called *Cooper's ligaments*, a type of connective tissue that supports the mammary gland lobules [*Moore and Dalley*, 2006]. The thickness of the skin around the breast normally ranges from 0.5 to 1 mm [*Netter*, 2006]. The breast is separated from the *pectoralis major muscle* (Figures 6.2, 6.3) by the *retromammary* space (Figures 6.3), which is filled with a loose connective tissue. This space also contains a small amount of fat that allows the breast some degree of movement on the *pectorial fascia* (Figures 6.2, 6.3), which is connected to the pectoralis major muscle [*Moore and Dalley*, 2006].

Stretching or softening of suspensory (Cooper) ligaments, which may occur during pregnancy or aging, leads to lowering ("sagging") of the breast form [*Tanner et al.*, 2001]. The glandular tissue is supported by estrogen. During menopause, the glandular tissue atrophies and ultimately disappears as the estrogen level decreases, leaving only fatty tissue within the skin [*Gray*, 1995; *Moore and Dalley*, 2006].

Modeling female breast tissue deformation gained interest in various applications during the last decade, including image registration [*Ruiter et al.*, 2003; *Schnabel et al.*, 2003; *Carter et al.*, 2006; *Roose et al.*, 2006a], surgery simulation [*Williams et al.*, 2003; *Roose et al.*, 2006b], X-ray mammography [*Samani et al.*, 2001; *Yin et al.*, 2004; *Pathmanathan et al.*, 2004], and biopsy planning [*Azar et al.*, 2000; *Azar et al.*, 2002]. *Azar et al.* [2002] proposed a FEM-based approach to model the deformation of the breast tissue during biopsy procedures. *Williams et al.* [2003] used finite element analysis to simulate the breast post-operative form in breast reconstruction surgery. Similarly, *Roose et al.* [2006b] simulated soft tissue deformation for breast augmentation planning.

As defined by *Schnabel et al.* [2003], image registration describes the process of establishing spatial correspondence between the features in an image pair, or a dynamic or temporal sequence of images, in order to relate them for diagnosis, image guidance, inspection of feature positions, or temporal monitoring. The images might be acquired using the same or different imaging techniques. Rigid-body registration describes differences in global patient positioning. For non-rigid registration, the transformation of features explains the deformations due to soft tissue properties, surgical intervention, temporal changes due to tumor growth, radiotherapy treatment, or geometric image distortion caused by the acquisition technique [*Schnabel et al.*, 2003]. *Schnabel et al.* [2003] and *Carter et al.* [2006] utilized the finite element method for breast image registration purposes. *Ruiter et al.* [2003] used a similar model to correlate MRI images of "undeformed" breasts with X-ray mammograms, which are typically taken when the breast is in highly deformed state (Figure 6.6).

Following *Malata et al.* [1994], *Balaniuk and Costa* [2006] stated that because of the difficulty in measuring volume, assessing symmetry, and evaluating changes in volume, projection, and surface area, the desired breast appearance and shape are currently determined only subjectively by surgeons and patients, rather than objectively. Unfortunately, this statement appears as accurate today as it was in 1994, although there have been works exploring psychological effects of patient expectations regarding post-operative appearance [e.g., *Meyer and Ringberg*, 1987]. In other works, the breast dimensions were studied with respect to the bra sizes [*Kanhai and Hage*, 1999; *Pechter*, 1999] and contribution of breast volume and weight to body fat distribution [*Katch et al.*, 1980].

(a) (b)

Figure 6.6. Breast deformation during X-ray mammography [*Sutton et al.*, 1999]: (a) craniocaudal and (b) localized compression views.

The breast, however, is a complexly shaped tissue structure, lacking definitive anatomical landmarks that can be used to evaluate the effects of breast surgery [*Balaniuk and Costa*, 2006]. This is why attempts to determine an ideal, reproducible method for *breast shape characterization* are still under way [*Vandeweyer and Hertens*, 2002; *Balaniuk and Costa*, 2006; *Catanuto et al.*, 2008].

As noted by *Williams et al.* [2003], there is currently no method to accurately predict the final breast shape and size in an individual patient after a surgical procedure. This is especially a challenge in reconstructive breast surgery where the goal is to achieve a natural appearance with symmetry. The current breast reconstructive procedures are performed based on the subjective judgment of the surgeon. With this in mind, *Williams et al.* [2003] studied the response of the breast to saline-filled breast implants and the transverse rectus abdominis myocutaneous (TRAM) flap [*Bostwick*, 1990]. In this technique, a wide ellipse of skin and fatty tissue are removed from the patient's abdomen and are either left attached to one of the two rectus muscles (pedicle TRAM), or completely removed along with a small plug of muscle (free TRAM); the flap is then shaped to form the breast mound [*Williams et al.*, 2003].

In their simulations of implant-based reconstruction, *Williams et al.* [2003] employed a simplified geometry for the undeformed shape of the breast, i.e., a half-sphere with a non-deformable posterior base. The half-sphere was modeled as a hollow shell object. To represent forces that stretch the skin in implant reconstruction, a hydrostatic load was applied normal to the shell to denote the static fluid pressure in a saline-filled breast implant. The thickness of the shell varied from 0.25 cm to 1 cm. Their simulation results are shown in Figure 6.7 and 6.8.

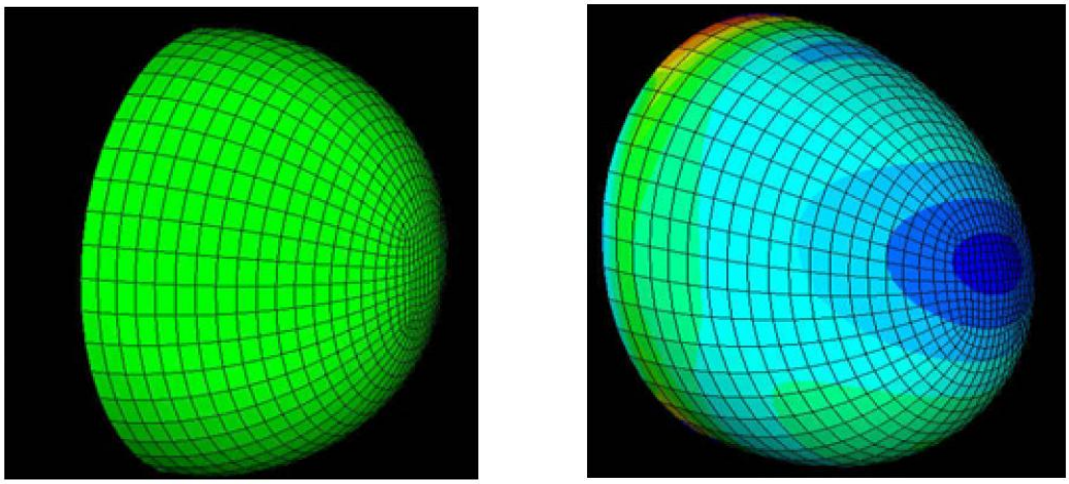

(a) (b)

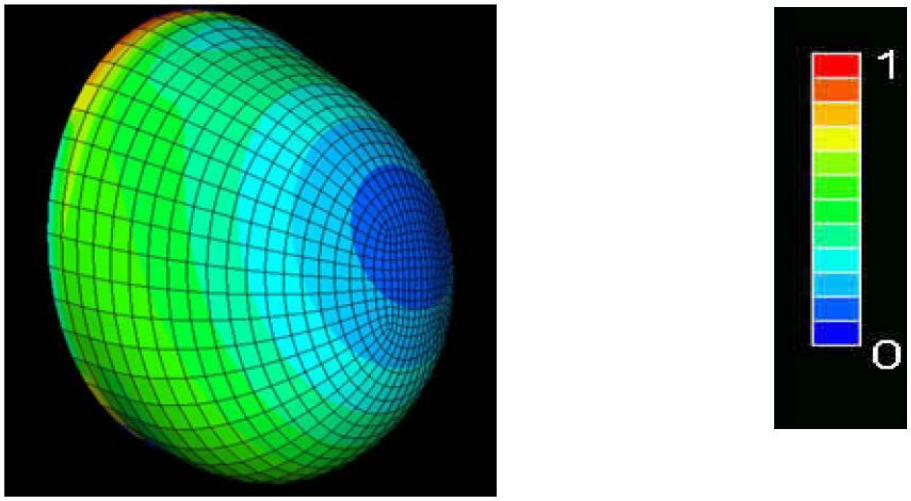

(c) (d)

Figure 6.7. Simulation of an implant reconstruction procedure [*Williams et al.*, 2003]: (a) initial undeformed shape of the breast model, (b) deformed shape for 1-cm shell thickness, (c) deformed shape for 0.25-cm shell thickness, and (d) legend for stress contour plots.

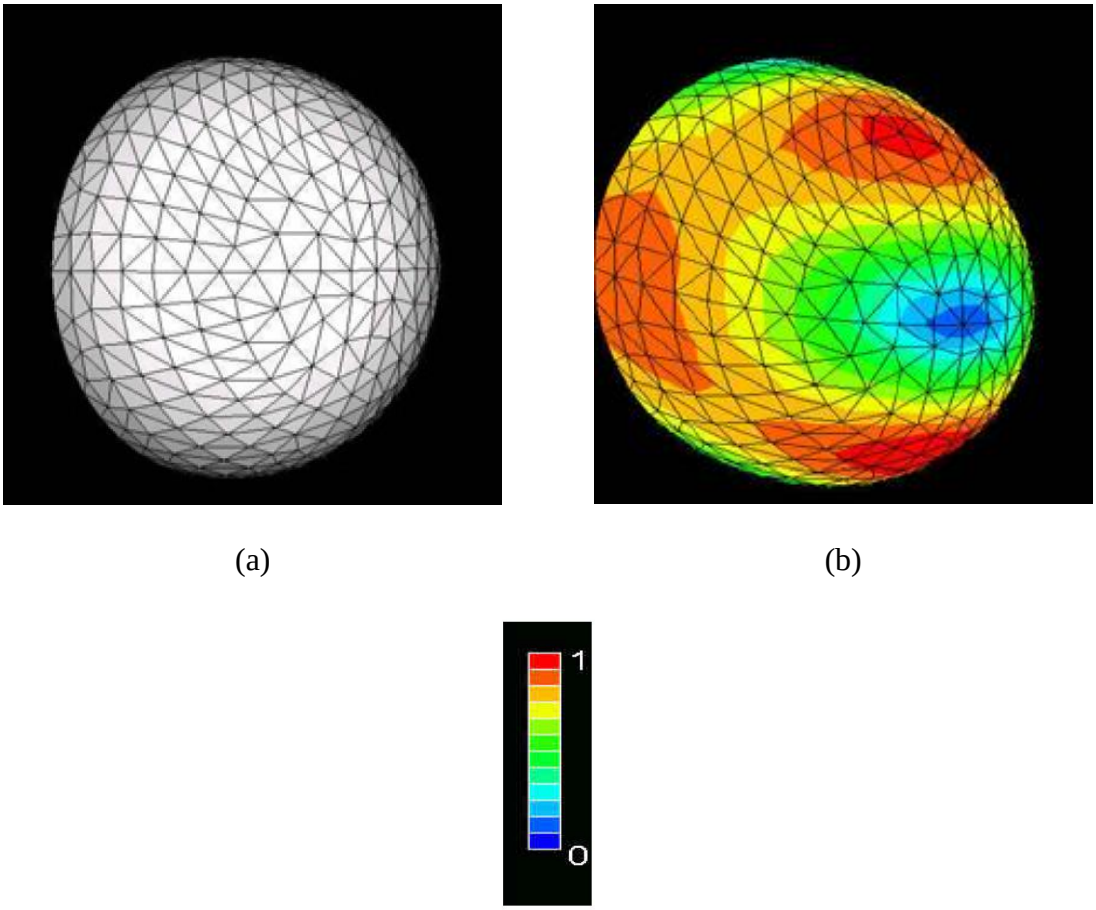

(a) (b)

(c)

Figure 6.8. Simulation of TRAM reconstruction procedure [*Williams et al.*, 2003]: (a) undeformed initial and (b) deformed shapes of the breast model. (c) Legend for stress contour plots.

To simulate TRAM reconstruction, *Williams et al.* [2003] modeled the breast by a solid half-sphere, with an overlying skin membrane that had a thickness of 1 mm. Mechanical tissue properties were incorporated using the Mooney-Rivlin strain energy density function based on published data for skin [*Silver*, 1987] and soft tissue [*Wellman*, 1998]. Figure 6.8 shows the results of their simulations.

Roose et al. [2006a] proposed a method to construct a 3-D breast model based on pictures taken with a 3-D camera. They also used a FEM breast model to predict the surgical outcome of the breast implant procedure. Specifically, they simulated the subglanular placement, where the implant is placed in front of the pectoralis major muscle (Figure 6.2, 6.3). Since muscular tissue is very stiff compared to breast tissue and the silicone or saline implant, *Roose et al.* [2006a] assumed that the muscle maintains its original shape. Hence, they only computed the deformation of the tissue volume enclosed between the outer muscle surface and the skin. In their simulations, the breast tissue was represented by a homogeneous, isotropic, linear elastic material with a Young's modulus of 48 kPa and a Poisson's coefficient of 0.45. Although, the latter was not explicitly included in the modeling, they were still able to simulate the breast augmentation procedure rather accurately (Figure 6.9a).

The insertion of the implant causes the breast tissue to move, while the stretched breast tissue exerts a load on the implant. To simulate the coupled deformation of the implant and the breast tissue, *Roose et al.* [2006a] assigned the corresponding boundary conditions to both meshes (tissue and implant) in order to mimic their effect on each other.

The most attractive feature of the approach of *Roose et al.* [2006a] is that it only requires a 3-D picture of the breast (using an inexpensive 3-D camera instead of more elaborate MRI or CT equipment) and an estimate of the breast tissue thickness as an input. However, *Roose et al.* [2006a] compute only the strain *increments* caused by the augmentation surgery (i.e., by implant) in the situation when the superposition principle is *not applicable* because the strains are not necessarily small. Yet, in their simulation, they still obtained good agreement with the post-operative breast shape of a real patient. This indicates that in their simulation the strains were, in fact, *small*. This was probably the case due to the large volume of the implant which was in the range of 245 cm^3 to 295 cm^3. The simulation result after augmentation is given in Figure 6.9b, where the left breast shows the position of the implant. A pre-operative 3-D picture of the breast is given in Figure 6.9c. While the breast tissue enveloping the implant undergoes considerable *displacements*, its deformation probably was limited because the tissue was concentrating in a rather thin layer, surrounding the implant (Figure 6.9b). Therefore, in spite of considerable increase in breast size in the case presented by *Roose et al.* [2006a], the deformation may have been essentially *linearly* elastic, and so the results of their simulation should have been expected to be quite accurate.

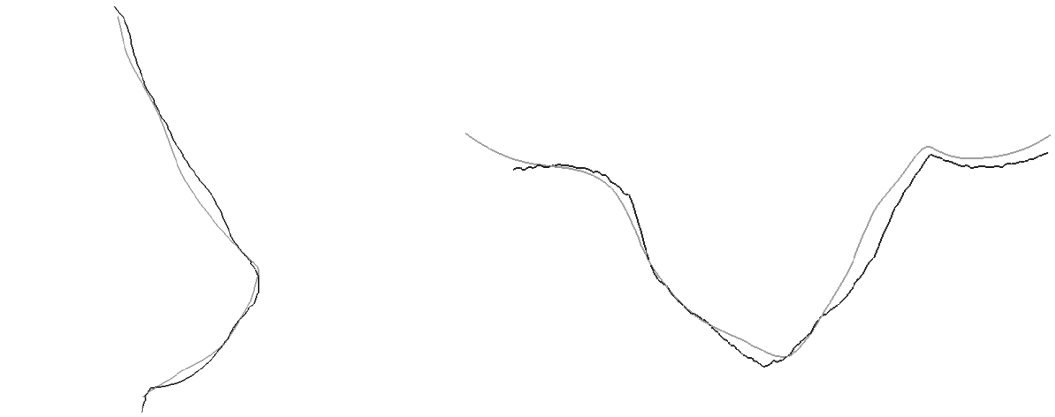

(a)

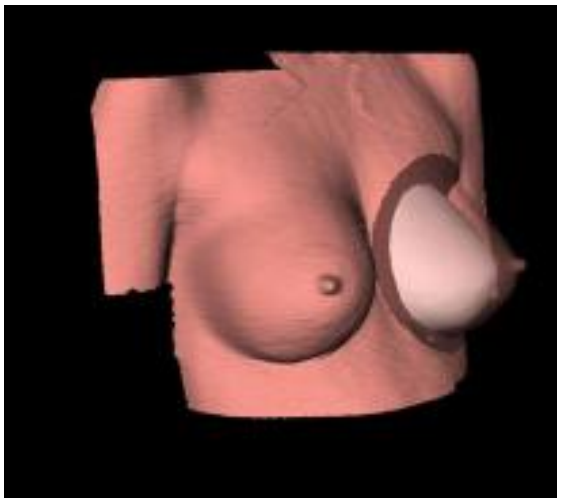

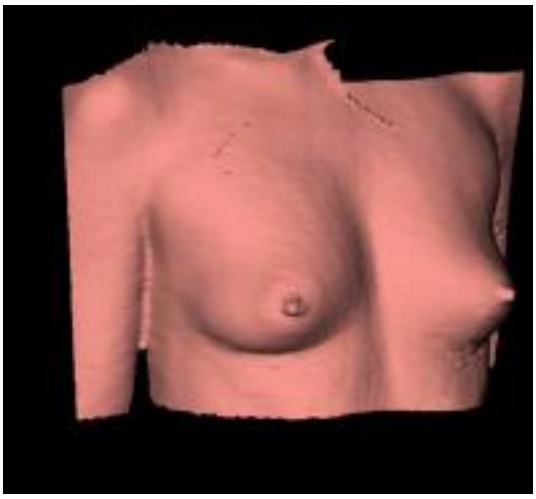

(b) (c)

Figure 6.9. Simulation of subglandular implant placement [*Roose et al.*, 2006a]: (a) breast contours in a horizontal and sagittal cross-sections (grey for simulated surface, black for real post-operative surface, (b) the result of the simulation after augmentation (left breast shows the position of the implant), and (c) pre-operative 3-D picture of the breasts.

However, it remains to be seen if their method will be as accurate for much larger strains, which are also characteristic for breast deformations (e.g., Figure 6.6). As mentioned *Roose et al.* [2006a], the future work includes addition of gravity forces to their model. This would be straightforward for a linear model, but the accuracy and convergence of their approach remain to be checked in the case of large-strains (in spite of the linear elastic material). Finally, not including the effect of skin on breast deformation, they may have omitted a significant factor affecting the results of many reconstructions and augmentation procedures that are based on adjusting stresses (tension) in the layer of skin enveloping the breast tissue. Even the initial attempt to include the skin by *Williams et al.* [2003] shows that the skin may be an important factor for breast deformation.

Pamplona and Alvim [2004] analyzed the stresses and strains that occur in breast skin immediately after a reconstruction surgery, which utilized expanders and implants. They adopted a circular breast geometry for the undeformed shape of the breast, which they modeled using planar membrane elements. The thickness of the elements was 7 mm. The analysis was divided into two steps. In the tissue expansion step, a normal traction (simulating internal pressure imposed by the extender) was imposed perpendicular to the membrane, which stretched the skin into the approximately semi-spherical shape (Figure 6.10a). The next step models removing the expander and positioning the implant. Using a hyper-viscoelastic constitutive skin model and assuming the anatomic implant shape, *Pamplona and Alvim* [2004] were able to simulate the relaxation of expanded tissue (Figure 6.10b). In spite of the considerable simplifications (e.g., breast modeled by a planar, circular membrane), the results obtained by *Pamplona*

and Alvim [2004] are encouraging and have potential for improvement of the expansion process and for optimization of the number, shape, and size of the expanders for real surgical procedures.

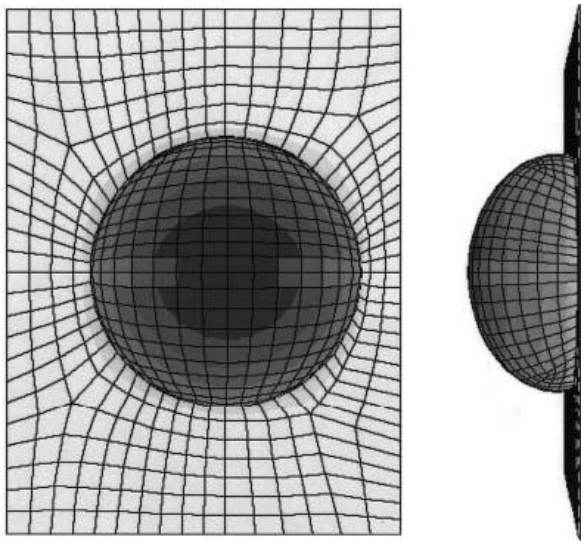

(a)

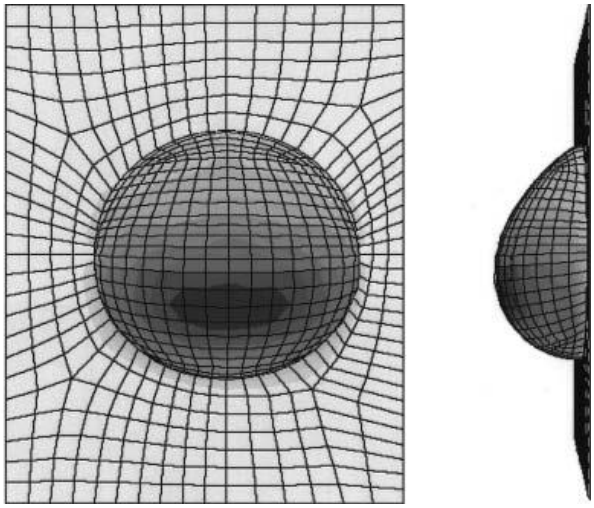

(b)

Figure 6.10. (a) Deformation during the tissue expansion step and (b) after the expander is substituted by the implant [*Pamplona and Alvim*, 2006].

6.2 Properties of Breast Tissue

There is a limited number of studies available in the literature on determining the mechanical properties of tissues that constitute breast. Small-strain elastic modulus values have been determined for fat and glandular tissue by the elastographic method, which is essentially a combination of medical imaging and acoustic excitation of the patient breasts. It has been shown that glandular tissue is approximately 5 times stiffer than fat [i.e., *Skovoroda et al.*, 1995; *Krouskop et al.*, 1998]. *Wellman and Howe* [1998] performed indentation tests on fat and glandular tissue and proposed a piece-wise linear model to characterize the behavior of these tissues for large-strain deformation. They suggested that the stiffness of the glandular tissue is approximately 5 times that of fat at 5% strain and that the ratio of elastic modulus of glands to the elastic modulus of fat exceeds 10 at 15% strain. *Azar et al.* [2004] pointed out that *ex-vivo* measurements of fat do not account for the effect of the suspensory (Cooper) ligaments on the overall behavior of fat tissue. According to *Krouskop et al.* [1998], at body temperatures, fat tissue behaves almost like a fluid. Since all measurements reported in the literature [*Wellman and Howe*, 1998; *Williams et al.*, 2003; *Tanner et al.*, 2006] have been made at room temperature, the published properties may not be representative for *in-vivo* fat tissue.

Properties of skin have been studied more thoroughly than those of fat and glands [e.g., *Agache et al.*, 1980; *Fung*, 1993; *Schneider et al.*, 1984]. Published data for the stress-strain relationship for the skin tissue suggests that the typical Young's modulus of skin $E \sim 1$ - 10 kPa [*Silver*, 1987; *Tanner et al.*, 2006], although it can be as high as $E \sim$

10^2 kPa [*Park*, 1984] or even $E \sim 10^3$ kPa [*Elden*, 1977]. *Agache et al.* [1980] reported that the stiffness of skin tissue generally increases with age.

6.3 Breast Deformation under Gravity

As noted by *Balaniuk and Costa* [2006], predicting the breast shape still remains an enigma because there are many uncertain variables including the curvature of the chest wall, the breast position (e.g., supine versus upright), and the absence of clear landmarks to define the breast form. In addition, the number of poorly defined variables becomes even greater after operating on the breast, when factors that could be considered include surgical technique, the plane of tissue dissection, the tissue compliance or elasticity, and the deformation of tissues surrounding the volume added (implant) or removed, among others [*Balaniuk and Costa*, 2006]. Yet, the breast is a much simpler part of the human body compared to the brain. This is why the results discussed in Chapter 5, as well as the results obtained in the works reviewed above, encouraged us to extend our brain modeling to the case of breast deformation.

As in brain modeling (Section 3.4), any breast simulation faces the issue of the unknown stress-free reference configuration. For example, when *Williams et al.* [2003] attempted to simulate the realistically reconstructed breast shapes, they attributed (at least, partially) the deficiency of the obtained results to the unknown geometry and unknown initial stresses in the breast that had undergone mastectomy. Similar to our brain approach [*Puzrin et al.*, 2006], *Rajagopal et al.* [2006] studied the effect of gravity on breast deformation employing a silicone breast model. Although it still remains to be

done, they were motivated by analyzing the errors arising from the use of an incorrect reference configuration, i.e., a stress-free, unloaded initial state, which was assumed to exist. *Rajagopal et al.* [2006] noted that the reference states used in previous works were in fact deformed, prestressed configuration, which may have affected the prediction accuracy.

Rajagopal et al. [2006] used their model to simulate the deformation due to gravity in order to obtain a qualitative prediction of the deformed shape for a patient in the supine position (e.g., for a breast biopsy). To recreate a realistic breast shape, they used MRI images of a real patient lying prone in an MRI scanner (Figure 6.11a). They computed both the supine breast deformation under the gravity loading (Figure 6.11b) and the reference configuration of the breast (although they do not describe the details and how exactly this reference configuration was computed).

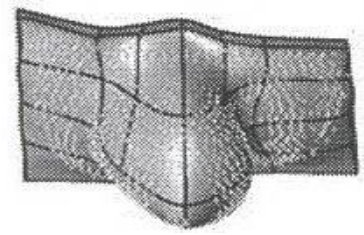

(a)

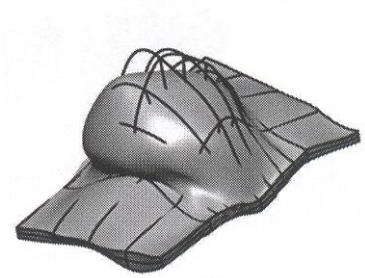

(b)

Figure 6.11. (a) Finite element model fitted to the skin surface data set of volunteer patient lying prone in the MRI scanner and (b) supine breast deformation of the same patient under the gravity loading [*Rajagopal et al.*, 2006]. The wire frame shows the reference configuration and the shaded surface illustrates the deformed FEM.

In this work, we investigate the influence of the stiffness of the breast tissue on the breast shape in the upright position. To this end, the breast is modeled by a hemi-ellipsoid with an overlying skin layer. To simplify the problem, we model both fat and gland tissues by the same homogeneous material with some average properties. We further call this material simply *breast tissue*. Therefore, the breast is modeled as a composite object with the inner surface of the skin bonded to the outer surface of the breast tissue. According to *Gray* [1995], the base of the breast has practically a circular cross-section (Section 6.1), and therefore, we employed the ellipsoid of revolution for the undeformed breast shape (Figure 6.12). The base of the ellipsoid is fixed (i.e., no displacements are allowed) to simulate the rigid interface between the pectoralis major muscle and the breast tissue (Figures 6.2, 6.3). Finally, the nipple and the areola are added to provide reference points on the model. Since the areola is mainly a pigmented skin and because the nipple is small, currently, both nipple and areola have the same mechanical properties as the skin. These can be easily changed in the future modeling.

The behavior of the skin is modeled as a homogeneous, isotropic, incompressible neo-Hookean material (Section 2.3), and the Mooney-Rivlin model (Section 2.3) is used to describe the breast tissue. Figure 6.12 shows the undeformed geometry of the breast model. The undeformed mesh of the FEM is also illustrated in Figure 6.12. We assume that stresses are zero in the undeformed state, which is certainly an assumption which remains to be tested. Strictly speaking, it is not even obvious that such a stress-free reference state exists (since actually the breast never experienced the stress-free environment).

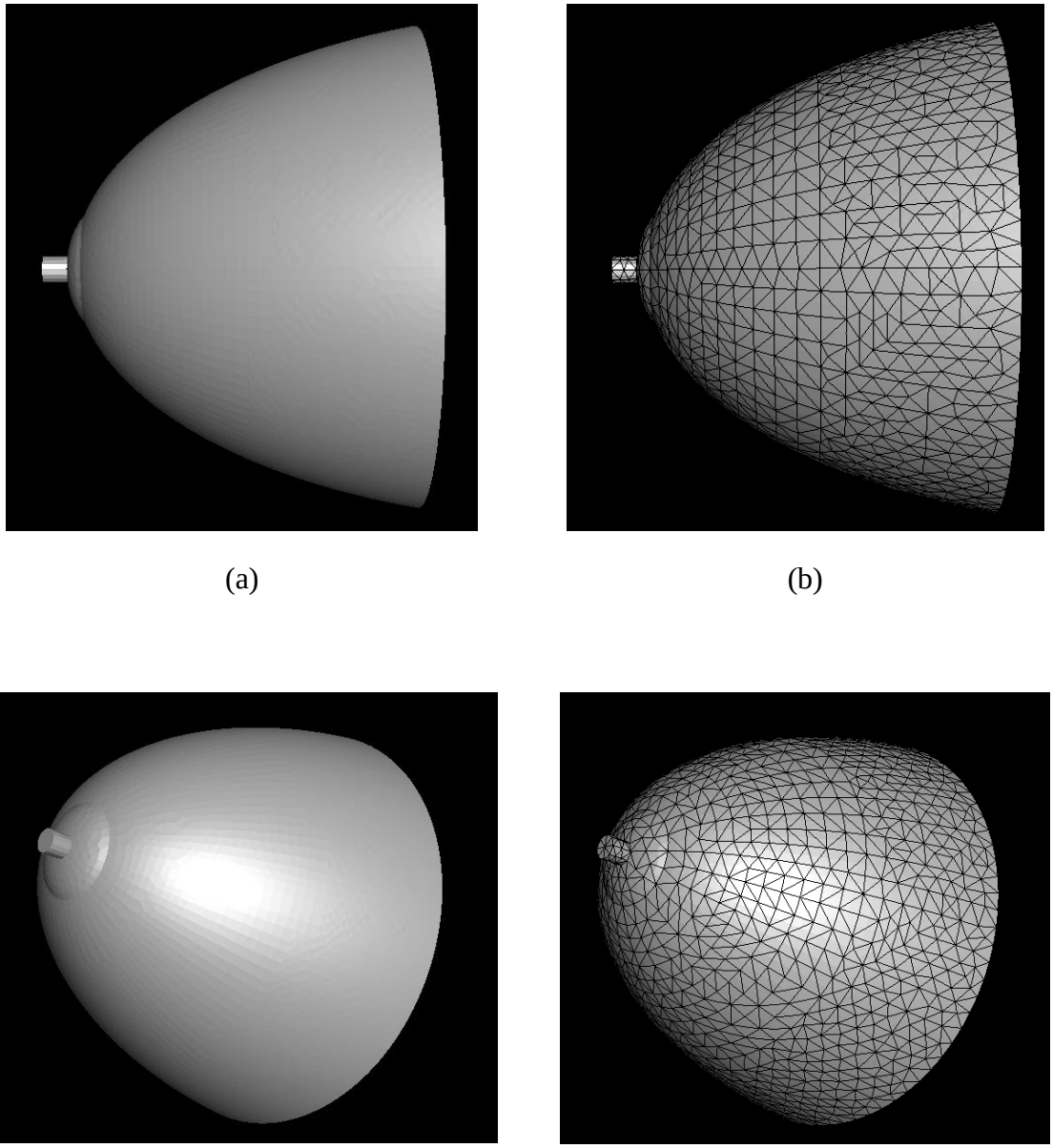

(a) (b)

(c) (d)

Figure 6.12. (a, b) Side and (c, d) perspective views of undeformed geometry of the breast model. (b, d) Undeformed FEM mesh of the breast model as seen in side and perspective views, respectively.

However, our results for brain modeling (Section 3.4) suggest that the stress-free reference configuration is a reasonable approximation in the case of brain deformation and comparable strains (up to 100%). Therefore, the assumption of the stress-free reference configuration may also be acceptable in the case of breast deformation. At the moment, the only real criterion of the validity of this assumption is the reasonably good agreement between the simulated breast form and that observed in the actuality [*Schider*, 1954, Figure 6.1].

As before, we employ the ABAQUS code [*ABAQUS*, 2004] for finite element analysis and meshed the model using 22783 modified second order tetrahedron hybrid elements labeled in ABAQUS C3D10MH [*ABAQUS*, 2004]. The model had 33960 nodes and we employed the non-linear solver based on the full Newton iterative algorithm. The average element aspect ratio was 1.70 with the worst aspect ratio of 2.95, which provided reliable convergence and improved accuracy of the calculations. It should be noted that the modified tetrahedron elements large distortion while hybrid elements are suitable for incompressible materials [*ABAQUS*, 2004]. Increasing the number of elements by 50% did not change the obtained results.

We let the created model deform under gravity. The direction of the gravitational acceleration is parallel to the base of the breast model (i.e., vertical in Figure 6.12 and subsequent figures). The effect of the skin modulus on the breast form was studied by performing successive simulations while increasing the value of the neo-Hookean modulus C_{10} (expression (2.3.3)) in each simulation. In the first simulation, the neo-Hookean modulus was set to $C_{10} = 1000$ Pa and was then progressively increased by 1000 Pa in the subsequent simulations. In the case of small-strains, the neo-Hookean model is

equivalent to the linear elastic model, and C_{10} = 1000 Pa corresponds to the Young's modulus $E \approx 5000$ Pa, which is in the range of skin properties measured in direct experiments (Section 6.2).

However, the data for the breast tissue available in the literature [i.e., *Wellman and Howe*, 1998; *Williams et al.*, 2003; *Tanner et al.*, 2006] did not result in realistically deformed breast shapes. For example, we used the Mooney-Rivlin parameters (expression (2.3.4)) determined by *Tanner et al.* [2006] by fitting the five-parameter model to the results of the tests with volunteers, when the volunteers' breasts were compressed by about 20%. An example of our simulation is shown in Figure 6.13. The breast deformation (Figure 6.13b) is in fact hardly noticeable compared to the undeformed shape (Figures 6.12a, 6.13a).

The only published parameter (at least, known to us) that produced somewhat reasonable results was C_{10} = 128.9 Pa reported by *Tanner et al.* [2006] for the neo-Hookean model. However, *Tanner et al.* [2006] were able to fit *the same* experimental results for *the same* two volunteers using *the same* neo-Hookean model with *nine* sets of parameters that differed by three orders of magnitude. This does not confirm the results of our simulations meaning that the breast and skin properties strongly affect the breast shape (as will be described below). This is why we chose to use constitutive parameters that result in a more accurate deformed shape rather than the parameters reported in the literature [*Wellman and Howe*, 1998; *Williams et al.*, 2003; *Tanner et al.*, 2006]. In fact, we believe that as a result of our simulation, we obtained a more realistic estimate of the Mooney-Rivlin parameters of the breast tissue.

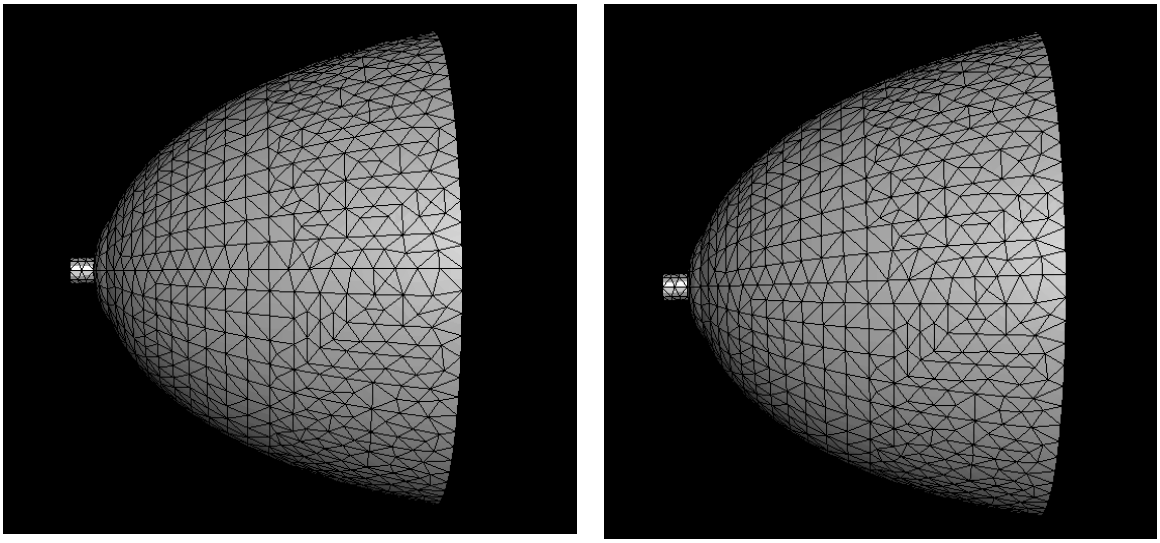

(a) (b)

Figure 6.13. (a) Undeformed and (b) deformed FEM meshes of the breast modeled using Mooney-Rivlin parameters (expression (2.3.4)) adopted from *Tanner et al.* [2006] (C_{10} = 42.83 kPa, C_{01} = −36.54 kPa, C_{20} = 51.83 kPa, C_{11} = 7.33 kPa, and C_{02} = 0.52 kPa).

Taking into consideration this argument, we chose the Mooney-Rivlin parameters $C_{10} = C_{01} = 50$ Pa for the breast tissue. Figures 6.14, 6.15, and 6.16 show the deformed shapes of the breast model for simulations with the three neo-Hookean moduli for skin (C_{10} = 1000 Pa, 2000 Pa, and 3000 Pa). The corresponding variations of the maximum principal stresses within the breast in the sagittal cross-section are presented in Figures 6.17, 6.18, and 6.19. As can be seen, the breast becomes higher with higher skin stiffness, and the tension in the skin becomes higher as well.

A similar result was obtained when we investigated the effect of the stiffness of the breast tissue on the breast form. In this simulation, we chose $C_{10} = 2000$ Pa for the neo-Hookean modulus of the skin layer and progressively increased the Mooney-Rivlin parameters for the breast tissue from $C_{10} = C_{01} = 50$ Pa to $C_{10} = C_{01} = 100$ Pa, and then to $C_{10} = C_{01} = 200$ Pa. The deformed shapes of the model for each simulation are given in Figures 6.15, 6.20, and 6.21. The maximum principal stress variations in the sagittal cross-section within the breast are shown in Figures 6.18, 6.22, and 6.23. It can be observed that as the firmness of the breast tissue decreases, the breast becomes lower and the downward displacement of the breast increases, resulting in the greater sagging and higher tension in the skin.

For convenience, we also showed the results of the same simulations in Figures 6.24-6.32. The deformations of the breasts with an identical breast tissue ($C_{10} = C_{01} = 50$ Pa) but different skin properties (C_{10} = 1000 Pa, 2000 Pa, and 3000 Pa) are compared in Figures 6.24 and 6.25, where the breast shapes are shown next to each other. The corresponding stresses are shown in Figure 6.26. The deformations of the breasts with the same skin ($C_{10} = 2000$ Pa) but different breast tissue properties ($C_{10} = C_{01} = 50$ Pa,

100 Pa, and 200 Pa) are shown together in Figures 6.27 and 6.28, while the stress states are compared in Figure 6.29. In Figure 6.30, the effect of skin stiffness and breast firmness on the maximum nipple displacement is presented. Finally, the variation of maximum principal stresses along the breast skin as a function of skin stiffness and breast firmness are given in Figure 6.31 and 6.32, respectively.

As can be seen from Figures 6.26, 6.29, 6.31, and 6.32 (as well as from Figures 6.15, 6.18, 6.19, 6.22, and 6.23), the maximum tensile stress is greatest in the skin and the entire skin is in tension. Mechanically, the breast skin is essentially a membrane supporting the breast structurally. As noted above, the tension in the skin decreases with the firmness of the breast tissue (Figure 6.29 and 6.32). Below the nipple, the tension in the skin increases with the stiffness of the skin (Figure 6.31). However, it is not possible to evaluate the effect of skin stiffness on the tension in the skin above the nipple, and, at best, it can be considered that it does not change with skin stiffness. This is a peculiar behavior, because in *both* cases the breast position tends to be higher. In other words, the tension in the skin does not necessarily correlate with the fact that the breast is lower or higher. Currently, adjusting the skin tension (i.e., by removing or adding a part of the skin) is a mainstream surgical procedure. Hence, this observation may be important for planning reconstruction and augmentation surgeries. One may even consider measuring the skin tension in the future as an objective way of surgery planning, which is not unreasonable from the engineering stand point.

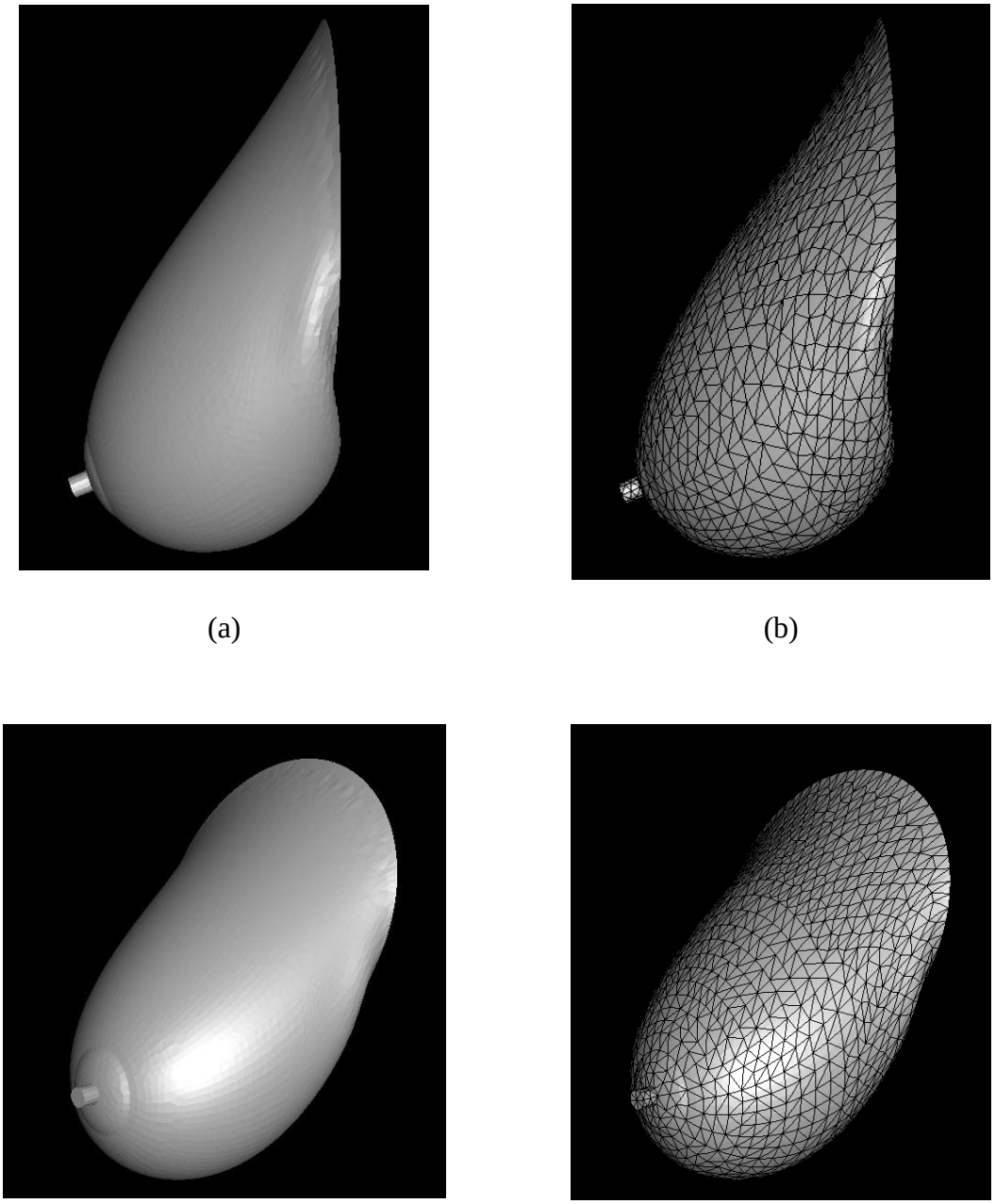

(a) (b)

(c) (d)

Figure 6.14. (a, b) Side and (c, d) perspective views of deformed geometry of the breast model. Deformed FEM meshes of breast model as seen in (b) side and (d) perspective views, respectively. The neo-Hookean skin modulus C_{10} = 1000 Pa, and Mooney-Rivlin parameters of the breast tissue $C_{10} = C_{01}$ = 50 Pa.

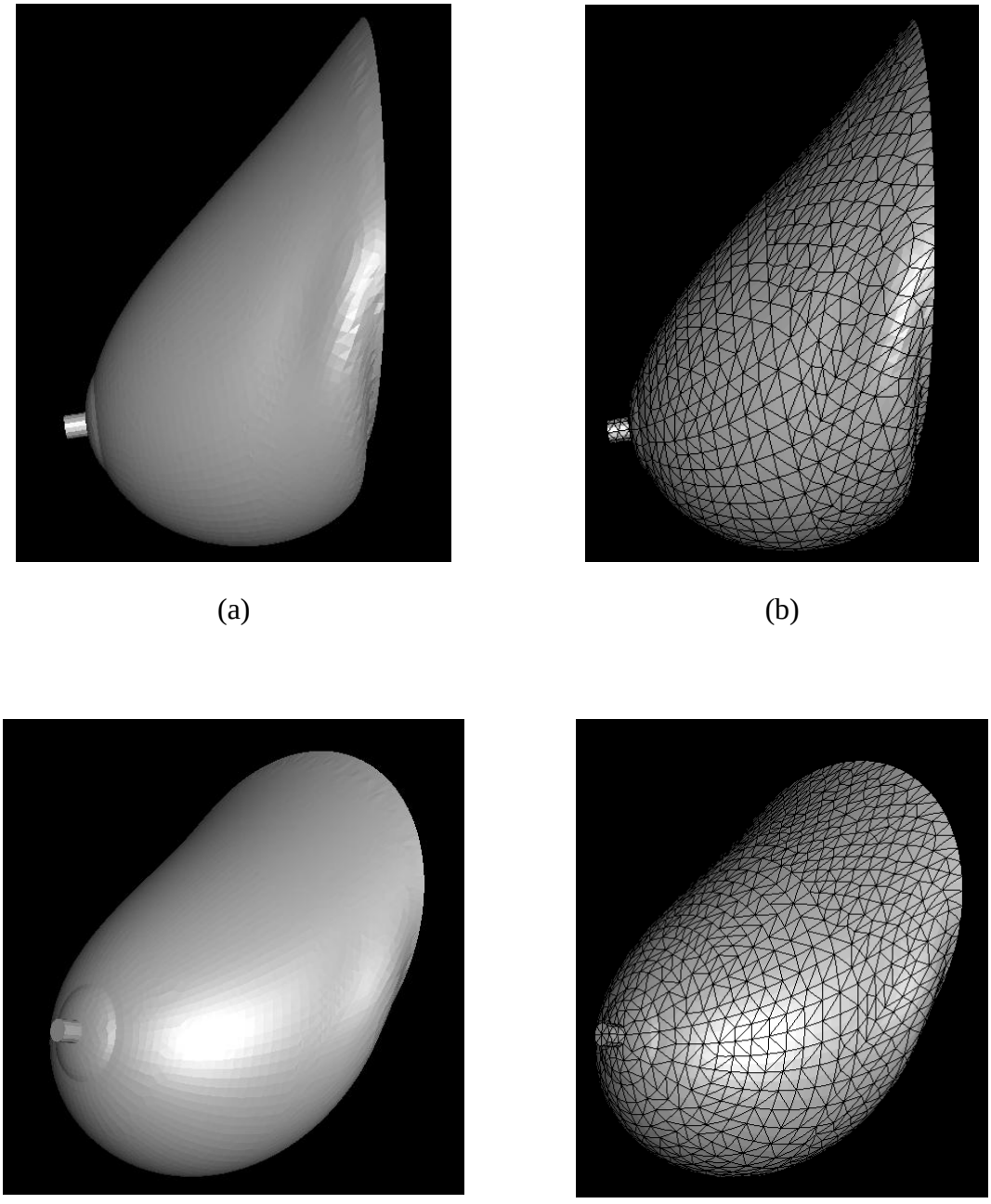

Figure 6.15. (a, b) Side and (c, d) perspective views of deformed geometry of the breast model. Deformed FEM meshes of breast model as seen in (b) side and (d) perspective views, respectively. The neo-Hookean skin modulus C_{10} = 2000 Pa, and Mooney-Rivlin parameters of the breast tissue $C_{10} = C_{01}$ = 50 Pa.

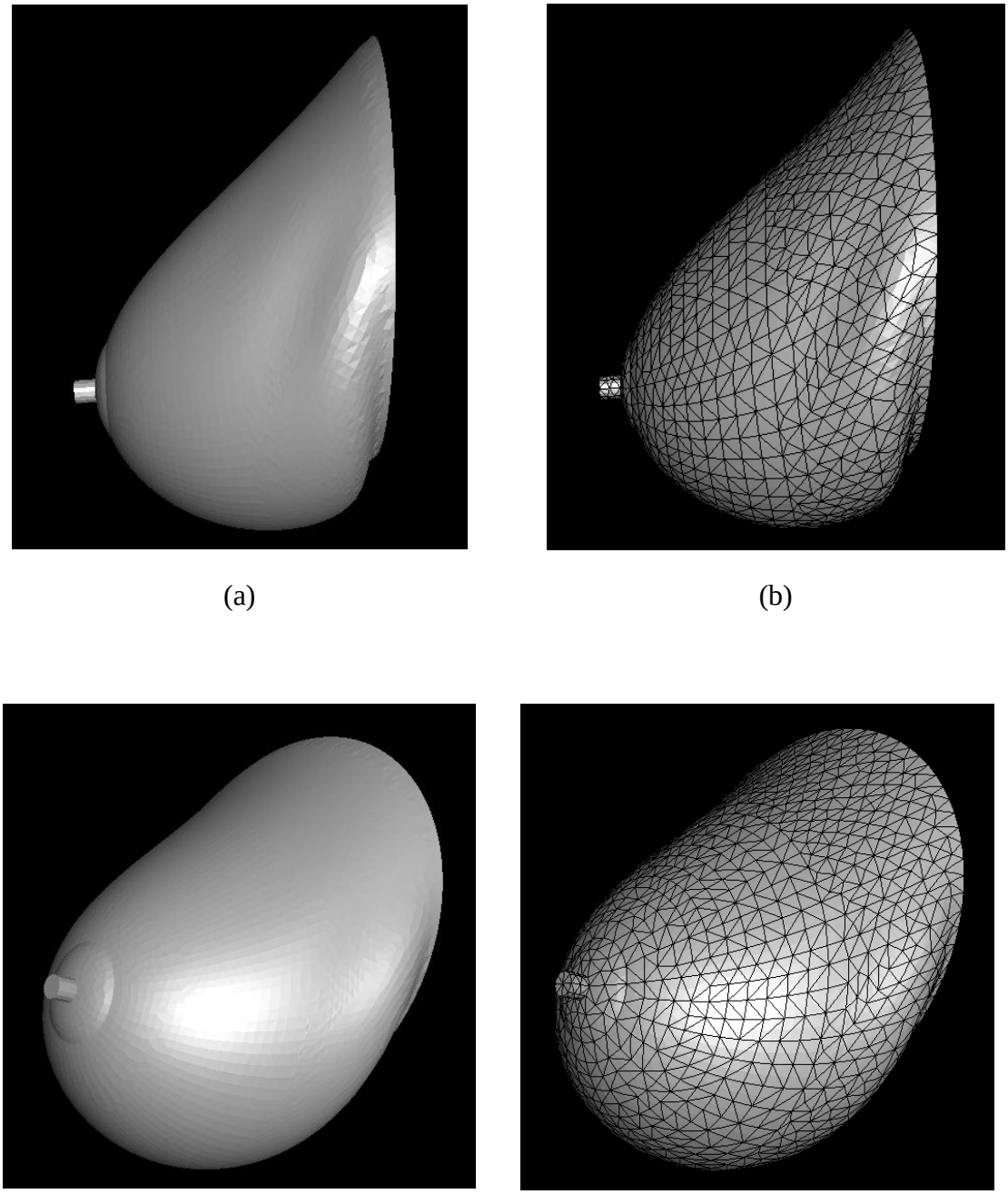

(a) (b)

(c) (d)

Figure 6.16. (a, b) Side and (c, d) perspective views of deformed geometry of the breast model. Deformed FEM meshes of breast model as seen in (b) side and (d) perspective views, respectively. The neo-Hookean skin modulus C_{10} = 3000 Pa, and Mooney-Rivlin parameters of the breast tissue $C_{10} = C_{01}$ = 50 Pa.

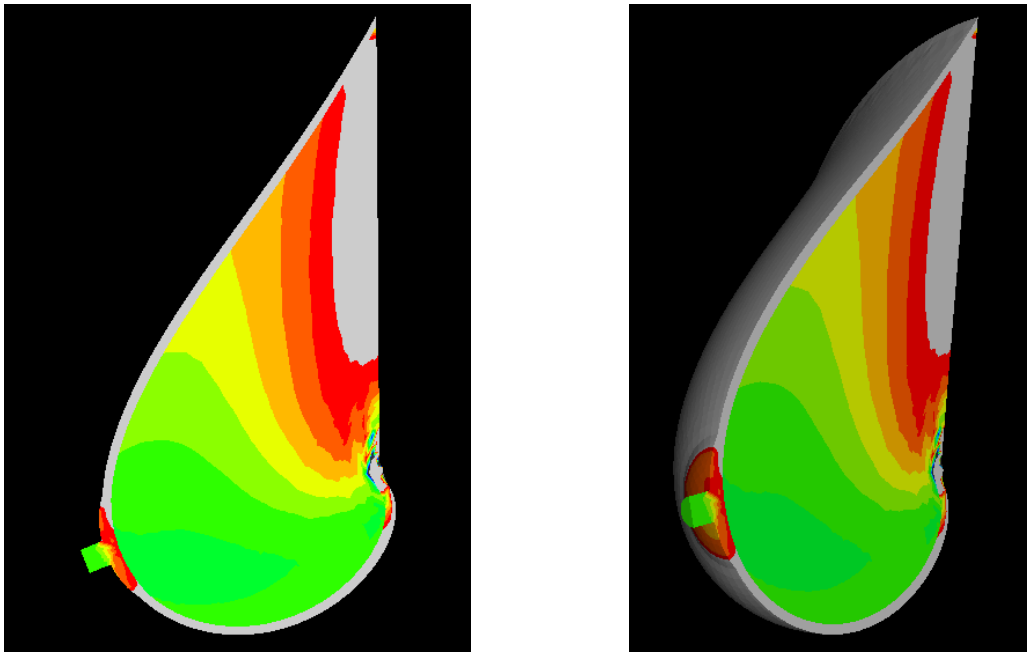

(a) (b)

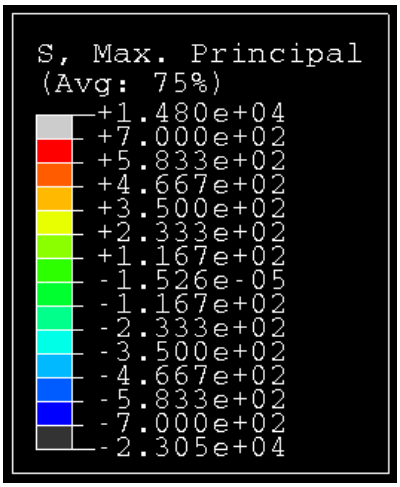

(c)

Figure 6.17. Variation of maximum principal stress in the breast model shown in sagittal cross-section. (a) Side view, (b) perspective view, and (c) legend for stress contour plots (Pa). The neo-Hookean skin modulus C_{10} = 1000 Pa, and Mooney-Rivlin parameters of the breast tissue C_{10} = C_{01} = 50 Pa.

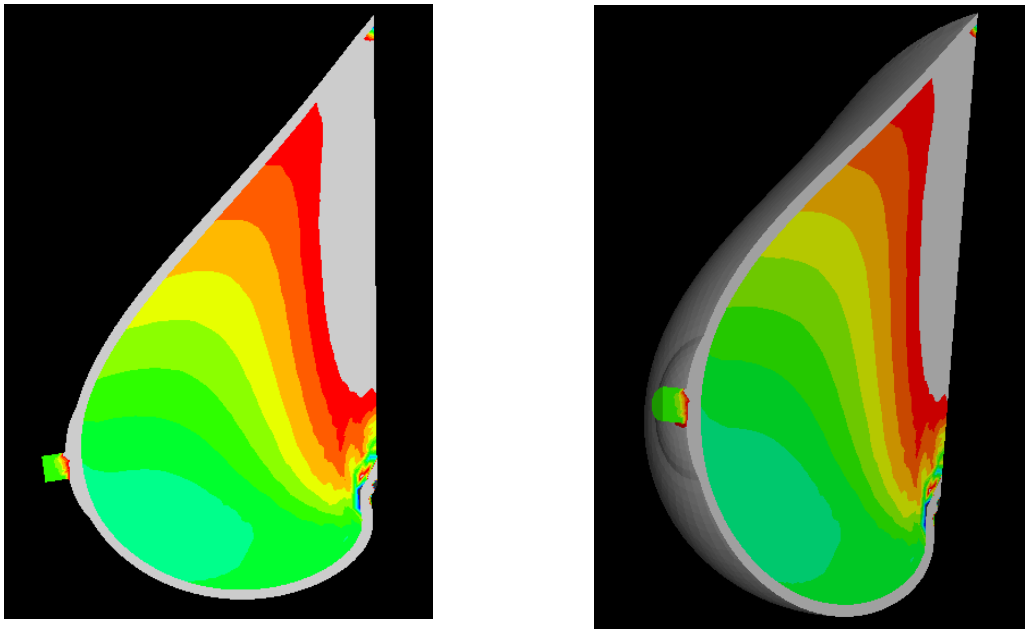

(a) (b)

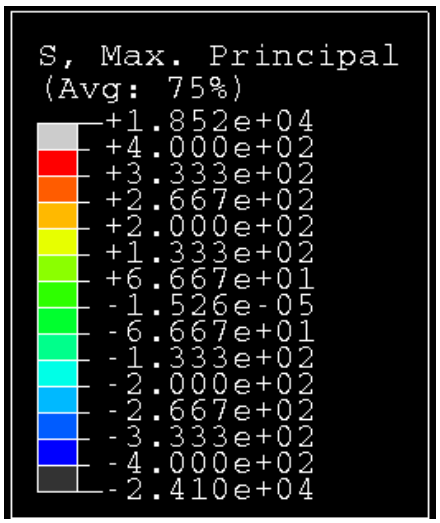

(c)

Figure 6.18. Variation of maximum principal stress in the breast model shown in sagittal cross-section. (a) Side view, (b) perspective view, and (c) legend for stress contour plots (Pa). The neo-Hookean skin modulus C_{10} = 2000 Pa, and Mooney-Rivlin parameters of the breast tissue C_{10} = C_{01} = 50 Pa.

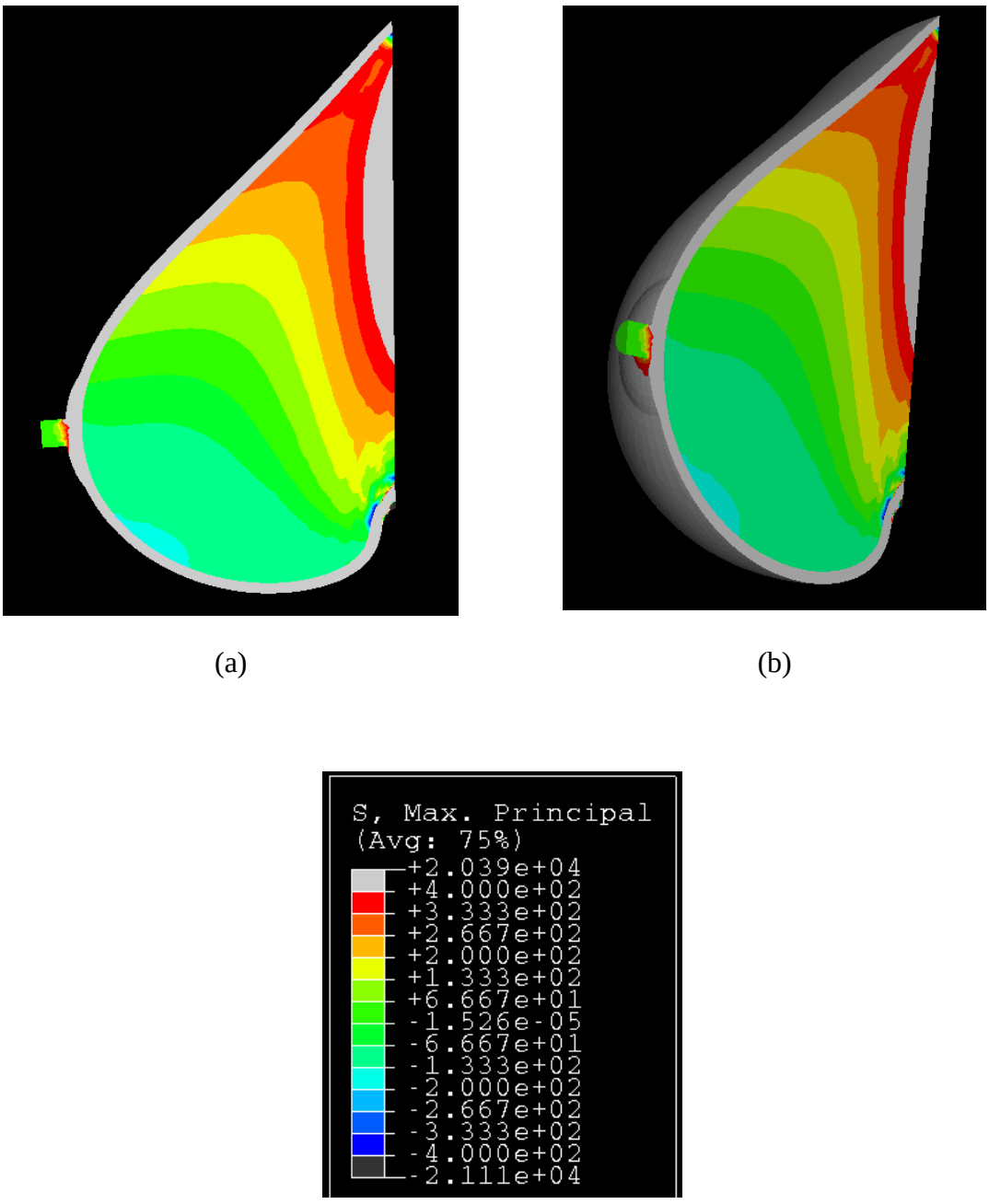

(a) (b)

(c)

Figure 6.19. Variation of maximum principal stress in the breast model shown in sagittal cross-section. (a) Side view, (b) perspective view, and (c) legend for stress contour plots (Pa). The neo-Hookean skin modulus C_{10} = 3000 Pa, and Mooney-Rivlin parameters of the breast tissue $C_{10} = C_{01}$ = 50 Pa.

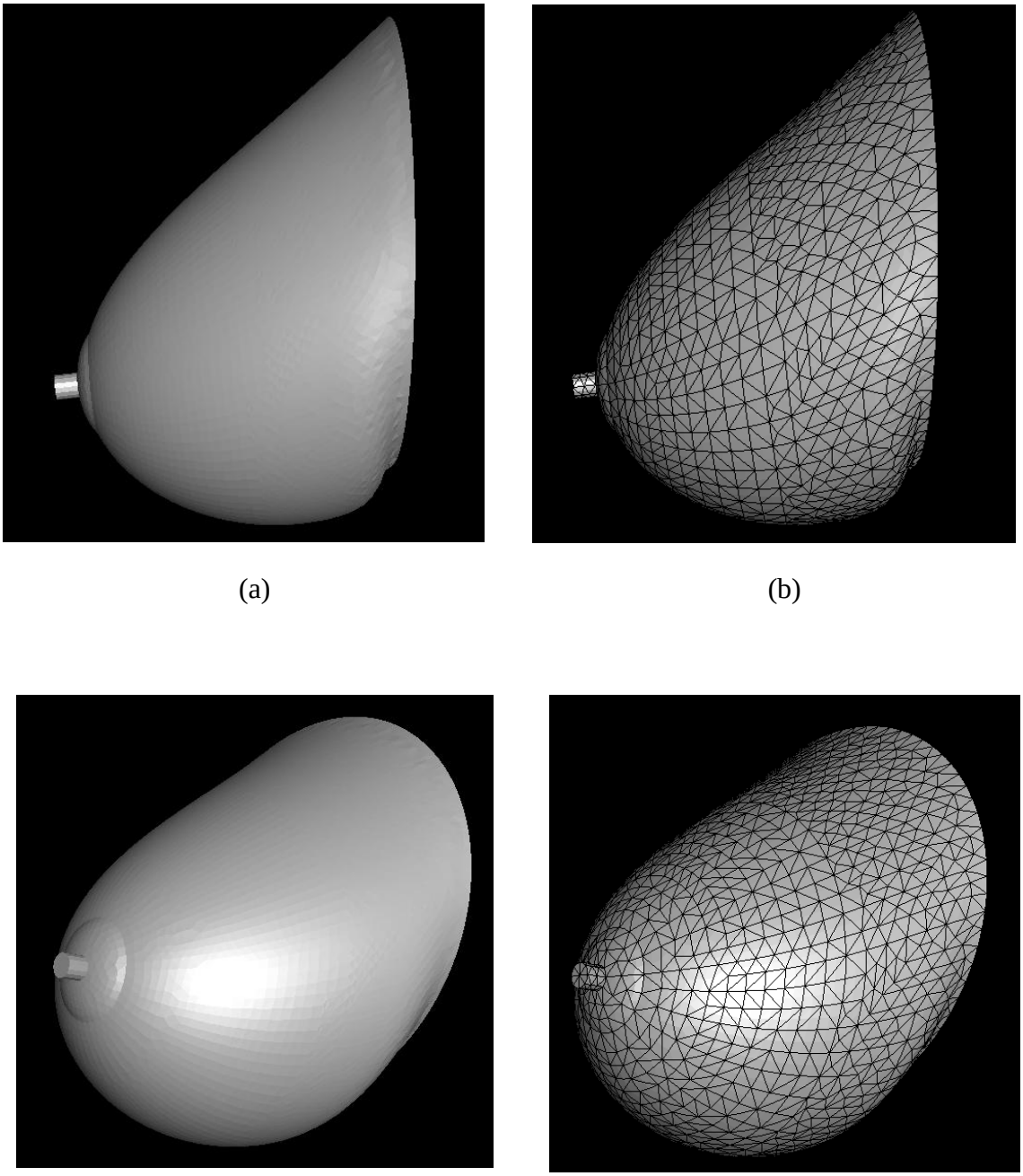

Figure 6.20. (a, b) Side and (c, d) perspective views of deformed geometry of the breast model. Deformed FEM meshes of breast model as seen in (b) side and (d) perspective views, respectively. The neo-Hookean skin modulus C_{10} = 2000 Pa, and Mooney-Rivlin parameters of the breast tissue $C_{10} = C_{01}$ = 100 Pa.

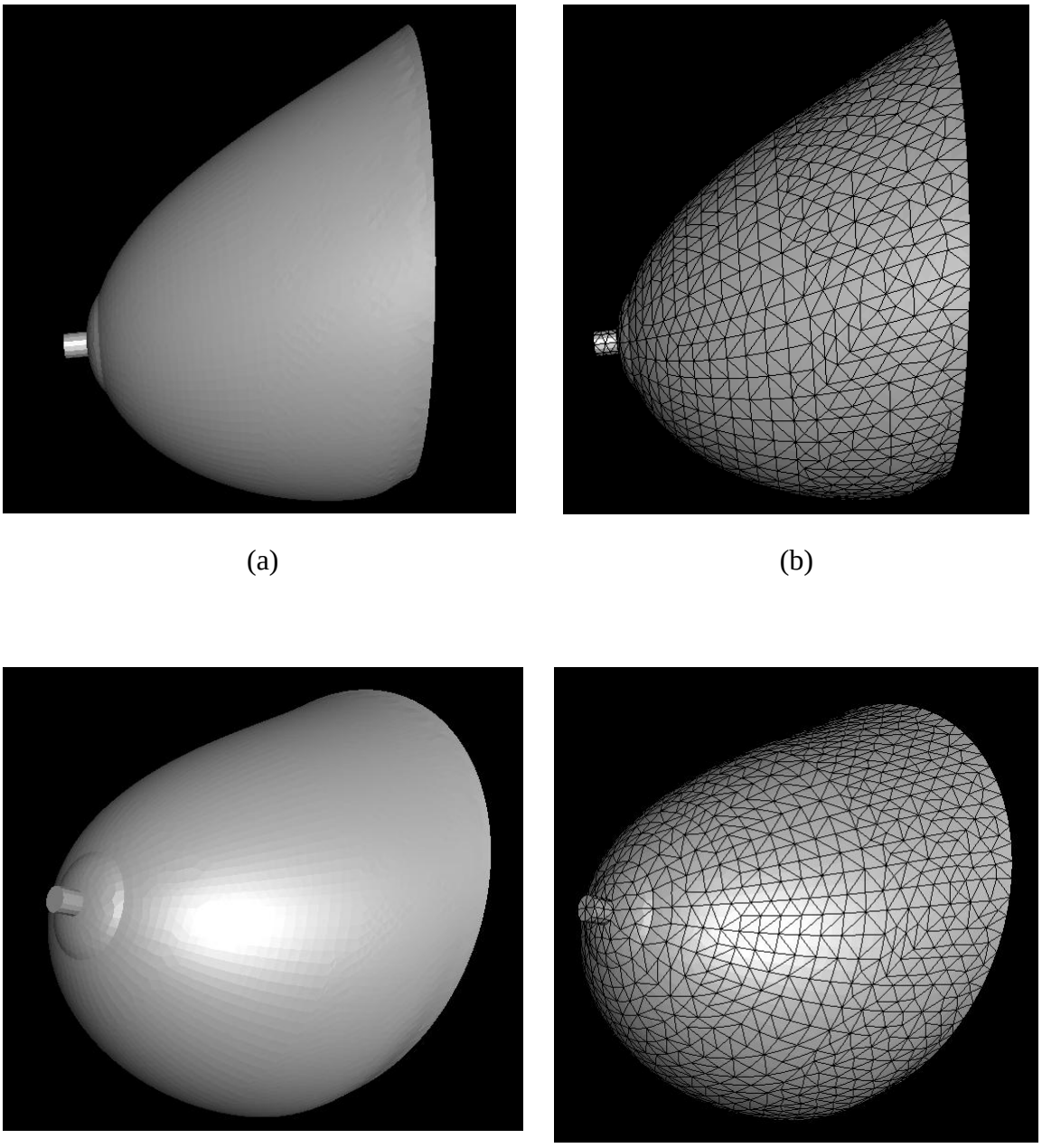

Figure 6.21. (a, b) Side and (c, d) perspective views of deformed geometry of the breast model. Deformed FEM meshes of breast model as seen in (b) side and (d) perspective views, respectively. The neo-Hookean skin modulus C_{10} = 2000 Pa, and Mooney-Rivlin parameters of the breast tissue C_{10} = C_{01} = 200 Pa.

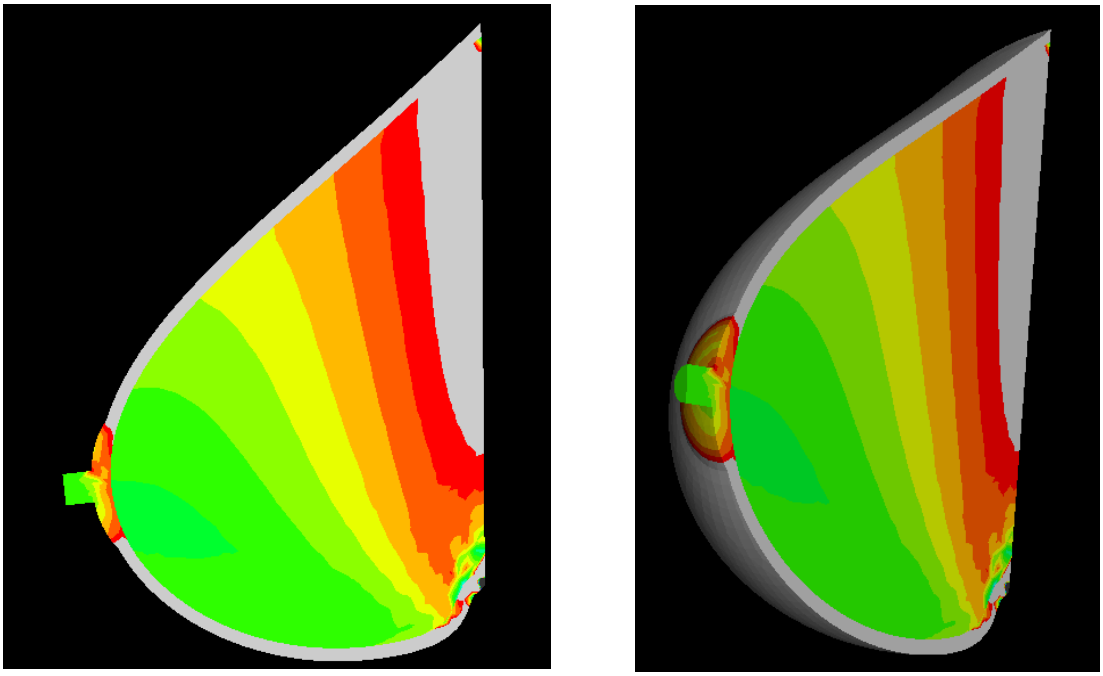

(a) (b)

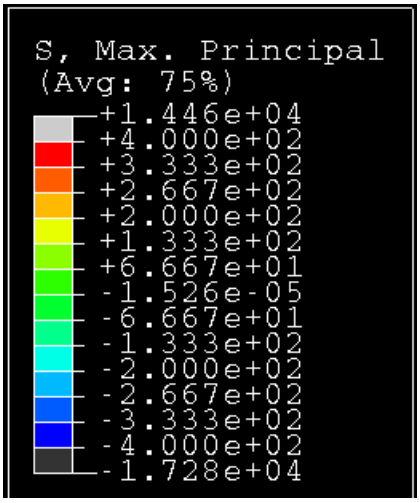

(c)

Figure 6.22. Variation of maximum principal stress in the breast model shown in sagittal cross-section. (a) Side view, (b) perspective view, and (c) legend for stress contour plots (Pa). The neo-Hookean skin modulus C_{10} = 2000 Pa, and Mooney-Rivlin parameters of the breast tissue C_{10} = C_{01} = 100 Pa.

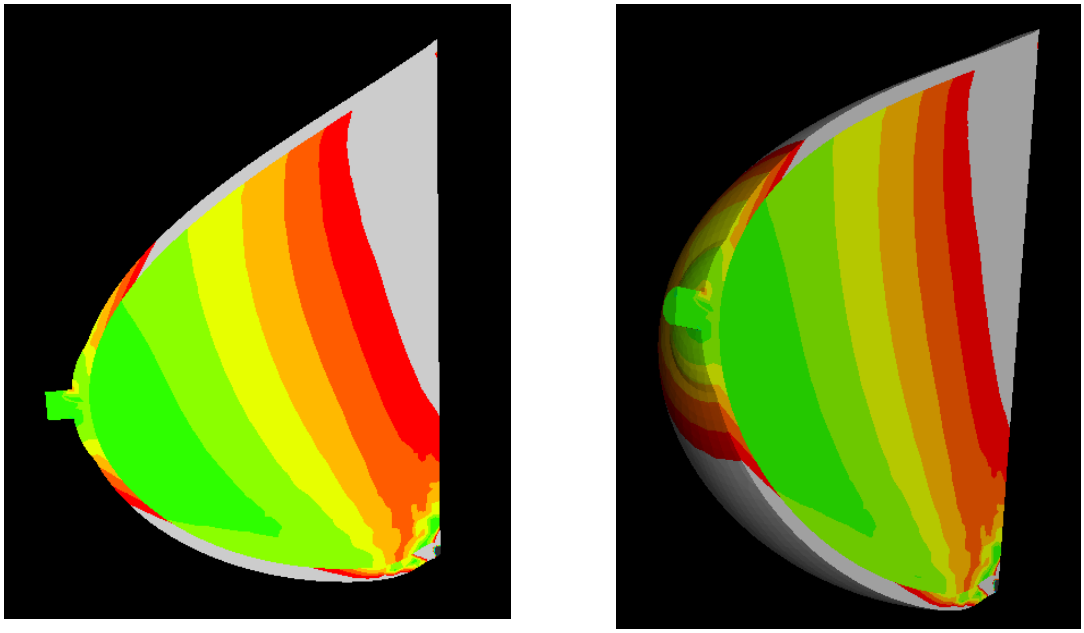

(a) (b)

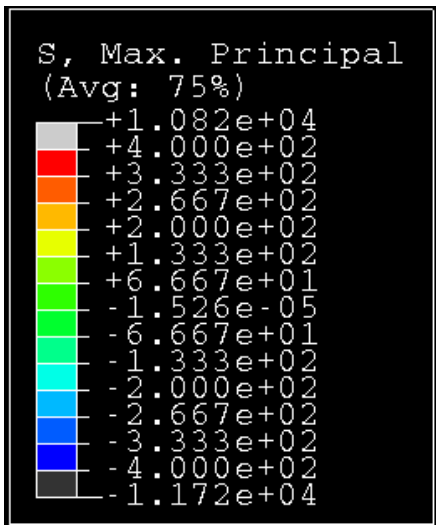

(c)

Figure 6.23. Variation of maximum principal stress in the breast model shown in sagittal cross-section. (a) Side view, (b) perspective view, and (c) legend for stress contour plots (Pa). The neo-Hookean skin modulus C_{10} = 2000 Pa, and Mooney-Rivlin parameters of the breast tissue C_{10} = C_{01} = 200 Pa.

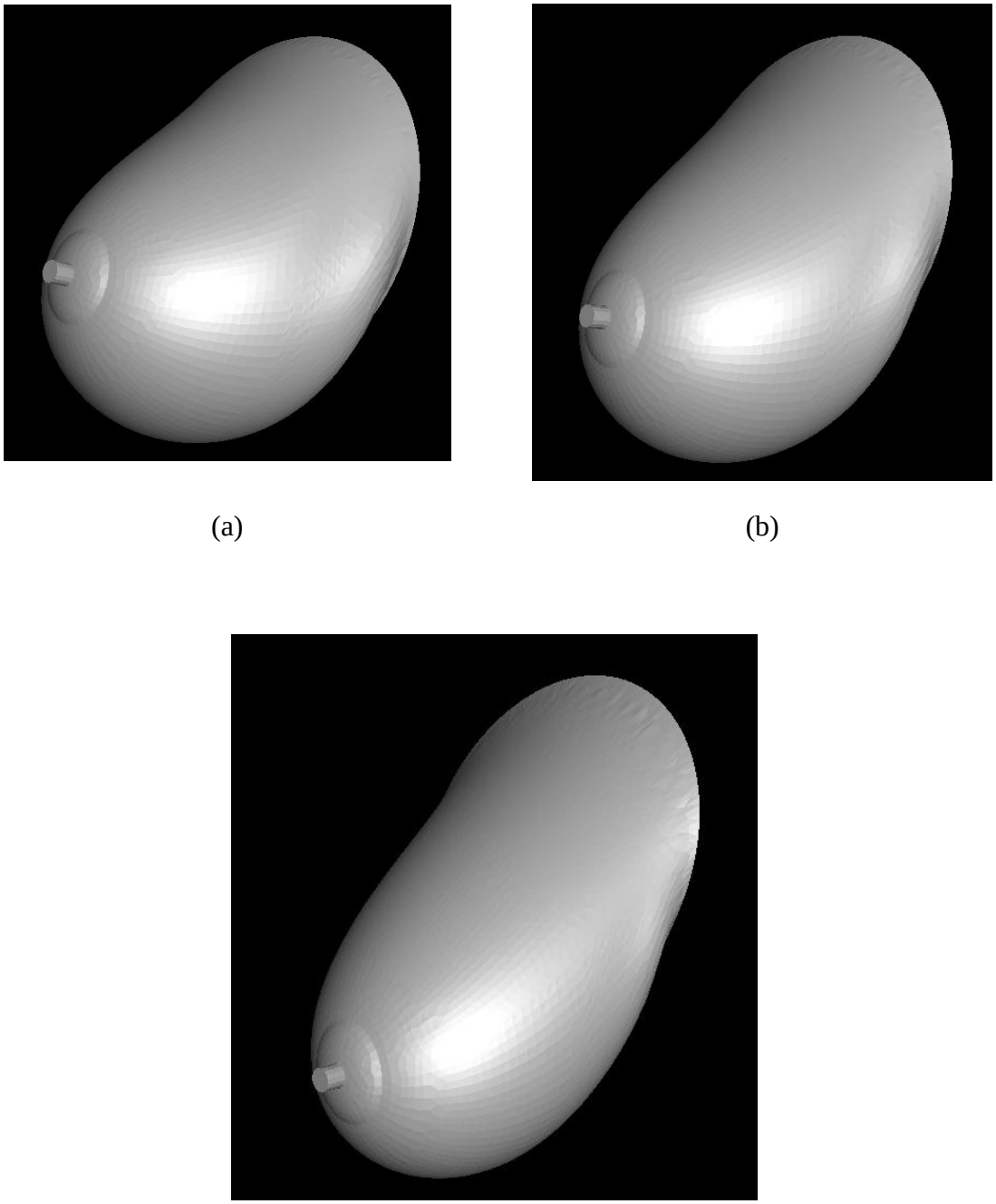

(a) (b)

(c)

Figure 6.24. Perspective views of deformed geometries of the breast models. The neo-Hookean skin modulus: (a) C_{10} = 3000 Pa, (b) C_{10} = 2000 Pa, and (c) C_{10} = 1000 Pa. Mooney-Rivlin parameters of the breast tissue $C_{10} = C_{01}$ = 50 Pa.

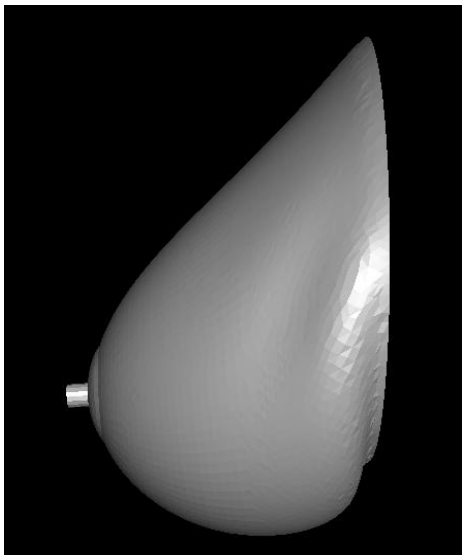

(a)

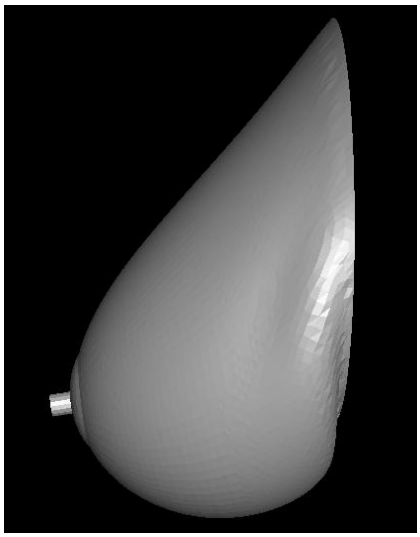

(b)

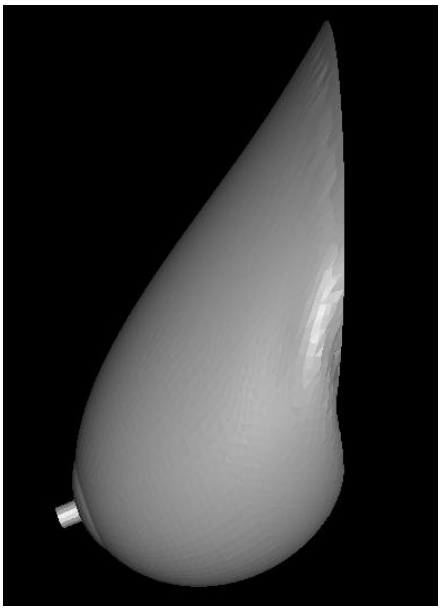

(c)

Figure 6.25. Side views of deformed geometries of the breast models. The neo-Hookean skin modulus: (a) C_{10} = 3000 Pa, (b) C_{10} = 2000 Pa, and (c) C_{10} = 1000 Pa. Mooney-Rivlin parameters of the breast tissue $C_{10} = C_{01}$ = 50 Pa.

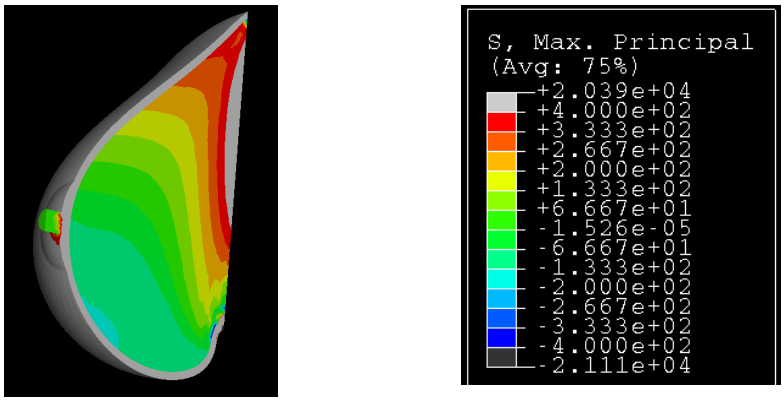

(a)

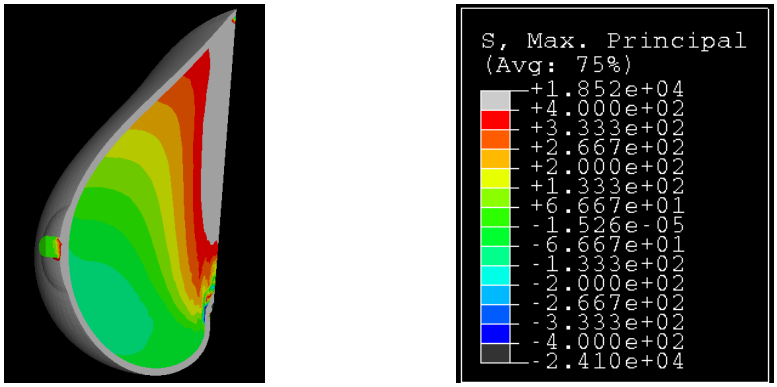

(b)

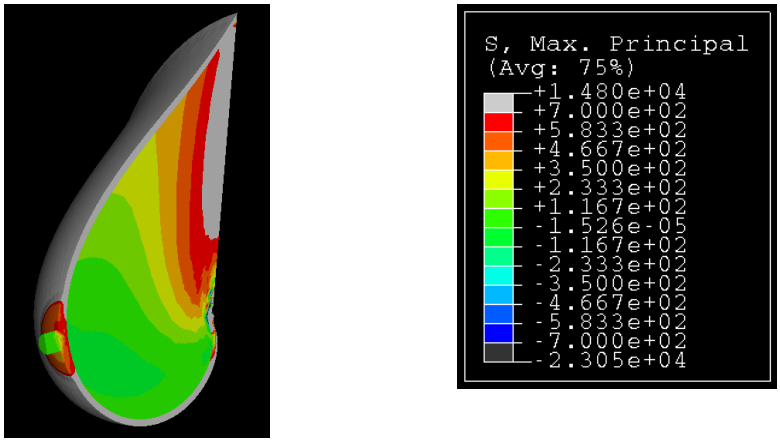

(c)

Figure 6.26. Variation of maximum principal stress in the breast models shown in sagittal cross-section. The neo-Hookean skin modulus: (a) C_{10} = 3000 Pa, (b) C_{10} = 2000 Pa, and (c) C_{10} = 1000 Pa. Mooney-Rivlin parameters of the breast tissue $C_{10} = C_{01}$ = 50 Pa.

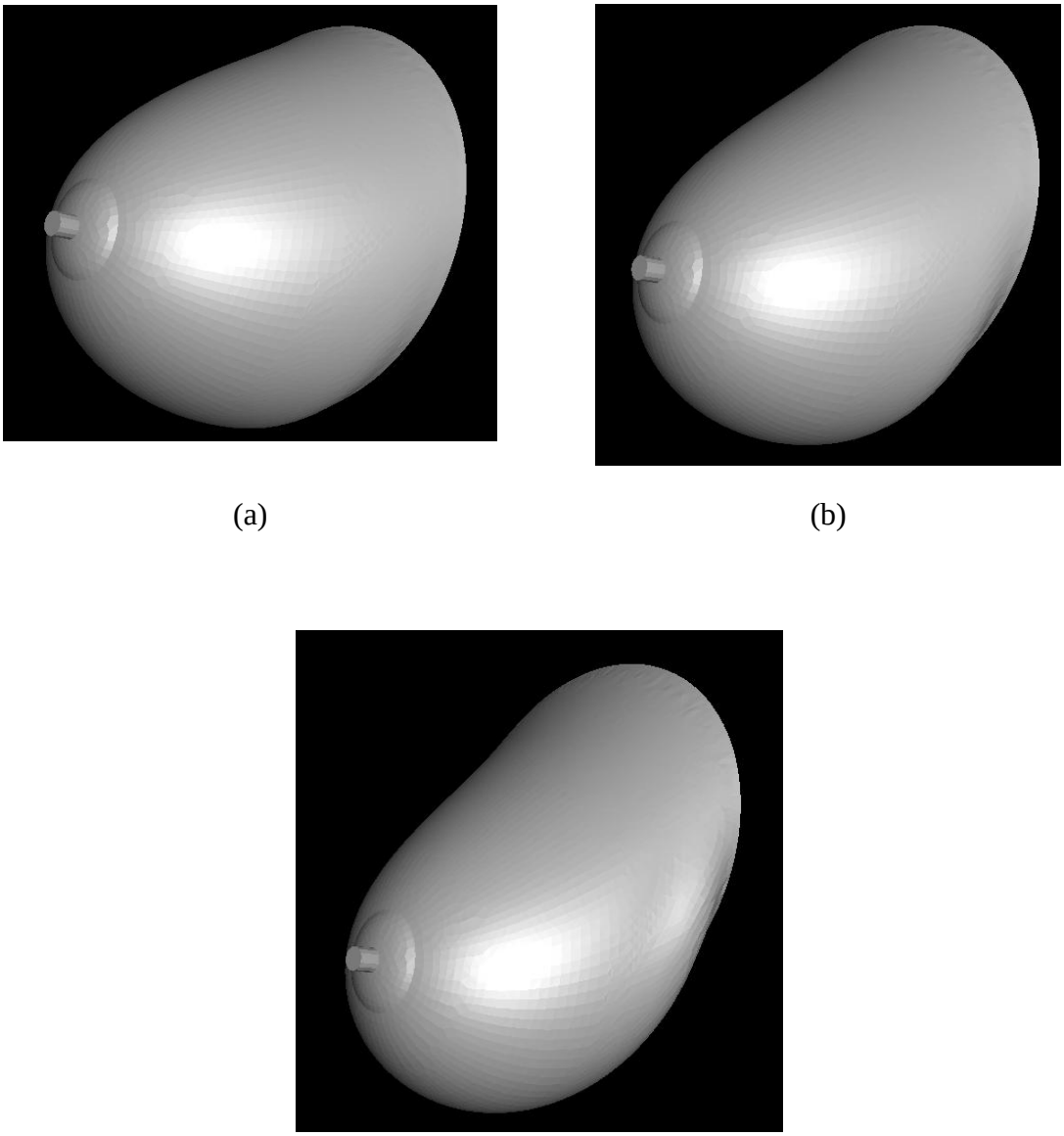

Figure 6.27. Perspective views of deformed geometries of the breast models. Mooney-Rivlin parameters of the breast tissue: (a) $C_{10} = C_{01} = 200$ Pa, (b) $C_{10} = C_{01} = 100$ Pa, and (c) $C_{10} = C_{01} = 50$ Pa. The neo-Hookean skin modulus $C_{10} = 2000$ Pa.

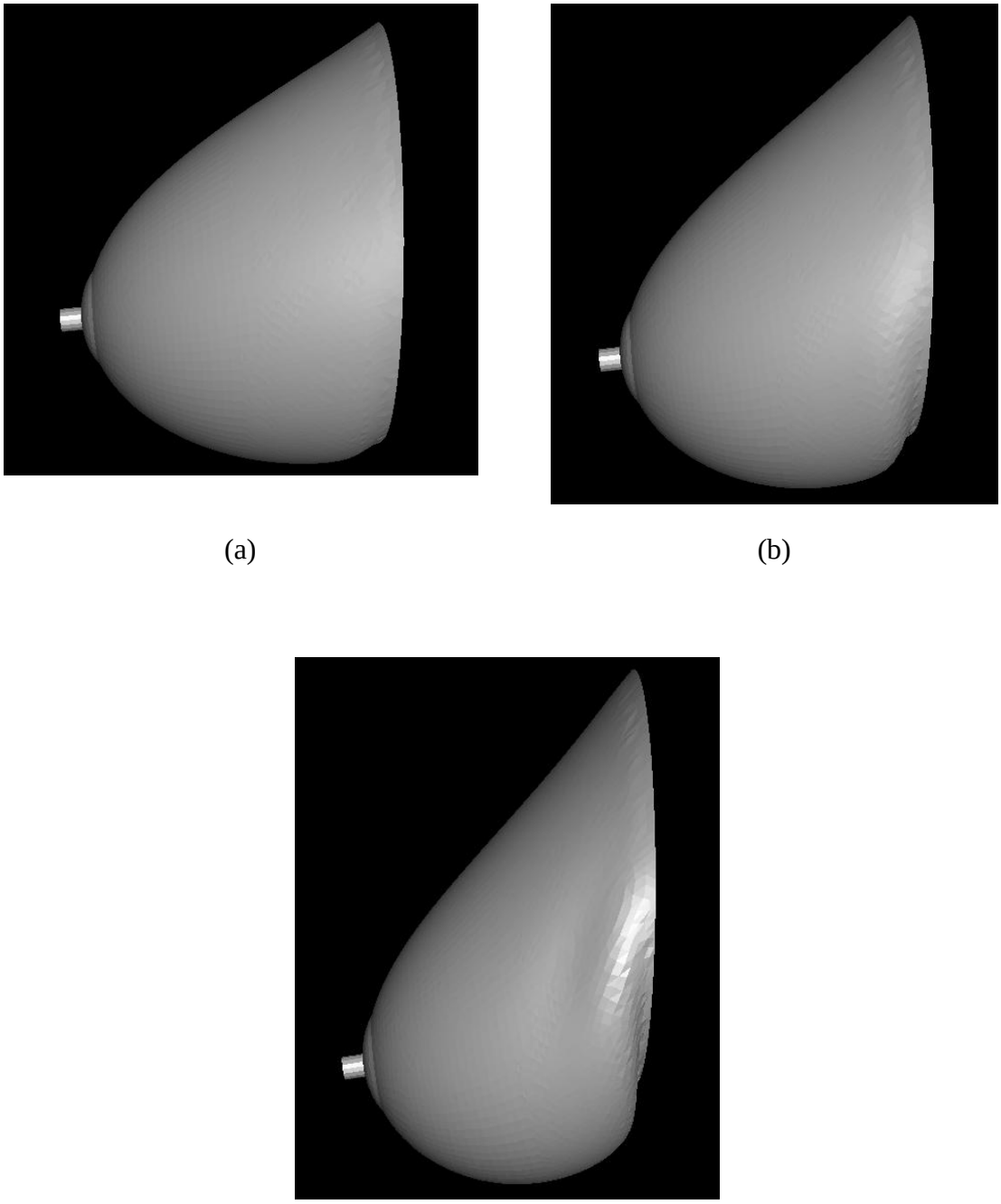

Figure 6.28. Side views of deformed geometries of the breast models. Mooney-Rivlin parameters of the breast tissue: (a) $C_{10} = C_{01} = 200$ Pa, (b) $C_{10} = C_{01} = 100$ Pa, and (c) $C_{10} = C_{01} = 50$ Pa. The neo-Hookean skin modulus $C_{10} = 2000$ Pa.

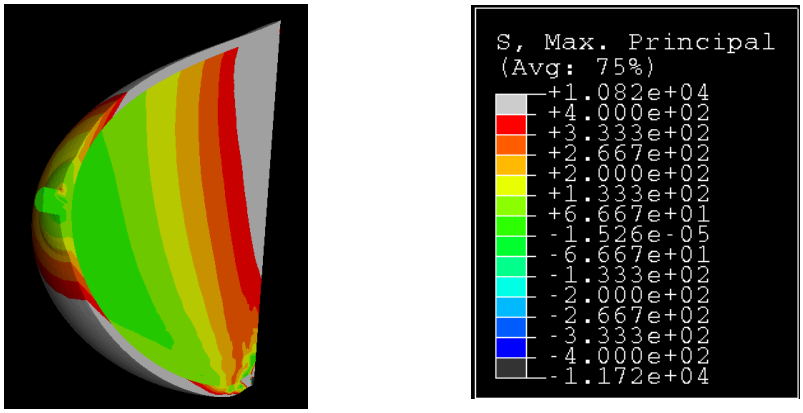

(a)

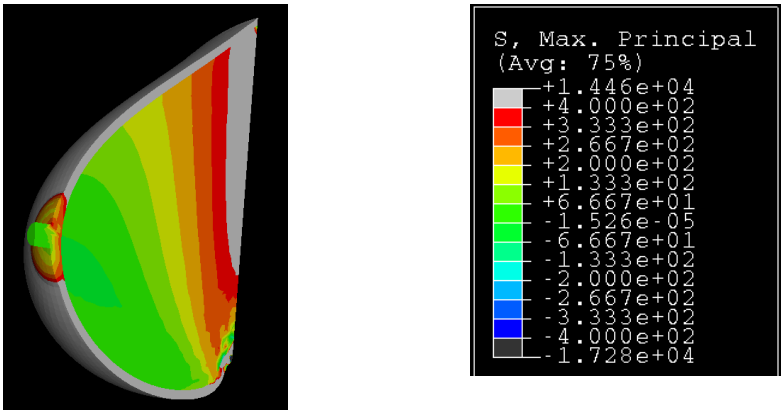

(b)

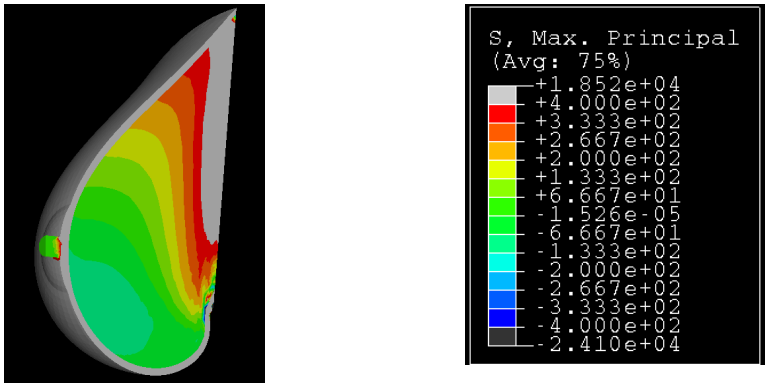

(c)

Figure 6.29. Variation of maximum principal stress in the breast models shown in sagittal cross-section. Mooney-Rivlin parameters of the breast tissue: (a) $C_{10} = C_{01} = 200$ Pa, (b) $C_{10} = C_{01} = 100$ Pa, and (c) $C_{10} = C_{01} = 50$ Pa. The neo-Hookean skin modulus $C_{10} = 2000$ Pa.

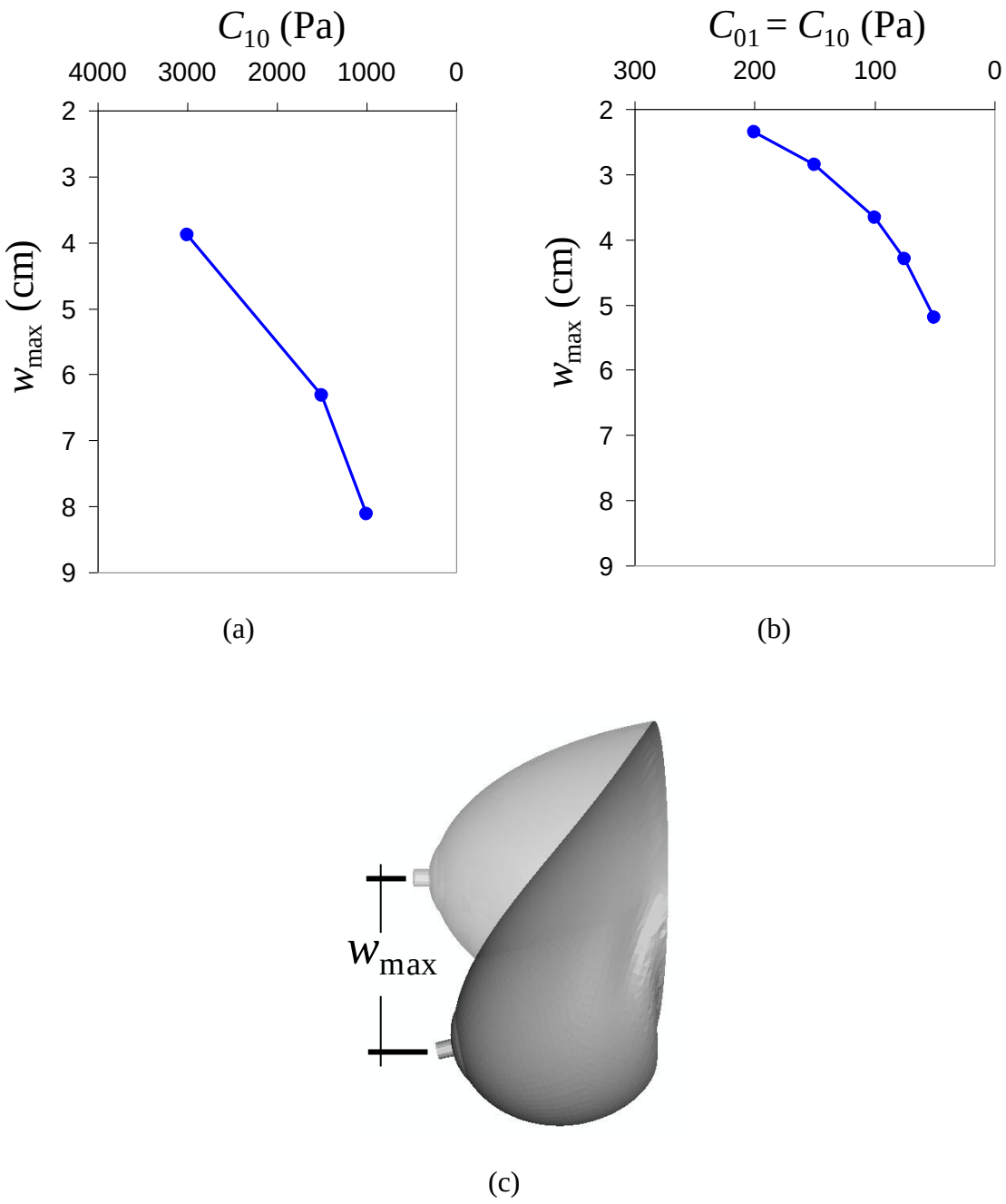

Figure 6.30. The effect of (a) skin stiffness and (b) breast firmness on the (c) maximum nipple displecement.

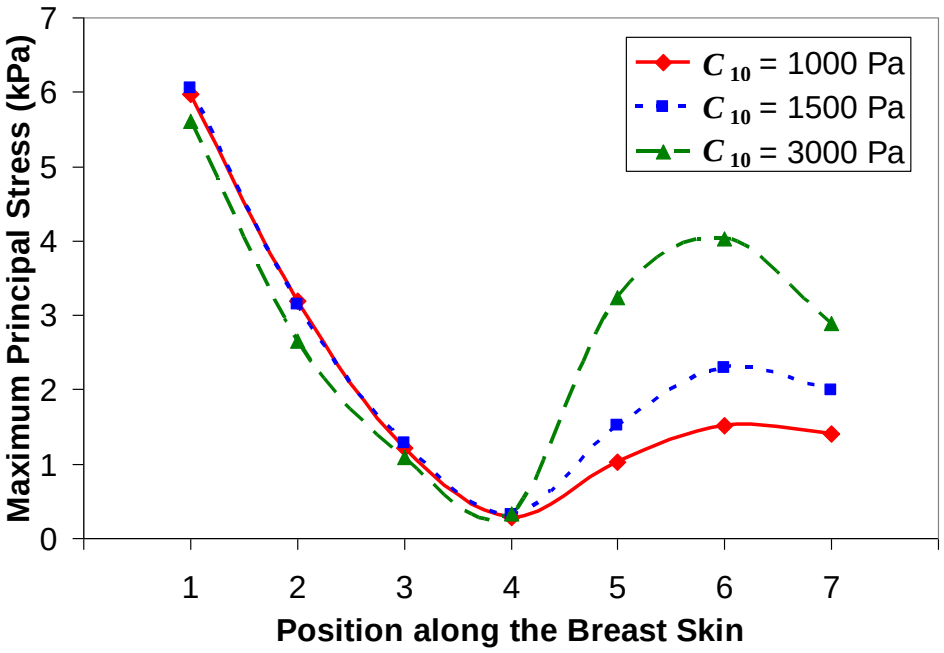

(a)

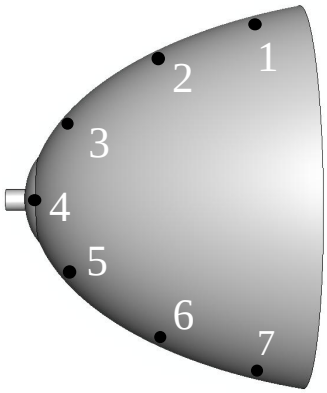

(b)

Figure 6.31. The effect of skin stiffness on the variation of (a) maximum principal stress (b) along the breast skin.

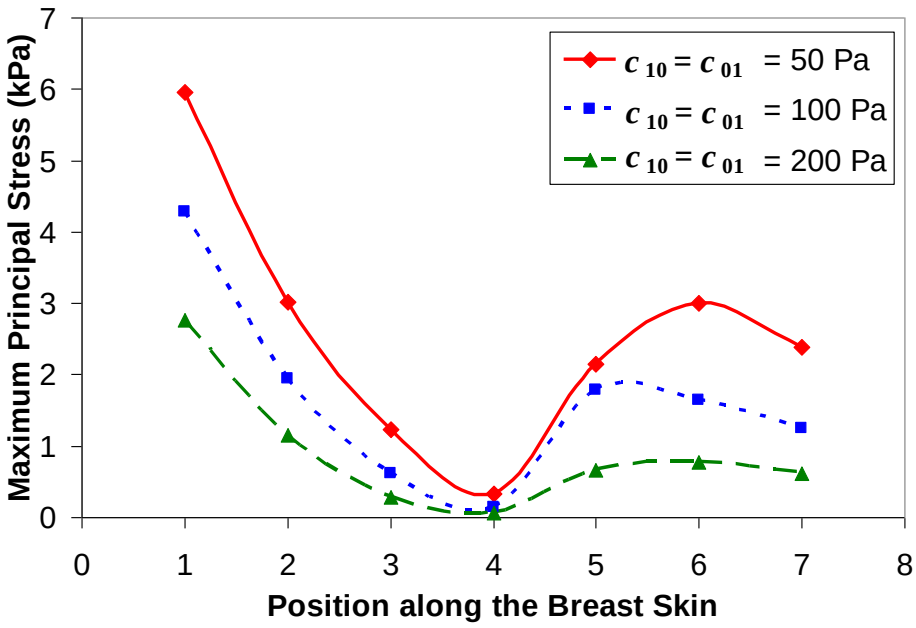

(a)

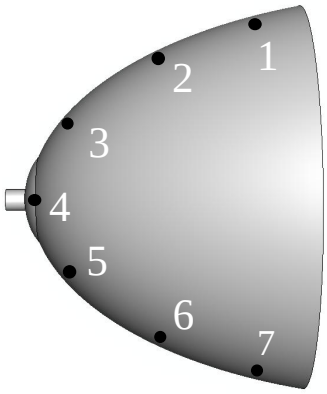

(b)

Figure 6.32. The effect of breast firmness on the variation of (a) maximum principal stress (b) along the breast skin.

6.4 COMSOL Multiphysics Simulations

In order to test our results, we also used a different commercially available software, COMSOL Multiphysics [*COMSOL*, 2005]. COMSOL Multiphysics is a general purpose software for solving problems that are based on partial differential equations (PDEs). COMSOL Multiphysics uses FEM for solving PDEs, and one of its advantages consists in the possibility of assigning different PDEs to different geometrical domains.

Using COMSOL Multiphysics, we represented breast by a body with two domains. We modeled the breast tissue by a continuous material, and the PDEs for a linear elastic shell were employed to simulate the overlying skin. As in ABAQUS simulations (Section 6.3), the behavior of the breast tissue was modeled by a homogeneous, isotropic, Mooney-Rivlin material. To study the effect of skin stiffness on the breast form, we chose the Young's modulus of the skin layer to be E = 2500 Pa and progressively decreased this value by 500 Pa in the subsequent simulations. In these simulations, the Mooney-Rivlin parameters of the breast tissue were $C_{10} = C_{01} = 80$ Pa. Two examples of the deformed breast shapes are given in Figure 6.33.

While the parameters of the ABAQUS and COMSOL Multiphysics simulations were somewhat different, the obtained results are quite similar and the same conclusions can be drawn. For example, Figure 6.33 suggests that, all the other parameters being the same, the breast with a more elastic skin is expected to be higher. Note that the slight "rippling" on the breast surface in Figure 6.33 is not mechanical, but rather the result of the graphical representation in COMSOL Multiphysics.

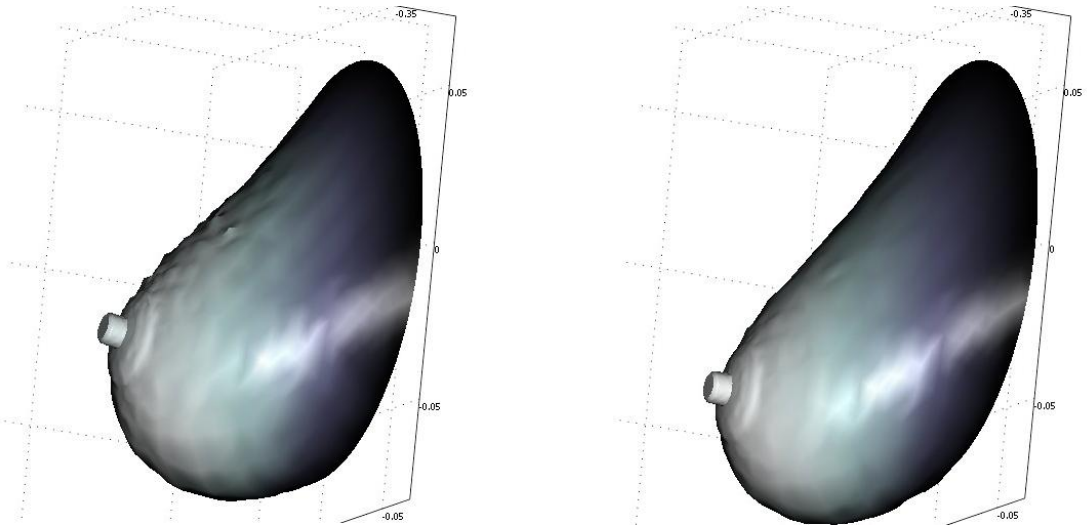

(a) (b)

Figure 6.33. Deformed geometries of the breast model. Simulations performed using COMSOL Multiphysics code. The skin Young's modulus is (a) E = 2500 Pa and (b) E = 1000 Pa. Mooney-Rivlin parameters of the breast tissue C_{10} = C_{01} = 80 Pa in both simulations.

6.5 Scaling of Breast Deformation

The forms produced by our numerical models (Figures 6.14 – 6.16, 6.20, 6.21) were encouraging because they closely resembled the forms of female breasts, but we were concerned because the magnitude of the moduli required to produce simulations with the proper forms (~ 10^2 Pa) were considerably less than the moduli reported in the literature (~ 10^3 to 10^5 Pa) [*Krouskop et al.*, 1998; *Tanner et al.*, 2001; *Roose et al.*, 2006a]. Below, we present a simple scaling analysis to evaluate this situation.

Consider a breast as a hemi-ellipsoidal beam (not necessarily thin) of length L cantilevered from a rigid substrate (Figure 6.34) and made of Mooney-Rivlin material. We will assume the beam (breast) is loaded by its own weight. The stress shearing the beam scales as

$$\sigma \sim \frac{\rho g V}{A} \tag{6.5.1}$$

where $V \sim Lr^2$ is the breast volume, $A \sim r^2$ is the breast area in the vertical cross section, L is the breast size (e.g., beam length), and r is the radius of breast base.

Breasts vary considerably in form, but considering the anatomical drawings in Figures 6.1 and 6.2 as well as typical breast shapes shown in [*Schider*, 1954] (Figure 6.1), we see that $L \approx r$. Therefore, according to (6.5.1),

$$\sigma \sim \rho g r \tag{6.5.2}$$

Likewise, the maximal breast displacements (usually of the breast nipple) in those pictures is roughly $w_{max} \sim r$, so that the corresponding strain scales as

$$\gamma \sim w_{\max} / r \sim \tan\alpha \sim 1 \tag{6.5.3}$$

According to (2.3.11),

$$\sigma \sim 4\gamma C \tag{6.5.4}$$

where C is a Mooney-Rivlin modulus and, for simplicity, we assumed that the Mooney-Rivlin moduli are of the same order ($C_{01} \sim C_{01} \sim C$).

Substituting (6.5.2) and (6.5.3) into (6.5.4), we finally obtain

$$C \sim \frac{1}{4}\rho g L \tag{6.5.5}$$

It seems reasonable to assume that L = 5 cm, $\rho = 10^3$ kg/m^3, and g = 10 m/sec^2 (we used the same values in numerical analysis). Then, (6.5.5) provides an estimate of the modulus: C = (1/4) 10^3 10 (5×10^{-2}) Pa $\approx 10^2$ Pa.

This value confirms our numerical results about the order of magnitude of the effective modulus of the breast.

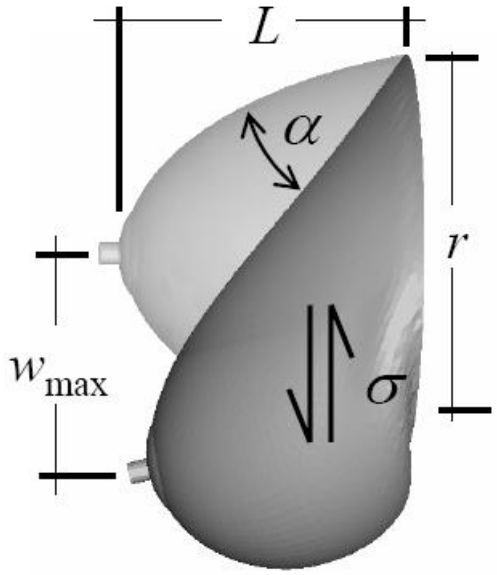

Figure 6.34. Schematic of the hemi-ellipsoidal breast cantilevered from a rigid substrate used in scaling of breast deformation.

6.6 Conclusions

Our results show that the stiffness of skin and the constitutive parameters of the breast tissue are important factors affecting breast shape. For example, a relatively high skin modulus is what causes a higher breast form, whereas low breast firmness results in lowering the breast (Figure 6.29). The skin modulus becomes more important to the overall breast form as the modulus of the breast tissue decreases.

The entire breast skin is in tension. The maximum tensile stress in the skin decreases with the firmness of the breast tissue and increases with the skin stiffness below the nipple. This is a peculiar behavior, because in both cases the breast position tends to be higher. In other words, the tension in the skin does not necessarily correlate with the fact that the breast is lower or higher. Currently, adjusting the skin tension (i.e., by removing or adding a part of the skin) is a mainstream surgical procedure. Hence, this observation may be important for planning of reconstruction and augmentation surgeries. One may even consider measuring the skin tension in the future as an objective way of surgery planning, which is not unthinkable from the engineering stand point.

On the other hand, the stress state in the breast tissue is more complex. The part of the tissue attached to the chest is in tension which gradually decreases and becomes compression in the part of the breast close to the nipple. When the implant is placed, the stress state may change from compression to tension in some areas of the breast (Figure 6.35) which may result in ruptures in the tissue. Therefore, this may also be an important observation for planning of reconstruction and augmentation surgeries.

The constitutive parameters reported in the literature for the breast tissue produced unrealistic breast shapes. Comparing breast deformations with observations is

an existing calibration technique for obtaining the breast tissue properties. Since our modeling produced realistic breast shapes, which can be confirmed by comparing our results with the typical breast types [*Schider*, 1954] (Figure 6.1), this indicates that as a result of our simulation, we obtained a more realistic estimate of Mooney-Rivlin parameters of the breast tissue than those available in the literature That is, for the typical neo-Hookean parameter of the skin tissue in the order of $C_{10} \sim 10^3$ Pa ($E \sim 10^4$ Pa), the Mooney-Rivlin parameters of the breast tissue $C_{10} \sim C_{01} \sim 10^2$ Pa. This is at least one to two orders of magnitude smaller than the published values. Our scale analysis also confirms this numerical result.

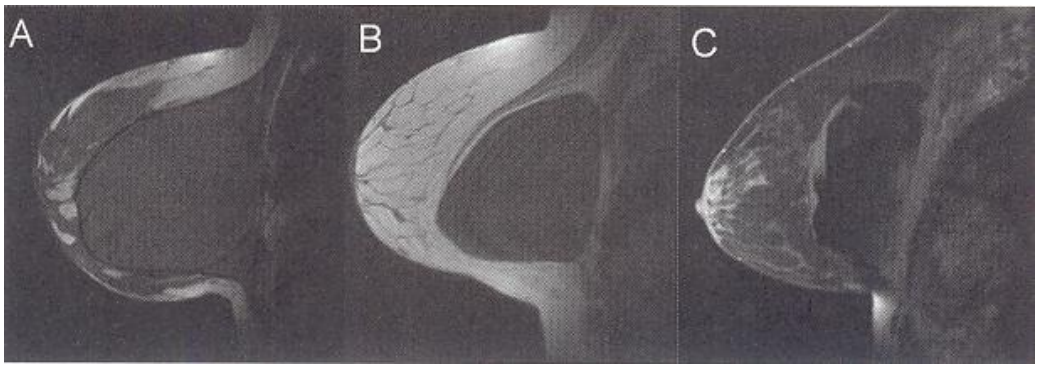

Figure 6.35. Breast implants are shown in three different patients [*Wu et al.*, 2006]. None of them has extra-capsular rupture due to breast augmentation. However, implant emplacements have likely changed the state of stress in the breast tissue from compression to tension, at least in some places (especially in case A), which may promote breast tissue rupture in the future.

CHAPTER VII

SUBDURAL HEMATOMA CAUSED BY VENTRICULOSTOMY: A SIMPLE MECHANICAL MODEL

7.1 Introduction

Subdural hematoma is a collection of blood over the brain surface (Figure 7.1a) between the dura and arachnoid matters (Figure 7.1b). It is a common brain disorder that frequently requires surgical intervention. Acute subdural hematoma is caused by rupturing of the bridging veins which pass from the brain to dura mater (Figure 7.2). The cranial ends of bridging veins are firmly connected to the dura, and cerebral ends are attached to the movable brain. The most fragile part of these veins is their portions in the subdural space [*Yamashima and Friede,* 1984]. Subdural space is defined as a potential space between the dura and arachnoid. Under normal conditions, dura and arachnoid (Figure 7.1b) are fixed to each other. When meningeal layers are forced to separate, delamination occurs along the dura-arachnoid interface (Figure 7.1b), which is the weakest plane of the meninges within the innermost layers of the dura. Consequently, even though there is no preexisting cavity, the subdural space can be created by straining the meninges [*Haines et al.*, 1993; *Nolte,* 2002].

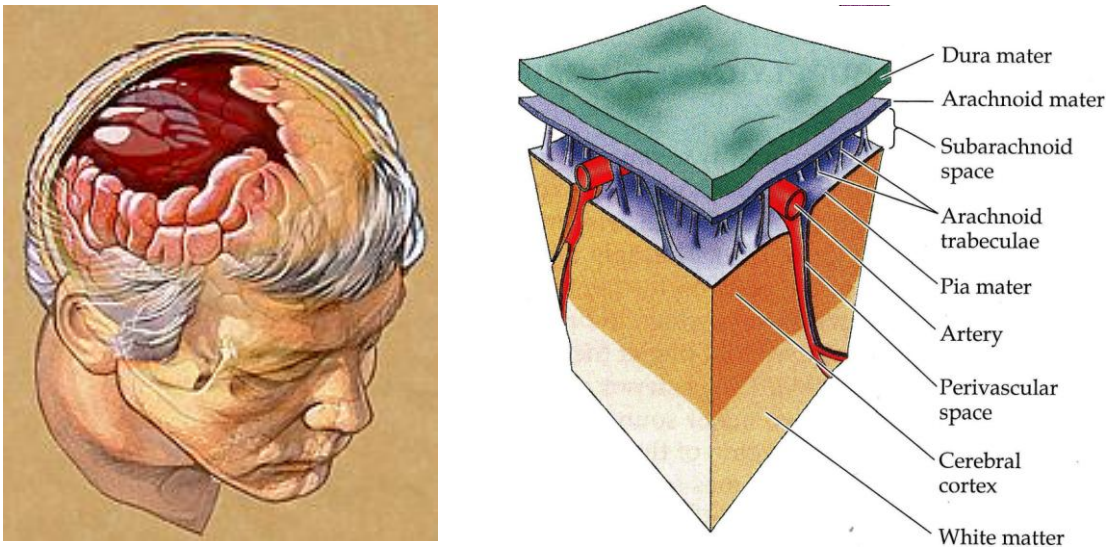

(a) (b)

Figure 7.1. Subdural hematoma. (a) View from above of an intracranial hematoma (subdural, subarachnoid, or epidural) shown as a pool of blood embedded in the brain [http://www.bcillustration.com]. (b) Principal parts of human brain adjacent to the skull [*Purves et al.*, 1997].

Figure 7.2. Specimen of the brain with dura mater showing bridging veins [http://www.acsu.buffalo.edu/~lcscott/shakenbabysyndrome.html].

The falx cerebri prevents the lateral movement of the brain, yet the brain is free to move in other directions. The movement of the brain within the cranial cavity may lead to traction on the meningeal layers. As a result, the dura-arachnoid interface (Figure 7.1b) may split to form the subdural space. This splitting may extend to the bridging veins (Figure 7.2), causing them to tear [*Yamashima and Friede*, 1984]. According to the contemporary view [e.g., *Nolte*, 2002; *Kumar et al.*, 2005], subdural hematoma may appear as blood from the ruptured veins filling the subdural space (Figure 7.3). As the subdural hemotama expands, the brain deforms and displaces (Figure 7.4). Depending on the location of the hematoma, herniations (displacements of brain material from one cranial compartment to another) can develop (Figure 7.5) and damage brain tissue [*Nolte*, 2002]. Treatment of both acute and chronic subdural hematomas often involves surgical craniotomy to decompress the subdural space and to remove blood clots (Figure 7.6).

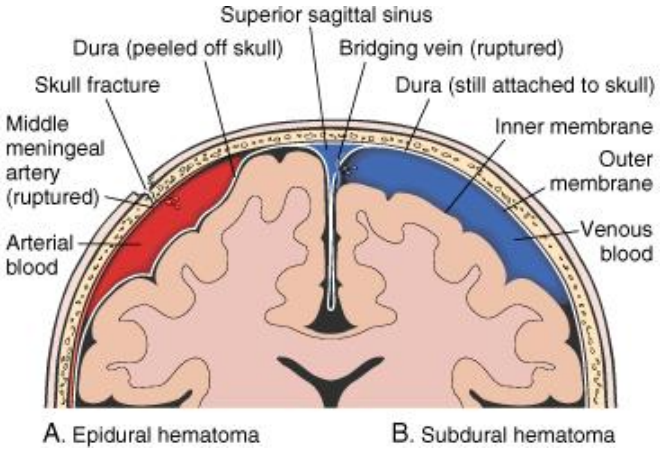

Figure 7.3. Schematics of epidural (a) and subdural (b) hematomas [*Kumar et al.*, 2005].

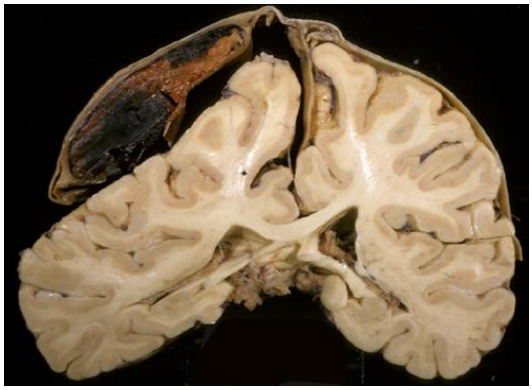

(a)

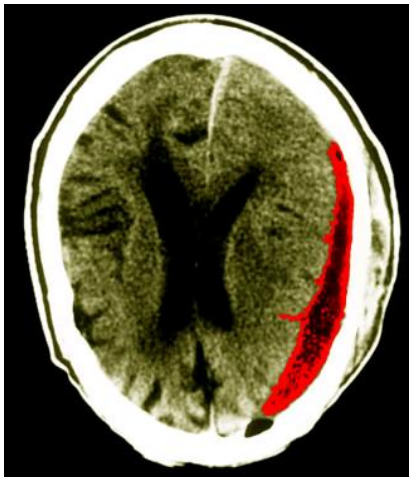

(b)

Figure 7.4. (a) Brain displacement caused by subdural hematoma [*Agamanolis*, 2007]. (b) CT scan of acute subdural hematoma [www.scottcamazine.com]. Ventricles are compressed and shifted laterally.

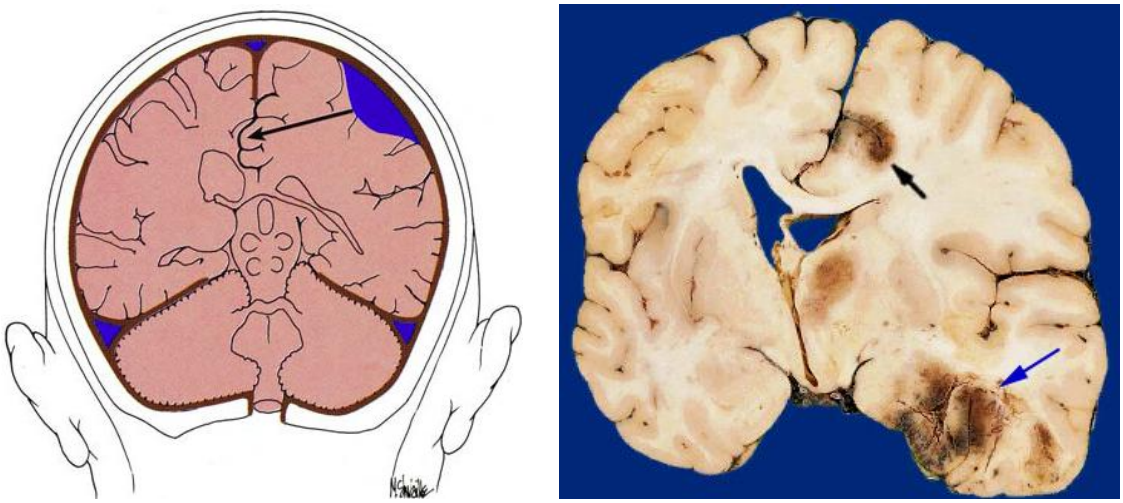

(a) (b)

Figure 7.5. (a) Herniation from one side of the falx cerebri to another as a result of subdural hematoma [*Nolte*, 2002]. (b) Subfalcine herniation associated with a one-sided cerebral mass lesion when the medial surface of the affected hemisphere is pressed against the firm falx cerebri and then herniates beneath it [*Ellison et al.*, 1998]. Note the gyri on the right compressed and flattened by subdural hematoma, which resulted in subfalcine herniation of the cingulate gyrus, with a secondary hemorrhagic infarction above that (black arrow). A midline shift from right to left is clearly seen.

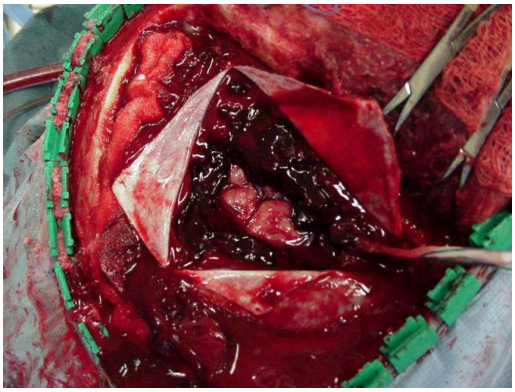

(a)

(b)

Figure 7.6. (a) Intraoperative photograph showing evacuation of an acute subdural hematoma [*Meagher and Young*, 2006], which is (b) currant jelly–like in appearance [http://www.geocities.com/drweightloss/neurosurgery/neurosurgery.html].

Subdural hematomas usually occur as a result of trauma [*Gennarelli and Thibault*, 1982; *Lee and Haut*, 1989; *Huang et al.*, 1999; *Goldsmith*, 2001]. Yet, it is well recognized that ventricular decompression can also result in subdural bleeding [*Grant et al.*, 1997; *Hellwig et al.*, 2005]. Thus, acute subdural hematoma may be caused by overdrainage – rapid drainage of cerebrospinal fluid (CSF) – during ventriculostomy operations. Although, there are many different shunt types designed to prevent overdrainage, subdural hematoma is still one of the major complications of and treating long standing hydrocephalus [*Koizumi et al.*, 1987; *Pudenz and Foltz*, 1991; *Grant et al.*, 1997; *Fukuhara et al.*, 2000; *Oi et al.*, 2000; *Chabrerie and Black*, 2002; *Ropper*, 2003; *Hellwig et al.*, 2005; *Kamel et al.*, 2006] as illustrated in Figure 7.7. For this reason, understanding the mechanism of subdural hematoma is important for development of more effective treatments that involve the ventriculostomy operations.

Figure 7.7. Bilateral subdural hematomas and dilated ventricular system [*Downie*, 2001]. An intraventicular shunt was inserted to treat chronic hydrocephalus. The rapid reduction in the hydrocephalus led to shrinkage of the brain from the cranial vault, resulting in rupture of dural veins and the subdural hematomas [*Downie*, 2001].

In this work, we develop a simple poroelastic model of ventriculostomy operation. Previously, several authors have developed mechanical models of hydrocephalus and shunting representing the brain tissue as a poroelastic material [e.g., *Nagashima et al.*, 1987; *Kaczmarek et al.*, 1997; *Tenti et al.*, 1999; *Levine*, 1999, 2000; *Taylor and Miller*, 2004; *Smillie et al.*, 2005; *Wirth and Sobey*, 2006; *Sobey and Wirth*, 2006]. In particular, *Levine* [1999] and *Smillie et al.* [2005] employed a spherically-symmetric brain model and obtained results that were in agreement with clinical observations. *Levine* [1999] incorporated the fluid absorption within the brain parenchyma in his model and compared different hypothesizes with clinical features of normal pressure hydrocephalus to understand how ventricular enlargement occurs

without excess intracranial pressure. In addition, *Levine* [2000] employed the brain model of *Levine* [1999] and showed that the absence of ventricular enlargement in pseudotumor cerebri (PTC) is consistent with the hypothesis that PTC is caused by reduced absorption of CSF, either from increased outflow resistance at the arachnoid villi or from blockage of the dural venous sinuses.

In the model of *Smillie et al.* [2005], the CSF, produced in the ventricles in the healthy brain, initially flows through the brain and the sylvius aqueduct into the subarachnoid space. While in the previous works, the aqueduct had been conceptually introduced as well [e.g., *Kaczmarek et al.*, 1997; *Levine*, 1999, 2000], *Smillie et al.* [2005] explicitly accounted for fluid flow in the aqueduct in their mathematical model of the human brain (Figure 7.8). This allowed them to simulate non-communicating hydrocephalus by blocking the CSF flow in the aqueduct. Because in their model the CSF production continues, the pressure in the ventricles grows, hydrocephalic brain deforms, and most of the flow occurs through the porous parenchyma into the subarachnoid space, where the CSF is absorbed into the bloodstream through the arachnoid villi. Their model is shown in Figure 7.8 and geometrically is similar to the model by *Kaczmarek et al.* [1997], who employed cylindrical symmetry. In both models, the size (thickness) of the subarachnoid space is considered negligible, and the authors simply assume that this is an infinitesimally thin interface or a boundary where the CSF absorbs.

To describe this absorption, *Smillie et al.* [2005] considered that the CSF absorption in the subarachnoid space occurs in the arachnoid villi. These are small granulations of the arachnoid that protrude into the dura mater and enable the CSF to pass into the bloodstream where it absorbs. While CSF production is pressure independent, the

rate of absorption depends upon the difference between the intraventricular and blood pressures [*Albeck et al.*, 1991; *Bradbury*, 1993]. As noted by *Smillie et al.* [2005], the structure of the arachnoid villi is such that even in the unlikely event of venous blood pressure exceeding the intraventricular pressure, no back flow will take place from the blood into the CSF system, so that the villi effectively act as a one-way valve for removal of CSF. Accordingly, they employed expression

$$Q_b = \begin{cases} \dfrac{p_b - p_s}{R\eta} & \text{if} \quad p_b \geq p_s \\ 0 & \text{if} \quad p_b < p_s \end{cases} \tag{7.1.1}$$

for the rate of absorption, where Q_b is the CSF volume absorbed from the subarachnoid space into the blood per unit time, p_b is the CSF pressure in the subarachnoid space (or in the brain parenchyma near the pial boundary), p_s is the sagittal sinus (blood) pressure, η is the CSF viscosity, and R is a coefficient that models the resistance to the CSF flow in the arachnoid villi. All parameters and their values used in this work are listed in Table 7.1 at the end of this section.

Expression (7.1.1) can be given a simple physical meaning, that is, flow of viscous liquid (CSF) between the subarachnoid space and the blood system via the system of arachnoid villi that are visualized as flow conduits. *Smillie et al.* [2005] also evaluated the value of constant R appearing in this expression. For this purpose, they assumed that in normal physiological conditions, the rate of CSF absorption in the subarachnoid space is equal to the rate of CSF production in the ventricles**,** Q_v. They employed the production rate $Q_v \approx 500$ ml/day in human adults that is relatively well known and independent of intraventricular pressure [*Bradbury*, 1993]. Using (7.1.1) and

normal physiological value of $p_b - p_s = 440$ Pa [*Smillie et al.*, 2005], they calculated $R \approx 8.5\times10^{13}$ m^{-3}. This is consistent with the observations on healthy subjects by *Albeck et al.* [1991] who measured the rate of fluid absorption with varying intracranial pressure and determined $R = 7\times10^{13} - 9\times10^{13}$ m^{-3}.

Smillie et al. [2005] utilized expression (7.1.1) in a mechanical model as the rule of CSF absorption from the subarachnoid space. Previous authors, had simply taken the fluid pressure p_b to be fixed and equal to the blood pressure, p_s [*Nagashima et al.*, 1987; *Kaczmarek et al.*, 1997; *Levine*, 1999, 2000], which corresponds to the extreme of zero resistance of the arachnoid villi, that is, $R = 0$ in (7.1.1). The absorption rule (7.1.1) was later used in numerical simulations of hydrocephalus [*Wirth and Sobey*, 2006; *Sobey and Wirth*, 2006].

Levine [1999] considered the trans-parenchymal absorption of CSF when a part of the fluid is absorbed by capillaries in the brain before reaching the subarachnoid space. To describe the CSF absorption inside the brain tissue, he used Starling's law, according to which the transcapillary exchange of interstitial fluid and blood plasma in parenchyma is linearly related to the net colloid osmotic and hydrostatic pressures. Assuming that the blood pressure, p_s, and the net colloid osmotic pressure remain constant, *Levine* [1999] introduced the volumetric absorption rule, $q_p = k_p(p - p_s)$, where q_p is the amount (volume) of fluid absorbed into the blood per unit volume of parenchyma per unit time, p is the local pressure of the interstitial fluid, and k_p is the coefficient of absorption, which is assumed to be a parameter of the parenchyma. This volumetric absorption rule is similar to (7.1.1), which also includes "Starling" component along with the

hydrodynamic resistance to the viscous fluid flow. The important difference is, however, that (7.1.1) assumes the surface absorption, that is, the all absorption occurs after fluid percolates through the parenchyma. Currently, it is not clear what part of interstitial fluid is absorbed in parenchyma before reaching the subarachnoid space [*Albright et al.*, 1998; *Levine*, 1999; *Weller*, 2005]. While warranted in carefully studied cases, such as that considered in *Levine*'s [1999] work, it is difficult to evaluate the importance of volumetric absorption in general. In the majority of mechanical models of hydrocephalus [*Hakim et al.*, 1976; *Nagashima et al.*, 1987; *Kaczmarek et al.*, 1997; *Tenti et al.*, 1999; *Levine*, 2000; *Tenti et al.*, 2000; *Taylor and Miller*, 2004; *Sivaloganathan et al.*, 2005a; *Sivaloganathan et al.*, 2005b; *Smillie et al.*, 2005], the volumetric absorption has been ignored. *Wirth and Sobey* [2006] and *Sobey and Wirth* [2006] included it in their numerical simulations and concluded that the effect of the volumetric absorption on hydrocephalus is undeniable. We also do not consider the volumetric absorption of the interstitial fluid in parenchyma, but discuss its effect in the end of the chapter.

In this work, we model the appearance of subdural hematoma caused by a ventriculostomy operation such as shunt insertion. Similar to the preceding works on hydrocephalus and pseudotumor cerebri of *Hakim et al.* [1976], *Nagashima et al.* [1987], *Kaczmarek et al.* [1997], *Tenti et al.* [1999], *Levine* [2000], *Taylor and Miller* [2004], *Smillie et al.* [2005], and *Fard et al.* [2007], we assume that CSF is completely produced in the ventricles and entirely absorbed in the subarachnoid space. We consider that prior to the operation, non-communicating hydrocephalus is fully developed owing to the obstruction of the sylvius aqueduct and that the CSF flow in the brain is in the steady-state regime. As noted by *Hakim et al.* [1976], the CSF pressure in the subarachnoid

space is not fully transmitted to the subdural space material in normal brain since the walls of subarachnoid space (i.e., pia and arachnoid) are connected by the arachnoid trabeculae (Figure 7.1b). Accordingly, we treat the subarachnoid space as a brain boundary, but introduce a mechanical traction (stress) boundary condition, which accounts for both the effects of the pressure in the subarachnoid space and deformation of trabeculae.

During the ventriculostomy operation, the pressure in the ventricles is reduced, and the brain pial boundary moves inwards, so that tension develops in the arachnoid trabeculae as they deform. Therefore, it is conceivable that the combined load on the arachnoid, resulting from the CSF pressure in the subarachnoid space and the tension created by the trabeculae, is tensile. Then, the normal traction transmitted by the arachnoid to the subdural space material is also tensile and may cause the separation along the dura-arachnoid interface (Figure 7.9), which we interpret as an onset of subdural hematoma.

In this work, we consider two stages of the hydrocephalus treatment. The first stage corresponds to a time scale of several hours of the ventriculostomy operation (shunt insertion) and immediately after. We simulate this stage by rapidly decreasing pressure in the ventricular cavity. The CSF flow in the brain tissue is time dependent, and because of the relatively low permeability of brain material, appreciable change of pressure distribution in brain takes longer time. Due to the fast change of the pressure in the ventricles, the pressure distribution within the brain parenchyma does not change significantly, and the brain response to ventriculostomy is mostly elastic. The second stage corresponds to a much greater time scale of the post-operative period and long-term

patient management. We model this stage by assuming that brain eventually reaches a new steady-state with both the CSF pressure and production rate reduced as a result of the ventriculostomy operation. Now, due to the noticeable change of the pressure distribution in the parenchyma, poroelastic effect contributes to the brain response to ventriculostomy and may be rather significant. Considering these stages allows us to introduce somewhat extreme, yet realistic cases, and obtain results in closed form.

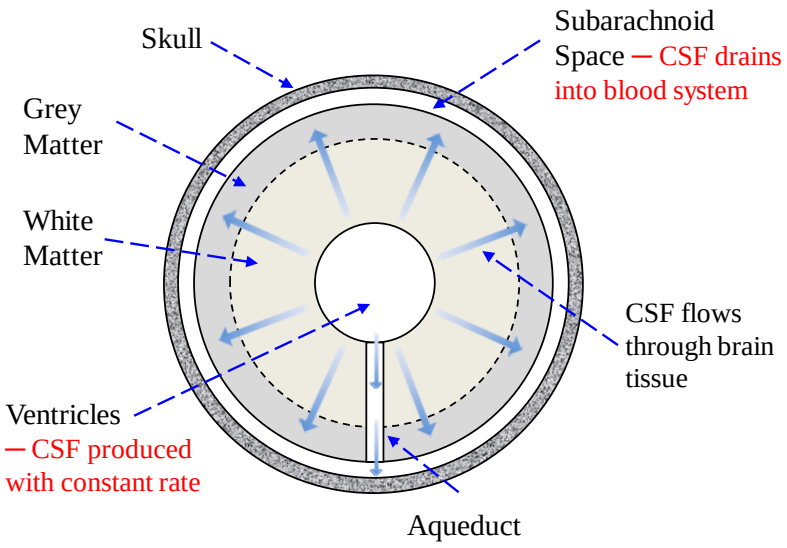

Figure 7.8. Brain model of *Smillie et al.* [2005].

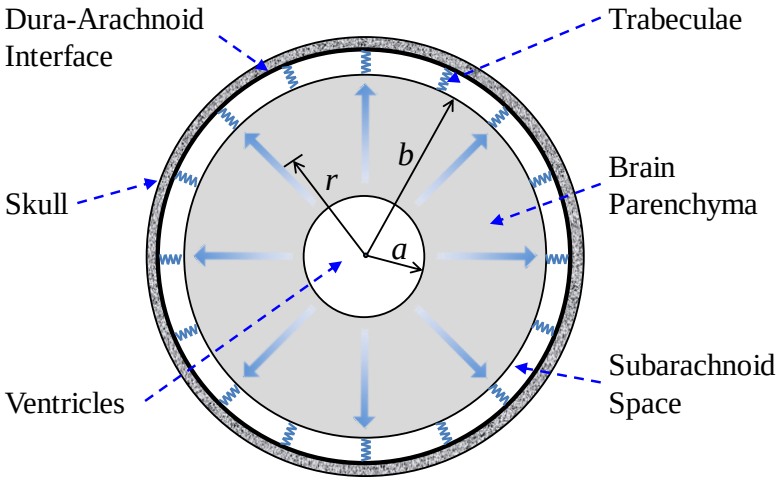

Figure 7.9. A simplified model of the human brain.

Table 7.1. Symbol definitions and parameter values

Symbol	Definition	Value
a	radius of ventricle	50 mm
b	radius of subarachnoid space	100 mm
B_v	parameter in eq. (7.5.3)	
B	Skempton's coefficient of brain tissue	1
E_u	undrained Young's modulus of brain tissue	10^4 Pa
E	drained Young's modulus of brain tissue	10^3 Pa
h	absorption parameter in eqs. (7.2.8), (7.2.9)	10^{-13} m
K	bulk modulus of brain tissue	
M	Biot's Modulus of brain tissue	∞
$p^0(r)$	distribution of pressure at the initial moment	
$p^i(r, t)$	distribution of pressure during ventriculostomy	
$p^\infty(r, t)$	distribution of pressure in long-term post-operative stage	
$p_b(t)$	CSF pressure in the subarachnoid space	
$p_a(t)$	CSF pressure in the ventricle	
p_s	sagittal sinus (blood) pressure	650 Pa
Q_b	rate of CSF absorption in the subarachnoid space	
Q_v	rate of CSF production before ventriculostomy	5.8×10^{-9} m^3/sec
Q_a	rate of CSF production after ventriculostomy	
R	resistance of CSF flow in the arachnoid villi	8.5×10^{13} m^{-3}
$u(r, t)$	distribution of displacement in the brain	
u_0	amount of displacement necessary to bring the arachnoid trabeculae to the unstreched state	
u_b	brain displacement at subarachnoid space	
V_{sa}	volume of subarachnoid space	
α	Biot's coefficient	1
κ	permeability of brain tissue	10^{-14} m^2
η	dynamic viscosity of CSF	10^{-3} Pa·sec
ϕ	porosity of brain parenchyma	20%
β	drained poroelastic parameter $(1 + \nu)/[(1 - \nu)3K]$ in (7.2.1), (7.2.2)	
$\sigma_{rr}^0(r, t)$	distribution of initial total radial stress in the brain	
$\sigma_{rr}^i(r, t)$	distribution of total radial stress in the brain during ventriculostomy	
$\sigma_{rr}^\infty(r, t)$	distribution of total radial stress in the brain in long-term post-operative stage	
σ_t	tensile strength of subdural space material	
ν	drained Poison's ratios of brain tissue	0.35
ν_u	undrained Poison's ratios of brain tissue	0.5
k	stiffness of the arachnoid trabeculae	
δ_0	average thickness of subarachnoid space at $t = 0$	
$\Gamma = b/a$	ventricular aspect ratio	2

7.2 Mathematical Model

The framework of the theory of poroelasticity has been initially developed to study deformation processes coupled with fluid flow in geomaterials [*Biot*, 1941; *Rice and Cleary*, 1976; *Detournay and Cheng*, 1993; *Wang*, 2002]. While mathematical equations used in brain biomechanics are essentially identical, below we employ the physical interpretation of poroelastic behavior of brain material offered by *Levine* [1999, 2000]. He considers the parenchyma as a porous solid permeated by two networks of fluid filled channels. The solid matrix consists of various brain tissue elements and that part of intracellular water which is not exchangeable with interstitial fluid when the brain is mechanically stressed. The first fluid network consists of the interstitial fluid in the interconnected, extracellular channels and includes that portion of the intracellular water which is exchangeable with interstitial fluid when the brain is subjected to mechanical load. The second fluid network consists the blood, mostly in the capillaries and veins.

It is interesting to point out that *Levine* [1999, 2000] suggested treating the parenchyma similarly to poroelastic soil that contains both water and pockets of air. In this analogy, the solid matrix of the parenchyma corresponds to the solid particles of the soil, the interstitial fluid corresponds to the water in the soil, and the blood is analogous to the pockets of air. He argued that although all of the solid and fluid elements in the brain are practically incompressible, the intravascular blood can be rapidly transferred extracranially, and the interstitial fluid is more slowly exchangeable with the extracranial space by absorption into the bloodstream. Therefore, the correspondence between the air in the soil and the blood in the cerebral vessels of the brain appears because both air and

blood show a relatively instantaneous compressibility in response to a mechanical load [*Levine*, 1999, 2000].

As a first approximation, we ignore the difference between grey and white matter and consider spherically symmetric brain model (Figure 7.9). The brain material is located at $a < r < b$, where r is the spherical coordinate, a is the radius of the ventricular cavity of a hydrocephalic brain, and b is the radius of the subarachnoid space (Figure 7.9).

Equilibrium condition in terms of displacements, $u(r, t)$, in the case of radial symmetry for poroelastic medium can be written as [*Detournay and Cheng*, 1993]

$$\frac{\partial}{\partial r}\left(\frac{1}{r^2}\frac{\partial}{\partial r}(ur^2)\right) = \alpha\beta\frac{\partial(p - p^0)}{\partial r} \tag{7.2.1}$$

where $\beta = (1 + \nu)/[(1 - \nu)3K]$, α is the Biot's poroelastic coefficient, K is the bulk modulus, ν is the Poisson's ratio of brain tissue, $p(r, t)$ is the CSF pressure distribution at time t, and $p^0(r) = p(r, 0)$ is the CSF pressure at the initial moment. We measure all pressures relative to the atmospheric pressure. The constitutive poroelastic relation is defined by [*Detournay and Cheng*, 1993]

$$\sigma_{rr} = \frac{1}{\beta}\frac{\partial u}{\partial r} + \frac{2\nu}{1-\nu}\frac{1}{\beta}\frac{u}{r} - \alpha(p - p^0) + \sigma_{rr}^0(r) \tag{7.2.2}$$

where $\sigma_{rr}(r, t)$ is the radial stress and $\sigma_{rr}{}^0(r) = \sigma_{rr}(r, 0)$ is the distribution of the initial stress. In poroelastic material, pressure distribution, $p(r, t)$, and volumetric strain,

$\varepsilon_v = \partial u/\partial u + 2u/r$, are related by the coupled diffusion equation [*Detournay and Cheng*, 1993]

$$\frac{1}{M}\frac{\partial p}{\partial t} + \alpha\frac{\partial}{\partial t}\left(\frac{\partial u}{\partial r} + 2\frac{u}{r}\right) = \frac{\kappa}{\eta}\left(\frac{\partial^2 p}{\partial r^2} + \frac{2}{r}\frac{\partial p}{\partial r}\right) \tag{7.2.3}$$

where κ is the permeability of the brain tissue, $M = (BK/\alpha)(1 - \alpha B)^{-1}$ is the Biot's modulus, and B is the Skempton's coefficient of brain tissue.

Equations (7.2.1), (7.2.2), and (7.2.3) connect three unknown functions, $u(r, t)$, $p(r, t)$, and $\sigma_{rr}{}^0(r, t)$. The initial displacements $u^0(r)$ can always be assumed zero everywhere in the brain. The initial pressure distribution, $p^0(r)$, can be reasonably constrained and will be discussed below considering CSF flow in brain as in porous medium. The initial stresses are generally not known, and we will discuss this situation later, as well. In any event, to complete the mathematical formulation of the problem, we still need to specify boundary conditions on the external, $r = b$, and internal, $r = a$, boundaries of the brain model (Figure 7.9). As well recognized, imposing appropriate boundary conditions is critically important for understanding hydrocephalus [e.g., *Tenti et al.*, 1999; *Levine*, 1999; *Smillie et al.*, 2005], pseudotumor cerebri [*Levine*, 2000], and subdural hematoma [*Hakim et al.*, 1976].

Before the ventriculostomy operation, the pressure boundary condition at $r = a$ can be defined as

$$-\frac{\kappa}{\eta}\frac{dp^0}{dr}\bigg|_{r=a} 4\pi a^2 = Q_v \tag{7.2.4}$$

This equation models the CSF inflow into the brain from the ventricles using the linear Darcy's law for fluid flow in porous medium [*Bear*, 1988; *Wang*, 2002]. Such a representation of brain tissue had been previously used by many investigators [*Nagashima et al.*, 1987; *Kaczmarek et al.*, 1997; *Kalyanasundaram et al.*, 1997; *Tenti et al.*, 1999; *Levine*, 1999, 2000; *Smillie et al.*, 2005; *Wirth and Sobey*, 2006; *Sobey and Wirth*, 2006].

We further assume that during ventriculostomy procedure, the pressure, $p_a(t)$, in the ventricles is either controlled by the surgeon or, at least, known. Then,

$$p(a,t) = p_a(t) \quad (t > 0) \tag{7.2.5}$$

where $p(r, t)$ is the distribution of CSF pressure in the brain. Similarly, the pressure in the subarachnoid space is denoted as $p_b = p(b, t)$, but it has to be defined as a result of the solution of the boundary value problem that will be formulated below. The subarachnoid space is thin compared to other brain layers, and in our model, it coincides with the external brain boundary, $r = b$. It is in mechanical equilibrium with the brain.

Following *Smillie et al.* [2005], we model CSF absorption from the subarachnoid space proportional to the difference between CSF and blood pressure as specified by (7.1.1). Some CSF, however, accumulates in the subarachnoid space as the brain boundary, $r = b$, deforms. This affects the CSF flow towards the brain boundary and the pressure boundary condition becomes coupled with brain deformation. Similar to *Smillie et al.* [2005], we use conservation of incompressible CSF to find this boundary condition.

Let the volume of subarachnoid space be $V_{sa}(t) = 4\pi b^2(\delta_0 + u_b)$, where δ_0 is the average thickness of subarachnoid space at $t = 0$ (Figure 7.10), that is, prior to the ventriculostomy operation. If time changes from t to $t + dt$, this volume changes by

$$dV_{sa} = \frac{dV_{sa}}{dt}\,dt = 4\pi b^2\,\frac{du_b}{dt} \tag{7.2.6}$$

where $u_b = u(r, t)$. However, this change is compensated by the CSF filling the space:

$$dV_{sa} = -4\pi b^2\,\frac{\kappa}{\eta}\frac{\partial p_b}{\partial r}\,dt + Q_b dt \quad (p_b \geq p_s) \tag{7.2.7}$$

where the first term in (7.2.7) is simply the result of linear Darcy's law for CSF flow in the brain material and the second term indicates the CSF absorption from the subarachnoid space to the blood system. Substituting (7.2.6) into (7.2.7) and using (7.1.1) for Q_b, we thus obtain

$$\frac{du_b}{dt} = \begin{cases} \dfrac{\kappa}{\eta}\dfrac{\partial p_b}{\partial r} + \dfrac{h}{\eta}(p_b - p_s) & (p_b \geq p_s) \\ \dfrac{\kappa}{\eta}\dfrac{\partial p_b}{\partial r} & (p_b < p_s) \end{cases} \tag{7.2.8}$$

which is the second boundary condition for pressure formulated at $r = b$. In (7.2.8), h models the absorption of CSF from the subarachnoid space. The parameter h in (7.2.8) is related to R in (7.1.1) as $h = 1/[4\pi b^2 R]$. Employing the values of $R = 8.5\times10^{13}$ m^{-3} and $b = 100$ mm used by *Smillie et al.* [2005], we find $h = 10^{-13}$ m.

Mathematically, condition (7.2.8) itself is an ordinary differential equation of the first order and requires an initial condition. Using $u_b{}^0 = u(b, 0) = 0$ as the initial

condition, *Smillie et al.* [2005] solved (7.2.8) numerically together with other equations they derived when they were modeling hydrocephalus. Here we note one simplification of condition (7.2.8), that is, the case when the left hand side in (7.2.8) can be ignored. This corresponds to assuming that $dV_{sa} = 0$ in (7.2.7) or, in another words, CSF does not accumulate in subarachnoid space, but rather is immediately absorbed into the blood system. This may be a sufficiently good approximation when the volume of the subarachnoid space does not change fast, i.e., at the onset of hematoma. When the hematoma grows, the changes of V_{sa} presumably can be much greater, but that is beyond the scope of this work. Last but not least, the left hand side in (7.2.8) can obviously be omitted in the steady-state case when d/dt is zero.

Hence, we consider $du_b/dt \approx 0$ in (7.2.8), so that the second boundary condition for pressure can be written on the subarachnoid-space "boundary" as

$$-\frac{\kappa}{\eta}\frac{\partial p}{\partial r}\bigg|_{r=b} = \begin{cases} \dfrac{h}{\eta}(p_b - p_s) & (p_b \geq p_s) \\ 0 & (p_b < p_s) \end{cases} \tag{7.2.9}$$

where as in (7.1.1), the term in the right hand side indicates that fluid flux into the bloodstream through the subarachnoid space is proportional to the difference of the corresponding pressures if $p_b > p_s$.

The traction boundary condition on the ventricular boundary can be written as

$$\sigma_{rr}(a,t) = -p_a \quad (t > 0) \tag{7.2.10}$$

where $\sigma_{rr}(r, t)$ is the distribution of the total radial stress in the brain. Note that hereafter compressive stresses are assumed to be negative, and we do not use the concept of effective stresses in this work.

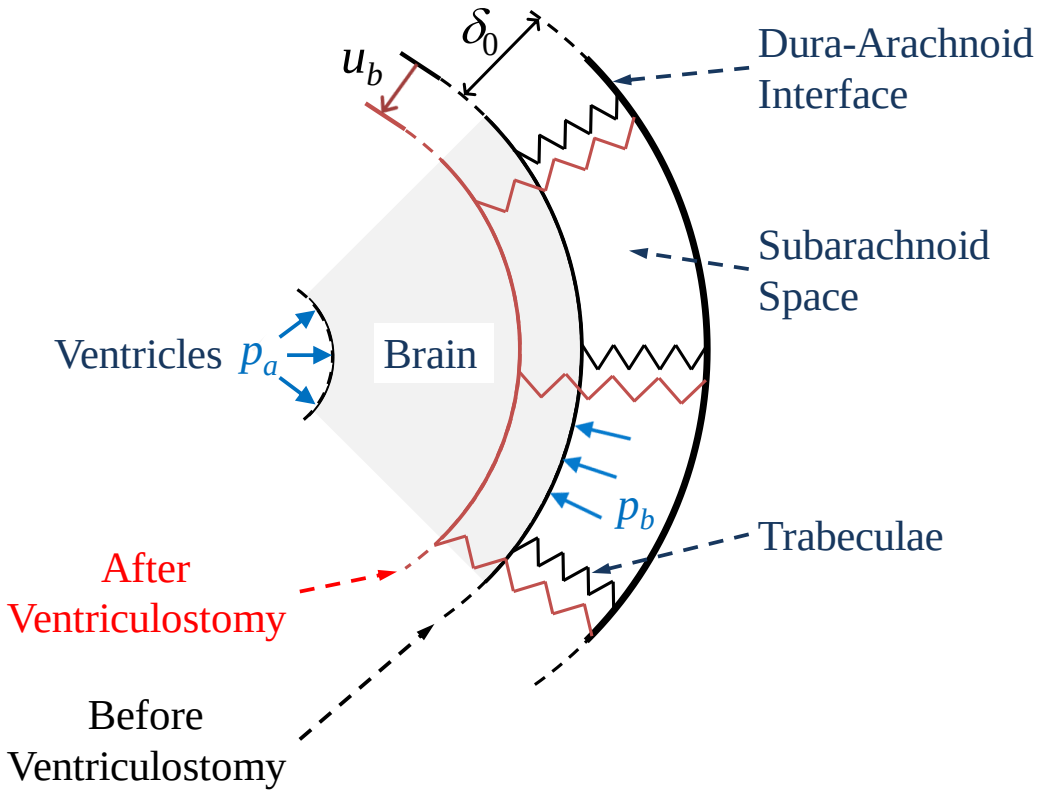

Figure 7.10. Spherically-symmetric model of the human brain and spring representation of the arachnoid trabeculae.

On the boundary $r = b$, which models the subarachnoid space, we postulate that

$$\sigma_{rr}(b,t) = -p_b - k(u_b + u_0) \quad (t > 0) \tag{7.2.11}$$

where $u = u(r, t)$ is the radial displacement in the brain during ventriculostomy, $u_b(t) = u(b, t)$ is the brain displacement at subarachnoid space, u_0 is the amount of displacement necessary to bring the arachnoid trabeculae to the unstreched state, and k is the combined stiffness of the arachnoid trabeculae (Figure 7.10). Parameter k is analogous to the effective spring constant if trabeculae are visualized as a set of springs as shown in Figure 7.10. In this figure $u_b < 0$ because we assume that a pressure decrease in ventricles, caused by ventriculostomy procedure, results in relaxations of springs-trabeculae and in the corresponding inward brain movement. For a similar reason, we also assume that in the initial state, trabeculae are stretched (say, by increased pressure p_a in the ventricles caused by hydrocephalus). Because we consider displacements and strains zero at the initial moment (that is just before the ventriculostomy procedure begins), we added u_0 into (7.2.11), so that $\Delta u = u_b + u_0$ is the average change of the dimension of trabeculae from the unstretched state. Since eventually we will only be interested in the change of stress state (because the initial stress state is not known), in the linear theory considered in this work, parameter u_0 should not appear in the final results.

7.3 Condition of Subdural Hematoma

Boundary condition (7.2.11) means that radial stress in the brain is equilibrated by the pressure in the subarachnoid space (first term) and the reaction of deformed trabeculea (second term). If $|u_b + u_0|$ is sufficiently large and p_b is sufficiently small, $\sigma_{rr}(b, t)$ in (7.2.11) may become positive (tensile).

In order to properly model the occurrence of a subdural hematoma during ventriculostomy operation, a condition of failure is introduced. We define the simplest condition of subdural hematoma as

$$\sigma_{rr}(b,t) = \sigma_t \tag{7.3.1}$$

where $\sigma_{rr}(b, t)$ is the radial stress in the subdural space material and σ_t is the tensile strength of this material.

In our model, we do not explicitly calculate the stress in the subdural space material. However, we evaluate the radial stress on the brain at the subarachnoid space edge, $\sigma_{rr}(b, t)$ (7.2.11). Since the brain is connected to arachnoid matter which is attached to dura (Figure 7.10), the subdural space material is under the same stress, $\sigma_{rr}(b, t)$.

The condition

$$\sigma_{rr}(b,t) - \sigma_t < 0 \tag{7.3.2}$$

should be maintained, that is the radial stress in the subdural space must be less than the strength of this material during the ventriculostomy operation. To the best of our

knowledge, no fundamental and systematic research has been conducted to characterize the failure properties (i.e., σ_t) of subdural space material.

Substituting (7.2.11) into (7.2.5), we find the conditions (7.3.1) and (7.3.2) in the forms of

$$p_b = -k(u_b + u_0) - \sigma_t \tag{7.3.3}$$

and

$$p_b > -k(u_b + u_0) - \sigma_t \tag{7.3.4}$$

respectively.

Before deformation (i.e., before ventriculostomy), $\sigma_{rr}(b, 0)$ should be compressive or at least smaller than σ_t. Substituting $u_b = 0$ into (7.2.11) and the result into (7.3.2), we find

$$-p_b - ku_0 < \sigma_t \quad (t = 0) \tag{7.3.5}$$

If condition (7.3.5) is not satisfied, a subdural hematoma appears before the ventriculostomy begins.

7.4 Parameters of Brain Tissue and Relevant Scales

In their recent review of the history of mathematical modeling of hydrocephalus, *Clarke and Meyer* [2007] note that one of the most frustrating aspects in the mathematical study of hydrocephalus is the lack of realistic estimates of the mechanical properties of the living human brain. They discuss the consequences of this issue on

understanding of low-pressure hydrocephalus. In particular, they suggest that permanent, nonelastic (or plastic) changes in brain material during deformation may be an important mechanism of low-pressure hydrocephalus [*Clarke et al.*, 2006]. They also suggest that given the often repetitive stresses inherent in patients who cycle through repeated shunt failures, a true elasto-plastic model, combining both types of deformation, is required. In a more general context, they conclude that clinical correlations are required to ensure the accuracy of the mathematical modeling.

Although we certainly share the frustration expressed by *Clarke and Meyer* [2007] regarding the estimates of the mechanical properties of the brain tissue, it is also interesting to point out recent works by *Levine* [1999, 2000] on low-pressure hydrocephalus and pseudotumor cerebri. Employing a simple spherically-symmetrical linear poroelastic model and in spite of uncertainty in physical properties of brain material, *Levine* [1999] was able to conclude that the seepage of CSF with efficient parenchymal absorption accounts for the clinical features of normal pressure hydrocephalus. Using a similar model and despite a number of simplifying assumptions (spherical symmetry and that brain tissue is both homogeneous and isotropic and has linear stress-strain behavior), *Levine* [2000] showed that small, normal, or slightly enlarged ventricles in pseudotumor cerebri are consistent with the theory of reduced CSF absorption [*Johnston et al.*, 1991]. As he stated, these simplifications make precise quantitative conclusions impossible, but do not affect the validity of the qualitative conclusions that can be drawn. This is the approach we utilized below. We begin with brain parameters that are relatively well known and are more concerned with orders of

magnitude than with precise values that are commonly patient specific and condition and time dependent.

Smillie et al. [2005] and *Kaczmarek et al.* [1997] chose values for the radii of the ventricles and the subarachnoid space which roughly correspond to their position in healthy adult human brain. For the ventricles and the subarachnoid space, they used 30 mm and 100 mm, respectively. *Hakim et al.* [1976] introduced the "ventricular aspect ratio," $\Gamma = b/a$, as a measure of the extent of the hydrocephalus. They estimated $\Gamma = 4$ for normal brain assuming the CSF in the ventricles is 1.6% of the total volume of the brain and used $\Gamma = 2$ for a typical case of adult hydrocephalus. As *Smillie et al.* [2005] and *Kaczmarek et al.* [1997], we choose $b = 100$ mm for the radius of the subarachnoid space, and following *Hakim et al.* [1976], we use the value of $a = 50$ mm for the radius of the ventricles a hydrocephalic brain.

The rate of CSF formation, Q_v, is reported to have an average value of 5.8×10^{-9} m^3/sec and a range of 4.5×10^{-9} -7.5×10^{-9} m^3/sec [*Czosnyka et al.*, 2004]. It is relatively constant and is not significantly affected by blood pressure and intraventricular pressure [*Nolte*, 2002]. For our calculations, we assume that it is constant and has a value of 5.8×10^{-9} m^3/sec (≈ 500 ml/day). Since for $a = 50$ mm, the ventricle volume is $V_v = (4/3)\pi a^3 \approx 500$ ml, the CSF in the ventricles is renewed daily assuming that all CSF produced in the ventricles enters brain parenchyma. Somewhat faster CSF renewal (approximately three times a day), which has been reported in the literature [*Nolte*, 2002], is still consistent with this time scale and can be explained by additional pathways for CSF removal from the ventricles to the blood system (such as spinal canal; e.g.,

Linninger et al. [2005]). These pathways are present in reality, but not accounted for in the spherical brain model under consideration.

CSF viscosity, η, is relatively well constrained. *Bloomfield et al.* [1998] measured the viscosity of CSF of patients undergoing brain surgery. They reported that the CSF is a Newtonian fluid, and its viscosity at the body temperature is in the range of $7\times10^{-4} - 10\times10^{-4}$ Pa·m**,** which is similar to distilled water. Therefore, we simply use the order-of-magnitude value of $\eta = 10^{-3}$ Pa·m.

As can be seen from expressions (7.2.1) – (7.2.3), poroelastic governing equations contain five independent parameters: three constitutive parameters β, ν, and α, one coupling parameter M, and one transport parameter κ/η. Because $\beta = (1 + \nu)/[(1 - \nu)3K]$ and $M = (BK/\alpha)(1 - \alpha B)^{-1}$, one can chose another set of five independent parameters: three constitutive parameters K, ν, and α, Skempton's coefficient B as a coupling parameter, and the same transport parameter κ/η. Since $K = 2G(1 + \nu)[3(1 - 2\nu)]^{-1}$, shear modulus G can also be used instead of K in this set. If the pressure in the material does not change, i.e., $p(r) = p_0(r)$, constitutive relation (7.2.2) reduces to purely elastic (Hooke's law). Therefore, in (7.2.2), both K and ν are drained parameters.

Another set of independent constants is often chosen to represent poroelastic response of a material to mechanical loading [*Detournay and Cheng*, 1993]: G, α, ν, and ν_u, where ν_u is undrained Poisson's ratio (transport parameter, κ/η, remains the same). Then, in (7.2.1) – (7.2.3), $M = 2G(\nu_u - \nu)[\alpha^2(1 - 2\nu_u)(1 - 2\nu_u)]^{-1}$ [*Detournay and Cheng*, 1993] and $\beta = (1 - 2\nu)]/[2(1 - \nu)G]$.

In geomechanics, where poroelastic theory was originated, the bulk modulus (both drained, K, and undrained, K_u) is often used instead of the shear modulus, G. In brain biomechanics, however, Young's modulus, E, is more frequently employed. Since it is difficult to perform a uniaxial test with brain tissue, one can simply think of its Young modulus as formally defined, for example, by $E = 3K(1 - 2\nu)$ or by $E = 2G(1 + \nu)$ with the corresponding expressions in the undrained case [see also *Smillie et al.*, 2005]. Then, $\beta = (1 + \nu)(1 - 2\nu)]/[(1 - \nu)E]$ and the set of five independent material parameters becomes E, ν, α, B (or M), and κ/η.

These material parameters are entirely macroscopic and do not require any microscopic consideration for formulating consistent boundary value problems. Yet, because the fragile character of brain tissue prohibits the employment of direct laboratory tests, micromechanical analysis on poroelastic parameters allows their evaluation in the important extreme case of incompressible fluid and solid constituents. That is, Biot's, α, and Skempton's, B, coefficients can be expressed as [*Detournay and Cheng*, 1993]

$$\alpha = 1 - \frac{K}{K_s}, \quad B = \frac{\alpha}{\alpha - \phi(1-\alpha) + \phi\dfrac{K}{K_f}} \tag{7.4.1}$$

where K_f and K_s are the bulk moduli of the liquid and solid phases (components) of the porous material, respectively, K is the effective (equivalent) drained bulk modulus of the porous material (mixture), and ϕ is its porosity fully saturated with the liquid. If $K/K_f << 1$ (incompressible liquid) and $K/K_s << 1$ (solid phase is much more rigid than

the bulk porous material), then, as follows from (7.4.1), $\alpha \approx 1$, $B \approx 1$, and, therefore, $M = (BK/\alpha)(1 - \alpha B)^{-1} \to \infty$ [*Detournay and Cheng*, 1993].

Since the CSF is largely (99%) composed of water [*Goldsmith*, 2001], in mechanical models of hydrocephalus, the brain tissue has been treated as a porous medium, the pore space of which is saturated with an incompressible fluid [e.g., *Nagashima et al.*, 1987; *Kaczmarek et al.*, 1997; *Tenti et al.*, 1999; *Levine*, 1999, 2000; *Taylor and Miller*, 2004; *Smillie et al.*, 2005; *Wirth and Sobey*, 2006; *Sobey and Wirth*, 2006]. The cells of the brain are also assumed to be incompressible [*Kaczmarek et al.*, 1997] and the deformational mechanisms of the solid material include the movement of axon fibers over each other [*Bilston et al.*, 2001]. In general, all solid and fluid elements in the brain can be considered as nearly-incompressible [*Levine*, 1999, 2000], but the whole structure is highly deformable in drained conditions [*Hakim et al.*, 1976; *Tenti et al.*, 2000]. Because, $K = 2G(1 + \nu)[3(1 - 2\nu)]^{-1}$, the drained Poisson's ratio, ν, of the brain parenchyma is unlikely to be too close to 0.5, and, as noted by *Smillie et al.* [2005], the values of ν such as 0.49, sometimes reported in the literature [*Nagashima et al.*, 1987] can be explained by using ν_u instead of ν. Therefore, we can indeed assume that $K/K_s << 1$ and $K/K_f << 1$, so that with sufficient accuracy $\alpha = 1$, $B = 1$ ($M = \infty$) for the brain parenchyma material. This is why most of investigators employed the values of $\alpha = 1$, $B = 1$ ($M = \infty$ or $M >> 1$) for modeling hydrocephalus [e.g., *Nagashima et al.*, 1987; *Kaczmarek et al.*, 1997; *Tenti et al.*, 1999; *Levine*, 1999; *Taylor and Miller*, 2004; *Smillie et al.*, 2005; *Wirth and Sobey*, 2006; *Sobey and Wirth*, 2006].

Due to biphasic nature of brain tissue, the stress-strain relationship of the brain is load and strain-rate dependent [*Miller and Chinzei*, 1997, 2002; *Clarke and Meyer*, 2007]. In the literature, the undrained or instantaneous values of Young's modulus for the brain, E_u, is reported to be in the range of $1-2\times10^4$ Pa [*Levine*, 1999]. Using the experimental data reported by *Miller* [1999], *Taylor and Miller* [2004] suggested that an appropriate value of drained Young's modulus for the brain, E, is 584 Pa. Given this, in this work, we use $E_u = 10^4$ Pa and $E = 10^3$ Pa.

There is a lack of experimental work for the characterization of brain tissue compressibility [*Kyriacou et al.*, 2002]. Under high-strain rate loading conditions, it may be incompressible, on the other hand, for much slower processes, it may be significantly compressible [*Kyriacou et al.*, 2002]. *Franceschini et al.* [2006] carried out an extensive experimental work to find Poisson's ratio of the brain tissue. In this work, they performed confined compression tests (oedometer tests) on samples collected from human autopsy. Using the initial (instantaneous) response of the brain sample to the uniaxial loading, they found what they call "initial, drained Poisson's ratio" of brain equal to 0.496. This corresponds to the short-term (instantaneous) response of the brain tissue and therefore, they essentially obtained undrained Poisson's ratio. Hence, their result, $\nu_u = 0.496$, is consistent with general understanding of brain parenchyma being nearly incompressible in undrained conditions [e.g., *Levine*, 1999, 2000; *Smillie et al.*, 2005]. Following *Kaczmarek et al.* [1997] and *Smillie et al.* [2005], we use drained Poisson's ratio, ν, equal to 0.35 in our calculations.

Based on the experimental results of *Reulen et al.* [1977] on diffusion of Na-fluorescein dye within the brain, *Kaczmarek et al.* [1997] calculated the permeability of

the white matter as 1.4×10^{-14} m^2. Since they expected that the permeability of the grey matter is lower than that of white matter, they used 1.4×10^{-16} m^2 for grey matter permeability in their calculations. *Smillie et al.* [2005] reported that this value of grey matter permeability lead to unrealistic pressure difference between ventricles and subarachnoid space and chose the higher value for both white and grey matter. Accordingly, we do not distinguish the permeability of two layers and set the value of 10^{-14} m^2. A set of parameter values is given in Table 7.1.

To the best of our knowledge, there is no experimental work, reported in the literature, characterizing mechanical behavior of the arachnoid trabeculea. However, based on clinical observations, we can estimate an approximate range for trabeculea rigidity, *k*, in (7.2.11). For example, *Hakim et al.* [1976] discussed that during sterotactic surgery of a normal brain, when the dura is opened, the brain does not protrude even though the pressure in the subarachnoid space is greater than the atmospheric pressure. This means that the arachnoid does not apply any stress on the dura in spite of the fact that the subarachniod space is pressurized (Figure 7.11).

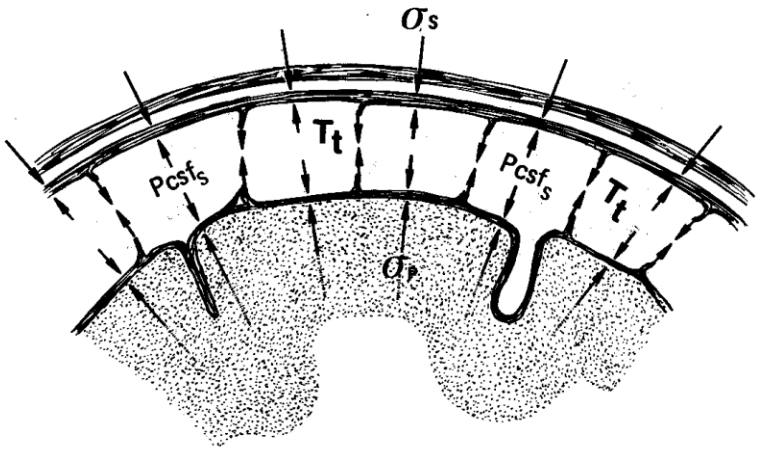

Figure 7.11. Schematic representation of forces exerted on meninges [*Hakim et al.*, 1976]. Here, σ_s is subdural stress, σ_p is pial stress, T_t is tension in the trabeculae, and $Pcsf_s$ is the subarachnoid pressure. Due to the small thickness of subarachnoid space, *Hakim et al.* [1976] assumed that $\sigma_s = \sigma_p$. Under normal conditions, $Pcsf_s >> \sigma_s$ and the subarachnoid pressure is equilibrated by the tension in the trabeculae [*Hakim et al.*, 1976].

For the normal brain, the boundary condition (7.2.11) can be written as (Figure 7.12a)

$$\sigma_{rr}^{0}(b) = -p_b^{0} - ku_0 \tag{7.4.2}$$

In this case, when the equilibrium is disturbed (i.e., by changing the intracranial pressure), the dura-arachnoid interface does not move since it is attached to stiff dura. However, when the dura is opened in sterotactic surgery, there is nothing restricting the movement of the dura-arachnoid interface. For example, *Hakim et al.* [1976] discussed that if the intracranial pressure is high, the brain bulges out of the opening in the skull immediately after the dura is opened. Accordingly, the expression (7.4.2) can be written as (Figure 7.12b)

$$\sigma_{rr}^{1}(b) = -p_b^{1} - k(u_1 + u_d) \tag{7.4.3}$$

where u_1 is the displacement of trabeculae from its undeformed state, u_d is the displacement of dura-arachnoid interface, $\sigma_{rr}^{1}(b)$ is the radial stress in the dura-arachnoid interface, and p_b^{1} is the pressure in subarachnoid space. In the case of sterotactic surgery of a normal brain, since the dura is opened, the radial stress on the dura-arachnoid interface is equal to zero ($\sigma_{rr}^{1}(b) = 0$), and according to *Hakim et al.* [1976], the brain does not protrude upon opening the dura, which means $u_d = 0$. Thus, using the expression (7.4.3), we obtain

$$p_b^{1} = -ku_1 \tag{7.4.4}$$

This is equivalent to the deformation, u_1, of a spring with spring constant k under the pressure p_b^{1} (note that in this work, the constant k has the units of Pa/m) (Figure

7.12b). This means that the CSF in the subarachnoid space applies pressure, p_b^1, on both the pial boundary of the brain and the arachnoid matter. Consequently, the "fixed" arachnoid and the "mobile" brain tend to move apart from each other and stretch arachnoid trabeculea by an amount of u_1. Assuming the change in the subarachnoid space pressure ($p_b^1 - p_b^0$) and thickness ($l_f^1 - l_f^0$) are negligible, the constant k can be estimated using

$$k = \frac{p_b^1}{u_1} \approx \frac{p_b^0}{u_0} = \frac{p_b^0}{l_f^0 - l_0} \tag{7.4.5}$$

where l_f is the thickness of subarachnoid space when the trabeculae are stretched and l_0 is the unstretched length of trabeculae. The maximum value, k_{max}, of the parameter k can be obtained for $l_0 \rightarrow l_f^0$ and $p_b^0 > 0$, which corresponds to infinitely stiff trabeculae. Then, $k_{max} = \infty$. Similarly, the minimum value, k_{min}, of the parameter k can be obtained for $l_0 = 0$, $p_b^0 > 0$, and the subarachnoid space thickness of 1 mm [*Jacobson et al.*, 1999] and $p_b^1 \sim 10^3$ Pa [*Goldsmith*, 2001]. We have $k_{min} = p_b^0 / l_f^0 \sim 10^6$ Pa/m.

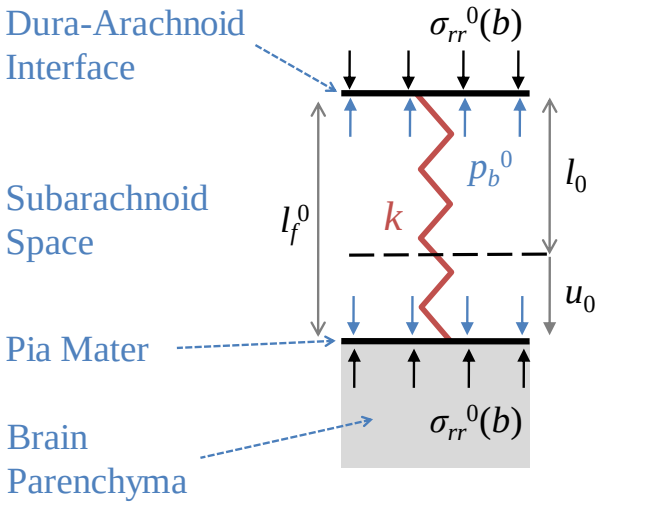

(a)

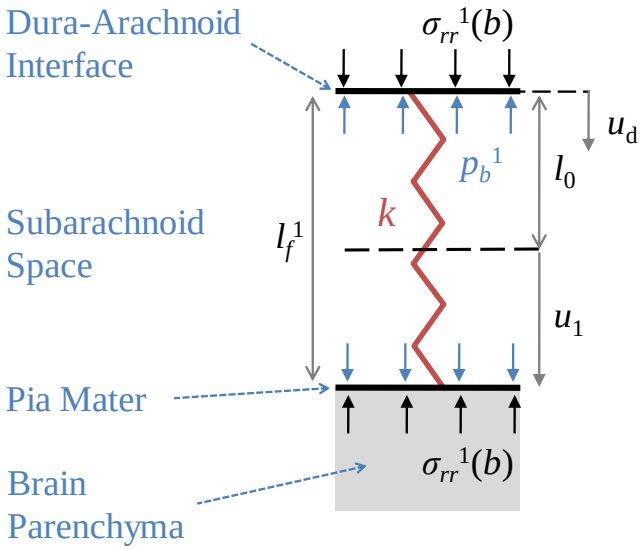

(b)

Figure 7.12. Schematic representation of forces exerted on meninges (a) before and (b) after sterotactic surgery of a normal brain. Here, l_0 is the thickness of subarachnoid space when the trabeculae are unstretched, k is the combined stiffness of trabeculae, u_0 and u_1 are the displacements of trabeculae from undeformed state before and after surgery, respectively; u_d is the displacement of dura-arachnoid interface when the dura is opened; l_f^0 and l_f^1 are the thicknesses of subarachnoid space before and after surgery, respectively.

Finally, in steady-state, the distribution of Darcy fluid velocity in the brain parenchyma can be written as $v = dr/dt = Q_v/(4\pi r^2)$. Then, $dt/dr = 4\pi r^2/Q_v$, so that the time needed for a fluid particle to percolate through the brain is estimated by $t \approx 4\pi(b^3 - a^3)/(3\phi Q_v)$, where ϕ is the porosity of brain parenchyma. Employing the value of $\phi = 20\%$, which is typically used in association with CSF flow through brain material [*Kalyanasundaram et al.*, 1997; *Sykova*, 2004], and the values for a, b, and Q_v, discussed above, we find that $t \approx 3\times10^6$ sec ≈ 1 month. In other words, it takes about a month for a particle of CSF, produced in the ventricle, to propagate through the brain tissue towards the subarachnoid space before it goes through the arachnoid villi into the bloodstream.

7.5 Distribution of CSF Pressure

In order to determine initial conditions for pressure distribution, the flow of CSF in the brain is described by steady-state diffusion equation at $t = 0$:

$$\frac{d^2 p^0}{dr^2} + \frac{2}{r}\frac{dp^0}{dr} = 0 \quad (a < r < b) \tag{7.5.1}$$

where superscript-zero denotes pressure before ventriculostomy (i.e., prior to deformation).

In this model, it is assumed that produced CSF, in the case of non-communicating hydrocephalus, flows through the brain towards the subarachnoid space. CSF is absorbed into the blood system based on the criterion (7.2.11). Note that h cannot have zero value in (7.2.11) because than CSF would be constantly accumulating in the brain. The pressure boundary condition at $r = a$ is given in (7.2.4).

Integrating equation (7.5.1) produces the expression

$$p^0(r) = p_s + \frac{\eta}{\kappa}\frac{Q_v}{4\pi b}\left[\frac{b}{r} + \frac{\kappa}{bh} - 1\right] \tag{7.5.2}$$

Substituting $r = b$ into (7.5.2) yields the initial pressure, $p_b^0 = p_s + \eta Q_v/(4\pi h b^2)$, in subarachnoid space. Therefore, the model is consistent with CSF production per (7.2.4), because $p_b^0 > p_s$ for any value of h, which is positive since it describes the absorption of CSF in the subarachnoid space. Note that brain permeability is not present in p_b^0.

Similarly, substituting $r = a$ into (7.5.2) yields the initial pressure in the ventricles

$$p_a^0 = p_s + B_v Q_v \tag{7.5.3}$$

where

$$B_v = \frac{\eta}{4\pi h\kappa}\left[\frac{\kappa}{b^2} + h\left(\frac{1}{a} - \frac{1}{b}\right)\right] \tag{7.5.4}$$

Now, assume that as a result of ventriculostomy, the pressure in the ventricular cavity is reduced to p_a^∞ and maintained for a period of time sufficient to achieve a new steady state in the brain. Yet, the obstruction impairing the circulation of CSF through the ventricular system still exists. Therefore, the pressure distribution in the brain is still described by (7.5.1). However, the boundary condition at $r = a$ is now different, that is, (7.2.4) is replaced by $p^\infty(a) = p_a^\infty$. After the operation, the boundary condition at $r = b$ is still described by (7.2.9), although, it is not obvious now what case in (7.2.9) to choose.

Let $p_a^\infty \geq p_s$. Integrating (7.5.1) and using (7.2.9), we find

$$p^{\infty}(r) = p_a^{\infty} - \frac{\eta}{4\pi\kappa B_v}(p_a^{\infty} - p_s)\left(\frac{1}{a} - \frac{1}{r}\right) \tag{7.5.5}$$

Based on the condition $p_a^{\infty} \geq p_s$, it can be concluded that $p_b^{\infty} \geq p_s$, that is, the pressure in the subarachnoid space, p_b, is greater or equal to the blood pressure, p_s. Hence, in the case of $p_a^{\infty} \geq p_s$, the choice of the first condition in (7.2.9) is consistent with the solution.

Now, let $p_a^{\infty} < p_s$. The second condition in (7.2.9) corresponds to $h = 0$ of the first condition in (7.2.9), so that substituting $h = 0$ into (7.5.5), we have $p(r) = p_a$. Hence $p_b^{\infty} = p_a^{\infty}$ and accordingly, $p_b^{\infty} < p_s$. In this case, all CSF produced in the ventricles is extracted and there is no CSF flow through the brain. According to our model, this would happen when the CSF pressure in the ventricles is reduced below the blood pressure. In contrast, solution (7.5.5) corresponds to some CSF flowing through the brain towards subarachnoid space where the CSF is absorbed into the blood system. In this case, the pressure in the ventricles is greater than the blood pressure. In steady state, the rates of absorbed and produced CSF are equal and can be calculated using (7.5.5) and (7.5.4):

$$Q_a = -\frac{\kappa}{\eta}\frac{\partial p}{\partial r}\bigg|_{r=a} 4\pi a^2 = \begin{cases} \dfrac{p_a^{\infty} - p_s}{B_v} & (p_a^{\infty} \geq p_s) \\ 0 & (p_a^{\infty} < p_s) \end{cases} \tag{7.5.6}$$

This expression shows that if $p_a^{\infty} < p_s$, all produced CSF is extracted from the ventricles through the inserted shunt, so that no fluid enters the brain parenchyma.

The pressure change in the ventricles can be related to CSF production rate using (7.5.3) and (7.5.6) as

$$p_a^{\infty} - p_a^0 = \begin{cases} -B_v(Q_v - Q_a) & (p_a^{\infty} \geq p_s) \\ -B_v Q_v & (p_a^{\infty} < p_s) \end{cases} \tag{7.5.7}$$

and we see that $Q_a < Q_v$ either for $p_a{}^{\infty} \geq p_s$ or $p_a{}^{\infty} < p_s$. This is of course expected since the pressure in the ventricles has been reduced as a result of ventriculosomy ($p_a{}^{\infty} < p_a{}^0$).

The pressure change across the brain can be written using expressions (7.5.5) and (7.5.6) as

$$p^{\infty}(r) - p^0(r) = (p_a^{\infty} - p_a^0)\frac{\eta}{4B_v \pi \kappa}\left(\frac{\kappa}{hb^2} + \frac{1}{r} - \frac{1}{b}\right) \quad (p_a{}^{\infty} \geq p_s,\ p_a{}^{\infty} < p_s) \tag{7.5.8}$$

Since $p_a{}^{\infty} < p_a{}^0$, we observe that $p^{\infty}(r) < p^0(r)$, i.e., as expected, the pressure across the brain reduces as a result of ventriculostomy operation.

An example of pressure distribution in the brain is given in Figure 7.13. The initial pressure distribution, $p_a{}^0$, is calculated using (7.5.2) together with the corresponding parameters tabulated in Table 7.1. We find the pressure difference between subarachnoid space and ventricles as 462 Pa (3.5 mm Hg). Using similar parameter values, *Smillie et al.* [2005] calculated a pressure difference of 660 Pa (~5 mm Hg) and considered that this value is within the range of observed intracranial pressures. The pressure response in the long term post-operative stage is also illustrated in Figure 7.13. First, we assume that the pressure in the ventricles, $p_a{}^{\infty}$, has the value of 1000 Pa (7.5 mm Hg) which is greater than sagittal venus pressure, p_s. This curve is plotted using the expression (7.5.5) for different values of κ/h. It is seen that pressure in the subarachnoid space is less than the ventricular pressure and the difference depends on the

value of κ/h. As the permeability increases or the CSF absorption in the subarachnoid space decreases, the transmantle pressure difference decreases. In fact, when the ventricular pressure is reduced below the sagittal sinus pressure, the absorption of CSF in subarachnoid space completely ceases and this results in zero pressure difference between the ventricles and subarachnoid space (Figure 7.13).

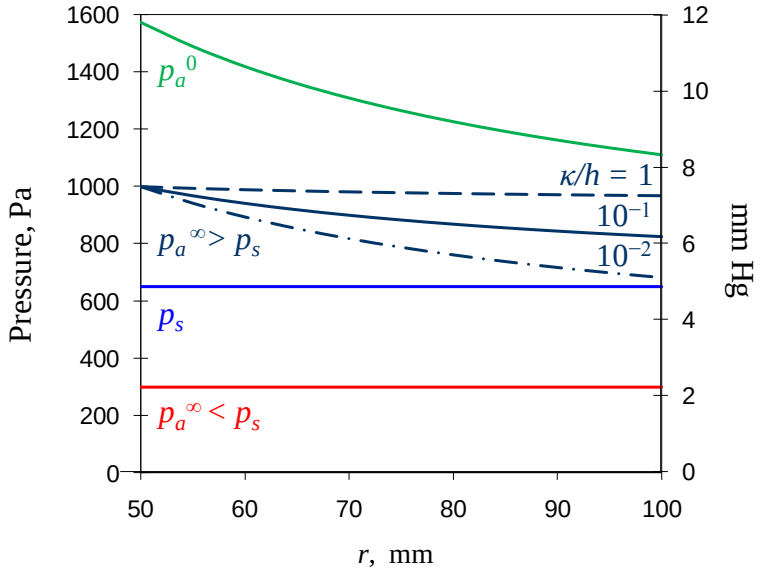

Figure 7.13. Pressure distribution within brain parenchyma before ventriculostomy and in long-term post-operative stage. Here, κ is the permeability of brain tissue, h is the absorption parameter, p_s is sagittal sinus (blood) pressure, p_a^0 and p_a^∞ are CSF pressure in the ventricle at the initial moment and in long-term post-operative stage, respectively.

7.6 Subdural Hematoma Caused by Ventriculostomy Operation

If the pressure distribution, $p(r)$, in the brain is known, equilibrium condition (7.2.1) and constitutive relation (7.2.2) relate distributions of displacements, $u(r)$, and radial stresses, $\sigma_{rr}(r)$, in the brain. Then, assuming that the distribution of the initial stresses, $\sigma_{rr}^{0}(r)$, is also know, both distributions of displacements, $u(r)$, and stresses, $\sigma_{rr}(r)$, are defined from the boundary conditions (7.2.10) and (7.2.11).

Suppose now that during the ventriculostomy operation the pressure in the ventricles is reduced rather quickly. We model this, to the first order, by assuming that the pressure in the ventricles is changed instantaneously from the value of $p_a^{\,0}$ to $p_a^{\,i}$. Due to such a fast decrease of pressure in the ventricles, the pressure distribution in the brain does not change:

$$p^i(r) = p^0(r) \tag{7.6.1}$$

where p^i is the pressure distribution in the brain Accordingly, on the internal boundary

$$\sigma_{rr}^i(a) = -p_a^i > -p_a^0 \tag{7.6.2}$$

Substituting (7.6.1) into (7.2.2), we arrive at the Hooke's law

$$\sigma_{rr}^i(r) = \frac{1}{\beta}\frac{\partial u}{\partial r} + \frac{2\nu}{1-\nu}\frac{1}{\beta}\frac{u}{r} + \sigma_{rr}^0(r) \tag{7.6.3}$$

and due to (7.6.1), the equilibrium condition (7.2.1) reduces to

$$\frac{\partial}{\partial r}\left(\frac{1}{r^2}\frac{\partial}{\partial r}(ur^2)\right) = 0 \tag{7.6.4}$$

The stress boundary condition on $r = b$ remains the same as (7.2.11) with $p_b = {p_b}^i = {p_b}^0$:

$$\sigma_{rr}^i(b) = -p_b^0 - k(u_b + u_0) \tag{7.6.5}$$

The boundary value problem (7.6.2) – (7.6.5) is equivalent to the elastic response of the brain to the pressure change in the ventricular cavity. Integrating (7.6.5), we have

$$u^i(r) = \frac{A_1}{3} r + \frac{A_2}{r^2} \tag{7.6.6}$$

where constants A_1 and A_2 can be found from the boundary conditions for stresses (7.6.2) and (7.6.5). Inserting (7.6.6) into (7.6.3) and the result into (7.6.2) and (7.6.5), we obtain:

$$\begin{cases} A_1 = C\beta \dfrac{3}{b^3}\left(2\dfrac{1-2\nu}{1+\nu} - k\beta b \dfrac{1-\nu}{1+\nu}\right)(p_a^i - p_a^0) \\ A_2 = C\beta\left[1 + k\beta b \dfrac{1-\nu}{1+\nu}\right](p_a^i - p_a^0) \end{cases} \tag{7.6.7}$$

where

$$C = \left[2\frac{1-2\nu}{1-\nu}\left(\frac{1}{a^3} - \frac{1}{b^3}\right) + kb\beta\left(\frac{1-2\nu}{1+\nu}\frac{2}{a^3} + \frac{1}{b^3}\right)\right]^{-1} \tag{7.6.8}$$

Hence, substituting (7.6.7) into (7.6.6), the radial displacement can be expressed as

$$u^i(r) = C\beta(p_a^i - p_a^0)\left\{2\frac{1-2\nu}{1+\nu}\frac{r}{b^3} + \frac{1}{r^2}\left[1 + k\beta b\frac{1-\nu}{1+\nu}\left(1 - \frac{r^3}{b^3}\right)\right]\right\} \tag{7.6.9}$$

In particular, the displacement $u_a^{\,i} = u^{\,i}(a)$ of the ventricle wall is given by

$$\frac{u_a^i}{a} = \frac{\beta(p_a^i - p_a^0)C}{a^3}\left[2\frac{1-2\nu}{1+\nu}\frac{a^3}{b^3} + 1 + k\beta b\frac{1-\nu}{1+\nu}\left(1-\frac{a^3}{b^3}\right)\right] \tag{7.6.10}$$

Since $p_a^{\,i} < p_a^{\,0}$ and $r < b$, we conclude from (7.6.9) and (7.6.10) that $u(r) < 0$, which, indeed, models ventriculostomy since all brain points displace inwards (Figure 7.10). In principle, displacement $u_a^{\,i}$ in (7.6.10) is an observable quantity, even by conventional CT or MRI methods utilized shortly after the ventriculostomy procedure. Unfortunately, currently little is known about the trabeculae properties, so that the value of k cannot be independently constrained. Therefore, we simply consider upper and lower limits. In the extreme of very rigid trabeculae or when the inward movement of the outer brain surface is prevented, perhaps, by tethering of the pia-arachnoid to the dura by fibrosis [*Levine,* 2000], we consider the expression (7.6.10) in the limit of $k \to \infty$. In another extreme of very soft or perhaps damaged trabelulae, we consider these expressions in the limit of $k \to 0$. Recalling that $\beta = (1 + \nu)(1 - 2\nu)]/[(1 - \nu)E]$, we then obtain

$$\frac{u^i(a)}{a} = \frac{(p_a^i - p_a^0)(1-2\nu)}{E}\left(1-\frac{a^3}{b^3}\right)\left[2\frac{1-2\nu}{1+\nu} + \frac{a^3}{b^3}\right]^{-1} \quad (k \to \infty) \tag{7.6.11}$$

and

$$\frac{u^i(a)}{a} = \frac{(p_a^i - p_a^0)}{E}\left(1+\nu+2(1-2\nu)\frac{a^3}{b^3}\right)\left[2\left(1-\frac{a^3}{b^3}\right)\right]^{-1} \quad (k \to 0) \tag{7.6.12}$$

Omitting the terms of the order of one, we have

$$\frac{u^i(a)}{a} \sim \begin{cases} \dfrac{p_a^i - p_a^0}{E}(1-2\nu) & (k \to \infty) \\ \dfrac{p_a^i - p_a^0}{E} & (k \to 0) \end{cases} \tag{7.6.13}$$

where in the case of hydrocephalous $p_a{}^i - p_a{}^0 \sim 10^3$Pa while the instantaneous Young modulus, $E \sim 10^4$ Pa [*Levine*, 1999]. Hence, we expect that $|u^i(a)/a| \sim 0.1$ or smaller, that is, the displacement of the ventricle wall of the order of a few millimeters. Therefore, the main part of the ventricle displacement (~ cm or greater) is expected to occur after the shunt installation during the subsequent post-operative period.

Similarly, inserting (7.6.6) into (7.6.3), gives the change in the radial stress. In particular, at $r = b$,

$$\Delta\sigma_{rr}^i(b) = \sigma_{rr}^i(b) - \sigma_{rr}^0(b) = -Ck\beta b(p_a^i - p_a^0)\frac{3}{b^3}\frac{1-\nu}{1+\nu} \tag{7.6.14}$$

and we see that $\Delta\sigma_{rr}{}^i(b) > 0$ because $p_a{}^i < p_a{}^0$ and $C > 0$. In other words, regardless of the parameter values, elastic response of the ventriculostomy operation (shunting) is a positive (tensile) change in the radial stress acting on the arachnoid, and, therefore, on the dura-arachnoid interface.

We further non-dimensionilize (7.6.14) as

$$\frac{\Delta\sigma_{rr}^i(b)}{\Delta p_a^i} = \frac{\sigma_{rr}^i(b) - \sigma_{rr}^0(b)}{p_a^0 - p_a^i} = \frac{3k_1(1-\nu)}{2(\Gamma^3 - 1) + k_1[2(1-2\nu)\Gamma^3 + 1 + \nu]} \tag{7.6.15}$$

where $k_1 = kb/E$ is the dimensionless rigidity of subarachnoid trabeculae.

The solution presented in this section corresponds to the purely elastic response of the brain to ventriculostomy and simulates rapid pressure drop in the ventricles. This corresponds to the most extreme case since the poroelastic effects are not involved. Yet, the radial stress in the subdural space increases as a result of rapid pressure release in the ventricles, which means that subdural hematoma may indeed happen.

7.7 Long-term Postoperative Stage

After a successful operation, the CSF pressure in the ventricles may again somewhat increase, but not to the level, p_a^0, prior to the ventriculostomy. For simplicity, we assumed that the pressure reached a steady-state distribution $p^\infty(r)$ with the value in the ventricular cavities $p_a^\infty < p_a^0$, although, perhaps, $p_a^0 > p_a^i$. At this postoperative stage, poroelastic effect becomes important, so that the equilibrium condition (7.2.1) and constitutive relation (7.2.2) read

$$\frac{\partial}{\partial r}\left(\frac{1}{r^2}\frac{\partial}{\partial r}(ur^2)\right) = \alpha\beta\frac{\partial(p^\infty - p^0)}{\partial r} \tag{7.7.1}$$

and

$$\sigma_{rr}^\infty(r) = \frac{1}{\beta}\frac{\partial u}{\partial r} + \frac{2\nu}{1-\nu}\frac{1}{\beta}\frac{u}{r} - \alpha(p^\infty - p^0) + \sigma_{rr}^0(r) \tag{7.7.2}$$

respectively. Here, $p^\infty(r)$ is given by (7.5.8) and the formulation of the boundary value problem is completed by the boundary conditions

$$\sigma_{rr}^\infty(a) = -p_a^\infty > -p_a^0 \tag{7.7.3}$$

and

$$\sigma_{rr}^{\infty}(b) = -p_b^{\infty} - k(u_b + u_0) \tag{7.7.4}$$

where p_b^{∞} is given as $p_b^0 = p_s + \eta Q_v/(4\pi h b^2)$.

The solution of the boundary value problem (7.7.1) – (7.7.4) for the long-term postoperative period is similar to the one considered previously for the ventriculostomy operation and to the well known solution of thermoelastic problem (with different boundary conditions) offered by *Timoshenko and Goodier* [1970]. Integrating (7.7.1), we have

$$u^{\infty}(r) = \frac{\alpha\beta}{r^2}\int_a^r [p^{\infty}(r) - p^0(r)]r^2 dr + \frac{A_1}{3}r + \frac{A_2}{r^2} \tag{7.7.5}$$

where again constants A_1 and A_2 can be found from the boundary conditions for stresses, (7.7.3) and (7.7.4). Substituting (7.7.5) into (7.7.2) and then into (7.7.3), (7.7.4), we find

$$\begin{cases} A_1 = 6A_2\dfrac{1-2\nu}{1+\nu}\dfrac{1}{a^3} - 3\beta\dfrac{1-\nu}{1+\nu}(p_a^{\infty} - p_a^0) \\ A_2 = \left\{\alpha p_*\left(2\dfrac{1-2\nu}{1-\nu} - k\beta b\right) + (p_a^{\infty} - p_a^0)\left[k\beta b\dfrac{1-\nu}{1+\nu} + \dfrac{\eta}{4\pi B\kappa}\left(\dfrac{1}{a} - \dfrac{1}{b}\right)\right]\right\}\beta C \end{cases} \tag{7.7.6}$$

where

$$p_* = \frac{1}{b^3}\int_a^b [p^{\infty}(r) - p^0(r)]r^2 dr \tag{7.7.7}$$

and the expression for C is given by (7.6.8). Here $p_* < 0$ because $p^{\infty}(r) < p^0(r)$.

During postoperative period, the brain response is characterized by not only elastic but also poroelastic properties since due to the poroelastic effect, the brain will experience additional contraction. For $r = a$, expression (7.7.5) gives the steady-state displacement of the ventricle wall:

$$u^{\infty}(a) = \frac{A_1}{3} a + \frac{A_2}{a^2} \tag{7.7.8}$$

The dependence of normalized displacements of ventricle wall, u_a^{∞}/u_a^{i}, on the normalized pressure change in the ventricles, $\Delta p_a^{\infty}/\Delta p_a^{0}$ is plotted in Figures 7.14. In these plots, while calculating u_a^{i}, we used, $E \sim 10^4$ Pa, the instantaneous value of the Young's modulus suggested by *Levine* [1999]. The ratio u_a^{∞}/u_a^{i} is sensitive to the variations in pressure change in the ventricles, particularly, for smaller values of κ_1 where $\kappa_1 = \kappa/(bh)$ is the dimensionless permeability of brain tissue. Using physical constants given in Table 7.1, a representative order of magnitude for κ_1 can be estimated as $\kappa_1 \sim 10^{-14}\ \mathrm{m}^2/(10^{-1}\ \mathrm{m} \cdot 10^{-13}\ \mathrm{m}) = 1$.

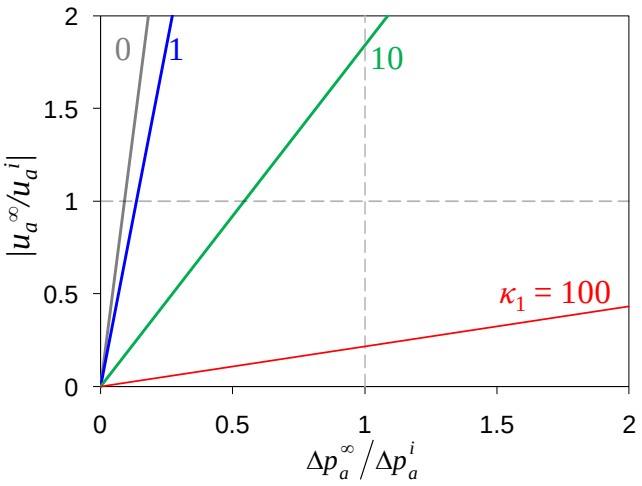

(a)

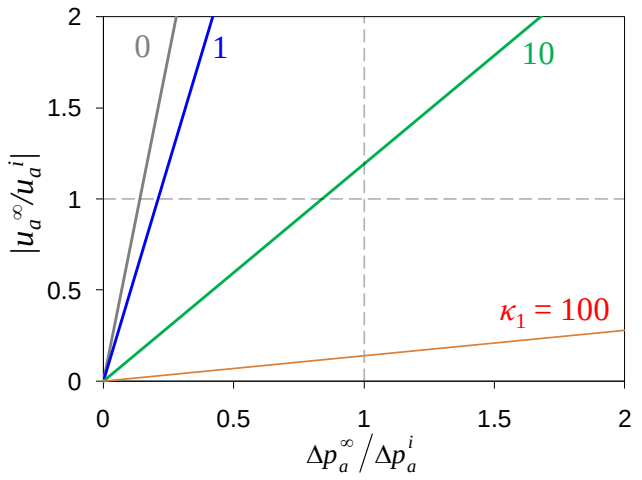

(b)

Figure 7.14. Dependence of normalized displacements of ventricle wall, $|u_a^{\infty}/u_a^{i}|$, on the normalized pressure change in the ventricles, $\Delta p_a^{\infty}/\Delta p_a^{0}$ for (a) $k_1 = 0$ and (b) $k_1 \to \infty$.

The change in the radial stress at $r = b$ can be obtained by substituting (7.7.5) and (7.7.6) into (7.7.2):

$$\Delta\sigma_{rr}^{\infty}(b) = \sigma_{rr}^{\infty}(b) - \sigma_{rr}^{0}(b) =$$
$$= -C\left\{3kb\beta\left[2\frac{1-2\nu}{1+\nu}\frac{\alpha p_*}{a^3} + \frac{p_a^{\infty} - p_a^0}{b^3}\frac{1-\nu}{1+\nu}\right] + 2\frac{1-2\nu}{1-\nu}(p_b^{\infty} - p_b^0)\left(\frac{1}{a^3} - \frac{1}{b^3}\right)\right\} \quad (7.7.9)$$

From $p^{\infty}(r) < p^0(r)$ and $p_* < 0$, we obtain $\Delta\sigma_{rr}{}^{\infty} > 0$ that is the change in the radial steady-state stress in the subdural space is always positive.

Using (7.5.4), (7.5.7), and (7.5.8), the expression (7.7.7) can be written as

$$p_* = (p_a^{\infty} - p_a^0)\left\{\frac{1}{3}\left(1 - \frac{a^3}{b^3}\right) - \frac{\eta}{4\pi B_v \kappa}\left[\frac{1}{3a}\left(1 - \frac{a^3}{b^3}\right) - \frac{1}{2b}\left(1 - \frac{a^2}{b^2}\right)\right]\right\} \quad (7.7.10)$$

Combining (7.7.6)-(7.7.7) and (7.7.10) with (7.7.9)

$$\frac{\Delta\sigma_{rr}^{\infty}(b)}{\Delta p_a^{\infty}} = \frac{\sigma_{rr}^{\infty}(b) - \sigma_{rr}^{0}(b)}{p_a^0 - p_a^{\infty}} =$$
$$= \frac{\Delta\sigma_{rr}^{i}(b)}{\Delta p_a^{i}}\left[1 - \frac{(1-2\nu)[2(1-\Gamma^3)(\kappa_1 - 1) + 3\Gamma(1-\Gamma^2)]\alpha k_1 + 2\kappa_1(1-\Gamma^3)}{3k_1(1-\nu)[\kappa_1 - 1 + \Gamma]}\right] \quad (7.7.11)$$

The variation of $\Delta\sigma_{rr}{}^{\infty}(b)/\Delta\sigma_{rr}{}^{i}(b)$ with $\Delta p_a{}^{\infty}/\Delta p_a{}^{i}$ is given in Figure 7.15. Depending on the value of κ_1 and k_1 in addition to $\Delta p_a{}^{\infty}/\Delta p_a{}^{i}$, the change in radial stress, $\Delta\sigma_{rr}(b)$, is either larger during the ventriculostomy or in the long term post-operative stage. This means that subdural hematoma can occur either shortly after a ventriculostomy or during the prolonged recovery stage. In a specific operation, the fact that hematoma did not appear during operation does not mean that it would not occur in

the long term as the radial stress in the subdural space material may still increase and cause hematoma. The dependence of $\Delta\sigma_{rr}(b)/\Delta p_a^{\infty}$ ((7.6.16) and (7.7.11)) on κ_1 and k_1 is shown in Figure 7.15 and Figure 7.16. From Figure 7.16, we observe that $\Delta\sigma_{rr}(b)/\Delta p_a^{\infty}$ increases with increasing κ_1 and k_1. It is sensitive to changes in κ_1, especially, when κ_1 is less than 10. In this range, a small change in the permeability of the brain material or in the absorption of CSF in subarachnoid space can considerably change the stresses in the subdural space material. On the other hand, $\Delta\sigma_{rr}(b)/\Delta p_a^{\infty}$ is not significantly affected by the variations in k_1. It has tendency to increase with increasing k_1. However, unlike κ_1, it is not possible to estimate a practical value for k_1 since the combined stiffness of trabeculae, k, is not known. For the case $\kappa_1 = 1$, the change in $\Delta\sigma_{rr}(b)/\Delta p_a^{\infty}$ may be clinically significant, especially, if k_1 is less than 10. The dependence of $\Delta\sigma_{rr}(b)/\Delta p_a^{\infty}$ ((7.6.16) and (7.7.11)) on Γ is illustrated in Figure 7.18. Model parameters used in these plots are tabulated in Table 7.1. It is seen that the ventricle size has a considerable effect on $\Delta\sigma_{rr}(b)/\Delta p_a^{\infty}$. The radial stress in the subdural space material increases as the ventricle size increases. In addition, the effect of κ_1 on $\Delta\sigma_{rr}(b)/\Delta p_a^{\infty}$ becomes more significant for smaller ventricles. Conversely, as the radius of the ventricle in a hydrocephalic brain increases, the dependence of $\Delta\sigma_{rr}(b)/\Delta p_a^{\infty}$ on k_1 becomes more significant.

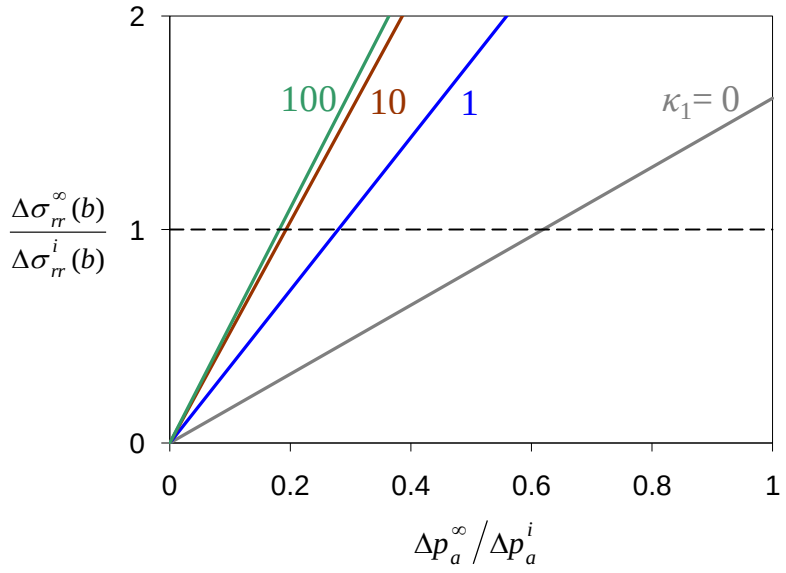

(a)

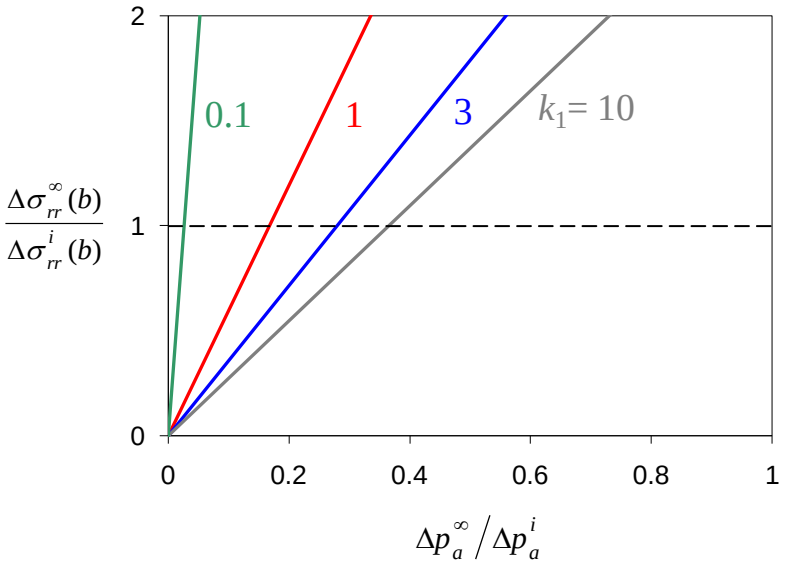

(b)

Figure 7.15. The variation of $\Delta\sigma_{rr}^{\infty}(b)/\Delta\sigma_{rr}^{i}$ (b) with $\Delta p_a^{\infty}/\Delta p_a^{i}$ for some values of (a) κ_1 and (b) k_1.

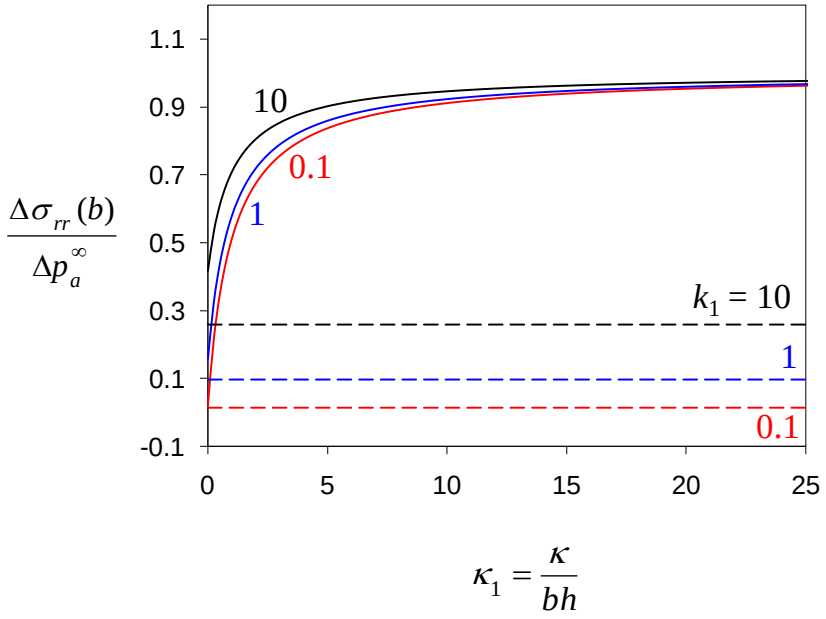

(a)

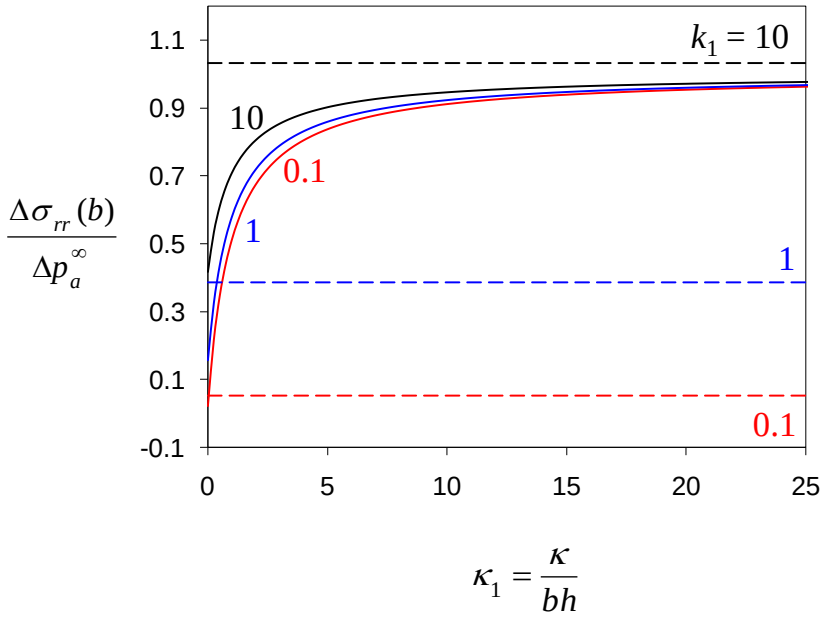

(b)

Figure 7.16. Dependence of normalized radial stress change, $\Delta\sigma_{rr}(b)/\Delta p_a^{\infty}$, on κ_1 for some values of k_1. Instantaneous stresses are plotted for (a) $\Delta p_a^{\infty}/\Delta p_a^{i} = 1$ and (b) $\Delta p_a^{\infty}/\Delta p_a^{i} = 0.25$. Dashed and solid lines correspond to the response of brain during ventriculustomy and in long-term post-operative stage, respectively.

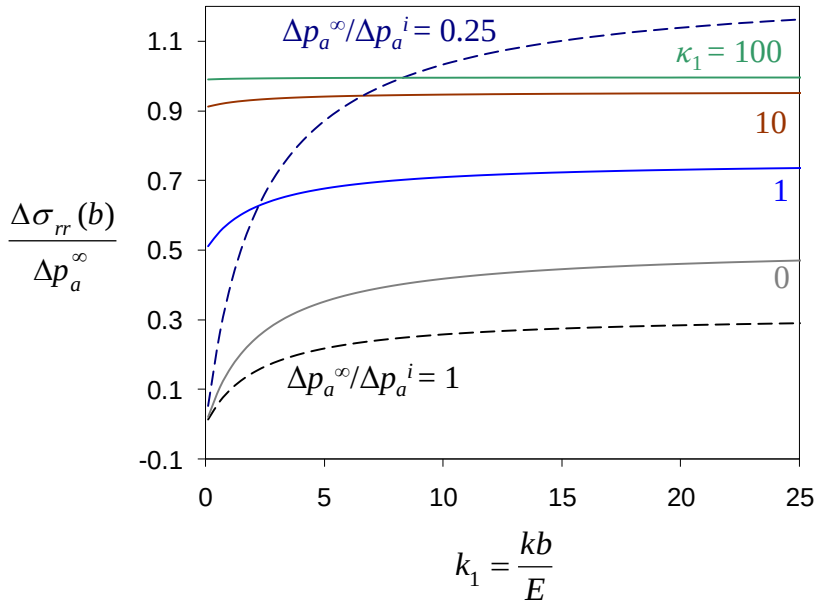

Figure 7.17. Dependence of normalized radial stress change, $\Delta\sigma_{rr}(b)/\Delta p_a^{\infty}$, on k_1 for some values of κ_1. Instantaneous stresses are plotted for $\Delta p_a^{\infty}/\Delta p_a^{i} = 1$ and $\Delta p_a^{\infty}/\Delta p_a^{i} = 0.25$. Dashed and solid lines correspond to the response of brain during ventriculustomy and in long-term post-operative stage, respectively.

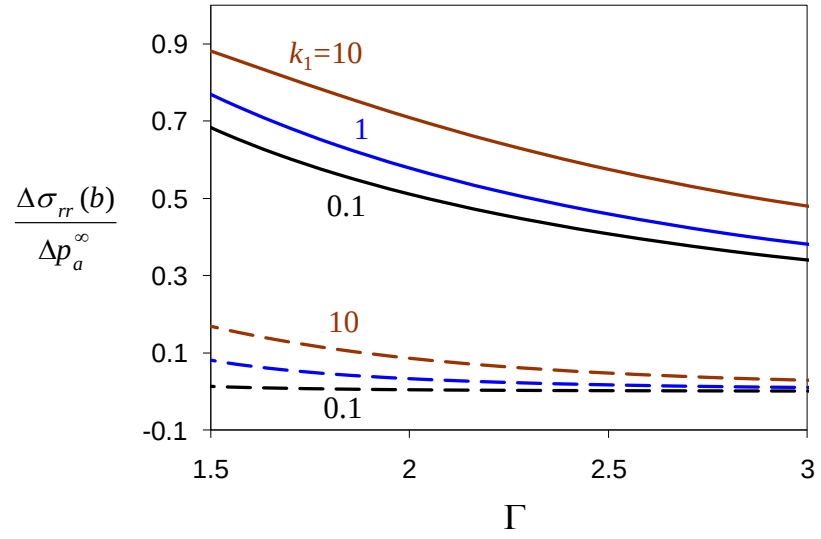

(a)

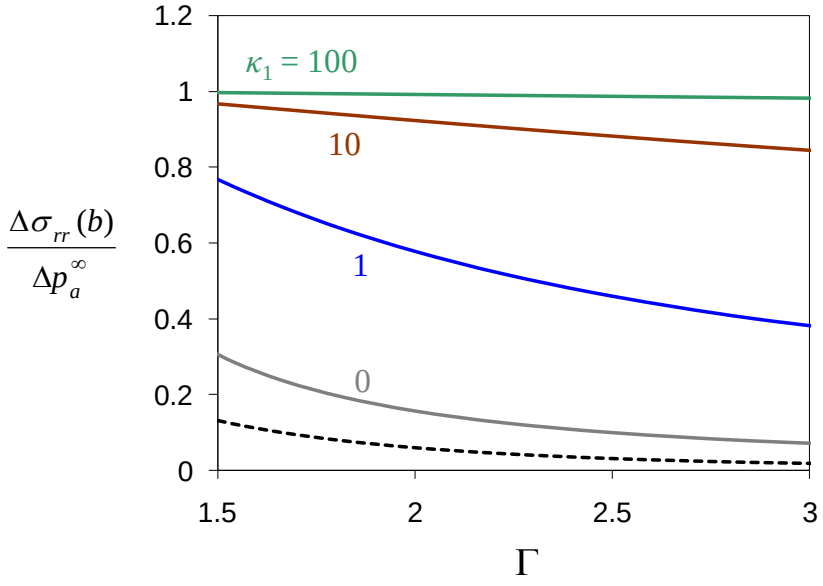

(b)

Figure 7.18. Dependence of normalized radial stress change, $\Delta\sigma_{rr}(b)/\Delta p_a^{\infty}$, on the ventricular respect ratio, Γ, for some values of (a) κ_1 and (b) k_1. Instantaneous stresses are plotted for $\Delta p_a^{\infty}/\Delta p_a^{i} = 1$. Dashed and solid lines correspond to the response of brain during ventriculostomy and in long-term post-operative stage, respectively.

It is likely that the behavior of the brain tissue is more complicated in the long term due to other time effects (e.g., viscoelasticity, plasticity). *Smillie et al.* [2005] successfully modeled hydrocephalus using a similar model and the time scale that we consider here is comparable. Consequently, we conclude that our model would also be in agreement with clinical observations.

7.8 Discussion

We developed a poroelastic model of the ventriculostomy procedure and studied the effect of model parameters on the radial stress increment at subdural space. However, this is not sufficient to model the appearance of subdural hematoma since the condition of failure, given in (7.3.1), is formulated based on total stress at the subdural space**.** Unfortunately, the distribution of the initial stresses in the brain is not known. It depends upon the history of a particular decease, say hydrocephalus, cerebral atrophy, or injury. The issue of the initial stresses is common for many disciplines. In earth sciences, for example, finding *in-situ* stresses in the lithosphere represents one of the most challenging and well recognized problems [*Engelder*, 1992; *Amadei and Stephansson*, 1997]. When these stresses are not known due to the complicated geological history of a particular rock formation, possible effect of human interference, for example, seismicity induced as a result of petroleum production [e.g., *Segall*, 1998; *Chapura and Germanovich*, 2004], is evaluated based on stress increments (changes) caused by this interference. Consequently, even though it is not possible to predict the occurrence of subdural hematoma unless initial stresses are known, the stress increments are still useful since they indicate the tendency for the hematoma to develop.

Following others [i.e., *Nagashima et al.*, 1987; *Kaczmarek et al.*, 1997; *Levine*, 1999; *Smillie et al.*, 2005], we used, for simplicity, the small-strain theory in our derivations. It is well known that soft biological tissues, including brain tissue, are highly non-linear materials and can undergo large deformations [*Fung*, 1993; *Miller and Chinzei*, 1997; *Holzapfel*, 2005]. Depending on the loading conditions, both linear and non-linear models have been used to describe the behavior of brain tissue [*Kyriacou et al.*, 2002]. During hydrocephalus, large deformation of the brain parenchyma can occur [*Kaczmarek et al.*, 1997; *Drapaca et al.*, 2006; *Franceschini et al.*, 2006]. Accordingly, it can be expected to have large deformations during reverse procedure, ventriculostomy operation, and thus, the large-strain theory is more appropriate. However, in this work, we are not concerned with developing a model capable of precisely predicting post-operative behavior of the brain but we intend to study the tendency for appearance of subdural hematoma due to ventriculostomy operation. Because of our particular goal, the small-strains assumption has a little effect on the validity of the conclusions drawn in this study.

An alternative to shunt placement for the treatment of non-communicating hydrocephalus is endoscopic third ventriculostomy (ETV). In this operation, instead of inserting an external shunt into intracranial cavity, the excess pressure in the ventricles is relieved by making a hole in the floor of third ventricle and re-establishing communication between ventricles and subarachnoid space [*Grant and McLone*, 1997; *Aschoff et al.*, 1999; *Hellwig et al.*, 2005]. To simulate the response of a hydrocephalic brain to ETV in the long term post-operative stage, we use the model developed in this section. We assume that the hydraulic conductivity of the hole created in the floor of

third ventricle is much larger than that of brain tissue. In this case, CSF produced in the ventricles flows through the hole instead of percolating through the brain parenchyma. Accordingly, CSF pressure in the subarachnoid space is not governed by the permeability of the brain. Moreover, the pressure in the ventricles is no longer controlled by the shunt but the hydraulic conductivity of the hole which connects ventricles and subarachnoid space. Therefore, in our ETV model, the ventricular pressure after operation is not completely arbitrary. Since the ventricles and subarachnoid space are in communication, the minimum possible pressure in the ventricles in the long term post-operative stage, p_a^{∞}, is the CSF pressure in subarachnoid space before the operation, p_b^{0}, and similarly, maximum possible subarachnoid space pressure is the pressure in the ventricles before the operation, p_b^{0}.

In order to incorporate these modifications in our model, we eliminate the effect of CSF diffusion through the brain on the boundary condition defined in expression (7.2.9) assuming there is no resistance to CSF absorption in subarachnoid space, i.e., $h \to \infty$, in the long term post-operative stage. For this case, the change in the radial stress at $r = b$ becomes

$$\sigma_{rr}(b) = -2\alpha p_* \frac{1-2\nu}{1-\nu} + \frac{A_1}{3\beta}\frac{1+\nu}{1-\nu} - \frac{2A_2(1-2\nu)}{\beta(1-\nu)b^3} + \sigma_{rr}^0(b) \tag{7.8.1}$$

where

$$\begin{cases} A_1 = 6A_2 \dfrac{1-2\nu}{1+\nu}\dfrac{1}{a^3} - 3\beta\dfrac{1-\nu}{1+\nu}(p_a^{\infty} - p_a^0) \\ A_2 = \left\{\alpha p_*\left(2\dfrac{1-2\nu}{1-\nu} - k\beta b\right) + (p_a^{\infty} - p_a^0)\left[k\beta b\dfrac{1-\nu}{1+\nu} + 1\right] - (p_b^{\infty} - p_b^0)\right\}\beta C \end{cases} \tag{7.8.2}$$

and

$$p_* = \frac{p_a^\infty - p_s}{3}\left(1-\frac{a^3}{b^3}\right) - \frac{p_a^\infty - p_b}{\frac{1}{a}-\frac{1}{b}}\left[\frac{1}{3a}\left(1-\frac{a^3}{b^3}\right) - \frac{1}{2b}\left(1-\frac{a^2}{b^2}\right)\right] \\ -\frac{\eta}{\kappa}\frac{p_a^0 - p_s}{4\pi b B_v^0}\left[\frac{1}{2}\left(1-\frac{a^2}{b^2}\right) + \left(\frac{\kappa}{bh_0}-1\right)\frac{1}{3}\left(1-\frac{a^3}{b^3}\right)\right] \tag{7.8.3}$$

where h_0 is the absorption parameter before the operation and

$$B_v^0 = \frac{\eta}{4\pi h_0 \kappa}\left[\frac{\kappa}{b^2} + h_0\left(\frac{1}{a}-\frac{1}{b}\right)\right] \tag{7.8.4}$$

The dependence of the radial stress change, $\Delta\sigma_{rr}(b)$, on κ_1 is shown in Figure 7.19. For these plots, we used a transmantle pressure difference of 30 Pa [*Linninger et al.*, 2007] and considered rigid trabeculea. The radial stress in the subdural space material decreases as a result of ETV whereas it increases after shunting (Figure 7.19). This explains the success of ETV which rarely leads to subdural hematoma [*Kim et al.*, 2004].

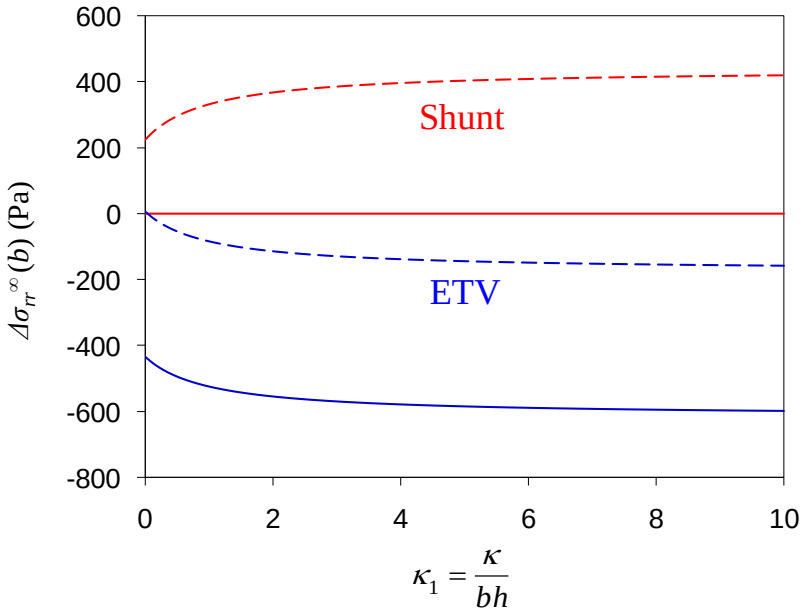

Figure 7.19. Dependence of the radial stress change, $\Delta\sigma_{rr}(b)$, due to shunting and ETV on κ_1. Transmantle pressure difference, $p_a^{\infty} - p_b^{\infty}$, is 30 Pa. Dashed lines correspond to $p_a^{\infty} = p_a^{0} = 1570$ Pa and solid lines correspond to $p_b^{\infty} = p_b^{0} = 1100$ Pa.

As in most of works modeling hydrocephalus [*Hakim et al.*, 1976; *Nagashima et al.*, 1987; *Kaczmarek et al.*, 1997; *Tenti et al.*, 1999; *Levine*, 2000; *Tenti et al.*, 2000; *Taylor and Miller*, 2004; *Sivaloganathan et al.*, 2005a; *Sivaloganathan et al.*, 2005b; *Smillie et al.*, 2005], we did not include the volumetric absorption of CSF in brain tissue in our model focusing on the onset of subdural hematoma resulting from the ventriculostomy treatment. To consider the effect of volumetric absorption, we follow *Levine* [1999], who, as mentioned above, used the volumetric absorption rule, $q_p(r) = k_p[p(r) - p_s]$, and employed the boundary conditions $p(a) = p_a$, $p(b) = p_s$, $\sigma_{rr}(a) = -p_a$, $u_r(b) = 0$. In this case, the diffusion equation (7.2.3) becomes

$$\frac{1}{M}\frac{\partial p}{\partial t} + \alpha\frac{\partial}{\partial t}\left(\frac{\partial u}{\partial r} + 2\frac{u}{r}\right) = \frac{\kappa}{\eta}\left(\frac{\partial^2 p}{\partial r^2} + \frac{2}{r}\frac{\partial p}{\partial r}\right) + q_p(r) \tag{7.8.5}$$

while equilibrium condition (7.2.1) and constitutive relation (7.2.2) remain the same [*Detournay and Cheng*, 1993]. *Levine* [1999] obtained the steady-state pressure

$$p^{\infty}(r) = p_s + (p_a - p_s)\frac{a\sinh\dfrac{b-r}{\sqrt{\kappa_2}}}{r\sinh\dfrac{b-a}{\sqrt{\kappa_2}}} \tag{7.8.6}$$

and stress change

$$\Delta\sigma_{rr}^{\infty}(r) = \frac{2(1-2\nu)}{1-\nu}\frac{\alpha(p_a - p_a^0)a}{\sinh\dfrac{b-a}{\sqrt{\kappa_2}}}\left[\frac{\sqrt{\kappa_2}\cosh\dfrac{b-r}{\sqrt{\kappa_2}}}{r^2} + \frac{\kappa_2\sinh\dfrac{b-r}{\sqrt{\kappa_2}}}{r^3}\right] - 4G\frac{C_1}{r^3} + \frac{2G(1+\nu)}{1-2\nu}C_2 \tag{7.8.7}$$

distributions in brain parenchyma. Here, $G = E/[2(1 + \nu)]$ is the shear modulus, coefficients

$$C_1 = \frac{(p_a^\infty - p_a^0)b^3}{2G\left[\Gamma^3 + \frac{1+\nu}{2(1-2\nu)}\right]} \times \left[\frac{1}{2} + \frac{(1-2\nu)\alpha\sqrt{\kappa_2}}{1-\nu}\left(\frac{\cosh\frac{b-a}{\sqrt{\kappa_2}} + \frac{1+\nu}{2(1-2\nu)\Gamma^2}}{a\sinh\frac{b-a}{\sqrt{\kappa_2}}} + \frac{\sqrt{\kappa_2}}{a^2}\right)\right] \tag{7.8.8}$$

$$C_2 = -\frac{p_a^\infty - p_a^0}{2G\left[\Gamma^3 + \frac{1+\nu}{2(1-2\nu)}\right]}\left[\frac{1}{2} + \frac{(1-2\nu)\alpha\sqrt{\kappa_2}}{1-\nu}\left(\frac{\cosh\frac{b-a}{\sqrt{\kappa_2}} - \Gamma}{a\sinh\frac{b-a}{\sqrt{\kappa_2}}} + \frac{\sqrt{\kappa_2}}{a^2}\right)\right] \tag{7.8.9}$$

and $\kappa_2 = \kappa/(\eta k_p)$.

For the radial stress in the subarachnoid stress, we have

$$\sigma_{rr}^\infty(b) - \sigma_{rr}^0(b) = \frac{2(1-2\nu)}{1-\nu}\frac{\alpha(p_a^\infty - p_a^0)a}{\sinh\frac{b-a}{\sqrt{\kappa_2}}}\frac{\sqrt{\kappa_2}}{b^2} - 4G\frac{C_1}{b^3} + \frac{2G(1+\nu)}{1-2\nu}C_2 \tag{7.8.10}$$

and coefficient k_p can be estimated from the condition that approximately one third of CSF is absorbed in the brain parenchyma. Then, the equation for k_p is

$$-\frac{\kappa}{\eta}\frac{\partial p}{\partial r}4\pi a^2\varepsilon = \int_a^b k_p[p^\infty(r) - p_s]4\pi r^2 dr \tag{7.8.11}$$

where the right hand side indicates the amount of CSF that enters brain (per unit time) through the ventricle walls at $r = a$ and the part $\varepsilon \approx 1/3$ of this amount that is absorbed in the brain, which is indicated by the left hand side.

Substituting (7.8.5) into (7.8.11), we obtain an equation

$$f = \kappa_3 \sinh\frac{\Gamma - 1}{\kappa_3} + \cosh\frac{\Gamma - 1}{\kappa_3} - \frac{\Gamma}{1-\varepsilon} = 0 \qquad (7.8.12)$$

for the dimensionless parameter $\kappa_3 = (1/a)[\kappa/(\eta\, k_p)]^{1/2}$. In the case of $\Gamma = b/a = 2$ and $\varepsilon = 1/3$, the solution of (7.8.12) is $\kappa_3 = 0.85$ (Figure 7.20), which constrains the coefficient of volumetric absorption, k_p. For the values of parameters a, κ, and η given in Table 7.1, $k_p \approx 5.5\times10^{-9}$ 1/(Pa·sec).

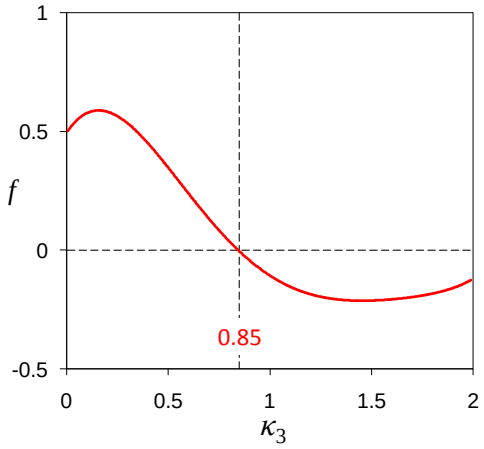

Figure 7.20. Solution of equation (7.8.12) in the case of $\Gamma = b/a = 2$ and $\varepsilon = 1/3$.

Levine's [1999] boundary conditions correspond to the limit of $h \to \infty$ and $k \to \infty$ in our model. This corresponds to $\kappa_1 \to 0$ and $k_1 \to \infty$ in (7.6.15), so that expressions (7.6.16) and (7.7.11) for radial subdural stresses result in

$$\frac{\Delta\sigma_{rr}^{i}(b)}{\Delta p_a^i} = \frac{\sigma_{rr}^{i}(b) - \sigma_{rr}^{0}(b)}{p_a^0 - p_a^i} = \frac{3(1-\nu)}{1+\nu+2(1-2\nu)\Gamma^3} \quad (h \to \infty, k \to \infty) \tag{7.8.13}$$

and

$$\frac{\Delta\sigma_{rr}^{\infty}(b)}{\Delta p_a^{\infty}} = \frac{\sigma_{rr}^{\infty}(b) - \sigma_{rr}^{0}(b)}{p_a^0 - p_a^{\infty}} = \\ = \frac{\Delta\sigma_{rr}^{i}(b)}{\Delta p_a^i} \frac{3(1-\nu)(\Gamma-1) + (1-2\nu)(2-3\Gamma+\Gamma^3)\alpha}{3(1-\nu)(\Gamma-1)} \quad (h \to \infty, k \to \infty) \tag{7.8.14}$$

respectively. Therefore, as follows from (7.8.13) and (7.8.14),

$$\frac{\Delta\sigma_{rr}^{\infty}(b)}{\Delta p_a^{\infty}} = \frac{3(1-\nu)(\Gamma-1) + (1-2\nu)(2-3\Gamma+\Gamma^3)\alpha}{(\Gamma-1)[1+\nu+2(1-2\nu)\Gamma^3]} \quad (h \to \infty, k \to \infty) \tag{7.8.15}$$

The variation of normalized stress changes (7.8.10) and (7.8.15) as a function of Poisson's ratio, *v*, are shown in Figure 7.21. Since the plot covers Poisson's ratio values corresponding to both drained and undrained conditions, in order to have conservative results, we use the undrained Young's modulus of the brain (Table 7.1) in (7.8.10). The volumetric absorption of CSF in the brain reduces the radial stress in the subdural space material and hence, the risk of appearance of subdural hematoma.

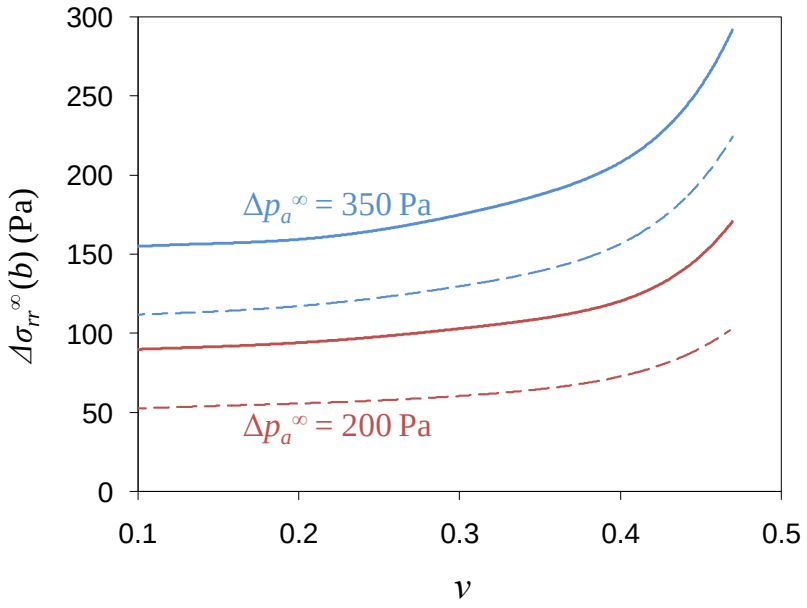

Figure 7.21. Dependence of the radial stress change, $\Delta\sigma_{rr}^{\infty}(b)$, on Poisson's ratio. Dashed and solid lines correspond to the response of brain to ventriculostomy with and without volumetric absorption of CSF in the brain, respectively.

7.9 Conclusions

In this work, we modeled the appearance of subdural hematoma as a result of a ventriculostomy operation. Similar to existing models of hydrocephalus, we treated the brain as a poroelastic hollow sphere. In order to simulate the subarachnoid space, we implemented a new boundary condition, which accounts for both the effects of pressure in the subarachnoid space and the deformation of subarachnoid trabeculae. We evaluated displacements and stresses in the brain due to a ventriculostomy operation. Our results show that reducing the ventricular pressure as a result of shunt emplacement can significantly increase normal stresses on the subdural interface. This can indeed cause subdural hematoma if the stresses become tensile and separate dura from the arachnoid mater. Our results also suggest that, subdural hematoma is more likely to happen in the long term post-operative recovery stage. Furthermore, subdural stresses strongly depend upon mechanical properties of brain tissue. For example, subdural stresses may be appreciably decreased by reducing the permeability of the brain material or increasing the absorption of cerebrospinal fluid in subarachnoid space. Similarly, decreasing the rigidity of trabeculae or increasing the stiffness of brain material may also reduce these stresses. This may have a significant clinical importance since it may become possible to avoid subdural hematoma by affecting the properties of the intracranial materials pharmacologically or by changing the initial stress state in the subdural space before the operation.

Based on clinical observations [*Hakim et al.*, 1976], we estimated the stiffness of trabeculae. Previously, this parameter has been unknown. We also discussed the success of the Endoscopic Third Ventriculostomy in the view of developed model. There is no

universally accepted model of cerebrospinal fluid (CSF) circulation within the cranial cavity. In this work, we assumed that CSF is produced in the ventricular cavity and absorbed in the subarachnoid space, and compared our results with an alternative model [*Levine*, 1999] in which CSF is allowed to be absorbed in brain parenchyma. We found that absorption of CSF in the brain parenchyma decreases the magnitude of tensile stress in the subdural space material and, therefore, the likelihood of subdural hematoma. This result may also be useful for future clinical practice if there will be a way to increase CSF absorption within physiologically acceptable limits.

CHAPTER VIII

CONCLUSIONS AND RECOMMENDATIONS

8.1 Conclusions

This dissertation proposes a new approach for modeling mechanical behavior of the *in-vivo* human brain tissue for applications in therapy and neurosurgery. We call this approach Image Guided Constitutive Modeling (IGCM). Importance of IGCM arises from the fact that image guided neurosurgery is mainly based on pre-operative (non-deformed) images of brain while the brain undergoes considerable deformations when the skull is opened. Such deformations strongly affect many high-risk neurosurgical operations and in some cases lead to fatal results. Applications of IGCM include subdural electrode placement in epilepsy surgery, brain shift compensation during craniotomy, needle guidance during brain biopsy, and simulating specific complicated neurosurgical procedures before performing them on real patients or for the purpose of training surgeons.

IGCM consists of defining the mechanical properties of the brain tissue *in-vivo* by taking the MRI or CT images of a brain response to ventriculostomy – the relief of the elevated intracranial pressure. Then, based on 3-D image analysis, the displacement fields are recovered from these images. Using inverse analysis and a robust numerical method allowing for reliable computations of large-strain deformations, constitutive parameters of the brain tissue are determined. In this work, the IGCM approach was tested in controlled laboratory experiments with silicone brain models mimicking the *in-vivo* brain

geometry, mechanical properties, and boundary conditions. The ventriculostomy was simulated by successively inflating and deflating internal cavities that model cerebral ventricles. The obtained CT images were analyzed to determine 3-D displacement fields, meshed, and incorporated into a finite element code. The subsequent inverse analysis allowed for determination of the hyper-elastic (neo-Hookean) constitutive parameter of the brain model material. The obtained mechanical properties have been verified with direct laboratory tests.

One important application of IGCM lies in treatment of tumors that cause non-communicating hydrocephalus. Hydrocephalus typically requires ventriculostomy, which can be used for obtaining the constitutive parameters of the brain tissue for each patient undergoing this procedure. When such a tumor needs to be removed, these parameters could be used for planning and guidance of the tumor resection operation on the same patient for whom they had been previously determined using the ventriculostomy and IGCM.

Therefore, successful image-based inverse 3-D finite element analysis of the simulated ventriculostomy procedure represents important steps towards the development of a method for a non-invasive derivation of the mechanical properties of *in-vivo* brain tissue, which has a number of clinical applications.

Other conclusions of this work include:

- If initial parameters in inverse analysis are varied when performing successive forward simulations until a reasonable match between experimental data and model

predictions is achieved, a convergent solution can be obtained. However, this does not guarantee the uniqueness of the solution.

- Neglecting gravity and hydrostatic pressure on the outer surface of the brain phantom may lead to significant differences in displacements. Since the inverse analysis is formulated using the displacement fields, this also affects the calculated model parameters. Moreover, stress state of the simulations performed without gravity and hydrostatic pressure on the outer surface are significantly different.

- In order to be able to calculate stresses and displacements during the operation, the relationship between configurations must be established. Since the reference configuration is gravity-free, it is not possible to predict the geometry and stress state of the body in this configuration. Even though the stress-free reference configuration assumption simplifies the problem, it is not possible to identify the geometry of the phantom in this configuration.

- Since the specific gravity of the brain and the silicone gel is close to unity, both materials practically suspend in the water and CSF. As a result, for all practical purposes, all deformations in the silicone phantom (and the brain tissue) are negligible under the hydrostatic boundary loading conditions in the initial configuration. Moreover, the corresponding hydrostatic stress state develops inside the material which is independent of the material parameters.

- In this work, the development of hydrocephalus was simulated rather than the ventriculostomy operation. However, due to the stress relaxation in the brain under

transmantle pressure gradients, the external and internal pressures subsequently equalize. Because of that, the generality of the proposed procedure is not affected.

- The neo-Hookean strain energy function is an effective model to describe the behavior of the silicone gel material.

- The first attempt to apply image based inverse 3-D finite element analysis to the simulated ventriculostomy procedure seems encouraging. This is the initial step towards the application of IGCM to such a complex phenomenon as the behavior of human brain during real ventriculostomy procedures.

Similar to brain tissue, there are other parts of the human body (such as liver, kidney, or breast) that can also be characterized by IGCM principles. In this thesis, we also developed a quantitative large-strain 3-D mechanical model of female breast deformation. Breast cancer is the second most prevalent cancer in women, and an operative mastectomy, in which breast tissue is removed, is frequently a part of the treatment. Women often choose to follow a mastectomy with a reconstruction surgery using a breast implant. Furthermore, there is a growing demand for breast augmentation for the sake of aesthetic improvement. Yet, millions of women requested revisional operations because the resulted breast form differed from their expectations. Accurate pre-operative simulation of these augmenting and reconstructive procedures is important. Additionally, a mechanical understanding of factors affecting breast deformation and shape, such as properties of skin and breast tissue, may affect the therapeutic procedures and non-operative augmentation techniques (e.g., choosing proper breast skin care).

Several modes of breast deformation were simulated in this work using finite element modeling. A rather realistic breast shape was obtained considering a hyper-elastic breast tissue enclosed in an elastic skin and loaded by gravity. The results show that the stiffness of skin and the constitutive parameters of the breast tissue are important factors affecting breast shape. For example, a relatively high skin modulus is what causes a higher breast form, while low skin modulus results in lowering the breast. The skin modulus becomes more important to the overall breast form as the modulus of the tissue decreases. Our computations indicate that the lowering of breast form with age can indeed be explained by changes in skin and tissue properties. Even more importantly, our results make it seem feasible that IGCM analyses could be used to improve how breast surgery is conducted by accurately predicting the resulting breast form.

Subdural hematoma (tearing and bleeding between scull and brain) is one of the major complications of the ventriculostomy operations. Understanding the mechanism of subdural hematoma is critically important for development of more effective medical treatments. In this work, we also modeled the appearance of subdural hematoma as a result of a ventriculostomy procedure. We treated the brain as a poroelastic hollow sphere and implemented a new boundary condition, which accounts for both the effects of pressure in the subarachnoid space and the deformation of subarachnoid trabeculae. Our results show that reducing the ventricular pressure in the ventricular cavity can significantly increase normal stresses on the subdural interface. This can indeed cause subdural hematoma if the stresses become tensile and separate dura from the arachnoid mater. Our results also suggest that, subdural hematoma is more likely to happen in the long term post-operative recovery stage. Furthermore, subdural stresses strongly depend

upon mechanical properties of brain tissue. This may have a significant clinical importance since it may become possible to avoid subdural hematoma by affecting the properties of the intracranial materials pharmacologically or by changing the initial stress state in the subdural space before the operation.

Based on clinical observations [*Hakim et al.*, 1976], we estimated the stiffness of trabeculae. Previously, this parameter has been unknown. We also discussed the success of the Endoscopic Third Ventriculostomy in the view of developed model. In addition, in this work, we assumed that CSF is produced in the ventricular cavity and absorbed in the subarachnoid space, and compared our results with an alternative model [*Levine*, 1999] in which CSF is allowed to be absorbed in brain parenchyma. We found that absorption of CSF in the brain parenchyma decreases the magnitude of tensile stress in the subdural space material and, therefore, the likelihood of subdural hematoma. This result may also be useful for future clinical practice if there will be a way to increase CSF absorption within physiologically acceptable limits.

8.2 Recommendations for Future Studies

In our opinion, the following issues deserve special attention in the future:

- The geometry for the ventricles used in this study is fairly simple. Ventricles with a more realistic geometry should be investigated.

- For the current work, a hyper-elastic constitutive model of the silicone gel seems to be a reasonable approximation as hydrocephalus develops over a few days. However,

in order to be able to generalize the proposed procedure for broader applications, e.g. for low to medium strain rates encountered during surgical intervention, the inverse analysis should be extended to allow for the hyper-viscoelastic constitutive models of brain tissue.

- For more realistic modeling of hydrocephalus, a model of a skull (covering the brain phantom) should be included both in experiments and finite element analysis.

- The mechanical behavior of the leptomeninges is not well understood. Research on the behavior of the brain-skull interface is as important as the research on the mechanical behavior of the brain tissue.

- Pia mater is attached to the surface of the brain. Due to its collagenous structure, it is expected to be stiffer than brain tissue. The effect of pia mater to the overall response of brain parenchyma should be investigated.

- Ventricles are lined with ependymal cells. The effect of ependymal lining of the ventricles on the response of the brain tissue to mechanical excitations should be further investigated.

- The volumetric response of the brain tissue must be characterized.

- Effect of microstructure of the brain to its overall deformation behavior should be investigated.

- Pathophysiologic consequences of hydrocephalus and their effect on the mechanical properties of the brain tissue must be addressed.

REFERENCES

"Birck Cox Medical Illustrations," http://www.bcillustration.com (Accessed December 25, 2007).

"Head Trauma, Subdural, Extradural," http://www.geocities.com/drweightloss/neurosurgery/neurosurgery.html (Accessed December 25, 2007).

"Shaken Baby Syndrome," http://www.acsu.buffalo.edu/~lcscott/shakenbabysyndrome.html (Accessed December 25, 2007).

ABAQUS® (2004) "ABAQUS/Standard Version 6.6-1, User's Manual and Theory Manual," Hibbit, Karlson and Sorensen, Inc.

Agache, P.G., Monneur, C., Leveque, J.L. and Derigal, J. (1980) "Mechanical properties and Young's Modulus of human skin in-vivo," Archives of Dermatological Research, 269, 221-232.

Agamanolis, D., "Traumatic brain injury – Subdural Hematoma," http://www.neuropathologyweb.org/chapter4/chapter4aSubduralepidural.html (Accessed December 25, 2007).

Albeck, M., Borgesen, S., Gjerris, F., Schmidt, J. and Sorensen, P. (1991) "Intracranial pressure and cerebrospinal fluid outflow conductance in healthy subjects," Journal of Neurosurgery, 74, 597-600.

Albright, P., Pollack, I.F. and Adelson, D.P. (1998) "Principles and practice of pediatric neurosurgery," Thieme Medical Publishers, Incorporated.

Amadei, B. and Stephansson, O. (1997) "Rock stress and its measurement," Chapman & Hall, 1st edition.

ANALYZE (2002) AnalyzeDirect, BIR, Mayo Clinic.

Arriada, N. and Sotelo, J. (2002) "Review: Treatment of hydrocephalus in adults," Surgical Neurology, 58, 377-84.

Aschoff, A., Kremer, P., Hashemi, B. and Stefan Kunze, S. (1999) "The scientific history of hydrocephalus and its treatment," Neurosurgical Review, 22, 67-93.

Aster, R.C., Borchers, B. and Thurber, C.H. (2005) "Parameter estimation and inverse problems," Elsevier.

Atkin, R.J. and Fox, N. (1980) "An introduction to the theory of elasticity," Dover Publications.

Audette, M.A. et al. (1999) "Level-set surface segmentation and fast cortical range image tracking for computing intrasurgical deformations," Medical Image Computing and Computer-Assisted Intervention (MICCAI), Cambridge, UK, 788-797.

Augenstein K.F., Cowan B.R., Legrice, I.J., Nielsen, P.M.F. and Young A.A. (2005) "Method and Apparatus for soft tissue material parameter estimation using tissue tagged magnetic resonance imaging," Journal of Biomechanical Engineering, 127, 148-157.

Azar, F.S., Metaxas, D.N. and Schnall, M.D. (2000) "A finite model of the breast of predicting mechanical deformations during biopsy procedure," IEEE Workshop on Mathematical Methods in Biomedical Image Analysis, South Carolina, USA, 38-45.

Azar, F.S., Metaxas, D.N. and Schall, M.D. (2002) "Methods for modeling and predicting mechanical deformations of the breast under external perturbations," Medical Image Analysis, 6(1), 127.

Azar, F.S., Metaxas, D.N. and Schall, M.D. (2004) "Methods for predicting mechanical deformations of the breast under external perturbations," Editor: Ciarlet, P.G., Computational Models for the Human Body, Special volume of Handbook of Numerical Analysis, Vol XII, Elsevier.

Azar, F.S., Metaxas, D.N., Miller, R.T. and Schall, M.D. (2000) "Methods for predicting mechanical deformations in the breast during clinical breast biopsy," Proceedings of the IEEE 26th Annual Northeast Bioengineering Conference.

Balaniuk, R. and Costa, I.F. (2006) "3D simulation of reconstructive breast surgery," In: 2nd Workshop on Computer Assisted Diagnosis and Surgery, 2006, Santiago.

Bear, J. (1988) “Dynamics of fluids in porous media,” Dover Publications.

Bilston, L.E. (2002) “The effect of perfusion on soft tissue mechanical properties: a computational model,” Computer Methods in Biomechanics and Biomedical Engineering, 5(4), 283-290.

Bilston, L.E., Liu, Z. and Phan-Thien, N (2001) “Large strain behaviour of brain tissue in shear: Some experimental data and differential constitutive model,” Biorheology, 38, 335-245.

Biot, M.A. (1941) “General Theory of three-dimensional consolidation,” Journal of Applied Physics, 12, 155.

Blinkov, S.M. (1968) “The human brain in figures and tables; a quantitative handbook,” Basic Books.

Bloomfield, I.G., Johnston, I.H. and Bilston, L.E. (1998) “Effects of proteins blood cells and glucose on the viscosity of cerebrospinal fluid,” Pediatric Neurosurgery, 28(5), 246-251.

Bostwick, J. (1990) “Plastic and reconstructive breast surgery,” Quality Medical Publishing Inc.

Bradbury, M. (1993) “Anatomy and physiology of CSF. In Hydrocephalus,” ed. Schurr, P. and Polkey, C., Oxford University Press, 19-47.

Bradshaw, D.R.S. et al. (2001) “Simulation of acute subdural hematoma and diffuse axonal injusry in coronal head impact,” Journal of Biomechanics, 34(1), 85-94.

Brands, D.W.A, Bovendeerd, P.H.M. and Wismans, J.S.H.M. (2002) “On the potential importance of non-linear viscoelastic material modeling for numerical prediction of brain tissue response: Test and application,” Stapp Car Crash Journal, 46,103-121.

Brands, D.W.A, Bovendeerd, P.H.M., Peters, G.W.M. and Wismans, J.S.H.M. (2000) “The large strain dynamic behavior of in-vitro porcine brain tissue and a silicone gel model material,” Stapp Car Crash Journal, 44, 249-260.

Brands, D.W.A, Peters, G.W.M. and Bovendeerd, P.H.M. (2004) "Design and numerical implementation of a 3-D non-linear viscoelastic constitutive model for brain tissue during impact," Journal of Biomechanics, 37, 127-134.

Carter, T.J., Tanner, C., Crum, W.R. and Hawkes, D.J. (2006) "Biomechanical model initialized non-rigid registration for image-guided breast surgery," Medical Image Computing and Computer Assisted Intervention (MICCAI), Copenhagen, Denmark, 104-112.

Catanuto, G., Spano, A., Pennati, A. Riggio, E., Farinella, G.M., Impoco, G., Spoto, S., Gallo, G. and Nava, M.B. (2008) "Experimental methodology for digital breast shape analysis and objective surgical outcome evaluation," J Plast Reconstr Aesthet Surg., 61 (3), 314-318.

Chanpura, R.A. and Germanovich, L.N. (2004) "Fault stability inside and near a depleting petroleum reservoir," in Proceedings of 6th North American Rock Mechanics Symposium (NARMS): Gulf Rocks 2004, Alexandria, VA: American Rock Mechanics Association.

COMSOL (2005) COMSOL Multiphysics, COMSOL Reaction Engineering Lab.

Chabrerie, A. and Black, P.M. (2002) "Ventricular shunts," Journal of Intensive Care Medicine, 17(5), 218-229.

Cheng, S. and Bilston, L.E. (2006) "Unconfined compression of white matter," Journal of Biomechanics, in press.

Chung, J., Rajagopal, V., Nielsen, P.M.F. and Nash, M.P. (2005) "Computational modeling of the breast during mammography for tumor tracking," Proceedings of the SPIE, Medical Imaging 2005: Physiology, Function, and Structure from Medical Images, 5746, 817-824.

Clarke, M.J. Maher, C.O., Nothdurft, G. and Meyer, F. (2006) "Very low pressure hydrocephalus. Report of two cases," J. Neurosurg, 105, 475-478.

Clarke, M.J. and Meyer, F.B. (2007) "The history of mathematical modeling in hydrocephalus," Neurosurgical Focus, Vol. 22, Number 44, Article E3.

Coats, B. and Margulies, S.S. (2006) "Material properties of porcine parietal cortex," Journal of Biomechanics, 39(13), 2521-2525.

Conner, E.S., Foley, L. and Black, P.M. (1984) "Experimental normal-pressure hydrocephalus is accompanied by increased transmantle pressure," Journal of Neurosurgery, 61, 322-327.

Czosnyka, M., Czosnyka, Z., Momjian, S. and Pickard, J.D. (2004) "Cerebrospinal fluid dynamics," Physiological Measurement, 25(5), R51-R76(1).

Detournay, E. and Cheng, A. H.-D. (1993) "Fundamentals of poroelasticity," Chapter 5, Comprehensive Rock Engineering, (J. Hudson, ed.), Vol. II, Pergamon Press, 113-169.

Dokos, S., Legrice, I.J., Smaill, B.H., Kar, J. and Young, A.A. (2000) "A triaxial-measurement shear-test device for soft biological tissues," Journal of Biomechanical Engineering, 122, 471-478.

Donnelly, B.R. and Medige, J. (1997) "Shear properties of human brain tissue," Journal of Biomechanical Engineering, 119, 423-432.

Dow Corning® (2005) Information about Dow Corning® brand dielectric gels. Dow Corning Corporation, Midland, Michigan 48686-0994.

Downie, A.C. (2001) "Tutorial: CT in Head Trauma," http://www.radiology.co.uk/srs-x/tutors/cttrauma/tutor.htm (Accessed December 25, 2007).

Drapaca, C.S., Tenti, G., Rohlf, K. and Sivaloganathan, S. (2006) "A quasi-linear viscoelastic constitutive equation for the brain: Application to hydrocephalus," Journal of Elasticity, 85, 65-83.

Einstein, A. (1916) "Die grundlage der allgemeinen relativitätstheorie," Annalen der Physik, 49, 769-822.

Elden, H.R. (1977) "Biophysical properties of skin," Wiley-Interscience.

Ellison, D., Love, S., Chimelli, L., Harding, B., Lowe, J., Roberts, G.W. and Vinters, H.V. (1998) "Neuropathology. A reference text of CNS pathology," Mosby, London.

Engelder, T. (1992) "Stress regimes in the lithosphere," Princeton University Press.

Estes, M.S. and McElhaney, J.H. (1970) "Response of brain tissue to compressive loading," ASME Paper No.70-BHF-13.

Fard, P.M.J., Tajvidi, M.R. and Gharibzadeh, S. (2007) "High-pressure hydrocephalus: A novel analytical modeling approach," Journal of Theoretical Biology, 248(3), 401-410.

Fergusson, J.E., Schor, A.M., and Howell, A. and Ferguson, M.W. (1992) "Changes in the extracellular matrix of the normal breast during the menstrual cycle," Cell Tissue Research, 268, 167-177.

Ferrant, M., Warfield, S.K., Nabavi, A., Jolesz, F.A. and Kikinis, R. (2000) "Registration of 3-D intraoperative MR images of the brain using a finite element biomechanical model," MICCAI 2000 Proceedings, Pittsburg, 19-28.

Fishman, R.A. (1992) "Cerebrospinal fluid in disease of the nervous system," Philadelphia, Saunders.

Franceschini, G. (2006) "The mechanics of human brain tissue," Ph.D. Dissertation, University of Trento.

Franceschini, G., Bigoni, D., Regitnig, P. and Holzapfel, G.A. (2006) "Brain tissue deforms similarly to filled elastomers and follows consolidation theory," Journal of the Mechanics and Physics of Solids, 54, 2592-2620.

Fukuhara, T., Vorster, S.J., Luciano, M.G. (2000) "Critical shunt-induced subdural hematoma treated with combined pressure-programmable valve implantation and endoscopic third ventriculostomy," Pediatric Neurosurgery, 33, 37-42.

Fung, Y.C. (1993) "Biomechanics. Mechanical properties of living tissues," Springer, New York.

Gefen, A. and Margulies, S.S. (2004) “Are in-vivo and in-situ brain tissues mechanically similar,” Journal of Biomechanics, 37, 1339-1352.

Gennarelli T.A. and Thibault L.E. (1982) “Biomechanics of acute subdural hematoma,” Journal of Trauma, 22(8), 680-686.

Germanovich L.N., Ozan, C., Murdoch L. and Mukundan, S. (2008). “A large-strain 3-D mechanical model of female breast deformation” (in preparation).

Goldsmith, W. (2001) “The state of head injury biomechanics: Past, present and future: Part 1,” Critical Reviews in Biomedical Engineering, 29, 5&6, 441-600.

Grant, J.A. and McLone, D.G. (1997) “Third ventriculostomy: A review,” Surgical Neurology, 47, 210-212.

Gray, H.F.R.S. (1995) “Anatomy, descriptive and surgical,” 15th Edition, Barnes & Noble.

Haines, D.E., Harkey, H.L. and Al-Mefty, O. (1993) “The “Subdural” space: A new look at an outdated concept,” Neurosurgery, 32, 111-120.

Hakim, S., Venegas, J.G. and Burton, J.D. (1976) “The physics of the cranial cavity, hemohydrocephalus, and normal pressure hyrocephalus: mechanical interpretation and mathematical model,” Surgical Neurology, 5, 187-210.

Hart-Smith, L.J. (1966) “Elasticity parameters for finite deformation of rubber-like materials,” Zeitschrift für Angewandte Mathematik und Physik, 17, 608-626.

Hellwig, D., Grotenhuis, J.A., Tirakotai, W., Riegel, T., Schulte, D.M., Bauer, B.L. and Bertalanffy, H. (2005) “Endoscopic third ventriculostomy for obstructive hydrocephalus,” Neurosurgical Review, 28, 1-34.

Holzapfel, G.A. (2000) “Nonlinear solid mechanics: A continuum approach for engineering,” John Wiley and Sons, Ltd.

Holzapfel, G.A. (2005) “Similarities between soft biological tissues and rubberlike materials,” In: P.-E. Austrell and L. Keri (eds.), "Constitutive Models for Rubber IV", A.A. Balkema Publishers: Leiden, 607-617.

Huang, H-M., Lee, M-C., Chiu, W-T, Chen, C-T. and Lee, S-Y. (1999) "Three-dimensional finite element analysis of subdural hematoma," Journal of Trauma, 47, 538-544.

Ivarsson, J. et al. (2000) "Strain relief from the cerebral ventricles during head impact: experimental studies on natural protection of the brain," Journal of Biomechanics, 33(2), 181-189.

Jacobson, E.E., Fletcher, D.P., Johnston, I.H. and Morgan, M.K. (1999) "Computer modelling of CSF flow in the subarachnoid space," J. Clinical Neuroscience, 6(6), 497-500.

Johnston, I., Hawke, S., Halmagyi, M. and Teo, C. (1991) "The pseudotumor syndrome: disorders of cerebrospinal fluid circulation causing intracranial hypertension without ventriculomegaly," Arch Neurol, 48, 740-747.

Joseph, C. (2006) "Pocket Anatomy, A complete guide to the human body for artists and students," Barron's, Hauppauge, New York.

Kaczmarek, M., Subramaniam, R.P. and Neff, S.R. (1997) "The hydromechanics of hydrocephalus: steady-state solutions for cylindrical geometry," Bulletin of Mathematical Biology, 59, 295-323.

Kalyanasundaram, S., Calhoun, V.D. and Leong, K.W. (1997) "A finite element model for predicting the distribution of drugs delivered intracranially to the brain," American Journal of Physiology - Regulatory, Integrative and Comparative Physiology, 273(5), 1810-1821.

Kamel, M.H., Murphy, M., Aquilina, K. and Marks, C. (2006) "Subdural haemorrhage following endoscopic third ventriculostomy. A rare complication," Acta Neurochirurgica, 148(5), 591-593.

Kanhai, R. and Hage, J. (1999) "Bra cup size depends on band size," Plast. Reconstr. Surg. 104, 300.

Katch, V.L., Campaigne, B., Freedson, P., Sady, S., Katch, F.I. and Behnke, A.R. (1980) "Contribution of breast volume and weight to body fat distribution in females," Am J Phys Anthropol. 53(1), 93-100.

Kauer, M., Vuskovic, V. and Dual, J. (2001) "Tissue aspiration and inverse finite element characterization of soft tissues," Computer Methods in Biomechanics and Biomedical Engineering, 4, 291-305.

Kim, B., Jallo, G., Kothbauer, K. and Abbott, I. (2004) "Chronic subdural hematoma as a complication of endoscopic third ventriculostomy," Surgical Neurology, 62(1), 64-68.

Klingbeil, W.W. and Shield, R.T. (1966) "Large-deformation analyses of bonded elastic mounts," Z.A.M.P. 17 (20), 281-305.

Koizumi, H., Fukamachi, A. and Nukui, H. (1987) "Postoperative subdural fluid collections in neurosurgery," Surgical Neurology, 27(2), 147-53.

Krouskop, T.A., Wheeler, T.M., Kallel, F., Garra, B.S. and Hall, T. (1998) "Elastic moduli of breast and prostate tissues under compression," Ultrasonic Imaging, 20, 260-274.

Kumar, V., Robbins, S.L. and Cotran, R.S. (2005) "Basis pathology," 7th Edition, Elsevier.

Kyriacou, S.K., Schwab C. and Humphrey J.D. (1996) "Finite element analysis of nonlinear orthotropic hyperelastic membranes," Computational Mechanics, 18, 269-278.

Kyriacou, K.K., Mohamed, A., Miller, K. and Neff, S. (2002) "Brain mechanics for neurosurgery: Modeling issues," Biomechanics and Modeling in Mechanobiology, 1(2), 151-164.

Lee, M.C. and Haut, R.C. (1989) "Insensitivity of tensile failure properties of human bridging veins to strain rate: implications in biomechanics of subdural hematoma," Journal of Biomechanics, 22, 537-542.

Levenberg, K. (1944) "A method for the solution of certain non-linear problems in least squares," Quart. Appl. Math., 2, 164-168.

Levine, D.N. (1999) "The pathogenesis of normal pressure hydrocephalus," Bulletin of Mathematical Biology, 61, 875-916.

Levine, D.N. (2000) "Ventricular size in pseudotumor cerebri and the theory of impaired CSF absorption," Journal of the Neurological Sciences, 177, 85-94.

Linninger, A.A., Tsakiris, C., Zhu, D.C., Xenos, M., Roycewicz, P., Danziger, Z. and Penn, R. (2005) "Pulsatile cerebrospinal fluid dynamics in the human brain," IEEE Transactions on Biomedical Engineering, 52(4), 557-565.

Linninger, A.A., Xenos, M., Zhu, D.C., Somayaji, R.C., Kondapalli, S. and Penn, R. (2007) "Cerebrospinal fluid flow in the normal and hydrocephalic human brain," IEEE Transactions on Biomedical Engineering, 54(2), 291-302.

Malata, C.M., Boot, J.C., Bradbury, E.T. et al. (1994) "Congenital breast asymmetry: Subjective and objective assessment," Br. J. Plast Surg, 47, 95-102.

Malvern, L.E. (1969) "Introduction to the mechanics of a continuous medium," Prentice-Hall, Inc.

Marquardt, D.W. (1963) "An algorithm for least-squares estimation of nonlinear parameters," Journal of the Society for Industrial and Applied Mechanics, 11(2), 431-441.

MATLAB (2007) The Mathworks Inc.

Meagher, R.J. and Young, W.F. (2006) "Subdural hematoma," http://www.emedicine.com/NEURO/topic575.htm (Accessed December 25, 2007).

Mendis, K.K., Stalnaker, R. L. and Advani, S.H. (1995) "A constitutive relationship for large deformation finite element modeling of brain tissue," Journal of Biomedical Engineering, 117, 279-285.

Merodio, J. and Ogden, R.W. (2003) "Instabilities and loss of elipticity in fiber-reinforced compressible non-linearly elastic solids under plane deformation," International Journal of Solids and Structures, 40, 4707-4727.

Metz, H., McElhaney, J. and Ommaya, A. (1970) "A comparison of the elasticity of live, dead and fixed brain tissue," Journal of Biomechanics, 3, 453-458.

Meyer, L. and Ringberg, A. (1987) "Augmentation mammaplasty-psychiatric and psychosocial characteristics and outcome in a group of Swedish women," Scand J Plast Reconstr Surg Hand Surg., 21(2), 199-208.

Miga, M.I., Paulsen, K.D., Hoopes, P.J., Kennedy, F.E., Hartov, A. and Roberts, D.W. (2000) "In-vivo quantification of a homogeneous brain deformation model for updating preoperative images during surgery," IEEE Transactions on Biomedical Engineering, 47(2), 266-273.

Miga, M.I., Roberts, D.W., Kennedy, F.E., Platenik, L.A., Hartov, A., Lunn, K.E. and Paulsen, K.D. (2001) "Computational modeling of retraction and resection for updating images during surgery," Neurosurgery, 49(1), 75-84.

Miller, K. (1998) "Modeling soft tissues using biphasic theory-a word of caution," Computer Methods in Biomechanics and Biomedical Engineering, 1, 216-263.

Miller, K. (1999) "Constitutive model of brain tissue suitable for finite element analysis of surgical procedure," Journal of Biomechanics, 32, 531-537.

Miller, K. and Chinzei, K. (2002) "Mechanical properties of brain tissue in tension," Journal of Biomechanics, 35, 483-490.

Miller, K. and Chinzei, K. (1997) "Constitutive Modeling of brain tissue: Experiment and theory," Journal of Biomechanics, 30(11/12), 1115-1121.

Miller, K., Chinzei, K., Orssengo, G. and Bednarz, P. (2000) "Mechanical properties of brain tissue in-vivo: Experiment and computer simulation," Journal of Biomechanics, 33, 1369-1376.

Miller, R.T., Smith, D.H., Chen, X. Xu, B.N., Leoni, M., Nonaka, M. and Meaney, D.F. (1999) "Comparing experimental data to traumatic brain injury finite element models," 43rd Stapp Car Crash Conference Proceedings, 303-311.

Miller, K., Taylor, Z. and Nowinski, W.L. (2005) "Towards computing brain deformations for diagnosis, prognosis and neurosurgical simulation," Journal of Mechanics in Medicine and Biology, 5(1), 105-121.

Mindermann, T. (1999) "Pressure gradients within the central nervous system," Journal of Clinical Neuroscience, 6(6), 464-466.

Monson, K.L., Barbaro, N.M., Goldsmith, W. and Manley, G. (2000) "Static and dynamic mechanical and failure properties of human cerebral vessels," Proceedings of Crashworthiness, Occupant Protection, and Biomechanics in Transportation Systems AMD-246/BED-49, 255-265.

Mooney, M. (1940) "A theory of large elastic deformation," Journal of Applied Physics, 11, 582-592.

Moore, K.L. and Dalley, A.F. (2006) "Clinically oriented anatomy," Baltimore: Lippincott Williams and Wilkins.

Moulton M. J., Cresswell L. L., Actis R. L. Myers, K. W., Vannier M. W. and Szabó, B. A. (1995) "An inverse approach to determining myocardial material properties," Journal of Biomechanics, 28, 935-948.

Mukundan, S. (2003) Personal Communication.

Nagashima, T., Tamaki, N., Matsumoto, S., Horwitz, B. and Seguchi, Y. (1987) "Biomechanics of hydrocephalus: a new theoretical model," Neurosurgery, 21, 898-904.

Netter, F.H. (2006) "Atlas of human anatomy," 4th edition, Saunders-Elsevier, Philadelphia, Pennsylvania, (www.netteranatomy.com).

Nolte, J. (2002) "The human brain: An introduction to its functional anatomy," Mosby, Inc.

Ogden, R.W. (1972) "Large deformation isotropic elasticity – on the correlation of theory and experiment for incompressible rubberlike solids," Proceedings of the Royal Society London Series A, 326, 565-584.

Ogden, R.W. (1997) "Non-linear elastic deformations," Dover Publications.

Oi, S., Shimoda, M., Shibata, M., Honda, Y., Togo, K., Shinoda, M., Tsugane, R. and Sato, O. (2000) "Pathophysiology of long-standing overt ventriculomegaly in adults," Journal of Neurosurgery, 92(6), 933-940.

Pamidi, M.R. and Advani S.H. (1978) "Nonlinear constitutive relations for human brain tissue," Journal of Biomechanical Engineering, 100, 44-48.

Pamplona, D.C. and Alvim, C.A. (2004) "Breast reconstruction with expanders and implants: A numerical analysis," Artificial Organs, Malden, 28, 353-356.

Pathmanathan, P., Gavaghan, D., Whiteley, J., Brady, M., Nash, M., Nielsen, P. and Rajagopal, V. (2004) "Predicting tumor location by simulating large deformations of the breast using a 3-D finite element model and nonlinear elasticity," MICCAI 2004, Lecture Notes in Computer Science 3216 and 3217 Springer-Verlag, 217-224.

Pechter, E. (1999) "Reply: Bra cup size depends on band size," Plast. Reconstr. Surg. 104: 300.

Pena, A., Bolton, M.D., Whitehouse, H. and Pickard, L.D. (1999) "Effects of brain ventricular shape on periventricular biomechanics: A finite-element analysis" Neurosurgery, 45(1), 107–116.

Penn, R.D., Lee, M.C., Linninger, A.A., Miesel, K., Lu, S.N. and Stylos, L. (2005) "Pressure gradients in the brain in an experimental model of hydrocephalus," Journal of Neurosurgery, 102, 1069-1075.

Prange, M.T. and Margulies, S.S. (2002) "Regional, directional, and age-dependent properties of the brain undergoing large deformation," Journal of Biomechanical Engineering, 124, 244-252.

Pudenz, R.H. and Foltz, EL. (1991) "Hydrocephalus: overdrainage by ventricular shunts. A review and recommendations," Surgical Neurology, 35(3), 200-212.

Purves, D., Augustine, G. J., Fitzpatrick, D., Katz, L.C., LaMantia, A.S. and McNamara, J.O. (1997) "Neuroscience," Sinauer Associated, Inc.

Puzrin, A., Ozan, C., Germanovich, L.N., Mukundan, S. and Skrinjar, O. (2006) "Inverse 3-D FE analysis of a brain surgery simulation," In Proceedings of Computational Biomechanics for Medicine Workshop of MICCAI'06.

Rajagopal, V., Nielsen, P.M.F. and Nash, M.P. (2004) "Development of a three-dimensional finite element model of breast mechanics," Proceedings of the 26th

Annual International conference of the IEEE EMBS, San Francisco, CA, Sept. 1-5, 5080-5083.

Rajagopal, V., Chung, J.-H., Warren, R., Highnam, R., Nash, M. and Nielsen, P. (2006) "Finite element modeling of breast biomechanics: Predicting the effect of gravity," Medical Image Computing and Computer Assisted Intervention (MICCAI), Copenhagen, Denmark, 94-103.

Raos, P. (1993) "Modelling of Elastic Behavior of Rubber and Its Application in FEA," Plastics, Rubber Compos. Proc. Appl., 19, 293-303.

Reulen, H., Graham, R., Spatz, M. and Klatzo, I. (1977) "Role of pressure gradients and bulk flow in the dynamics of vasogenic brain edema," Journal of Neurosurgery, 46, 24-35.

Rice, J.R. and Cleary, M.P. (1976) "Some basic stress diffusion solutions for fluid-saturated elastic porous media with compressible constituents," Reviews of Geophysics and Space Physics, (14), 227.

Rivlin, R.S. (1984) "Forty years of nonlinear continuum mechanics," Proceedings of the IX International Congress on Rheology, Mexico, 1-29.

Rivlin, R.S. (1948) "Large elastic deformations of isotropic materials. IV. Further developments of the general theory," Philosophical Transactions of the Royal Society of London, A241, 379-397.

Robbins and Cotran (2005) "Pathologic basis of disease," 7th Edition, Elsevier.

Roose, L., Maerteleire, W.D., Mollemans, W., Maes, F. and Suetens, P. (2006a) "Simulation of soft-tissue deformations for breast augmentation planning," ISBMS 2006, LNCS 4072, 197-205.

Roose, L., Mollemans, W., Loeckx, D., Maes, F. and Suetens, P. (2006b) "Bio-mechanically based elastic breast registration using mass tensor simulation," MICCAI 2006, LNCS 4191, 718-725.

Ropper, A.H. (2003) "Neurological and neurosurgical intensive care," Lippincott Williams & Wilkins.

Reulen, H. J., Graham, R., Spatz, M. and Klatzo, I. (1977) "Role of pressure gradients and bulk flow in dynamics of vasogenic brain edema," J. Neurosurgery, (46), 24.

Ruiter, N.V., Müller, T.O., Stotzka, R., Gemmeke, H., Reichenbach, J.R. and Kaiser, W.A. (2003) "Finite Element simulation of the breast's deformation during mammography to generate a deformation model of registration," Proceedings of the Workshop on Bildverarbeitung fuer die Medizin, Informatik Aktuell, 86-90.

Sahay, K.B., Mehrotra, R.,Schdeva, U. and Banerji, A.K. (1992) "Elastomechanical characterization of brain tissues," Journal of Biomechanics, 25(3), 319-326.

Samani, A., Bishop, J., Yaffe, M.J. and Plewes, D. B. (2001) " Biomechanical 3-D finite element modeling of the human breast using MRI data," IEEE Transactions on Medical Imaging, 20(4), 271-279.

Scanlon, V.C. and Sanders, T. (2007) "Essentials of anatomy and physiologhy," 5th edition," E.A. Davis Publishing Company, Philadelphia, Pennsylvania.

Schider, F. (1954) "An atlas of anatomy for artists," 6th Edition, Dover.

Schnabel, J.A., Tanner, C., Castellano-Smith, A.D., Degenhard, A., Leach, M.O., Hose, D.R., Hill, D.L.G. and Hawkes, D.J. (2003) "Validation of non-rigid image registration using FEM: Application to breast MR images," IEEE Trans. Medical Imaging, 22(2), 238-247.

Schneider, D.C., Davidson, T.M. and Nahum, A.M. (1984) "In-vitro biaxial stress-strain response of human skin," Archives of Otolaryngology, 110, 329-333.

Scott Camazine, www.scottcamazine.com (Accessed December 25, 2007).

Segall, P. and Fitzgerald., S.D. (1998) "A note on induced stress changes in hydrocarbon and geothermal reservoirs," Tectonophysics, 289, 117-128.

Silver, F. (1987) "Biological materials: Structure, mechanical properties, and modeling of soft tissues," New York University Press.

Sivaloganathan, S., Stastna, M., Tenti, G. and Drake, J.M. (2005a) "Biomechanics of the brain: A theoretical and numerical study of Biot's equations of consolidation

theory with deformation-dependent permeability," International Journal of Non-Linear Mechanics 40(9), 1149-1159.

Sivaloganathan. S., Stastna, M., Tenti, G. and Drake, J.M. (2005b) "A viscoelastic model of the brain parenchyma with pulsatile ventricular pressure," Applied Mathematics and Computation, 165(3), 687-698.

Skovoroda, A.R., Klishko, A.N., Gusakyan, D.A., Mayevskii, Y.I., Yermilova, V.D., Oranskaya, G.A. and Sarvazyan, A.P. (1995) "Quantitative analysis of the mechanical characteristics of pathologically changed soft biological tissues," Biophysics, 40, 1359-1364

Skrinjar, O.M., Studholme, C., Nabavi, A. and Duncan, J.S. (2001) "Steps toward a stereo-camera-guided biomechanical model for brain shift compensation," Lecture Notes in Computer Science: IPMI, 183-189.

Smillie, A., Sobey, I. and Molnar, Z. (2005) "A hydroelastic model of hydrocephalus," Journal of Fluid Mechanics, 539, 417-443.

Smith, B, Rinaudot G.R., Reed K.A. and Wright, T. (1988) "Initial graphics exchange specification (IGES) version 4.0," NBSIR 88-3813.

Sobey, I. and Wirth, B. (2006) "Effect of nonlinear permeability in a spherical model of hydrocephalus," Mathematical Medicine and Biology, 23, 339-361.

Stephensen, H., Tisell, M. and Wikkelso, C. (2002) "There is no transmantle pressure gradient in communicating or non-communicating hydrocephalus," Neurosurgery, 50(4), 763-773.

Subramaniam, R.P., Neff, S.R. and Rahulkumar, P. (1995) "A numerical study of the biomechanics of structural neurologic diseases," In A. Tentner (Ed.), High Performance Computing-Grand Challenges in Computer Simulation Society for Computer Simulations, San Diego, 552–60.

Sutton, D., Reznek, R. and Murfitt, J. (1999) "Textbook of radiology and imaging," 6th edition, Churchill Livingstone Publishers, Edinburgh, Scotland.

Sykova, E. (2004) "Diffusion properties of the brain in health and disease," Neurochemistry International 45, 453-466

Sykova, E., Mazel, T., Vargova, L., Vorisek, I. and Kubinova, S.P. (2000) "Extracellular space diffusion and pathological states," progress in brain research, 125, 155-178.

Tanner, C., Degenhard, A., Schnabel, J., Smith, A., Hayes, C., Sonoda, L., Leach, M., Hose, D., Hill, D. and Hawkes, D. (2001) "A method for the comparison of biomechanical breast models," IEEE Workshop on Mathematical Methods in Biomedical Image Analysis, 11-18.

Tanner, C., Schnabel, J., Hill, D., Hawkes, D., Leach, M. and Hose, D. (2006) "Factors influencing the accuracy of biomechanical breast models," Am. Assoc. Phys. Med., 33(6), 1758-1769.

Tarantola, A. (1987) "Inverse problem theory," Elsevier: Amsterdam.

Taylor, Z. and Miller, K. (2004) "Reassessment of brain elasticity for analysis of biomechanics of hydrocephalus," Journal of Biomechanics, 37, 1263-1269.

Tenti, G., Sivaloganathan, S. and Drake, J. (1999) "Brain biomechanics: steady-state consolidation theory of hydrocephalus," Can. Appl. Maths, Q7, 93-110.

Tenti, G., Drake, J. and Sivaloganathan, S. (2000) "Brain biomechanics: Mathematical modeling of hydrocephalus," Neurological Research, 22, 19-24.

Timoshenko, S.P., and J.N. Goodier (1970), Theory of elasticity, McGraw-Hill, NewYork, NY.

Toporek, C. and Robinson, K. (1999) "Hydrocephalus: A guide for patients, families, and friends," O'Reilly Media, p.355.

Vandeweyer, E. and Hertens, D. (2002) "Quantification of glands and fat in breast tissue: An experimental determination," Annals of anatomy, 184, 2, 181-184.

Velardi, F., Fraternali, F. and Angelillo, M. (2006) "Anisotropic constitutive equations and experimental tensile behavior of brain tissue," Biomechanics and Modeling in Mechanobiology, 5, 53-61.

Wang, H. (2002) "Theory of linear poroelasticity with applications to geomechanics and hyrdogeology," Princeton University Press.

Weller, R.O. (2005) “Microscopic morphology and histology of the human meninges,” Morphologie, 89, 22-34.

Wellman, P. (1998) “Breast tissue stiffness in compression is correlated to histological diagnosis,” Technical report, Harvard Bio-Robotics Lab.

Wellman, P.S. and Howe, R.D. (1998) “Breast tissue stiffness in compression is correlated to histological diagnosis,” Harward Bio-Robotics Lab. Report, #98-121.

Williams, C., Kakadaris, I.A., Ravi-Chandar, K., Miller, M.J. and Patrick, C.W. (2003) “Simulation studies for predicting surgical outcomes in breast reconstructive surgery,” MICCAI, LNCS 2878, 9-16.

Wirth, B. and Sobey, I. (2006) “A cylindrically symmetric and fully three dimensional poroelastic model for the onset and treatment of hydrocephalus,” Mathematical Medicine and Biology, 23, 363-388.

Wittek, A., Kikinis, R., Warfiled, S. K. and Miller, K. (2005) “Brain shift computation using fully nonlinear biomechanical model,” Proceedings of MICCAI’05, Palm Springs, California, 583-590.

Wittek, A., Miller, K., Kikinis, R. and Simon K. Warfield, S.K. (2006) ”Patient-specific model of brain deformation: Application to medical image registration,” Journal of Biomechanics, Article in Press.

Wu, J.Z., Dong, R.G. and Schopper, A.W. (2004) “Analysis of effects of friction on the deformation behavior of soft tissues in unconfined compression tests,” Journal of Biomechanics, 37, 147-155.

Wu, D.H., Archer, A.G., Hast, L.J., Elledge, B., Beall, D., Walter, M., Edwards, S.M., Webb, H.R., Greer, B.J. and Rubesova, E. (2006) “Fundamentals of achieving functional and anatomical imaging with breast MRI: Physical and clinical concepts,” Ed: Suri, J.S. and Rangayyan, R.M., Recent Advances in Breast Imaging, mammography, and Computer-Aided Diagnosis of Breast Cancer, Bellingham, Wash, 51-109.

Yamashima, T. and Friede, R.L. (1984) “Why do bridging veins rupture into the virtual subdural space,” Journal of Neurology, Neurosurgery, and Psychiatry, 47, 121-127.

Yin, H.M., Sun, L.Z., Wang, G., Yamada, T., Wang, J. and Vannier, M.W. (2004) "ImageParser: A Tool for finite element generation from three-dimensional medical images," BioMedical Engineering OnLine, 3(31).

Zhang, L., Bae, J., Hardy, W.N., Monson, K.L., Manley, G.T., Goldsmith, W., Yang, K.H. and King, A.I. (2002) "Computational Study of the contribution of the vasculature on the dynamic response of the brain," Stapp Car Crash Journal, 46, 145-163.

Zoghi-Moghadam, M., Sadegh, A. and Watkins, C. (2003) "Arachnoid trabeculae and csf roles in blunt head impact," Proceedings of IMECE'03, ASME International Mechanical Engineering Congress, Washington, D.C., 317-318.